CRANFIELD UNIVERSITY

Michael Anthony Cooper

SIMULATING ACTUATOR ENERGY DEMANDS OF AN AIRCRAFT IN FLIGHT

SCHOOL OF ENGINEERING

Department of Aerospace Engineering

Ph.D. THESIS
Academic Year: 2014

Supervisor: Dr Craig Lawson
February 13, 2014

Cranfield University

School of Engineering
Department of Aerospace Engineering

Ph.D. THESIS

Academic Year: 2014

Michael Anthony Cooper

Simulating Actuator Energy Demands of an Aircraft in Flight

Supervisor: Dr Craig Lawson

February 13, 2014

This thesis is submitted in partial fulfilment of the requirements for the degree of Doctor of Philosophy

Abstract

This thesis contributes towards the discipline of whole aircraft simulation; modelling flight dynamics and airframe systems simultaneously. The objective is to produce estimates of the dynamic power consumption characteristics of the primary flight control actuation system when executing manoeuvres. Three technologies are studied; the classic hydraulic actuators and the electromechanical and electro-hydrostatic types that are commonly associated with the more electric aircraft.

Models are produced which represent the flight dynamics of an aircraft; these are then combined with low frequency dynamic functional models of the three actuator technologies and flight controllers. The result is a model, capable of faster than real time simulation, which produces estimates of actuator power consumption as the aircraft follows predefined trajectories.

The model is used to quantify the energy consumption as a result of different manoeuvre rates when executing banked turns. The result from an actuation system point of view alone is that the lower the turn rate, the lower the overall energy used. The tradeoff is that the turn radius becomes larger.

The use of the model can be extended to assist with additional design challenges such as actuator design and specification. Using methods to size actuators based on stall force and no load speed properties leads to oversizing of the control system. Performing dynamic analyses is usually a combined task of laboratory based actuator test rigs stimulated by input data gathered

during flight tests. The model in this work provides a method of generating data for preliminary design; therefore reducing the amount of flight testing required in a design and certification programme.

The major results discovered using the tools developed in this thesis are that a hydraulically powered aileron uses 4.23% more energy to achieve a turn at a heading rate of 0.03 rad/s compared to a 0.005 rad/s manoeuvre in the same conditions. The electromechanical actuator (EMA) uses 1.67% more and the electrohydrostatic actuator (EHA) uses 1.54% more to achieve the same turns. It implies reduced turn rate turns would have the largest benefit for reducing energy consumption in current hydraulically powered actuation systems, compared to electrical actuators.

Acknowledgement

This thesis has consumed more days, nights and weekends than I would wish to put a number on. A student working towards a doctorate will find themselves 'in the office' at most times of the day; whether behind a computer or at home with work on the mind. Those that have not suffered it will not understand it, but those that have; will never regret it.

Me, I find my forehead slightly flattened from the number of times head has met desk; as I cried for Matlab's prowess at producing undecipherable error messages. I reminisce of solving the umpteenth 'one more problem' while friends and family suggested much more exciting events than wearing the lettering off my keyboard. Indeed, it was pointed out early on that while a supervisor is imperative for technical guidance; a good part of their purpose is to maintain the sanity of their students on the lonely journey.

Unfortunately, I cannot say the same for those two keyboards that decided to part ways with me in the process; but my supervisor did a marvellous job of balancing support, guidance and leaving the student to their own devices (and providing the odd sanity check). To him I offer my greatest thanks; both for the support and the opportunity.

Academia aside, I loathe to think where I would be without the personal support that has endured the last four years with me. My partner Claire has smiled and nodded through countless boring descriptions of the finer points of aileron behaviour. She knew when to give me space (during the

aforementioned head-meeting-desk periods) and when to provide support. My house mate Shakeel provided seemingly endless discussion on the topics of simulation, flight dynamics, actuator mechanics, aerodynamics and generally anything too geeky to be mentioned in general society.

A document such as this would probably be most appropriately measured by mass or volume, rather than word counts or pages. A publication of this mass can hardly go without gratitude towards my parents, who have pushed me, supported me and criticised me when appropriate.

Cranfield itself has provided a raft of support which does not fit anywhere else in this acknowledgement; the Clean Sky team, Daniele, Usman, Ravinka and Shinkafi for discussions on the sponsoring industrial project and otherwise. Barry Walker who, quite frankly, the experimental work would not have been possible without.

Unwittingly, those that have made work at Cranfield more difficult also deserve thanks; you bestow upon people the experience of what is inevitable in professional life, thus you allow us to grow.

Contents

List of Figures

List of Tables

Nomenclature

Term	Description	Units
A_c	Piston area	m^2
a	Actuator base mount to control surface mount distance	m
α	Angle of attack	rad
α_w	Angle of attack at the wing that the control surface is attached to	rad
h	Altitude	m
A_w	Area of control surface	m^2
b	Wing span	m
b_0	Actuator base mount to rod end neutral distance	m
β	Angle of sideslip	rad
β	Angle between lengths a and c in control surface installation geometry	rad
$\dot{\beta}$	Angle of sideslip rate	$rads^{-1}$
β_e	Bulk modulus of fluid	Pa
b	Actuator base mount to rod end distance	m
B_v	Viscous friction coefficient	Nsm^{-1}
$\bar{c}$	Mean aerodynamic chord of wing	m
C_{12}	Leakage flow coefficient (past the piston)	$m^3s^{-1}Pa$
C_C	Coulomb friction coefficient	N
$\bar{c}_c$	Mean aerodynamic chord of control surface	m
C_{coul}	Coulomb friction coefficient	N
C_D	Drag coefficient	-
c_h	Hinge moment coefficient	-
$c_{h\alpha}$	Hinge moment derivative due to angle of attack	-
$c_{h\delta}$	Hinge moment derivative due to control surface deflection	-
C_L	Lift coefficient	-

Term	Description	Units
C_l	Rolling moment coefficient	-
c	Actuator rod end to control surface mount distance	m
C_m	Pitching moment coefficient	-
C_n	Yawing moment coefficient	-
C_Y	Side force coefficient	-
D	Pump displacement	m^3rad^{-1}
δ	Control surface position	rad
δ_a	Aileron position	rad
δ_e	Elevator position	rad
δ_r	Rudder position	rad
δ_{tc}	Throttle command	-
D	Aerodynamic drag	N
E	Total energy	J
$\dot{E}_s$	Specific energy rate	$Jskg^{-1}$
η_{bs}	Ball screw efficiency	-
η_c	Cylinder efficiency	-
η_m	Motor efficiency	-
η_p	Pump efficiency	-
η_{vdp}	Efficiency of variable displacement pump	-
$\mathbf{F}$	Force vector	N
$\mathbf{F}_a$	Aerodynamic force vector	N
$\mathbf{F}_b$	Force vector expressed in the body frame $\mathcal{F}^b$	N
$\mathbf{F}_g$	Gravity force vector	N
$\mathbf{F}_i$	Force vector expressed in the inertial frame $\mathcal{F}^i$	N
F_L	Load force	N
$\mathbf{F}_p$	Propulsive force vector	N
$\mathcal{F}^b$	Body reference frame ($\mathcal{F}^{v2}$ rotated by ϕ)	-
$\mathcal{F}^v$	Vehicle reference frame (Centered on aircraft CG, aligned with $\mathcal{F}^i$)	-
$\mathcal{F}^{v1}$	Vehicle reference frame 1 ($\mathcal{F}^v$ rotated by ψ)	-
$\mathcal{F}^{v2}$	Vehicle reference frame 2 ($\mathcal{F}^{v1}$ rotated by θ)	-
F_s	Stall force	N
F_x	Force in x direction in the body frame $\mathcal{F}^b$	N
F_y	Force in y direction in the body frame $\mathcal{F}^b$	N
F_z	Force in z direction in the body frame $\mathcal{F}^b$	N
γ	Flight path angle w.r.t. air mass	rad
g	Acceleration due to gravity	ms^{-2}

Term	Description	Units
$\mathbf{h}$	Angular momentum vector in inertial frame $\mathcal{F}^i$	Nms
$\oslash$	Hadamard division (element-wise vector division)	-
$\mathbf{h}^b$	Angular momentum vector in body frame $\mathcal{F}^b$	Nms
i_a	Armature current	A
I_{DC}	Current required on the DC link bus in the power converter	A
I_V^*	Torque motor current normalised by its saturation current	-
J	Total inertia of motor and load	kgm^2
$\mathbf{J}$	Inertia matrix	kgm^2
J	Inertia of rotating components seen by motor	kgm^2
$\bar{J}$	Reflected inertia	kgm^2
J_{bs}	Inertia of ball screw	kgm^2
J_m	Inertia of motor	kgm^2
K_{cm}	$\tanh(x)$ crossover sharpness	-
K_{EI}	TECS elevator loop integral gain	-
K_{EP}	TECS elevator loop proportional gain	-
K_m	Transmission and material stiffness	N^{-1}
K_t	Torque constant of motor	NmA^{-1}
K_{TI}	TECS throttle loop integral gain	-
K_{TP}	TECS throttle loop proportional gain	-
K_v	Velocity constant of motor	Vsrad^{-1}
L	Moment about x axis in the body frame $\mathcal{F}^b$	Nm
L_a	Armature inductance	H
L_c	Actuator piston stroke	m
L_t	Torque motor inductance	H
M	Moment about y axis in the body frame $\mathcal{F}^b$	Nm
m	Aircraft mass	kg
M	Mach number	-
M_l	Load mass	kg
$\mathbf{M}$	Total externally applied moment vector	Nm
$\mathbf{M}_a$	Aerodynamic moment vector	Nm
$\mathbf{M}^b$	Total externally applied moment vector in body frame $\mathcal{F}^b$	Nm
$\mathbf{M}_p$	Propulsive moment vector	Nm
M_v	Servovalve peak amplitude ratio	-
N	Moment about z axis in the body frame $\mathcal{F}^b$	Nm

Term	Description	Units
ω_a	Angular velocity of motor	rads^{-1}
$\boldsymbol{\omega}_{b/i}$	Angular velocity of aircraft in body axes, w.r.t. inertial frame	rads^{-1}
ω_n	Servovalve spool undamped natural frequency	rads^{-1}
P	Pressure	Pa
p	Ball screw pitch	m
p	Roll rate expressed in the body frame $\mathcal{F}^b$	rads^{-1}
p_d	Down position expressed in the inertial frame $\mathcal{F}^i$	m
P_{Dr}	Power loss from three phase diode rectifier	W
p_e	East position expressed in the inertial frame $\mathcal{F}^i$	m
$P_{fluid(pump)}$	Fluid power from pump	W
ϕ	Euler roll angle	rad
Φ''	Aerofoil trailing edge shape factor	-
P_l	Pressure dropped across the load	Pa
P_{Loss}	Pressure loss	Pa
p_n	North position expressed in the inertial frame $\mathcal{F}^i$	m
P_s	Supply pressure (across pump)	Pa
ψ	Euler yaw angle	rad
P_t	Tank pressure	Pa
ΔP_v	Pressure dropped across the servo valve	Pa
q	Dynamic pressure	Pa
q	Pitch rate expressed in the body frame $\mathcal{F}^b$	rads^{-1}
Q_{12}	Leakage flow rate past the piston	m^{3}s^{-1}
Q_c	Flow rate at cylinder	m^{3}s^{-1}
Q_e	External leakage flow rate	m^{3}s^{-1}
Q_i	Flow rate at cylinder inlet	m^{3}s^{-1}
Q_{in}	Net flow rate at cylinder inlet	m^{3}s^{-1}
Q_L	Load flow rate	m^{3}s^{-1}
Q_o	Flow rate at cylinder outlet	m^{3}s^{-1}
Q_{out}	Net flow rate at cylinder outlet	m^{3}s^{-1}
Q_P	Pump flow rate	m^{3}s^{-1}
Q_R	Rated flow rate	m^{3}s^{-1}
r	Yaw rate expressed in the body frame $\mathcal{F}^b$	rads^{-1}
R_a	Armature resistance	Ω
R_F	Resistance of a rectifier diode during conduction	Ω

Term	Description	Units
ρ	Air density	kgm^{-3}
R_t	Torque motor resistance	Ω
$\mathcal{R}_v^b$	Rotation matrix from vehicle to body frame	-
S	Wing planform area	m^2
T	Total torque on motor	Nm
τ	Reflected inertia	kgm^2
$\frac{t}{\bar{c}}$	Aerofoil thickness ratio	-
T_{coul}	Torque applied by Coulomb friction	Nm
T_e	Electromagnetic torque of motor	Nm
θ	Euler pitch angle	rad
θ_m	Motor angular position	rad
T	Thrust	N
T_{com}	Thrust command	N
T_{req}	Thrust required	N
T_L	Load torque on motor	Nm
T_ω	Torque applied by viscous friction	Nm
$T_{\dot{\omega}}$	Torque required to accelerate an	Nm
u	Forward velocity expressed in the body frame $\mathcal{F}^b$	ms^{-1}
v	Sideways velocity expressed in the body frame $\mathcal{F}^b$	ms^{-1}
V_0	Fluid volume in transmission lines	m^3
V_{01}	Dead volume in chamber 1	m^3
V_{02}	Dead volume in chamber 2	m^3
V_{1c}	Volume displaced by piston translation in chamber 1	m^3
V_{2c}	Volume displaced by piston translation in chamber 2	m^3
V_a	Armature voltage	V
V_{emf}	Back emf voltage	V
V_F	Rectifier diode forward voltage drop	V
$\mathbf{V}_g$	Velocity vector w.r.t. the ground, expressed in the inertial frame $\mathcal{F}^i$	ms^{-1}
$\mathbf{V}_g^b$	Velocity vector w.r.t. the ground, expressed in the body frame $\mathcal{F}^b$	ms^{-1}
V_{La}	Voltage across armature inductance	V
V_{Ra}	Voltage across armature resistance	V
V_T	True airspeed	ms^{-1}
V_t	Fluid volume between pump and transmission lines	m^3

Term	Description	Units
$\dot{V}_T$	Flight path acceleration	ms^{-2}
w	Downwards velocity expressed in the body frame $\mathcal{F}^b$	ms^{-1}
W	Weight	N
x	Actuator displacement	m
$\dot{x}$	Actuator piston velocity	ms^{-1}
$\dot{x}_{NL}$	No load actuator piston velocity	ms^{-1}
x_l	Load mass position	m
x_m	Motor equivalent translational position (through gearbox and screw pitch)	m
ζ	Servovalve spool damping ratio	-

Acronyms

Term	Description
6-DOF	6 Degree Of Freedom
A/P	Autopilot
AC	Alternating Current
AOA	Angle Of Attack
BLDC	Brushless Direct Current
CAS	Calibrated Airspeed
CFD	Computational Fluid Dynamics
COTS	Commercially Available Off-the-shelf
DC	Direct Current
EBHA	Electrical Backup Hydrostatic Actuator
EDP	Engine Driven Pump
EHA	Electrohydrostatic Actuator
EHA-FP	Fixed Pitch Electrohydrostatic Actuator
EHA-VP	Variable Pitch Electrohydrostatic Actuator
EHL	Elastohydrodynamic Lubricant
EMA	Electromechanical Actuator
EMF	Electromotive Force
EMI	Electromagnetic Interference
EPAD	Electrically Powered Actuation Design
ESHA	Electro-Servohydraulic Actuator
FAA	Federal Aviation Administration
FBW	Fly-By-Wire
FCS	Flight Control System
FMC	Flight Management Computer
FRT	Faster Than Real Time
HTTB	High Technology Test Bed
HUD	Head Up Display
IAP	Integrated Actuator Package
IGBT	Insulated-gate Bipolar Transistor
MDP	Motor Driven Pump

Term	Description
MIMO	Multi Input - Multi Output
MTBF	Mean Time Before Failure
PBW	Power-By-Wire
PFD	Primary Flight Display
PI	Proportional + Integral
PID	Proportional + Integral + Differential
PIV	Proportional + Integral + Velocity
PWM	Pulse Width Modulation
RAT	Ram Air Turbine
RMS	Root Mean Square
RT	Real Time
SISO	Single Input - Single Output
SR	Switched Reluctance
SRPM	Switched Reluctance Permanent Magnet
STAR	Standard Terminal Arrival Route
TECS	Total Energy Control System
THCS	Total Heading Control System
TTB	Time-To-Bank
UAV	Unmanned Aerial Vehicle
VDP	Variable Displacement Hydraulic Pump

Chapter 1

Introduction

1.1 Overview and Motivation

Trajectory optimisation is a field which dates back to the beginnings of conscious life; how to get from A to B in the shortest time or expending the minimum amount of energy possible. It is a problem which affects many people; from how long it takes to navigate across a city using in-car navigation, to how much fuel is burnt by an aircraft on an intercontinental flight.

In the earliest days a biological computation took place inside an organism, which combined knowledge about itself such as its size and made a decision of whether it should go around an obstacle or over it. These same situations occur in modern engineering problems such as that of an aircraft navigating an icing cloud. Depending on the severity of the conditions, the pilot is presented with the decision of flying through the weather system with anti-icing systems engaged or to navigate around it.

From an energy perspective both options demand an increase in fuel burn from the 'good weather' flight path, but making a well informed decision requires good knowledge of the power consuming airframe systems involved. The decision is not binary since more than one system can be involved in executing a manoeuvre; in this case the aircraft has the option to fly over the

weather system (which increases the demands on the environmental control system and engines), but may avoid ice protection system energy penalties.

This thesis investigates one small facet of this problem; how much energy does an aircraft consume while manoeuvring? This question can be answered using many techniques with varying levels of fidelity. The most basic can be estimating average power and multiplying it by time, the most detailed would likely involve flight testing on real hardware. The work presented herein seeks to quantify the dynamic energy consumption of the flight control system at a functional level through simulation.

To date, conducting experiments of actuator power consumption requires knowledge about how the actuators are utilised during flight. This can range from rudimentary estimations using step responses for preliminary work, but is often extended throughout a whole flight using '*typical*' duty cycles. This data can either be estimated using such approximations as the 80:20 rule [1] or quantified from test flights as presented by Simsic [2]. The word typical is emphasised because it is an important question - what is typical? Simsic's work is deduced from a mission profile of a military transport aircraft - is this necessarily applicable to a civil transport aircraft?

Other authors have performed actuator analysis using confidential data supplied uniquely to the them as a result of their relationship with an airframe manufacturer [3, 4]. This is ideal and perhaps the only solution when the utmost realism is desired, for situations such as certification.

This leaves a gap in the methodology for both the preliminary design of actuators and top level aircraft energy analysis and prediction for trajectory optimisation tasks. Neither of the two methods mentioned previously have the flexibility to model *other* manoeuvres. If the aim is to analyse total aircraft energy consumption in dynamic situations such as navigating weather

systems, using *typical* input data to estimate actuator power consumption is not going to provide the fidelity required.

Another possibility is investigating the relationship between manoeuvre rates and actuator transient energy demands. Whilst it is possible to fly an aircraft and record signals such as control surface deflections and actuator power, this costs money and only provides a limited set of input data. The data is limited to the aircraft type, the trajectories flown and to the variables which are measured and recorded during the sample flights. Preliminary test data can instead be generated using a 6 degree of freedom (6-DOF) flight dynamics model which is fast, cost effective and can generate any number of datasets for any trajectory of interest. This data can be generated, saved and used independently for actuator simulation and design work. This thesis seeks to develop this concept further by integrating low frequency functional actuator models with an aircraft model. This will allow their dynamic interactions and the power consumption of the actuators to be quantified.

Indeed, it is common to include actuator models in 6-DOF aircraft models to represent the lag between the control surface command and position response for flight control system (FCS) design. In these cases the models are either first, second or higher order transfer function models which are only interested in the dynamic position response [5]. This thesis seeks to integrate system models for the actuators, modelling the main internal mechanisms such as motor parameters and hydraulic pressures. By integrating the actuator models with corresponding control systems and 6-DOF model, multidisciplinary cooperation is encouraged between the flight control, actuation system and power system design teams. The combined model allows, for example, the realisation early on in a project that a specific actuator design does not have the required force, speed or frequency response characteristics.

This will become evident because the actuator models emulate the reduction in performance and increasing efficiency as load increases, thereby affecting how the whole aircraft manoeuvres. Classically, this is something that is only possible further into a design project where the cost of redesign has increased.

The challenge is to design actuator models which provide a reasonable level of detail of the power losses whilst still allowing faster than real time (FRT) simulation. This is a key requirement if complete flight trajectories are going to be simulated; it is not practical to have a model for this purpose which works at real time (RT) or slower because of the length of a commercial aircraft flight.

1.2 Research Novelty and Publications

There are multiple components in this thesis which contribute to knowledge in engineering modelling and simulation. Firstly, dynamic models are developed which simulate the motion and power consumption of hydraulic, electromechanical and electro-hydrostatic actuators at functional level. These have been adapted from literature where the modelling aim is generally to represent the dynamic motion and frequency response for control design tasks. To simulate a wide frequency range accurately requires detailed models, inherently this also means comparatively slow simulations. The models produced in this work are capable of achieving significantly faster than real time speeds.

The presented work also contributes to the field of complete aircraft simulation; where flight dynamics models are coupled with various systems models such as actuators or environmental controls systems. To the best of the author's knowledge, the method presented in this thesis is the only continuous-

time simulation of an aircraft with realistic actuator models in the loop for power consumption estimation. Additionally, three actuator technologies are included; the current state of the art (hydraulic systems) and the two most prominent electrically powered alternatives (electromechanical and electro-hydrostatic).

With the compliment of a flight control and guidance system, the complete aircraft model becomes capable of quantifying the dynamic power consumptions of the actuators as the aircraft flies a predefined trajectory. This makes it possible to simulate a flight from takeoff to landing, while generating data for both the peak and average powers and how much energy is consumed. This data can be used in place of flight test data in the preliminary design of actuators, allowing the creation of data for arbitrary trajectories, weather conditions, aircraft types and so forth. This would supersede the use of average duty cycles in sizing actuators and quantifying power consumption, which can often lead to significant overestimation of the capacity required. Aside from the actuators themselves, the transient power consumption data is useful to engineers who design the secondary power systems. Having data available (without great expense) to analyse the system response to peak and average power demands critical to designing efficient systems.

Publications

- 28th International Congress of the Aeronautical Sciences, Brisbane, Australia, 2012. *"Towards Trajectory Prediction And Optimisation For Energy Efficiency Of An Aircraft With Electrical And Hydraulic Actuation Systems"*, Cooper, M. A., Lawson, C. P., Quaglia, D., Zammit-Mangion, D., and Sabatini, R. [Published]

- AIAA Journal of Aircraft. *"Simulating Aircraft Manoeuvres to Min-*

imise Actuator Energy Consumption", Cooper, M. A., Lawson, C. P. [Submitted]

1.3 Thesis Structure

This thesis begins with a review of the relevant literature in all the technical areas covered by the research; by definition this section is long because of the wide scope of the topic. Relevant actuation technologies, aircraft flight dynamics modelling, aerodynamic load estimation, flight control and guidance literature are all covered in this section.

Secondly the high speed actuator models are developed for use in the subsequent sections. The unsuccessful experimental validation of the actuator models is presented next.

The following section covers the integration of the actuators, aircraft, aerodynamic load estimator and flight controller into a unified model of an aircraft and its actuation system. Once the integrated aircraft model is complete, the method used to analyse the actuator power consumption while executing different rate turns is defined. This method is then applied to two diverse aircraft types; firstly an Airbus A320 transport aircraft and secondly a small UAV, the Aerosonde weather reconnaissance vehicle.

The final section draws conclusions on the method as a whole, before recommending directions for future development of the strategy.

Chapter 2

Literature Review

2.1 The Case for Optimisation

Commercial aviation is a success story of the 20$^{\text{th}}$ century. In a little under 100 years the industry has progressed from achieving the first powered, controlled and sustained flight of a heavier-than-air vehicle; the 1903 Wright Flyer to a point where, by the year 2000, 22 million registered departures occurred in the year 2000 around the world [6]. 5 million of these commercial flights took off from the European Union and 9.8 million departed from the United States. Compared with aircraft in history, the passengers on board these flights travel in *relative* comfort and most importantly, with a very high safety factor.

Moving into the 21$^{\text{st}}$ century, the challenges move on to maximising aircraft efficiency and finding novel ways to provide power in order to minimise our environmental impact. This is not limited to making modifications to the aircraft themselves, it also requires optimisation of the air traffic network, management systems and flight trajectories. Indeed, it is not a trivial problem since the system as a whole is not optimised by improving one aircraft's trajectory at the expense of another's; it is a complex multi-domain optimisation task requiring knowledge of many characteristics of the aircraft

and environment.

Considering first the aircraft's environment, which may include both the natural environment (terrain and weather systems) and man made environment (other aircraft); it can be appreciated that large numbers of aircraft converging on a hub airport such as Heathrow would ideally be scheduled to join the standard terminal arrival route (STAR) at specific times in order to avoid any aircraft flying holding patterns. By doing this an aircraft spends less time in the air, producing thrust and generating emissions and noise.

This type of problem was addressed by the Schiphol Night Time Continuous Descent Approaches project [7] which used a ground based planning system to communicate with flight management computers on board inbound aircraft. By giving the planning system the ability to optimise the inbound aircraft's planned times of arrival it could ensure they arrive with suitable spacing in between them to avoid entering holding patterns and generating unnecessary noise over Amsterdam at night.

The next part of the puzzle is to take into account the natural environment, choosing optimum routes over terrain while avoiding weather systems if necessary. An extension to this is to use the weather where possible by using jet streams or other tail winds to save fuel. Frequently the jet stream route is longer (Figure 2.1); depending on daily variations and the aircraft entry and exit points this may not always present the most economic transit between two city pairs. The computation required to optimise this is significant and strongly coupled with the aircraft performance itself; as mentioned previously, the task of optimising the air traffic system is not trivial.

This brings the subject onto optimising the aircraft itself. This may consist of several tasks; from optimising the airframe to minimise mass and drag, improving the efficiency of the propulsion and on-board secondary power con-

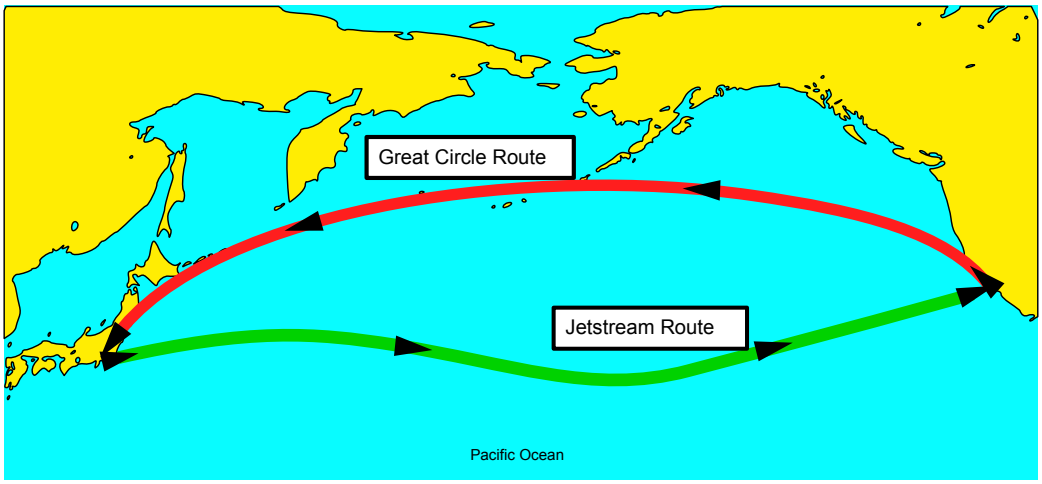

Figure 2.1: Great circle and jet stream routes between Japan and North America

sumers to optimising the avionics and how the aircraft is actually flown. The overall power required to maintain an aircraft in steady level flight depends on the drag D and velocity V_T of the aircraft, as represented in Figure 2.2. The power required from the engines is calculated using the product of these two components;

$$P = DV_T \tag{2.1}$$

demonstrating that reducing the power consumption due to thrust either means flying slower or reducing airframe drag by optimising shape and surface finish. Although this is the most significant energy demand on the aircraft, the power off-takes required to drive the secondary power consumers is substantial. Around 95% of the total energy produced by the engines is used to power airframe systems during the descent, landing and taxi phases (see Figure 2.3) [8].

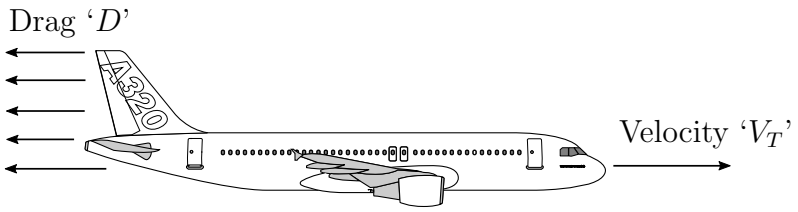

Figure 2.2: Contributions to overall aircraft power required for flight

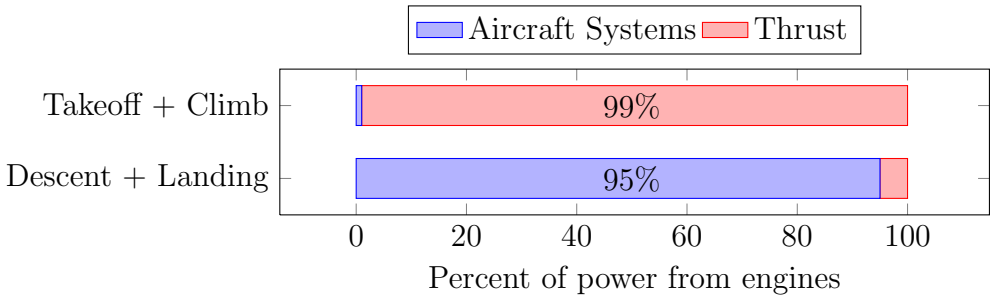

Figure 2.3: Ratio of engine power usage at different flight phases [8]

2.2 Combined Aircraft and Systems Simulation

Commonly simulations are performed at component or subsystem level; only the behaviour of the system of interest is represented and it is considered to be isolated. This is acceptable for component specification of that system alone, but when considering the integration of that system at aircraft level things become more complicated. There are interactions between power consumers, their suppliers and also between different subsystems. For example; the engine, environmental control system and wing ice protection systems are all linked at the compressor stage of the turbofan engine.

This problem drives the development of full aircraft simulations; but classically this requires simplified models because of limited computing power. Having separate models of the same subsystem complicates the design process, since changes in the design requires multiple models to be updated. Aside from this, there is of course the problem that using simplified versions

of the models means potentially important behaviour is ignored until the real hardware is integrated; a point at which design revisions can be costly.

Classical simulation uses a single solver which iterates the differential equations which characterise the system. Because each time step is based on the previous time step, it is not straightforward to distribute the simulation between different threads. To overcome this limitation with software such as Simulink, multi-threaded simulation must be achieved in a less ideal way by simply duplicating the simulation and executing multiple cases at once. Indeed, this is only of benefit when, for example, parameter sweeps are being performed. It is of no use when a single, long and complex simulation is desired.

This issue has been identified and a solution presented in the form of distributed transmission line modelling using software such as Hopsan [9]. This software has the capability of distributing each subsystem to a different processor core, computer or geographical site. The numerical solution is robust, fast, and allows the source code to be kept secret from other collaborators as discussed by Krus *et al.* [10, 11, 12, 13, 14]. This software is still in development, but its potential to advance the field of complete aircraft simulation is highly regarded. However, Hopsan is not used in this work for several reasons; the Author is very familiar with Simulink which is an established and well supported commercial software. Although free, Hopsan is a development software with an unknown amount of support, basing a thesis on software in this form is potentially hazardous. It is however recognised that the research performed in this thesis will push the limits of the single solver simulation engine in Simulink. For longer term future development involving more diverse subsystems, distributed solvers are likely to form the keystone in scalable complexity simulations.

2.3 Actuation Systems

This section seeks to provide a background of flight control actuation systems. It will cover briefly their history from the earliest days of aviation, through to the current technology in commercial service today before finishing at the state of the art to be used in next generation aircraft. With regards to the development of the current state of the art, major technology demonstration programmes will be presented which have pioneered the current technology readiness level.

2.3.1 Current Actuator Trends and the More Electric Aircraft

Actuator technology has progressed significantly since the days of the first flying machines; the Wright Brothers' 'Flyer' was mechanically controlled using a system of cables and pulleys. The pilot was the source of energy to power the system; he wore a cage around the waist that was connected to the trailing edges of the wing tips and the rudders via cables. When the pilot wanted to induce a roll he moved his hips in a lateral direction, pulling the cable and warping the wings. This caused a variation in the span wise lift distribution across the wings and hence, a rolling moment.

Very few aircraft are still controlled this way, only ultralight hobby aircraft such as microlights are equipped with wing warping control systems. General aviation aircraft are most often made of aluminium or composite materials, neither of which provide the flexibility required for wing warping systems.

Modern aircraft are equipped with hinged control surfaces which have the same effect of varying the lift distributions across the respective aerodynamic surfaces. A summary of the control surfaces and their effects can be found

in [15]. These hinged actuators can be effected using cables and pulleys on smaller aircraft, where the aerodynamic loading is not above that which a human can reasonably handle and manipulate. Once an aircraft reaches a certain size it becomes impossible to implement a pilot powered control system as the aerodynamic surfaces have to be large. The larger a control surface becomes, the greater the aerodynamic forces on it are and the greater the hinge moments and stick forces become.

To succeed in building large aircraft it is clear that more powerful actuation techniques are required; this led to the development of mechanically signalled hydraulic systems to provide control surface power. These systems will not be covered in this work as the mechanical signalling limits the possibility of implementing electronic control techniques.

The most common form of actuator signalling in modern aircraft is that of the electro-hydraulic servovalve; an electrically signalled, hydraulically powered system. In these systems a low power electronic signal is sent to the actuator which commands the hydraulic valve into a position that allows or blocks hydraulic fluid flow into the cylinder, in response to the pilot's command. These systems provide the high energy density required to move the control surfaces, but also enable easy integration with on-board flight control computers. This technology is known as fly-by-wire (FBW) and was first used commercially in a full authority configuration on the Airbus A320 [16] when it first flew in February 1987.

In a current FBW aircraft the majority of actuator control functions are still provided by the central flight control computer. This centralised loop closure means longer signal propagation latencies than local controllers and greater susceptibility to electromagnetic interference (EMI). A current trend is towards the implementation of 'smart' actuators - those which have lo-

calised control computers which provide at minimum loop closure, but can possibly provide an array of other benefits such as actuator specific health monitoring, fault prognosis and reporting back to the central computer. This means the actuators can be certified individually and the flight control computer becomes functionally simpler [17].

Recent trends have been towards delivering the power for the actuators in an electrical form in an effort to reduce the life cycle costs of maintaining the aircraft by removing the hydraulic systems [18]. There are numerous other benefits to this technology which will be covered throughout the course of this work. The principle of 'power-by-wire' is not a new idea; as early as 1944 electrically powered actuation systems in the forms of electromechanical and electric motor driven localised hydraulic systems were developed [19]. They have not achieved widespread acceptance as yet due to concerns about mechanical jamming and the heat produced while holding a load at zero velocity.

One of the earliest commercial trade studies to be undertaken on the topic of electromechanical actuation is that conducted in [20], where the authors summarise the research completed by Boeing and Rockwell in the 1980s. The results from these preliminary studies are by no means groundbreaking; Boeing concluded their baseline aircraft would remain roughly the same mass when switched to electromechanical actuation, while Rockwell predicted a 21.5% increase in aircraft mass. What can be noticed however is that in both cases, the mass of the aircraft's secondary power systems decreased when EMAs were introduced. The authors of this work concluded that the overall aircraft mass did not decrease because Boeing and Rockwell did not completely remove the previous secondary power systems (hydraulic and bleed air systems) from the models; couple this with the increased weight

Table 2.1: Table showing estimated mass reductions achievable by replacing the third hydraulic system with two electrical systems to power electric actuators [21]

Aircraft	Mass reduction
A31X	70 kg
A320	100 kg
A340	250 kg
A380	450 kg

of the electric actuators themselves and the authors' conclusions begin to make sense. In effect, the hypothetical aircraft were fully equipped to supply both electric and hydraulic actuators. In a later study van den Bossche estimated the mass reductions obtainable by removing the third hydraulic system (and all associated peripherals) to be those shown in Table 2.1.

The drive to produce power-by-wire actuators did not stop there; Lucas Aerospace have produced a number of designs for aircraft applications which have been successfully flight tested [22]. The majority of these are in non-flight critical roles such as nose-wheel steering; only the actuators that have been designed for aerodynamic control surfaces will be covered here.

Leonard wrote a paper which succinctly describes the potential benefits of electrical actuation systems (EMAs specifically) over hydraulic systems [23]. The author's list, quoted from the referenced paper is:

1. Energy conservation
2. Life cycle cost
3. Operational readiness/dispatch reliability
4. Reduction in aircraft weight
5. Reduced system development and test efforts
6. Improved survivability

7. Consolidation of energy/power sources into one (electrical)
8. Increased ability to disburse fighter/attack aircraft to remote sites due to reduced and more easily accomplished maintenance

Jones published an impartial assessment of the more electric aircraft, which seeks to estimate the effect on fuel savings and life cycle cost changes as a result of the future development of electric secondary power systems [24]. The study is not limited to actuation systems, it also extends to the environmental control system. The author highlights that although there are savings to be made in some configurations, it really depends on the platform and the level to which the more electric principle is applied. As previously noted, the potential energy savings are up for discussion, but widely accepted is the reduced maintenance cost and both scheduled and unscheduled downtime.

Whilst the items noted by the author were related to military fighter aircraft, many of the benefits apply equally to any type; from transport aircraft to unmanned aerial vehicles (UAVs). The referenced paper talks directly about EMAs, but the benefits will be parallel to any technology which replaces a centralised fluidic system with an electrical power distribution network.

This work is not seeking to exhaustively cover the entirety of next generation actuators, the scope of this is far too great for a single document. The most notable of the future technologies are the 'smart material actuators' or piezo-electric actuators [25] which are based on the properties of certain materials changing shape when an electric field is applied across them. These can be very accurate and highly efficient but currently the supporting electronics are bulky and unsuitable for aircraft use.

2.3.2 Hydraulic Actuators

2.3.2.1 Description

Hydraulic actuators are the mainstay of the majority of modern aircraft FCSs; they are used where an aircraft is large or is designed to fly at high speeds where the pilot cannot apply sufficient force to move or hold flight control surfaces in position. The hydraulic system adds supplementary force assistance to the pilot's command with a circuit minimally consisting of a hydraulic pump to pressurise the system, supply lines to distribute the fluid, various valves for protection (overpressure valves) and operation (shut-off valves, servovalves) and a series of hydraulic cylinders. The technology is well established and understood so the basics will not be covered in any more detail, for a thorough description of hydraulic systems please refer to references [26, 27].

The baseline aircraft used for the development of this research is the Airbus A320; this is equipped with three hydraulic systems, the blue, green and yellow as shown in Figure 2.4. Each is pressurised to 3000 psi in normal operation and each is equipped with its own fluid reservoir. The green system is powered by an engine driven pump (EDP) in engine 1 and the yellow system is powered by an EDP in engine 2, whilst the blue system is pressurised by an electric motor driven pump (MDP). The three systems are provided for redundancy purposes; should engine failures occur in flight, hydraulic power can be supplied to all surfaces from a single engine. In the event of a dual engine failure the blue system can be powered by the ram air turbine (RAT) [28], providing reduced control effectiveness but a safe means to land the aircraft.

Hydraulic actuators on aircraft can be considerably more intelligent than

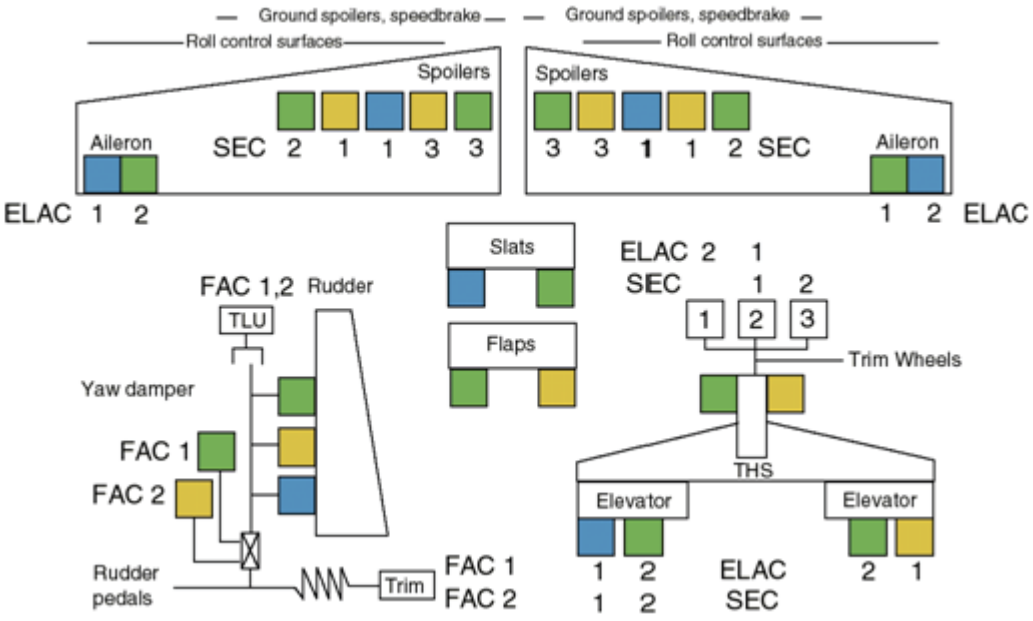

Figure 2.4: Airbus A320 flight control hydraulic system breakdown [29]

just a simple ram and valve; work published in 1989 documents the development of 'smart' hydraulic actuators [30]. These are actuators which have an electronic interface built into them to implement local closed loop control in a transparent manner. This is a benefit when it comes to designing the computer systems for an aircraft; the closed loop control functions are segregated from the centralised system making development and certification simpler. Additionally, the circuit length for the controllers becomes shorter, the signal propagation delay decreases and the susceptibility to EMI decreases substantially. Other advantages include specialised health monitoring of each individual actuator, localised fault detection, isolation and redundancy management.

2.3.2.2 Development Programmes

Hydraulic actuation systems have been in operation for many years now. Instead of discussing development programmes and flight tests as has been covered for the two electrical actuators, this section instead focuses on the modelling and simulation of hydraulic actuation systems.

In current commercial transport aircraft, hydraulic flight control actuation systems are the current technology of choice for primary flight control. As with a large number of engineering design challenges, computer simulation is being developed to assist and further optimise designs for minimum weight and cost while maximising performance, reliability and efficiency. The simulation assisted design approach is summarised by Lantto *et al.* for the Saab Gripen [31] and Mautin using the Airbus A340-500/600 development programme as a case study [32]. The author discusses the weakness of the steady state design technique where cylinders, pumps and distribution networks are sized based on the steady state speed and load estimates. These are estimates because the actuation system is not a steady state device in operation - an estimate has to be made for what the average and peak load design points will be. This is difficult since it is highly variable and dependent on environmental factors, essentially it is impossible to select an optimum for all cases. The steady state sizing technique produces an overestimate for the required capacity because the pumps have to be sized using the estimated total peak flow required, to ensure all surfaces can move at their maximum rates at the same time. Indeed, in normal operation this may be an unlikely scenario.

The dynamic simulation sizing technique avoids this situation by allowing the much more realistic estimation of flow and pressure demands. It allows

accurate sizing of dynamic components as well; for example, it allows the pump to be sized to provide the maximum flow for 95% of cases while local accumulators are designed to supply the 5% of peak loads which are rare and very short lived. These rare loading conditions may only occur under the circumstances of the most severe gust loads the aircraft is certified for. As such it does not make sense to choose a larger than statistically necessary pump when local energy storage can smooth the peak loads.

When these dynamic actuation system models are combined with an aircraft model as in Mautin's work, a complete actuation system load testbed is obtained to assess the system during manoeuvres. The author notes that simulation can also be used to aid with certification and solving in-service problems that may occur. As with any modelling task, the biggest limitation is the accuracy and speed of the models. Mautin discusses this and suggests the benefit of having relationships with component suppliers to ensure they provide accurate simulation models as part of the delivery process.

There are numerous options when it comes to simulation modelling languages, Mautin and Airbus use SABER, AMESim and HOPSAN are options while Simulink is most common. Blackman developed a modular approach using Simulink which consists of a library of hydraulic components to allow the drag and drop construction of complex hydraulic system models. The library contains blocks for pumps, accumulators, actuators, tees, orifices, transmission lines, valves and fluid properties (among others) [33]. This idea has also been adopted by Mathworks and implemented in SimScape; an object oriented, multidisciplinary graphical modelling language [34]. The package created by Blackman - 'Abex Hydrolink', is validated experimentally for a variable displacement pump and shows good results [35]. Unfortunately, no benchmarks of simulation speed were published but based on experience

with SimScape, it can be assumed by the level of detail it provides that it is computationally intensive.

2.3.2.3 Robust Design

Classically, hydraulic actuators use proportional servovalves which can be adjusted continuously to any desired position to produce any desired actuator velocity (dependent on system pressure and flow rate). These valves can be unreliable and expensive as they contain a large number of moving parts. There have been several techniques suggested to reduce the complexity of the control valves; one of which is a direct drive servovalve which avoids the requirement for a torque motor to control a hydraulic amplifier to drive the control spool (see section 3.1.3 on page 136 for more information). Galatolo *et al.* created a linear motor which controls spool position directly, by attaching permanent magnets to the main flow control spool and having quadruple redundant field windings on the stator [36]. Nguyen implemented a rotary direct drive servovalve which is motivated by the same design goals, but has a rotary motor and rotary valve connected on the same shaft [37]. Both of these valves have the benefit of reducing part count and complexity while also avoiding the constant metering flow required in a classic hydraulically amplified servovalve. This improves the efficiency of the valve markedly, as discussed by Scheffel [38].

A revised system put forward by Jenney suggested the use of binary valves [39], controlled by pulse width modulated (PWM) signals; these contain fewer moving parts in order to keep system cost low and improve reliability. The technique can cause stepping of the actuator linear motion if the applied frequency is too low, but due to the slight compressibility of the fluid acting as a low pass filter the actuator response will become smoother as frequency

increases. The results produced by the author show the binary valve controlled actuator to have equal or improved response characteristics compared to a proportional servovalve actuator.

In work similar to Jenney, Escobosa demonstrates the benefits of discrete flow valves in situations where position sensorless operation is necessary or desirable [40]. The design put forwards is based around a small piston with a known fluid volume which completely fills and empties its chamber in one cycle. Since each cycle outputs a known fluid volume, the actuator velocity is directly proportional to the frequency at which the valve is operating. Whilst there will be some inaccuracy involved, the discrete nature of the valve is what allows the actuator to work without position feedback. Theoretically, all that needs to be done is pulse counting to achieve set displacement targets. The most unique feature of the valve however is its ability to function pneumatically should a catastrophic hydraulic fluid loss occur. This is not normal operation as air is too compressible to provide accurate and repeatable actuations, but compared with complete loss of hydraulic control in flight it is a welcome advantage. In regards to civilian airliner use, sensorless operation would provide an extra layer of fault tolerance beyond that of feedback sensor redundancy; if all sensors failed the system could still operate safely, albeit with reduced accuracy.

2.3.2.4 Component Specification

Pump The pump in a servohydraulic system converts energy from a mechanical form to a fluidic form. It can be thought of as the hydraulic equivalent of an electrical power supply; the pump rotates at a constant speed and the piston displacement is controlled to maintain 3000 psi across the terminals. While there are dynamic characteristics to the pressure compensation

servo control loop, for the purposes of functional dynamic modelling this can be ignored. The pump characteristics required then reduce to the supply pressure and maximum flow rate. For the A320 this data is sourced from Eaton aircraft datasheets [41] or for more detailed information on efficiency and other data; the datasheet for the pumps themselves [42]. For specifying pumps of different performances, other manufacturer datasheets can be found such as Parker [43].

Control Valve In a servohydraulic actuator the control valve has a dominant role in defining the performance of the actuator as a whole. The bandwidth, accuracy and flow capacity are all important characteristics in selecting a valve. Modern aircraft can have several types, from mechanical feedback nozzle-flapper or jet pipe servovalves to modern direct drive valves with electronic feedback [44, 45, 46]. Each type has its benefits, particularly the direct drive valve for modern actuators since the lack of a constant pilot flow reduces the energy losses in the valve. However, since the aim of modelling the electro-servohydraulic actuators (ESHAs) is to represent the baseline performance of current aircraft in service, the valve selection made for this work is the flapper-nozzle servovalve type.

Producing an accurate model which represents the dynamic motion and power loss characteristics of a real system is challenging because there are many nonlinear behaviours inside a fluidic power system. It is not possible to predict 100% accurately using analytical methods, experimentation is required to validate the performance of individual components and the system as a whole. In a complex installation such as an aircraft, it is difficult to estimate losses in the distribution piping without knowing specifics of the type and gauge of the tubes, the number and geometry of tees or elbows or

other system specifics. This applies to the servovalves too, as demonstrated by Menshawy in an experiment to identify the performance of a proportional valve [47]. The author uses standard models but has to use curve fitting to represent deviations from analytical characteristics - which are unique to the experimental layout. Without having access to privileged information on design specifics or experimental apparatus, it is decided to derive relevant variables from manufacturer datasheets for commercial available components.

Cylinder The hydraulic cylinder is a standard component which has been in use since the industrial revolution. Characterising models means finding properties such as piston area, leakage and friction from manufacturer datasheets. Of course, it is ideal to find parameters from the specific cylinder of interest but this is not always possible. Using commercially available off-the-shelf (COTS) products such as those from Bosch-Rexroth [48] is an easy way to source data for similar (but probably lower performing) components.

2.3.3 Electromechanical Actuators

2.3.3.1 Description

Electromechanical actuators (EMAs) are electrically powered actuators which are equipped with mechanical gearing, used frequently to convert rotary motion from a motor to linear motion (although rotary versions are available). A diagram of a common EMA configuration is shown in Figure 2.5, where the power is provided by a brushless direct current (BLDC) motor which drives a ball screw through a gearbox.

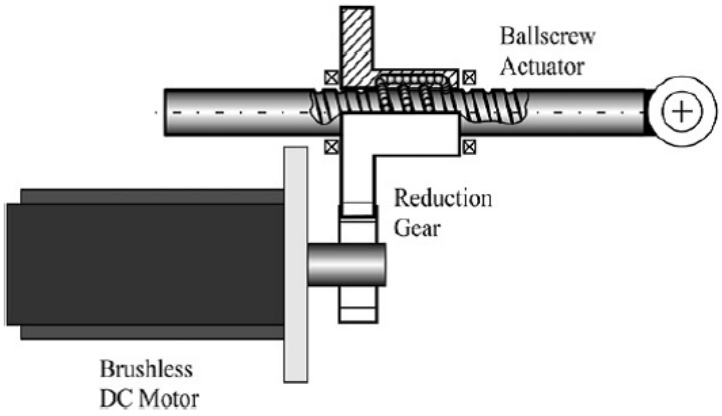

Figure 2.5: Diagram of a basic EMA [49]

These actuators have been considered for aircraft flight control use for some time but the same questions appear repeatedly, quoted here from Leonard's 1984 summary of then-current EMA developments [23]:

1. Are the electrical power systems as reliable and trustworthy as the typical aircraft hydraulic systems?
2. Can EMAs perform satisfactorily, that is, match the performance of hydraulic actuators?

3. Can redundant EMAs be designed to equal the flight safety reliability of dual-tandem hydraulic actuators?
4. Can the heat problem be solved, or will it compromise the design, performance, safety and/or use of the aircraft?

The answers to these questions become more and more positive as commercial and academic research continues in the area. As with any new safety-critical technology, electric actuation will not gain widespread acceptance until it has proven itself in service for a number of years. This was pointed out by Davis in an early Moog technical bulletin [50] which sought to design and construct two EMAs, one of fractional horsepower (1/4 hp) and a second of three horsepower. The designs proved successful and were able to meet performance specifications required of aircraft servoactuators. When the paper was written in 1984 the limiting factor on performance and reliability was the power electronics which supply the motor; highly reliable and fast switching insulated-gate bipolar transistors (IGBTs) of today were not available. As this literature review progresses, it will become clear that a large proportion of work is focused on improving the performance and reliability of the electrical components.

A significant issue facing the successful operation of an EMA is controlling the heat it produces, particularly when exerting a stationary force [51, 52]. Pointon proposes three different thermal management techniques [1] to keep the device temperature down, two based on cold plates which conduct heat away and a third based on phase change materials. The author concludes that ram air cooled plates are suitable for providing the necessary heat radiation but that further work needs to be completed to assess which system proves the most effective per unit mass.

2.3.3.2 Flight Test and Development Programmes

It is a well understood fact that, although useful in development stages, laboratory simulations of actuators do not replicate the conditions on an aircraft perfectly. For this reason flight testing is a key part of the development cycle in order to gain confidence in a technology. This section seeks to give an overview of some key flight testing programmes from the first of the modern development programmes in the 1980s through to the commercial use on the Boeing 787.

Lockheed One of the earliest programmes was undertaken by Lockheed and Sundstrand and investigated the performance of power-by-wire actuators; beginning in 1981 the two companies produced a flight-worthy EMA for the C-141 aircraft aileron [53, 54]. This aircraft first flew on the 11th February 1986 with its port aileron actuator replaced with an electric actuator whilst its starboard aileron had the original hydraulic actuator. This aircraft accumulated a flight time of around 14 hours with the test actuator in place and was largely successful in demonstrating the feasibility of electromechanical primary flight control actuators. Some problems were highlighted such as increased sensitivity to autopilot inputs and variable performance due to temperature; considering it was a first test issues like this are to be expected.

The success of this work lead onto two projects; one is the 'Electric Starlifter Reliability and Maintainability Technology Insertion Program' project which began in 1989, where Lockheed proposed the gradual replacement of a C-141B's primary flight control surfaces with electrically actuated alternatives [55]. The intention was to install a new actuator every 6 months from December 1992 to June 1993; releasing the aircraft each time for real world use to gain experience with the new actuators.

The second project was based on the C-130 high technology test bed (HTTB) and sought to equip the ailerons (and tabs) and rudder (and tab) with electric actuators, although only the tabs would be powered by EMAs. The ailerons would be powered by EHAs and the rudder by an integrated actuator package (IAP). At the time of publishing, the report produced from the project had only succeeded in demonstrating linear EMAs on the rudder tab, and a rotary EMA for stability and control augmentation functions.

Lucas Aerospace Lucas Aerospace is another company that has undertaken EMA research programmes [22]. Beginning in 1968 a design was produced for missile control surfaces which featured a single direction motor, ball screw and two clutches to enable bidirectional motion of the output. These were qualified in 1973 and 800 units were produced.

Between 1977 and 1979 actuators were designed to control the elevation and bearing of missile launchers. The advancements made with these actuators was using an H-bridge inverter and armature controlled DC motor; this allowed an increased torque level and improved controllability from previous designs.

From 1985 Lucas developed high bandwidth and high current EMAs for missile fin control surfaces which achieved a -3 dB bandwidth of 20 Hz. This was achieved using improved four quadrant H-bridge inverters to control the motor.

It was in 1988 that Lucas developed their first EMA for installation on an aircraft. The design was conducted with the assistance of a commuter jet manufacturer to ensure it fit the aircraft envelope, although it was only ever used for bench testing. This actuator used a brushless DC motor powered from the 270 VDC bus which is typical on board modern aircraft, allowing

lower current levels and thus improving the reliability of the inverter switching devices.

In 1990 the EMA technology was extended to interface digitally with the flight control system of a missile fin actuator, previously signalling had been analogue. In the same year development began on a large aircraft aileron actuator; this was a major step for the technology as it was the first time it had been employed (by Lucas) in a primary flight control role. This demanded high reliability, high temperature stability and damping mode fault tolerance to be designed in.

NASA, US Air Force, Navy Whilst not specifically related to aircraft, NASA has conducted research on a very high power EMA (40 hp) for thrust vector control of a space launch vehicle [56, 57, 58]. The programme began in 1990 and the results of a laboratory test were published in 1996. This actuator is beyond the requirements of aircraft control surface actuation due to its size, but a common problem with EMA technology is addressed. Often, the drive electronics are of a significant size and produce a large amount of heat; the NASA project looks to use a specially designed induction motor which is controlled by a field-oriented vector controller that uses zero-crossing (resonant) switching to reduce the EMI and component stress. The power converter switches at the frequency of the supply line (not the motor), minimising the use of extra components in adjusting the frequency and hence, reducing converter size. In laboratory experiments the actuator performance is verified up to a power rating of about 15 hp. The overall efficiency including the drive electronics was found to peak at around 65% although Fulmer notes this will increase as the power level increases.

Further EMA development was achieved by the US Air Force, Navy and

NASA on the electrically powered actuation design (EPAD) program which commissioned the design of a high performance EMA for the port aileron of an F-18 research aircraft. The programme, which began in 1980, found the actuator performance was excellent, with better frequency response than the hydraulic actuator it replaced. The biggest problem encountered was the thermal performance of the actuator; two tests had to be aborted due to rising temperatures. The worst case operating point for the EMA was the constant force exerted while the flaps were deflected between 30° and 45°, this was a surprise to the design team who suspected the worst heat loads would occur during highly dynamic aerobatic flight regimes. By installing heatsinks on the motor to increase conductivity to the surrounding airframe, the thermal performance was significantly improved.

In a final report by the contractor which designed the EMA for the EPAD project (MPC Products Corporation) [59], the most fundamental lesson to be learnt from the study is that of duty cycle. As highlighted in the previous paragraph, specifying the duty cycle of the actuator correctly is key to designing a lightweight actuator which is capable of delivering the performance required while maintaining thermal stability. This is a key conclusion from the literature review; without having flight test data it is difficult to assess what the duty cycles of the actuation systems might be in a dynamic aircraft. Relying on steady state *typical* duty cycle data in a design can lead to situations like this where an actuator is over or undersized.

The knowledge gained on the EPAD project was used to implement EMA actuators on the X-43A hypersonic research vehicle [60]. After one failed first flight, this aircraft first achieved Mach 6.83 on March 27, 2004 and then Mach 9.68 on November 16, 2004. The EMAs are small but high bandwidth, providing control of two wings, two rudders and an engine cowl door. The

project made use of simulation to a large extent in the design of the vehicle as a whole; the referenced document focuses on the modelling of the actuators. It is interesting because the failure of the first flight highlights the problem with mathematical modelling and simulation; in the words of the investigation team responsible for finding the source of the fault:

> *The Hyper-X Launch Vehicle failed because the vehicle control system design was deficient for the trajectory flown due to inaccurate analytical models which overestimated the system margins.*

The failure highlights that when a design is based heavily on models which are assumed to be correct, if it turns out that the accuracy is not sufficient to match real world behaviour (across the whole frequency range of interest) the end result can be catastrophic. Nevertheless, the succeeding successful flights demonstrate the performance capability of EMAs.

Gulfstream Moving on to more recent flight tests, GE Aviation have been involved with Gulfstream Aerospace Corporation's 'Advanced Flight Control Technology Demonstrator' project tasked with designing an EMA spoiler system [61]. The company provided four of the six spoiler actuators, each of which was controlled locally. This aircraft utilised a distributed architecture where the speed and position loops are closed by a processing unit dedicated to actuator control, often situated near the actuator to minimise the susceptibility to EMI. The end result of the flight test programme; beginning on the 26th September 2006 and continuing for the following weeks was a success. Although detail in the referenced document is low, the author states that the actuators performed to specification and suffered no failures.

2.3.3.3 Robust Design

There are many techniques available to mitigate the risk of single point failure modes in electric actuators; Charrier and Kulshreshtha summarise the technologies in reference [18]. These include dual wound electric motors with dual encoders, dual actuator position sensors and five phase motor drive topologies. Whilst the actuators themselves may incur a greater weight penalty in comparison with two hydraulic rams, when considering the removal of the other components in a hydraulic supply system (reservoirs, fluid, supply lines, heat exchangers, various types of valves and pumps) the tradeoff may be acceptable. A more detailed review of the reliability considerations at component level is provided in this section.

Power Screw The questions of reliability relate firstly to the possibility of mechanical jams in an EMA which have proven unlikely in established hydraulic cylinders. Due to the nature of EMAs they can be particularly susceptible to contamination (ice or dirt) or potential overloading, damaging the gears or lead screw irreparably and causing a jam in flight. Secondly, electrical failures can occur in the motor and servo drive which the system needs to be able to tolerate. There are numerous methods to solve these issues, some of which are proposed, along with a detailed list of possible faults in reference [62].

The screw itself is the cause of most concern for power screw actuators; the tight tolerance requirements to achieve minimum backlash mean any wear on the screw can cause severe degradation in performance or even seizure. Perni *et al.* describe the techniques used by Umbra Group to produce significantly improved reliability of the ball screw actuators used on the Boeing 777 flap system [63]. Firstly is the use of an induction hardened stainless steel called

Cronidur to produce the screw and secondly is the use of silicon nitride balls in the nut. The hardened steel has proven itself through fatigue tests (Figure 2.6) and in service on the 777; being removed from the aircraft after 4-8 years and still in nearly new condition.

Silicon nitride ball bearings are harder and smoother than steel balls and therefore allows more efficient ball screws. However, the friction between two ceramic balls is higher than that of two steel balls, and their contact will lead to increased surface roughness. For this reason either a spacer is required between balls or an alternating arrangement of ceramic and steel balls. If the steel balls are made smaller than the ceramic balls they take no load but roll with the ceramic balls and reduce friction further. This arrangement is shown in Figure 2.7.

The final improvement in reliability noted by Perni is derived from improved material selection of the wipers attached to the nut. The function of the wiper is essentially as a seal against contaminants in the ball screw races, physically pushing any dirt away as the nut moves. Using a modern PTFE wiper allows a tight seal with low friction and a long lifetime.

By combining a Cronidur ball screw with alternately spaced silicon nitride balls and PTFE wipers in the ball race grooves dramatically reduces the cost of ownership of the actuator and improves reliability significantly.

Motor Aside from improving the materials used to reduce the failure rate as just described, there are numerous methods to actively tolerate component failures. These may involve having multiple motors with some form of torque or speed summing gearbox as presented by Annaz [64, 65] which are tolerant of up to two failed motors (out of four). This method provides true redundancy but increases weight and actuator volume; another method

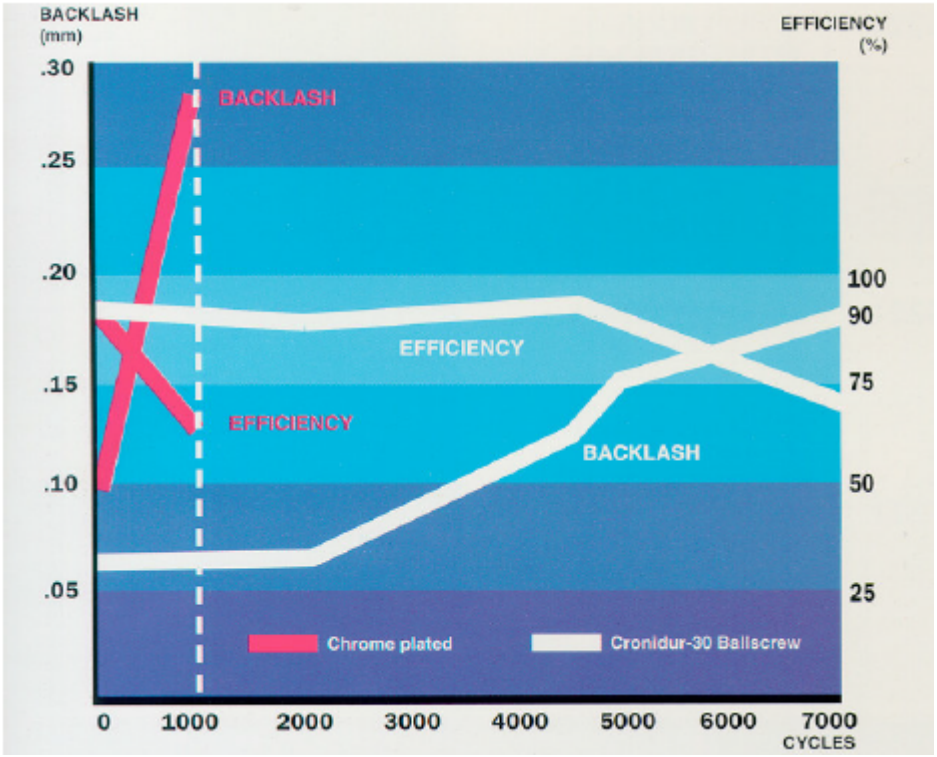

Figure 2.6: Fatigue performance graph of chrome plated vs. Cronidur ball screws with ceramic balls [63].

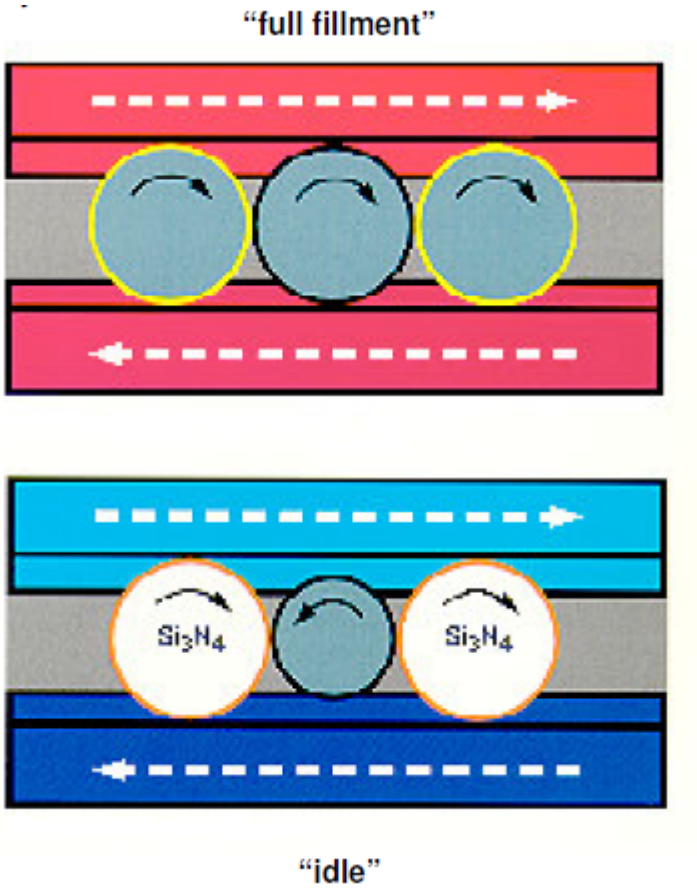

Figure 2.7: Ball bearing arrangement in Umbra EMAs [63]

which allows a more compact solution is to have multiple redundant windings in a single motor housing. This provides tolerance against electrical failures such as winding short or open circuits, but not against a mechanical jam of the rotor due to seized bearings. This is investigated by Raimondi *et al.* for brushless motors in spoiler actuation applications and shown to have good success at handling the most common failure modes [66].

Another method of increasing the reliability of an EMA is to remove the gearbox from the assembly (see Figure 2.8 for clarification). The mechanical parts are the cause of the majority of jams and removing them improves a device's mean time before failure (MTBF). Current EMA designs feature high speed, low torque motors which operate in the range 3000-9000 rpm. These are not directly suitable for flight control actuation as the stall load capability is so low. The function of the gearbox is to convert the high speed, low torque of the motor to the low speed, high torque required to drive the ball screw. Gerada *et al.* developed a 22 pole motor to operate at low speeds with a high torque capability [67, 68] to eliminate the gearbox from the actuator. The design operates as planned but suffers from high stator harmonics. A side effect of this work is that one source of energy loss in the system is removed, potentially leading to a more efficient system; although this is likely compensated for by the high motor losses.

Servo Drive Of the whole actuator package, van den Bossche notes the electronic control and servo drives are predicted to be the least reliable component [69]. Providing redundant electronic controllers are therefore imperative to the safe operation of electric actuators in primary flight control applications. Both Raimondi, Garcia and Bennett discuss this topic [66, 62, 70] and the general idea is to provide physically isolated control of each phase

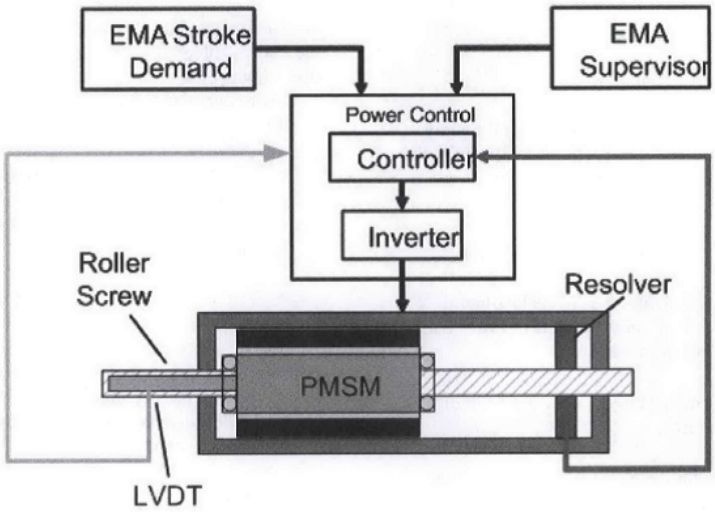

Figure 2.8: Sketch of gearless direct drive EMA [62]

in the motor. By ensuring physical separation a single fault is less likely to affect more than one phase winding.

Health Monitoring The final topic worth mentioning regarding robust design is health monitoring and fault prognosis. This involves the use of sensors and data logging to record information about how an actuator is used and the conditions it has been used in. The data can then be analysed to assess the likelihood of failure and need for repairs or replacement without needing to access difficult to reach actuators.

There are essentially three styles of health monitoring identified by Babinski [71]:

- State of integrity

  Is the actuator operating within its primary design specification?

- Performance based

  Store load and speed data to help estimate wear

- Predictive monitoring

  Compile the above data to predict future failures

This concept is particularly useful because without it component servicing schedules often depend on the number of hours in service. In service, the wear on the actuators will depend entirely on the conditions and manner in which it used. Since service lifetime is set with some safety margin, there is a possibility of extending the safe lifetime by using health prognostics with negligible impact on safety.

With the ability to analyse the data without removing actuators from the airframe, maintenance programs can become much more cost effective. Isturiz predicted the cost of different types of maintenance [72]:

- Corrective maintenance: 71.46 €/hour
- Preventative maintenance: 28.88 €/hour
- Maintenance inspection: 8.19 €/hour
- Health monitoring: 4.99 €/hour

The lower maintenance cost is offset by the greater initial outlay for the more sophisticated actuators, at around €6700 for the health monitored version and €5000 for a regular actuator. However, the number of hours the actuator will be in service is more than enough to recoup the additional expenditure, making the technology interesting indeed to aircraft operators.

2.3.3.4 Regeneration

Regeneration in an EMA is inherently caused by the requirements to design an actuator with a fail-operative mode; where the actuator can be back

driven by the control surface so it does not become jammed in a deflected state. Provision has to be made for this behaviour to dissipate or store the electrical energy that is generated by the back driven motor. If not, large voltages are created at the output of the servo-drive which can cause a reduction in servo-drive lifetime, arcing or even destruction of the solid state transistor outputs.

There are three main techniques; dissipation, storage or return to supply. The simplest is to have a resistive load which is switched into the circuit when the motor is being back driven. This dissipates the energy as heat to the surrounding environment, but since the resistance must be capable of dissipating peak powers of several kilowatts this is likely to mean a large mass. The trade off for accepting this mass penalty is a simpler system design. One criticism of dissipative techniques is their perceived wastefulness; but although peak power is high the overall energy transferred by the actuation system is relatively low. This means the amount of energy available for regeneration is even smaller due to the actuators' poor efficiency under aiding loads [3, 73].

The second technique is energy storage which has been investigated by Lowe [74]. There are several possibilities from battery storage to capacitors; in the referenced publication the chosen scheme is a supercapacitor because of the requirement to withstand thousands of charge-discharge cycles and dissipation of a large amount of power (2 kW). The author concludes that the energy storage architecture is viable and has a far lower mass and volume than an equivalent dissipative schematic. Whether or not the amount of energy available to be harvested is considered worthwhile, the mass saving alone could make it an attractive option to system designers.

The third regeneration concept is investigated by Trentin [4] using a two

stage matrix inverter to feed energy back to the supply. The referenced paper achieves this under laboratory conditions; extending the process to a complete aircraft power system is a significantly more complex task to ensure supply stability. Assuming this challenge is suitably handled, delivering energy back to the supply means it is possible to avoid using either capacitor storage or dissipative resistors. Trentin concludes that even though the amount of energy to be regenerated during real flight profiles is minimal, the mass saving achieved by not having supercapacitors or power resistors to handle the high peak powers could be significant.

2.3.3.5 Component Specification

Designing an EMA is a challenge. Producing a flightworthy actuator which meets the performance specification at or below the target mass is a multidisciplinary optimisation task. There are many parameters to select, from high level values such as ball screw pitch down to lower levels such as how many windings to use in the motor. This section aims to review some of the relevant methods in literature for selecting and sizing the various components.

Motors One decision that has to be made when designing an EMA is what type of motor to use. Most working models to date have been equipped with permanent magnet BLDC motors as they have a good dynamic performance, high energy density and high reliability as they have no commutator or brushes [75]. This reduces the EMI significantly and improves both reliability and efficiency; however, since commutation must be achieved electronically the controller becomes more complex and rotor position feedback is required. BLDC motors are equipped with Hall effect sensors which provide

high enough resolution rotor position feedback to control the trapezoidal back electromotive force (EMF) profile of the BLDC motor. In aerospace applications the highest affordable energy density is sought after, often at the cost of controller complexity. Botten provides a summary of the types of electrical machines which are suitable for flight control electric actuators; BLDC, switched reluctance (SR) and brushless alternating current (AC) motors [76].

An improvement to a standard BLDC motor which can increase reliability is the use of interior permanent magnets, as described in reference [77]. In brief, the permanent magnets are located internally to the rotor which provides an improved flux linkage between the magnets and the windings (the effective air gap is reduced) and reduces the mechanical fragility of the brittle magnetic material.

The SR motor is very similar in structure to the BLDC motor, the stators of each motor are essentially the same and the difference lies in the rotor. In a SR motor the rotor is made of a nonmagnetic material and relies on the reluctance induced by two opposite electromagnets to provide torque. Using a suitable switching algorithm, a rotating reluctance torque can be created to drive the rotor continuously. The major drawback of the technology is the high torque ripple, which can be improved by using more poles.

In addition to high torque capability, the SR motor has an added reliability feature. In BLDC motors the primary component of torque is contributed by the permanent magnets, this can be problematic as permanent magnets can demagnetise at high temperatures. The primary component of torque in SR motors is from the reluctance of the motor, meaning its operation can be guaranteed even at high temperatures. This may be just as well when the biggest design challenge is handling the high heat output of the motor, as experienced by Gribble *et al.* on spoiler actuators [51].

Wang *et al.* proposed an evolved SR motor for EMA use; the switched reluctance permanent magnet (SRPM) motor [78]. The difference is that by including permanent magnets in the rotor, some assistance torque is provided, but otherwise it is identical to an SR motor.

Brushless direct current (DC) motors are not the only option available however, there are suitable brushless AC motors which present their own advantages. AC induction motors are of a lightweight construction, yet their ruggedness has been proven with an estimated 70 to 80 per cent of all motor drives in industry being of this type [79]. A summary of different types of electric drives can be found in the aforementioned reference.

The challenge with AC motors is the complexity of the servodrive and feedback sensors. While a three phase AC induction motor is physically very similar to a three phase BLDC motor, the back EMF has a sinusoidal shape (due to a slightly different stator winding arrangement) which reduces torque ripple, machine noise and overall energy losses. A downside to this is that an encoder is required on the motor shaft rather than just Hall effect sensors; increasing cost and complexity in the design. It does also mean that vector field control techniques can be used to minimise copper losses by ensuring zero phase lag between voltage and current. As with BLDC motor drives the control signals must be provided by an inverter fed from a DC bus.

It is possible to rectify the aircraft AC power supply onto a DC link and use an inverter as a variable frequency drive. The DC link has to be a heavy bus bar and would ideally be avoided. The solution is to use a Matrix Converter which uses nine digitally controlled switches to form a direct AC-AC frequency converter. This also avoids having heavy and unreliable electrolytic capacitors which would be needed for the rectifier circuit in a classic rectifier-inverter topology. The Matrix Converter principle is success-

fully developed and demonstrated by Wheeler *et al.* in a test bench proven rudder EMA actuator [80].

Summarised by Elbuluk and Kankam are a number of different speed sensorless induction motor control techniques which can control the speed and torque of a motor without the aid of a speed transducer [81, 82]. The benefit of this is that removing the encoder from the rotor shaft alleviates a possible source of failure; when a high maintenance encoder is coupled with a low maintenance motor unnecessary downtime will occur just to keep the sensors operational. The referenced sensorless control techniques implement the highly efficient field-oriented control and couple it with various digital software controls. Whilst the theoretical performance and reliability of these drives is good, their performance with time-variant aerodynamic loads and varying motor parameters over time remains to be proven. One particular challenge with sensorless techniques is that they often rely on some form of back EMF measurement which requires the motor to be rotating fast enough to make the back EMF discernible. When the motor is stationary or reversing (speed close to zero) sensorless control often provides poor control accuracy.

For the benefits which sensorless control provides to robustness, they do not come without a detriment to accuracy and performance. This is demonstrated by Conard *et al.* who designed a controller for an induction motor which can either use a speed sensor or a model predictive sensorless scheme [83]. The results show that although sensorless techniques do work, the dynamic performance is significantly reduced.

No matter what type of electrical machine is chosen, one fact that remains true is the requirement of a servo-motor drive. There are many different types, for example DC motors may have simple PWM voltage controlled drives or complex (but efficient) vector control techniques. For AC motors

this could be a variable frequency drive supplied from a rectified DC link to a matrix inverter which avoids the need for a rectifier. This thesis focuses on the actuators' internal components and does not seek to represent the power losses in the electrical servo drive. By necessity, the modelling of the actuators has to be fairly 'top level' to achieve high simulation speeds; specific modelling of the losses in the servo drive such as the work published by Torabzadeh-Tari or Maré [84, 3] can be time consuming and a unique task in its own right. For this reason it is left in the remit of future work.

Geartrain Specifying the components in an EMA requires similar trade-offs to be made as with any other field of engineering. Increasing the load capacity invariably means increasing the mass by requiring more substantial power screws, nuts and motors. Increasing the force capacity in this way also increases the inertia of the rotating components; it can be appreciated that by designing for an unnecessarily high load capacity, the dynamic performance of an actuator would be reduced. From this simple example it is easy to visualise the challenge facing actuator designers.

Motor designers are tasked with increasing the energy density of their components while maintaining high reliability. Power screw designers are trying to balance the force capacity (size) of a lead screw and the friction that occurs between the nut and screw. Both of these domains invariably require materials engineers to develop improved alloys and heat treatment processes to improve the beneficial properties and increase reliability whilst keeping the mass down.

There are any number of techniques to select components; from simple steady state calculations matching motor no load speed to the desired output no load linear speed, or using optimisation algorithms to select optimal val-

ues. The decision of which method to use depends on the desired outcome; if a simple, quick estimation is the aim then hand calculations are acceptable. If the objective is to mass manufacture actuators for certification and commercial use then the extra time taken to use optimal methods may increase profitability.

One such optimisation technique is presented by Haskew [85]; his method is based on constructing an equivalent circuit in the phasor domain, then deriving the equations which represent the maximum torque demand and the input power. These equations are combined using relative weighting into an objective function which is minimised using constraints of the motor's rated torque and speed. Since the values describing each component are interrelated (i.e. screw pitch, damping, inertia and mass), the task is to find solutions which provide the optimal parameters that respect physical constrains such as maximum speed and material strength. Although the author could not justify creating multiple actuators with a variety of internal component sizes, he validates the model by showing that the minimum load force is where the objective function minimum is to be found.

A choice that has to be made is the type of power screw to use. The most economical is the acme screw which is essentially just a lubricated nut on a screw, but the maximum speed is limited and efficiency is low. A common solution to alleviate these problems is to switch to a ball screw, which transfers the load force from screw to nut across a recirculating channel of ball bearings. The efficiency of this system is much higher since the friction is significantly reduced, but by reducing the effective contact area the load ratings are reduced. A solution to this is to use satellite roller screws which, although slightly less efficient than ball screws have higher load capacity, impact rating, stiffness and speed. A satellite roller screw has helical

rollers assembled in a planetary arrangement around the lead screw and encapsulated by a nut. This converts rotary motion to linear motion with high efficiency, and importantly with a greater contact area than is provided by ball bearing contacts (demonstrated in Figure 2.9). The clearest way to present the differences between roller screws and ball screws is using a table, as shown in Table 2.2.

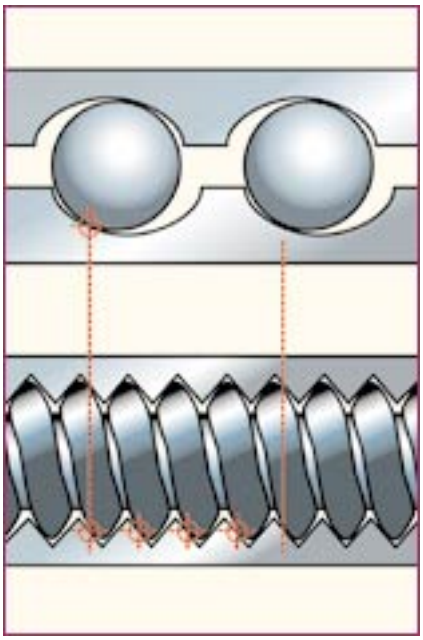

Figure 2.9: Roller screw and ball screw load bearing diagram [86]

This type of screw is combined with a gearless direct drive motor by Grand and Valembois [87] to achieve a lightweight, low inertia EMA with minimal backlash for thrust vector control of a missile launcher. Although the authors have not considered mechanical redundancy due to the intended application, the published actuator design has many benefits in primary flight control applications. The direct drive scheme shown in Figure 2.10 removes the gearbox which is usually required to reduce the motor speed to match the power screw. This has the benefits of reducing mass and inertia, increasing

Table 2.2: Roller screw, ball screw and hydraulic cylinder comparison [86]

	Roller Screws	Ball Screws	Hydraulic cylinders
Load ratings	Very High	High	Very High
Lifetime	Very long, many times greater than ball screw	Moderate	Can be long with proper maintenance
Speed	Very high	Moderate	Moderate
Acceleration	Very high	Moderate	Very high
Electronic Positioning	Easy	Easy	Difficult
Stiffness	Very high	Moderate	Very high
Shock Loads	Very high	Moderate	Very high
Relative Space Requirements	Minimum	Moderate	High
Friction	Low	Low	High
Efficiency	>90%	>90%	<50%
Installation	Compatible with standard servo electronic controls	Compatible with standard servo electronic controls	Complex, requires servo-valves, high pressure plumbing, filtering pumps, linear positioning and sensing
Maintenance	Very low	Moderate	Very high
Environmental	Minimal	Minimal	Hydraulic fluid leaks & disposal

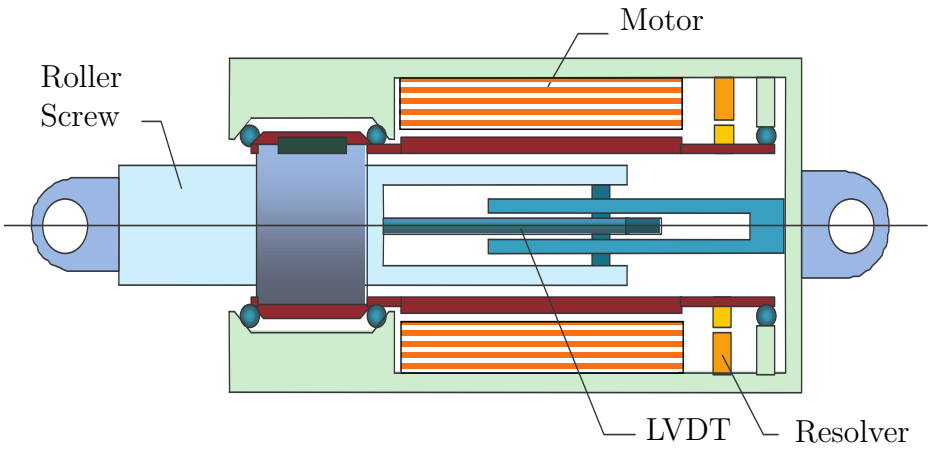

Figure 2.10: Concentric direct drive EMA with motor connected directly to the screw nut [87]

MTBF due to the lower part count and increasing stiffness in the drive train.

The motor in the referenced paper is also of a very compact design; Goodrich applied a hollow shaft BLDC motor with the roller screw in the centre gap, which significantly reduces the size of the overall actuator. By employing a field vector control scheme to the motor, the power transfer is optimised; causing reduced losses and therefore a reduction in motor size required to meet the performance specification.

Choosing the type of technologies in an actuator is one problem, another is sizing the components to achieve the specified performance. This involves selecting many parameters which are interrelated, from relatively few input parameters. This presents a challenge since there are many constraints on the selection of components; there are material properties such as contact stress and rotational speed limits, thermal dissipation and electrical current limits. To aid with this task Budinger *et al.* derived scaling laws for the preliminary sizing of components in EMAs [88], which are based on the physical constraints that define the actuator behaviour. The scaling laws require information about reference products from which to base the scaled estimates,

achieved and validated in the referenced paper using datasheet parameters of commercial components. This technique is ideally suited to assisting with the preliminary simulation based design of actuators, providing estimates of component variables based on some reference.

2.3.4 Electro-hydrostatic Actuators

2.3.4.1 Description

Electro-hydrostatic actuators are simply electrically powered localised hydraulic systems [see Figure 2.11]; they come in two main forms, one with a constant speed motor and variable displacement pump (EHA-VP) and another with a variable speed motor and fixed displacement pump (EHA-FP). The two architectures are modelled and investigated in detail by Frischemeier [89], who concludes that for primary flight control duty cycles the EHA-FP is more appropriate than the EHA-VP actuator.

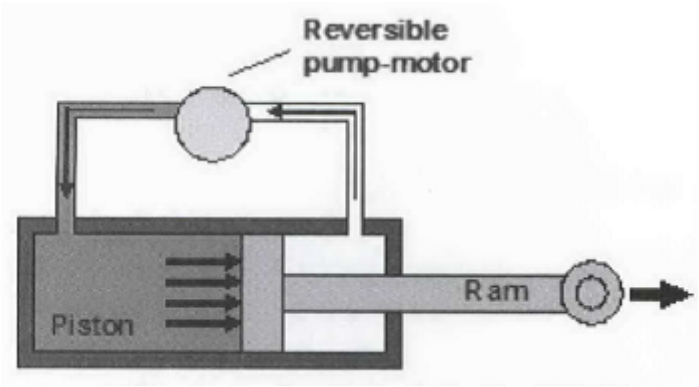

Figure 2.11: Sketch of an electro-hydrostatic actuator [62]

During flight, the most common loading condition is zero velocity at constant load; in this condition the EHA-VP wastes a lot of energy as the motor is always spinning at its constant operating speed, despite only supplying enough fluid to account for leakages. This generates heat and reduces lifetime of the motor. On the other hand, the EHA-FP motor spends most of the flight spinning at a very low speed, thereby avoiding the problems of the constant speed motor.

There are other reasons why EHA-VP actuators may be selected in cer-

tain applications; since a constant speed motor is simple to control and the low inertia of the swashplate in a variable displacement pump allows high frequency reversals compared to the fixed displacement pump actuator. At high loads, the energy losses between the two types of EHA are very similar so the EHA-VP actuator makes most sense in applications with high loads and regular direction reversals such as in excavators [90]. In the EHA-FP the output piston is controlled by the speed and torque of the electric motor; meaning sophisticated controls are required for efficient operation. This actuator will also have a slower dynamic response due to the higher inertia of the motor compared to the EHA-VP swashplate but much lower losses at low loads.

There are other designs researched in literature, one uncommon approach is the pump and valve combined EHAs which use a variable speed, unidirectional motor and bidirectional servo valve [91]. The motor is speed controlled to provide the required amount of pressure for the applied load while the servo valve controls the direction of the flow. This configuration provides a number of unique control problems which are discussed in the referenced paper. This actuator could provide high dynamic response since the motor does not need to be reversed to change the piston direction of travel, but where very high bandwidths are not required the addition of the servo valve induces an additional source of power loss in the hydrostatic circuit. By using an EHA-FP, this is avoided and a reduced dynamic response is accepted.

A novel design is proposed by Rammer *et al.* which replaces the rotary electrical motors entirely with a piezo pump [92]. The operational mechanism of this actuator is similar to any piston pump except that energy is supplied by a connecting shaft made from a piezoelectric material. As the piezo material is exposed to an AC voltage, it expands and contracts cycli-

cally causing the piston to move up and down in the cylinder. By using rectifying valves, the fluid flow is constrained to travel in only one direction. In the referenced document the authors note the technology has the potential to reach very high specific power capacities, but at the time of writing more work was needed.

A final point of interest is the development of standards for the specification and design of EHAs. In the past there have not been standard methods by which a user should specify the required performance of an aerospace grade actuator. This was discussed by Arnaud in 1998 [93] and has lead to the publication of BS ISO 22072 in 2011 [94]. Any EHA procured or produced today should comply with these standards.

2.3.4.2 Flight Test and Development Programmes

This section seeks to cover major development programmes undertaken in industry and academia. Primarily the section will cover flight tests that have occurred, before moving onto studies where the focus has been on modelling and simulation only.

Flight Testing Electrohydrostatic actuators have one key benefit over electromechanical actuators when it comes to integrating them with an airframe; the component which connects to the flight control surface is a well established and proven technology. The failure modes of hydraulic cylinders are well understood, implementing fail-operative mode is as simple as providing a bypass valve with a metering orifice to allow damped movement of the piston under external load. This makes certification more straightforward than for a mechanical transmission, for that reason EHA technology is in use in a primary flight control role today on the Airbus A380.

Leading up to the current state of the art have been a number of flight test programmes committed to evaluating EHA actuators in service [22]. From 1990 to 1993 the Lucas Aerospace model 91E05 (an EHA-VP design) underwent successful flight testing in an unspecified aircraft rudder application. As described in section 2.3.4.5 on page 63, this actuator produces significant amounts of heat which requires active cooling. The subsequent test actuators, 91E06 - 91E08 improved the efficiency and power capacity but still require active cooling to ensure continuous operation.

Lucas have also been responsible for developing an electrical backup hydrostatic actuator (EBHA), which commenced in 1991 and by 1994 had logged 50 flight hours. This is an interesting actuator as it is one of the few that provide true redundancy by having energy supplied to it in two different forms; while this is useful in the transition stages between today's standard hydraulic systems and tomorrow's electrical systems, it will not allow for a weight reduction that is as significant as a purely electric actuator.

In 1992, a collaboration between Lucas and Aerospatiale (now Airbus) saw the first flight of an EHA on a commercial aircraft [95]; an A320 equipped with an EBHA powering an aileron. The hydrostatic components in the actuator were a fixed displacement pump type (EHA-FP) using a commercially available hydraulic pump. This caused a higher overall mass than would be achievable with specifically designed components, but this is to be expected from a prototype. The pump proved to be the least efficient part of the whole actuator; the author notes a highly efficient small displacement pump would be more suited to EHA applications. The heat output was very good and a maximum of 25 °C temperature difference was seen between the hottest and coolest parts of the actuator, using only convective cooling.

This test was subsequently followed by an EHA actuator on an A330/A340

inboard aileron [95] which flew in 1999. This actuator was improved from the A320 EBHA with the use of a specially designed bent axis pump and a 'no-back' system to prevent the load driving the motor. This reduces the thermal output and allows both a mass reduction of 10% and an improvement in efficiency.

Between 1993 and 1997 the 'EPICA' project investigated EHA-FP actuators under laboratory conditions and in flight [90]. The actuator was installed on a single aileron on an Airbus A321 aircraft [21]; it showed good performance in flight and remained below critical temperatures. The outcome of the project was a success and Liebherr-Aerospace helped prove the EHA-FP in primary flight control applications on commercial aircraft.

Following on from the 'EPICA' project was 'ELISA' which began in 1999 and sought to investigate the application of the EHA actuators previously proven up to ∼2 kW on very large aircraft; up to ∼45 kW. Moorhouse *et al.* published a paper looking at the feasibility of such large actuators using simulation and laboratory testing, although at the time of publishing progress had only reached 'derisk' testing to ensure the concept was viable [96].

In 2001 Moog published the results from a detailed design study for an EHA on the inboard aileron of an A340 [97]. As current suppliers of the hydraulic servocontrol for this surface, Moog were in a unique position to analyse and compare the feasibility of an EHA replacement. The report provides a table of component efficiencies (Table 2.3) which add up to an overall total of 54.8%. Moog point out that when the actuator is specified by no load rate and stall force, the envelope of the EHA-FP is greater than that of the equivalent hydraulic actuator. There is even the possibility to design the controller to mimic the load-speed envelope of the hydraulic actuator it replaces, allowing lower heat generation and thus reduced mass. With

Table 2.3: EHA component power, losses and efficiencies [97]

Item	Total Power (kW)	Loss (kW)	Efficiency of Item
ECU	6.115	0.167	97.3%
Motor	5.948	0.412	93.1%
Pump	5.536	1.159	78.3%
Manifold	4.177	0.560	86.6%
Actuator	3.617	0.392	89.2%
Load	3.225	–	–

respect to an EHA in standby mode, the damping of the actuator makes it suitable to replace a hydraulic cylinder but the report notes the EHA has a mass which is 11.4 kg heavier than an ESHA.

The final case study of interest is the Airbus A380, which is the first aircraft to feature power-by-wire (PBW) actuators on the primary flight controls of a commercial transport [98, 69, 99]. As shown in Figure 2.12 it can be seen that EHAs are installed on the inboard ailerons, mid ailerons and elevators whilst EBHAs are used on the rudder and spoilers. The removal of a complete hydraulic system and replacement with two electric systems has reduced the mass of the A380 by around 450 kg, while actually increasing reliability. By having four power distribution networks instead of three and medium energy dissimilarity, a single failure such as a maintenance problem is prevented from affecting all hydraulic systems at once.

After a long design and qualification process which involved a lot of the preliminary work published in the above references, the first all electric flight of a commercial aircraft occurred on 29th August 2005 on A380 airframe MSN1 [100]. Certification in a civilian aircraft requires consideration of several factors which have not yet been mentioned, such as adherence to fire prevention standards as the aileron actuators are located in proximity to the

wing fuel tanks. Also required is the minimisation of EMI which is achieved by attaching the servo drive to the actuator to ensure minimum cable lengths and shielding of high frequency switching components. Related to this is the required immunity to external EMI and lightning strikes which was not such a problem with hydraulic actuators.

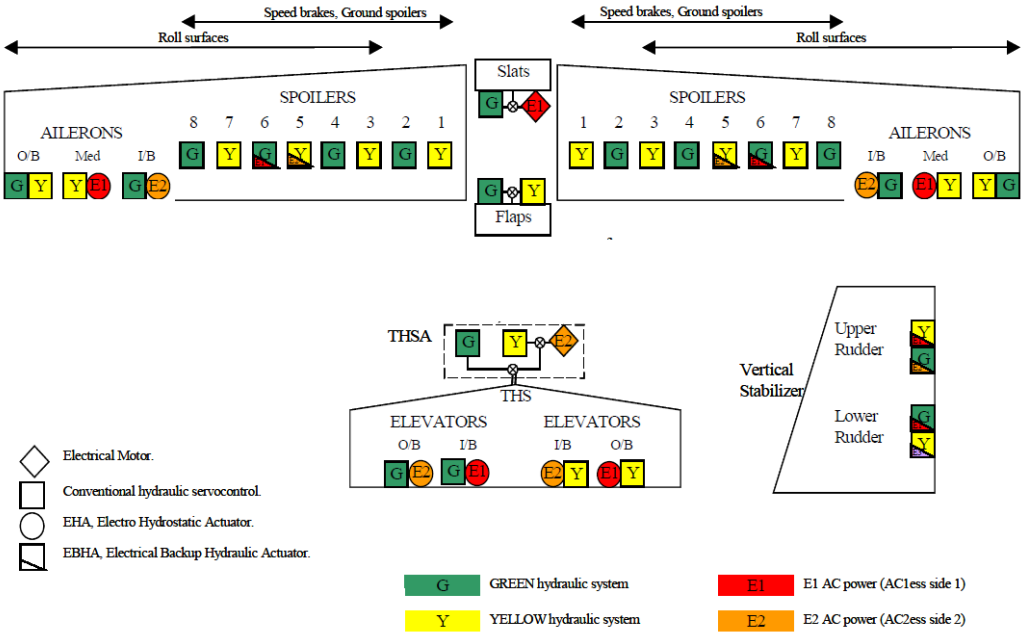

Figure 2.12: A380 actuator power distribution [69]

Looking to the future, one possibility for extending the use of EHAs is the decentralisation of the slat and flap actuators. Aircraft even as recent as the A380 [99] have a series of mechanical linkages that run in a spanwise direction from the centre of the aircraft to the wingtips, with a series of gearboxes located to offtake power for the flaps and slats. A brief history of the high lift device actuator schemes used by Airbus and Boeing can be found in reference [101], as well as potential uses as local electrically powered flap actuators. Classical mechanical systems are often powered by a centrally located, hydraulically driven motor, where the mechanical power distribution

guarantees symmetrical operation of the high lift devices. In designs such as this, the network of torque transmission tubes can have a significant cost penalty on the aircraft and an electrically powered distributed system can be appealing. Until recently, the certification bodies required that the high lift devices be geared together to ensure symmetric operation; but now a system without mechanical linkages can be certified if it provides another method of guaranteeing symmetrical deployment.

Modelling and Simulation Simulation is an important aspect in design and qualification of EHAs, particularly because of the increased complexity of the hydrostatic transmission when compared with the EMA. Since the medium is fluidic, care needs to be taken to ensure cavitation does not occur and that a minimum pressure is maintained in all parts of the hydrostatic circuit. This will require the addition of a fluid refeeding circuit comprising of either a smaller charge pump or accumulator and shuttle valves to control the additional fluid flow. There also needs to be relief valves to ensure the pressure remains below a safe maximum in the case of overloading of the hydraulic piston. Although this configuration can be seen in many publications on EHAs; it is demonstrated, modelled and validated through experimentation by Crowder [102]. This work is interesting because it highlights the accuracy which modelling can achieve, *when the modelling parameters are known*. The simulation results published by Crowder show a good match with the experimental actuator even during regeneration, but since the work was in a fairly early stage greater knowledge of the system parameters were expected to be gathered later in the project.

An EHA has the same hydraulic ram as a conventional ESHA but different power supplies. The dynamics of the piston and attached control surface

depend strongly on the coupled behaviour of the pump, motor and hydrostatic transmission. Kang *et al.* modelled the control surface and couplings as well as an EHA to assess the dynamic response of a complete flight control configuration [103]. The authors compare the system with that of a fourth order model of a conventional hydraulic servosystem and finds the high frequency performance of the EHA is superior to that of an ESHA. The work is not validated experimentally but the reason for the improved high frequency response is assumed to be the reduced volume of compressible fluid in the EHA, reducing the capacity of the 'oil spring' low pass filter effect.

A detailed document was written by Pastrakuljic [104] which describes the nonlinear modelling of an EHA and has been referred to heavily in the EHA modelling section of this thesis in section 3.3 starting on page 187. The author constructs a nonlinear model from first principles and validates it against a prototype actuator that was already in existence. The accuracy was found to be reasonable but optimisation was required to identify some of the unknown internal parameters. The problem with highly nonlinear models is that they inevitably require more component values to characterise them, for example the unusable 'dead volume' which exists in a hydraulic cylinder. Also, the model was recreated from the referenced document in the preliminary stages of this work and although the detail was high, execution speed was not fast enough to allow coupling with a 6-DOF aircraft model while achieving FRT simulation.

Another author which has constructed a full nonlinear model of an EHA is Kang [105]; although similar in many ways to the previously referenced documents, the author uses a continuous function of friction to represent the piston. Commonly, a discontinuous function is used to model Coulomb friction which is more accurate, but also more difficult for a numerical in-

tegration solver to handle; thus slowing the simulation speed down. Since frequent reversals are necessary in modelling flight control actuators it is comprehensible that continuous friction models can accelerate simulation speed significantly, albeit at a loss of accuracy around breakaway.

In another paper, Kang uses direct feedback to compensate for pressure (i.e. load) in the control system which shows a significantly improved control response under dynamic loading conditions [106]. A similar technique is used for the servo controls of the high speed actuators modelled in this thesis, presented in the modelling section 3 on page 125.

All of the detailed nonlinear models referenced so far use the fluid compressibility equation to model the chamber on each side of the piston separately. This is the 'correct' way to represent the true behaviour of a hydraulic piston since each chamber is physically separate. It is indeed required to model the piston in this way for models that require accurate simulation of the accumulator and anti-cavitation check valves, since these are inherently asymmetric with respect to the pressures on each side of the piston. It does however mean each chamber acts like an individual spring, which can cause oscillations of the piston and increases the order of the model. These components are not directly related to the main power losses of the actuator; for power loss estimation it is plausible to reduce these two compressibility equations into a single delta pressure across the piston [107]. Asymmetric behaviour can not be simulated so refeeding circuits can be removed and the whole model becomes much faster to simulate.

An interesting development in the modelling of systems is the use of object oriented techniques which facilitate 'graphical' construction of models. These allow the equations which describe the properties of a component to be grouped together into blocks which can be connected to form a complete

system of, for example, motor, pump and cylinder. This technique has several advantages, firstly the model is visually much more similar to the block diagram of the real system and therefore makes model formulation faster and less error prone (once the blocks have been created and verified in isolation). Secondly the inter-block connections can carry multiple signals as in the real world; a single connection can carry both torque and velocity signals in the same way that a physical shaft can. Thirdly, the segregation of 'nodes' or blocks allows for the use of distributed simulation which is naturally designed for multithreaded computation [108].

There are other visual modelling tools such as the commercial 'SimScape' language produced by Mathworks [34, 109]. This does not have the capacity to allow distributed solvers, but does provide the object oriented modelling functionality. This was initially attempted with the models in this thesis but the problem is that the user has little control over the fidelity of the equations used in the blocks. It is not possible to modify them to use simple first order approximations when appropriate for the design at hand. Another problem is that they can encourage a *laissez faire* attitude in inexperienced modellers, who wish to avoid complex, but often beneficial understanding of the detailed modelling task.

A final mention is made about collaborative integration of multiple software applications in the simulation of an actuator. Li and Wang use this technique to create a multidisciplinary model of an EHA by simulating the fluidic subsystem using the commercial hyraulic simulation package AMEsim and the mechanical and electrical subsystems in Simulink [110]. The referenced paper shows improved accuracy of the combined software simulation over classic Simulink model, but it is suspected that this is also matched by a corresponding decrease in simulation speed. Added to this is the difficulty

in ensuring compatibility between various softwares from different manufacturers and it is considered a wise choice to avoid going down this path for this thesis.

2.3.4.3 Robust Design

Fault tolerant design of an EHA is not as difficult as it is for an EMAs. The hydraulic cylinder in an EHA is identical to that in a classic hydraulic servo system, which has proven its reliability over many years of in-flight service. The cylinder itself has a much lower probability of jamming than a mechanical transmission; even in the event of a failure upstream of the cylinder, a bypass valve can be opened to enable the damped fail-operative mode [95].

The actuator manufacturer Moog has conducted studies [111] to ascertain the feasibility of implementing multiple redundancy in EMAs, EHAs and integrated actuator packages (IAP – these are the same as EHA-VPs with variable swashplate angle pumps and a constant speed motor) with good success. The referenced actuators are not direct replacements for aircraft; they have been designed to operate within specification for 100 space flights, in conditions similar to those which a Space Shuttle or the International Space Station would experience. However, the principles of operation remain the same and Moog has demonstrated the possibility of implementing two-fault tolerance on electric actuators.

One solution to providing control surface level redundancy is to simply use more actuators in parallel. Waffner has produced a triplex redundant EHA system for research and development which uses three similarly performing actuators (which can be different units) [112]. This provides the obvious benefits of a triplex redundant system, but because of the integrated nature

of the EHA, the repair of a failed actuator is handled in a modular fashion. A single actuator can be disconnected independently of the other two and replaced very quickly.

It could be argued that using a simplex analogue control valve is a potential single point of failure in an actuator, for which potential digital valve redundancy solutions have been suggested. Siivonen presents a solution using multiple redundant binary servo valves to, amongst other features, provide redundancy against single valve failures [113]. In this architecture there are many small binary valves in parallel which are controlled digitally to provide a quantized control of the flow rate. When a single failure occurs the remaining valves can continue to supply fluid to the cylinder but at a flow rate reduced by the proportion of total flow which the failed valve carried.

Skormin and Apone have developed an on-line health monitoring tool for variable displacement pumps which is capable of recognising a number of failure patterns [114], such as excessive leakage and fluid contamination. Directly, this would only be relevant to the EHA-VP but the principles could be applied to a fixed displacement pump. By using health monitoring, the EHA will be equipped with the same benefits that are described regarding the EMA prognostics in section 2.3.3.3 on page 32.

As part of a robust design it is important to take into account the possible causes of reduced reliability, from the earliest stages in a design. These can be wide ranging from contaminated fluids/lubricants to excessive vibration which has not been considered during the specification stages. Perhaps the most significant of these over the lifetime of the actuators is operating temperature. Having tools to predict and analyse the potential heat generation and performance of cooling components can avoid expensive and time consuming changes late in the design cycle. There are many techniques of

achieving this, from equation based methods presented by Johansson *et al.* [115], to finite element modelling and Bondgraph modelling as described by Takebayashi [116]. The first method essentially is a summation of heat flows in the various components in the actuator, while the latter method is particularly suited to high speed simulation of complex structures such as heatsinks. Both of these methods are designed to produce faster and easier results than the most detailed and challenging computational method, computational fluid dynamics (CFD).

2.3.4.4 Regeneration

Regeneration for an EHA is very much the same problem that is faced by the EMA. For that reason, the principles will not be repeated here. Instead please refer to section 2.3.3.4 on page 38.

2.3.4.5 Component Specification

Motor There are a range of motors that can be used in EHAs, and the most suitable types depend on the whether a fixed pitch or variable pitch EHA is being used. For the EHA-FP, an easily controllable BLDC motor is usually chosen. The performance requirements are very similar to the motors used to power EMAs and will not be repeated. Please refer to section 2.3.3.5 on page 40.

The variable displacement EHA-VP is usually driven by an AC induction motor, powered directly from an aircraft's 115V power supply. This motor is mechanically connected to a variable displacement hydraulic pump (VDP), but from then on the system is the same as the variable speed motor EHA-FP. The benefit of this configuration is that the motor can be operated

constantly at its most efficient speed, requiring no power conversion electronics and also reducing I^2R heating losses [117]. This argument does not always hold true however; in circumstances where an actuator is not moving the motor will still have to run at full speed, generating a lot of heat just to provide enough flow to compensate for piston leakage. A tradeoff is made in selecting variable swashplate angle piston pumps over fixed displacement types; additional complexity is added to facilitate changing the swashplate angle. This can reduce the reliability of the actuator but in situations where fast dynamic response is a key design goal this may be an acceptable compromise.

Cylinder The cylinder used for the EHA is identical to that used for the ESHA, since the load, stroke and speed requirements are the same. The literature relating to this can be found in section 2.3.2.4 on page 22.

2.3.5 Power Loss Modelling

Modelling the losses in an actuator is one of the most important factors in this work; quantifying the inefficiencies is vital to estimating the energy consumption and dynamics of the different technologies [118]. However, it is not a straightforward task and a lot of work has gone into modelling friction in mechanical and hydraulic systems. The problem is, friction is affected by many factors - a ball screw is not just a case of steel on silicon nitride rolling friction since the lubricant acts as an elastohydrodynamic lubricant (EHL) and is strongly affected by temperature, cleanliness and many other conditions. The friction depends on the tribological properties of the materials in contact and there will be some sliding before the balls begin to roll in an EMA because of the Herzian contact area. All of these things make it

difficult to *accurately* produce predictions of friction which are true to their real world components which are the subject of this simulation exercise.

Attempts can become quite complex and use a variety of techniques from simple approximations [119, 120, 121] to complex analytical solutions [122, 123] or multidisciplinary simulation [124, 125]. The methods presented by Olaru and Puiu are not validated against experimental ball screws so although they produce usable estimates they are unlikely to be perfect. The more detailed a model becomes, the modeller finds themselves in a predicament of how to obtain values to parametrise the more detailed simulations.

The answer is of course, to conduct an experiment to deduce what the unknown variables might be. One such work was undertaken by Kim and Chung who used limit cycle analysis to parameterise friction models [126], another by Kamalzadeh uses least squares system identification [127]. This process is typical of design tasks that will be followed by material actuators being procured, but it does not help those who wish to conduct simulations of multiple actuators without following it up with an experimental stage. This would be true of a software tool intended to assist with preliminary design of user specified aircraft configurations, where actuator characteristics such as ball screw pitch or hydraulic cylinder area are design variables. In these cases, first order approximations must be accepted because it is not feasible to back up every design iteration with manufactured test components from which accurate friction coefficients are derived.

There are several published experiments which investigate friction models against real world actuators. Lampaert uses four existing models to compensate for low velocity tracking errors in ballscrew driven machine tools [128]. These models are aimed specifically at modelling the nonlinear behaviour at low velocity due to effects such as hysteric pre-sliding (based on displace-

ment) and the transition to the sliding regime (based on velocity). The goal is not to model power losses, but to improve the accuracy of linear proportional + integral + differential (PID) controllers for table positioning. Since friction is one of the major sources of energy loss in a system, this work is also applicable to actuator power consumption modelling. Compounding this fact is that flight control actuators spend the vast majority of their operating life at low velocity, reversing direction frequently. That said, some friction models are computationally intensive so a tradeoff in FRT simulation has to be made between friction fidelity and simulation speed.

A piece of work which focuses on the modelling of losses in the whole system including servodrive, motor and roller screw is presented by Karam [129]. The author presents a complete investigation, firstly designing simulation models followed by the design of a test rig. The apparatus is then used to perform system identification experiments which are intended specifically to parameterise the friction model in the simulation. The referenced document provides the equations used to represent friction and the results of the identification task but the results are not directly applicable to other actuators which do not have the same specifications. The author notes in a later paper that the method is designed to be non-intrusive to the actuator and can be performed on a simple test bench [130]. This is ideal for detailed investigations but unfortunately, without the means to acquire a real actuator the results cannot be used directly in this thesis, except to highlight what the method would be in an ideal situation.

The most straightforward, yet important functions of friction is the velocity dependent viscous friction. This is frequently represented by a linear function as shown in Figure 2.13

One of the most computationally challenging forms of friction to simulate

correctly in a dynamic model is Coulomb friction. When using a numerical solver such as those in Simulink, a discontinuity in the friction function at $\dot{x} = 0$ forces a variable step solver to reduce the timestep as the direction reverses. A common discontinuous representation of the Coulomb friction is based on a function depending on the sign of the velocity, as shown in Figure 2.14. This function is discontinuous and difficult to solve because at $\dot{x} = 0$ there is no definite value for the friction force; it is equal all values in the range $\pm F_{r_C}$. This makes sense in the real world; while an object is stationary the Coulomb friction will apply a force equal and opposite to any applied force which intends to slide the object, until the magnitude exceeds the breakaway force.

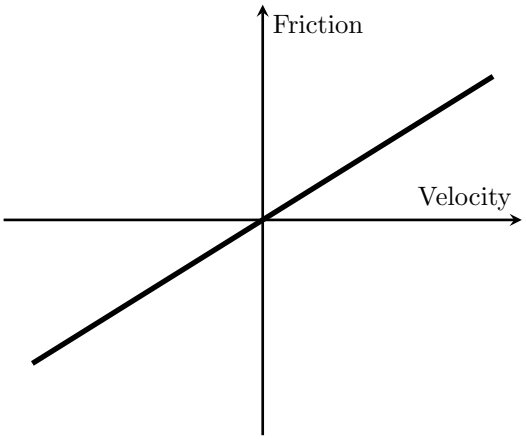

Figure 2.13: Viscous friction function using B$\dot{x}$

This presents a problem for the numerical solver at crossover since the instantaneous change in friction force causes the error tolerance to be exceeded, forcing the reduction of the step size until the error in each timestep is less than the tolerance. The solution will *never* be identical to the discontinuous friction function because it is impossible to have a continuous time solver holding two values at one instant in time. The timestep adaptation algorithm will nevertheless attempt to by taking ever reducing steps which causes the

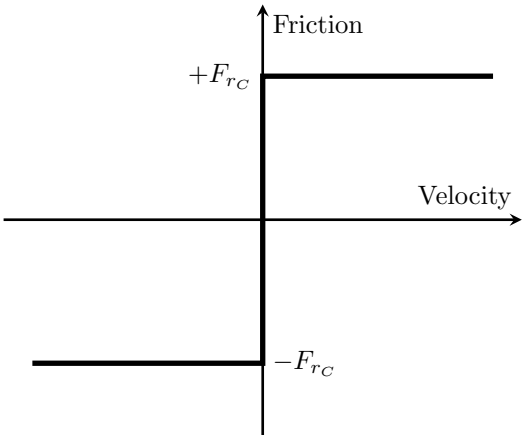

Figure 2.14: Discontinuous Coulomb friction using sign($\dot{x}$)

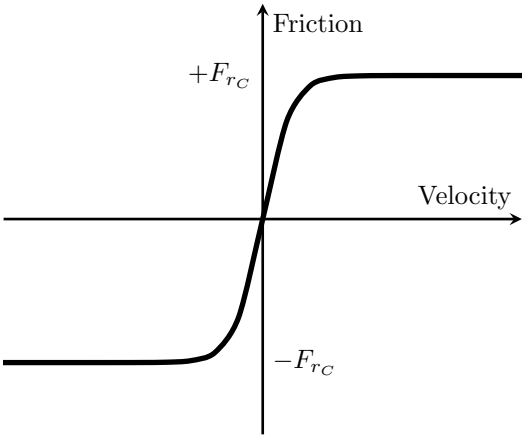

Figure 2.15: Continuous Coulomb friction using tanh($\dot{x}$)

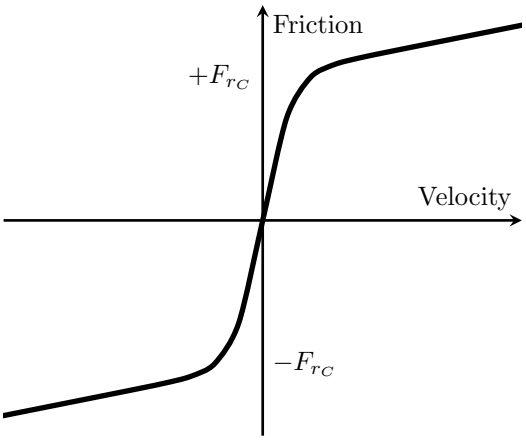

Figure 2.16: Continuous friction model using tanh($\dot{x}$) + B$\dot{x}$

simulation to slow down significantly. In the theoretical case where the error tolerance is set to zero, the simulation would freeze at the discontinuity as the timesteps are reduced towards zero (with no limits), eventually resulting in a math error.

There is no real solution to this (*in Simulink*), a common workaround is to use a continuous friction model such as a tanh function which equals zero at zero velocity (shown in Figure 2.15). This is trading off realism for speed - the object's friction will now not oppose an applied force when the velocity is zero and it will accelerate when a force below the real world breakaway force is applied. This presents a problem for modelling losses because overcoming Coulomb friction from stationary is a regular occurrence on a flight control actuator. For this work, this is a sacrifice that has to be made to achieve FRT simulation on a single processor. Other models such as that presented by Majd provide a detailed, continuous representation of friction both near zero velocity and away from it [131]. This technique improves over a rudimentary tanh function because it allows estimation of the Stribeck friction, but it retains the weakness of having zero friction force at zero velocity.

Given the limited experimental remit of this thesis it is decided to opt for a simple friction model since the numerical values of any model cannot be trusted without experimental validation. Therefore, by choosing a technique that requires the least variables and represents the simplest (and perhaps most unrealistic) case, the model will be fast and avoids introducing unfounded estimates of friction characterisation parameters. The model used is a combination of the viscous friction and continuous Coulomb frictions; shown in Figure 2.16. This allows the work to progress in order to focus on the wider task of simulating the aircraft, actuators and control systems in a unified model. **It does however mean the results cannot be used to**

draw validated conclusions of which actuators are the most efficient since friction plays a dominant role in assessing this.

When performing an early design assessment of an actuator, the only source of energy loss data is the from the manufacturer datasheet. As highlighted by Maré, the information provided by different manufacturers can be somewhat lacking - often 'mechanical efficiency' data is given which may not convey information regarding how the losses vary with load, speed or temperature [132]. The referenced paper presents a method for systems modellers to estimate dynamic friction forces using provided mechanical efficiency data. The same technique is then also applied to a hydraulic pump specific to an EHA with good success. What is particularly evident from the data presented by Maré is the accuracy with which the friction models represent varying load forces and speed. There are some issues at low speed and load for the hydraulic pump model due to the strong nonlinearities in the real system, but compared to a friction model which relies solely on speed as an input the improvement is extremely good.

A noteworthy paper is presented by Maré which compares the energy losses of the three actuator technologies investigated in this thesis [3]. The author has conducted a detailed study of losses in all the major components; including electrical losses in the servodrive, leakage flow in the hydraulic pump and the continuous metering losses in the servovalve. The loss models are provided in a general form which require populating with realistic component properties derived either from datasheets and/or experimentation. Maré arranges the models for inverse simulation which calculates aircraft power supply demands from control surface deflection and load force data. This method does not require a control system so definitely has the potential to increase simulation speed if ideal actuator power consumption is the only

analysis of interest.

Using the methods provided by Maré and Karam [132, 3, 129, 130] to increase the fidelity of the system level loss estimation is considered to be an ideal direction for improving the method defined by this thesis. The increased fidelity of the friction representation is thought to provide the most significant improvement to the accuracy of the overall method. Maré presented a paper which summarises the options available for system-level modelling of friction for virtual prototyping; the referenced article is noted for being an ideal starting point for the progression of this work [133].

Including detailed friction models has the downside of requiring a more complex control algorithm to provide good response with the inclusion of, for example, Stribeck friction. This requires extra time to design and test the improvements if the forward modelling method is used. Alternatively, restructuring the actuator models to an inverse format or using non-causal simulation software such as Dymola would provide a simulation speed increase, but the parallel representation of the real aircraft would be lost. Also, the modelling of the control algorithm is neglected so the energy efficiency of different control techniques cannot be investigated.

Indeed, this work focuses on the modelling of the actuators themselves and ignores the losses in the generation and supply systems. Lauckner describes the hydraulic system on the Airbus A380 and points out that one of the greatest sources of continuous loss is in the engine driven pumps [134]. This is because of the continuous operation and constant 5000 psi pressure across them, driving a leakage flow for cooling through the case drain and back to the reservoir. On many aircraft the radiative cooling of the pipes provides a sufficient means of keeping the system temperature within specified limits, but with the very high capacity of the A380's hydraulic system

this is not possible and requires active cooling. These losses represent a significant portion of the complete system's energy losses and would be an ideal addition to the future improvement of this thesis.

The importance of studying the complete system is noted by Maré; actuation system energy consumption is comparatively low on the whole aircraft level - less than 1 kJ (delivered to load) for an aileron on a two hour, A320 size, commercial transport aircraft flight [73]. The mass of the actuation system is not negligible and should be taken into account when analysing technology options. It is conceivable that overall aircraft efficiency may decrease if actuators are optimised for minimum energy alone - possibly at the expense of increased overall mass.

2.4 Aircraft Modelling

The aircraft model used in this work is a 6 degree of freedom (6-DOF) rigid body model based on Newton's second law. The model is not novel and the full derivation will not be reproduced; for a full background the reader should refer to textbooks covering the complete derivation [135, 136, 137, 138]. The method presented in this section derives the equations of motion in vector form and is quoted here from [139]. This method is used because it formulates the equations in the most computationally efficient manner as used by the Mathworks' Aerospace Blockset.

The equations of motion are implemented using the block '6DoF (Euler Angles)' for simplicity and efficiency of programming. The documentation for the block can be found in reference [140]. The notation for the frames of reference are shown in Figure 2.17.

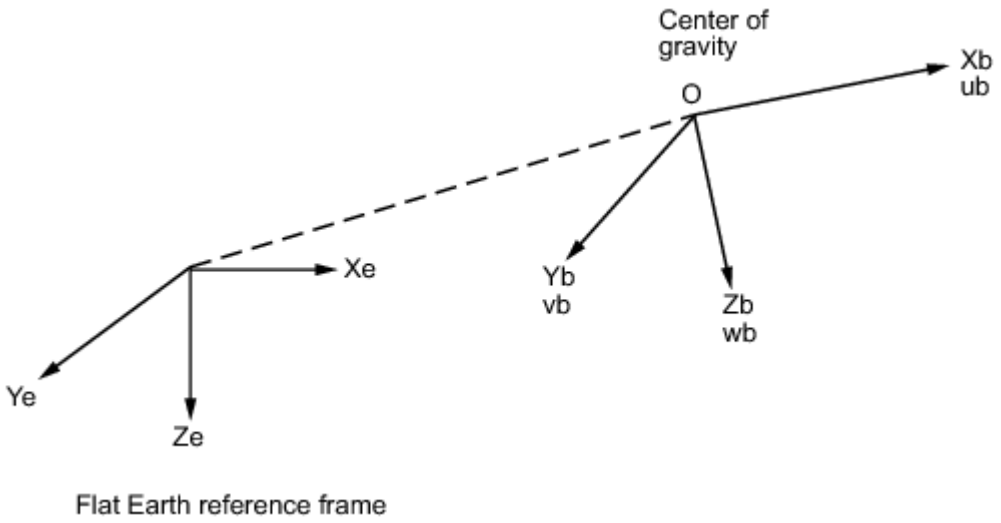

Figure 2.17: Representation of body fixed and earth fixed reference frames [140]

2.4.1 Coordinate Frames

The coordinate frames used for the derivation in this section follow standard aerospace flight dynamics notation; for reference please see chapters 2 and 3 in [139]

2.4.2 Kinematics

2.4.2.1 Translational Velocity

Aircraft velocity is most frequently expressed in the body axes; it is an inertial velocity projected into the body axes for use with the aerodynamic modelling of the aircraft. The position of the aircraft is usually referred to the inertial frame and relating the two requires the differentiation of the position vector and rotation from inertial to body axes.

The rotation matrix from vehicle frame (attached to the aircraft but aligned with inertial axes) to body frame $\mathcal{R}_v^b$ is defined in literature as:

$$\mathcal{R}_v^b \triangleq \begin{pmatrix} c_\theta c_\psi & c_\theta s_\psi & -s_\theta \\ s_\phi s_\theta c_\psi - c_\phi s_\psi & s_\phi s_\theta s_\psi + c_\phi c_\psi & s_\phi c_\theta \\ c_\phi s_\theta c_\psi + s_\phi s_\psi & c_\phi s_\theta s_\psi - s_\phi c_\psi & c_\phi c_\theta \end{pmatrix} \tag{2.2}$$

where

$$c_\phi \triangleq \cos\phi \qquad\qquad s_\phi \triangleq \sin\phi$$

Using the rotation matrix (2.2), the aircraft position in the inertial frame p_n, p_e and p_d can be related to the velocity in body frame u, v and w:

$$\frac{d}{dt}\begin{pmatrix} p_n \\ p_e \\ p_d \end{pmatrix} = \mathcal{R}_b^v \begin{pmatrix} u \\ v \\ w \end{pmatrix} = \left(\mathcal{R}_v^b\right)^\top \begin{pmatrix} u \\ v \\ w \end{pmatrix} \tag{2.3}$$

Which gives:

$$\begin{pmatrix} \dot{p}_n \\ \dot{p}_e \\ \dot{p}_d \end{pmatrix} = \begin{pmatrix} c_\theta c_\psi & s_\phi s_\theta c_\psi - c_\phi s_\psi & c_\phi s_\theta c_\psi + s_\phi s_\psi \\ c_\theta s_\psi & s_\phi s_\theta s_\psi + c_\phi c_\psi & c_\phi s_\theta s_\psi - s_\phi c_\psi \\ -s_\theta & s_\phi c_\theta & c_\phi c_\theta \end{pmatrix} \begin{pmatrix} u \\ v \\ w \end{pmatrix} \tag{2.4}$$

2.4.2.2 Rotational Velocity

The relationship between angular positions ϕ, θ, ψ and velocities p, q, r are based on three coordinate frames; a series of intermediate rotations from inertially oriented vehicle axes to the body frame. The order of rotation is first around the yaw axis by angle ψ ($\mathcal{F}^v \rightarrow \mathcal{F}^{v1}$),

$$\mathcal{R}_v^{v1}(\psi) = \begin{pmatrix} \cos\psi & \sin\psi & 0 \\ -\sin\psi & \cos\psi & 0 \\ 0 & 0 & 1 \end{pmatrix} \tag{2.5}$$

second is a rotation around the pitch axis by angle θ ($\mathcal{F}^{v1} \rightarrow \mathcal{F}^{v2}$)

$$\mathcal{R}_{v1}^{v2}(\theta) = \begin{pmatrix} \cos\theta & 0 & -\sin\theta \\ 0 & 1 & 0 \\ \sin\theta & 0 & \cos\theta \end{pmatrix} \tag{2.6}$$

and finally around the roll axis by angle ϕ ($\mathcal{F}^{v2} \rightarrow \mathcal{F}^{b}$).

$$\mathcal{R}^{b}_{v2}(\phi) = \begin{pmatrix} 1 & 0 & 0 \\ 0 & \cos\phi & \sin\phi \\ 0 & -\sin\phi & \cos\psi \end{pmatrix} \tag{2.7}$$

The body frame angular rates can be referred to the derivatives of the Euler angles by applying the correct rotations in the correct order:

$$\begin{pmatrix} p \\ q \\ r \end{pmatrix} = \begin{pmatrix} \dot{\phi} \\ 0 \\ 0 \end{pmatrix} + \mathcal{R}^{b}_{v2}(\phi) \begin{pmatrix} 0 \\ \dot{\theta} \\ 0 \end{pmatrix} + \mathcal{R}^{b}_{v2}(\phi)\mathcal{R}^{v2}_{v1}(\theta) \begin{pmatrix} 0 \\ 0 \\ \dot{\psi} \end{pmatrix} \tag{2.8}$$

$$= \begin{pmatrix} 1 & 0 & -\sin\theta \\ 0 & \cos\phi & \sin\phi\cos\theta \\ 0 & -\sin\phi & \cos\phi\cos\theta \end{pmatrix} \begin{pmatrix} \dot{\phi} \\ \dot{\theta} \\ \dot{\psi} \end{pmatrix} \tag{2.9}$$

By inverting equation (2.8), an expression for the three angular position states in terms of the Euler angles and body axis rates is obtained:

$$\begin{pmatrix} \dot{\phi} \\ \dot{\theta} \\ \dot{\psi} \end{pmatrix} = \begin{pmatrix} 1 & \sin\phi\tan\theta & \cos\phi\tan\theta \\ 0 & \cos\phi & -\sin\phi \\ 0 & \sin\phi\sec\theta & \cos\phi\sec\theta \end{pmatrix} \begin{pmatrix} p \\ q \\ r \end{pmatrix} \tag{2.10}$$

2.4.3 Rigid Body Dynamics

2.4.3.1 Translational Motion

The basis of modelling motion stems from Newton's second law which considers the acceleration of a particle when acted on by an external force in

an inertial reference frame. This is stated as:

$$\mathbf{F}_i = \mathsf{m}\frac{d\mathbf{V}_g}{dt_i} \tag{2.11}$$

where m is the mass of the particle, $\mathbf{V}_g$ is the velocity vector of the aircraft with respect to the ground, $\frac{d}{dt_i}$ is the time derivative with respect to the inertial frame and $\mathbf{F}_i$ is the sum of all external forces including aerodynamic, gravitational and propulsive forces.

The derivative of velocity with respect to the inertial frame can be related to the body frame by including the angular motion of the body frame around the inertial frame:

$$\frac{d\mathbf{V}_g}{dt_i} = \frac{d\mathbf{V}_g}{dt_b} + \boldsymbol{\omega}_{b/i} \times \mathbf{V}_g \tag{2.12}$$

where $\boldsymbol{\omega}_{b/i}$ is the angular velocity of the particle with respect to the inertial frame. Equations (2.11) and (2.12) can be combined to express Newton's second law with the derivative of velocity expressed in the body frame:

$$\mathbf{F}_i = \mathsf{m}\left(\frac{d\mathbf{V}_g}{dt_b} + \boldsymbol{\omega}_{b/i} \times \mathbf{V}_g\right) \tag{2.13}$$

When considering aircraft manoeuvres and the effects of control surface inputs it is most convenient to express equation (2.13) in the body axes.

$$\mathbf{F}_b = \mathsf{m}\left(\frac{d\mathbf{V}_g^b}{dt_b} + \boldsymbol{\omega}_{b/i}^b \times \mathbf{V}_g^b\right) \tag{2.14}$$

where

$$\mathbf{V}_g^b = \begin{pmatrix} u \\ v \\ w \end{pmatrix} \qquad \boldsymbol{\omega}_{b/i}^b = \begin{pmatrix} p \\ q \\ r \end{pmatrix} \qquad \mathbf{F}_b = \begin{pmatrix} F_x \\ F_y \\ F_z \end{pmatrix} \tag{2.15}$$

By considering the time differential of $\mathbf{V}_g^b$ with respect to the body axes, from the position of an observer on the moving body, the body axis acceleration can be defined as:

$$\frac{d\mathbf{V}_g^b}{dt_b} = \begin{pmatrix} \dot{u} \\ \dot{v} \\ \dot{w} \end{pmatrix}$$

Expanding the cross product in equation (2.14) and rearranging for acceleration, the body axis accelerations are obtained:

$$\begin{pmatrix} \dot{u} \\ \dot{v} \\ \dot{w} \end{pmatrix} = \begin{pmatrix} rv - qw \\ pw - ru \\ qu - pv \end{pmatrix} + \frac{1}{\mathsf{m}} \begin{pmatrix} F_x \\ F_y \\ F_z \end{pmatrix} \tag{2.16}$$

2.4.3.2 Rotational Motion

Newton's second law applied to rotational motion is defined as:

$$\mathbf{M} = \frac{d\mathbf{h}}{dt_i} \tag{2.17}$$

where $\mathbf{h}$ is the angular momentum and $\mathbf{M}$ is the sum of the externally applied moments, assuming the moments are applied around the centre of gravity. As with the translational forces it is most useful to obtain the equations of angular motion in the body frame by first referring the derivative to the body frame[1]:

$$\mathbf{M} = \frac{d\mathbf{h}}{dt_i} = \frac{d\mathbf{h}}{dt_b} + \boldsymbol{\omega}_{b/i} \times \mathbf{h} \tag{2.18}$$

[1]More information can be found in equation 2.17 in reference [139] or Tewari gives a good explanation and diagram under the title of 'changing vectors' [138]

then adjusting moments and angular velocities to body frame:

$$\mathbf{M}^b = \frac{d\mathbf{h}^b}{dt_b} + \boldsymbol{\omega}^b_{b/i} \times \mathbf{h}^b \tag{2.19}$$

For a rigid body the inertia matrix **J** is defined as:

$$\mathbf{J} = \begin{pmatrix} \int (y^2 + z^2)\, d\mathsf{m} & -\int xy\ d\mathsf{m} & -\int xz\ d\mathsf{m} \\ -\int xy\ d\mathsf{m} & \int (x^2 + z^2)\, d\mathsf{m} & -\int yz\ d\mathsf{m} \\ -\int xz\ d\mathsf{m} & -\int yz\ d\mathsf{m} & \int (x^2 + y^2)\, d\mathsf{m} \end{pmatrix} \tag{2.20}$$

$$\triangleq \begin{pmatrix} J_x & -J_{xy} & -J_{xz} \\ -J_{xy} & J_y & -J_{yz} \\ -J_{xz} & -J_{yz} & J_z \end{pmatrix} \tag{2.21}$$

The diagonals are the *moments of inertia* which quantify the aircraft's opposition to angular acceleration. When the inertia is considered with respect to the body frame the values will remain constant, i.e. $\frac{d\mathbf{J}}{dt_b} = 0$. By considering the definition of angular momentum and derivative,

$$\mathbf{h}^b = \mathbf{J}\boldsymbol{\omega}^b_{b/i} \tag{2.22}$$

$$\frac{d\mathbf{h}^b}{dt_b} = \mathbf{J}\frac{d\boldsymbol{\omega}^b_{b/i}}{dt_b} \tag{2.23}$$

equation (2.19) can be rewritten:

$$\mathbf{M}_b = \mathbf{J}\frac{d\boldsymbol{\omega}^b_{b/i}}{dt_b} + \boldsymbol{\omega}^b_{b/i} \times \left(\mathbf{J}\boldsymbol{\omega}^b_{b/i}\right) \tag{2.24}$$

The value represented by $\frac{d\boldsymbol{\omega}^b_{b/i}}{dt_b}$ is the angular acceleration of the body,

referred to the body frame. It follows that

$$\frac{d\boldsymbol{\omega}_{b/i}^{b}}{dt_b} = \dot{\boldsymbol{\omega}}_{b/i}^{b} = \begin{pmatrix} \dot{p} \\ \dot{q} \\ \dot{r} \end{pmatrix} \tag{2.25}$$

Substituting (2.25) into (2.24) and rearranging to have the derivative on the left hand side:

$$\dot{\boldsymbol{\omega}}_{b/i}^{b} = \mathbf{J}^{-1}\left[-\boldsymbol{\omega}_{b/i}^{b} \times \left(\mathbf{J}\boldsymbol{\omega}_{b/i}^{b}\right) + \mathbf{M}^{b}\right] \tag{2.26}$$

To calculate the inverse of the inertia matrix, the assumption is made that the aircraft is symmetric about the xz plane, implying $J_{xy} = J_{yz} = 0$ and the overall inertia simplifies to:

$$\mathbf{J} = \begin{pmatrix} J_x & 0 & -J_{xz} \\ 0 & J_y & 0 \\ -J_{xz} & 0 & J_z \end{pmatrix} \tag{2.27}$$

The inverse of the inertia matrix is then given by:

$$\mathbf{J}^{-1} = \frac{\text{adj}\,(\mathbf{J})}{\det\,(\mathbf{J})} \tag{2.28}$$

$$= \frac{\begin{pmatrix} J_x J_z & 0 & J_y J_{xz} \\ 0 & J_x J_z - J_{xz}^2 & 0 \\ J_{xz} J_y & 0 & J_x J_y \end{pmatrix}}{J_x J_y J_z - J_{xz}^2 J_y} \tag{2.29}$$

$$= \begin{pmatrix} \frac{J_z}{\Gamma} & 0 & \frac{J_{xz}}{\Gamma} \\ 0 & \frac{1}{J_y} & 0 \\ \frac{J_{xz}}{\Gamma} & 0 & \frac{J_x}{\Gamma} \end{pmatrix} \tag{2.30}$$

where $\Gamma = J_x J_z - J_{xz}^2$. Next, defining the external moments applied to the aircraft in the body frame:

$$\mathbf{M}^b = \begin{pmatrix} L \\ M \\ N \end{pmatrix} \tag{2.31}$$

The vector $\boldsymbol{\omega}_{b/i}^b$ from equation (2.26) can be expanded to the cross product equivalent matrix:

$$\left[-\boldsymbol{\omega}_{b/i}^b\right]_\times \triangleq \begin{pmatrix} 0 & r & -q \\ -r & 0 & p \\ q & -p & 0 \end{pmatrix} \tag{2.32}$$

Then, equations (2.25), (2.30), (2.32), (2.27), (2.15) and (2.31) can be

substituted into (2.26).

$$\begin{aligned}
\begin{pmatrix}\dot{p}\\ \dot{q}\\ \dot{r}\end{pmatrix} &= \begin{pmatrix}\frac{J_z}{\Gamma} & 0 & \frac{J_{xz}}{\Gamma}\\ 0 & \frac{1}{J_y} & 0\\ \frac{J_{xz}}{\Gamma} & 0 & \frac{J_x}{\Gamma}\end{pmatrix}\left[\begin{pmatrix}0 & r & -q\\ -r & 0 & p\\ q & -p & 0\end{pmatrix}\begin{pmatrix}J_x & 0 & -J_{xz}\\ 0 & J_y & 0\\ -J_{xz} & 0 & J_z\end{pmatrix}\begin{pmatrix}p\\ q\\ r\end{pmatrix} + \begin{pmatrix}L\\ M\\ N\end{pmatrix}\right]\\
&= \begin{pmatrix}\frac{J_z}{\Gamma} & 0 & \frac{J_{xz}}{\Gamma}\\ 0 & \frac{1}{J_y} & 0\\ \frac{J_{xz}}{\Gamma} & 0 & \frac{J_x}{\Gamma}\end{pmatrix}\left[\begin{pmatrix}J_{xz}pq + (J_y - J_z)qr\\ J_{xz}(r^2 - p^2) + (J_z - J_x)pr\\ (J_x - J_y)pq - J_{xz}qr\end{pmatrix} + \begin{pmatrix}L\\ M\\ N\end{pmatrix}\right]\\
&= \begin{pmatrix}\Gamma_1 pq - \Gamma_2 qr + \Gamma_3 L + \Gamma_4 N\\ \Gamma_5 pr - \Gamma_6\left(p^2 - r^2\right) + \frac{1}{J_y}M\\ \Gamma_7 pq - \Gamma_1 qr + \Gamma_4 L + \Gamma_8 N\end{pmatrix}
\end{aligned} \tag{2.33}$$

The Γ values have been written in shorthand and are described as follows:

$$\begin{aligned}
\Gamma_1 &= \frac{J_{xz}(J_x - J_y + J_z)}{\Gamma}\\
\Gamma_2 &= \frac{J_z(J_z - J_y) + J_{xz}^2}{\Gamma}\\
\Gamma_3 &= \frac{J_z}{\Gamma}\\
\Gamma_4 &= \frac{J_{xz}}{\Gamma}\\
\Gamma_5 &= \frac{J_z - J_x}{J_y}\\
\Gamma_6 &= \frac{J_{xz}}{J_y}\\
\Gamma_7 &= \frac{(J_x - J_y)J_x + J_{xz}^2}{\Gamma}\\
\Gamma_8 &= \frac{J_x}{\Gamma}
\end{aligned}$$

2.4.4 Equations of Motion

Now the kinematic and dynamic equations for translational and rotational motions (2.4), (2.10), (2.16) and (2.33) can be combined to form the 12 state 6-DOF equations of motion for the aircraft studied in this thesis. These equations do not currently have external force calculation from the aerodynamics, gravity and propulsion which will be provided in the next section.

$$\begin{pmatrix} \dot{p}_n \\ \dot{p}_e \\ \dot{p}_d \end{pmatrix} = \begin{pmatrix} c_\theta c_\psi & s_\phi s_\theta c_\psi - c_\phi s_\psi & c_\phi s_\theta c_\psi + s_\phi s_\psi \\ c_\theta s_\psi & s_\phi s_\theta s_\psi + c_\phi c_\psi & c_\phi s_\theta s_\psi - s_\phi c_\psi \\ -s_\theta & s_\phi c_\theta & c_\phi c_\theta \end{pmatrix} \begin{pmatrix} u \\ v \\ w \end{pmatrix} \tag{2.34}$$

$$\begin{pmatrix} \dot{u} \\ \dot{v} \\ \dot{w} \end{pmatrix} = \begin{pmatrix} rv - qw \\ pw - ru \\ qu - pv \end{pmatrix} + \frac{1}{\mathsf{m}} \begin{pmatrix} F_x \\ F_y \\ F_z \end{pmatrix} \tag{2.35}$$

$$\begin{pmatrix} \dot{\phi} \\ \dot{\theta} \\ \dot{\psi} \end{pmatrix} = \begin{pmatrix} 1 & \sin\phi \tan\theta & \cos\phi \tan\theta \\ 0 & \cos\phi & -\sin\phi \\ 0 & \sin\phi \sec\theta & \cos\phi \sec\theta \end{pmatrix} \begin{pmatrix} p \\ q \\ r \end{pmatrix} \tag{2.36}$$

$$\begin{pmatrix} \dot{p} \\ \dot{q} \\ \dot{r} \end{pmatrix} = \begin{pmatrix} \Gamma_1 pq - \Gamma_2 qr \\ \Gamma_5 pr - \Gamma_6 \left(p^2 - r^2\right) \\ \Gamma_7 pq - \Gamma_1 qr \end{pmatrix} + \begin{pmatrix} \Gamma_3 L + \Gamma_4 N \\ \frac{1}{J_y} M \\ \Gamma_4 L + \Gamma_8 N \end{pmatrix} \tag{2.37}$$

2.4.5 External Forces and Moments

The equations of motion allow the estimation of aircraft trajectory and acceleration but require additional inputs to function. The equations derived

in the previous section are capable of representing any object with left-right symmetry in three dimensional space; they need representations of external forces and moments to characterise them to model aircraft flight. This can become a wholly complex task which is beyond the scope of this work - this section intends only to describe the method used in this work and not to provide a course in flight mechanics. Only the main forces and moments will be covered here and detailed explanations can be found in the references mentioned in section 2.4 on page 73.

The forces and moments on the aircraft can be described using the vectors **F** and **M** respectively:

$$\mathbf{F} = \mathbf{F}_g + \mathbf{F}_a + \mathbf{F}_p \tag{2.38}$$

$$\mathbf{M} = \mathbf{M}_a + \mathbf{M}_p \tag{2.39}$$

where subscript a denotes the forces and moments caused by aerodynamic effects, p the forces and moments due to propulsion and g for the force due to gravity.

2.4.5.1 Gravitational Forces

The gravity force acts from the aircraft centre of gravity towards the centre of the Earth. Expressed in the vehicle frame $\mathcal{F}^v$ (attached to body, aligned with inertial axes), the gravity force vector can be described by:

$$\mathbf{F}_g^v = \begin{pmatrix} 0 \\ 0 \\ \mathsf{m}g \end{pmatrix} \tag{2.40}$$

Since the equations of motion in section 2.4.4 have been derived for body

axis forces and velocities, the gravity vector must be rotated from vehicle frame $\mathcal{F}^v$ to body frame $\mathcal{F}^b$.

$$\mathbf{F}_g^b = \mathcal{R}_v^b \begin{pmatrix} 0 \\ 0 \\ \mathsf{m}g \end{pmatrix} = \begin{pmatrix} -\mathsf{m}g \sin\theta \\ \mathsf{m}g \cos\theta \sin\phi \\ \mathsf{m}g \cos\theta \cos\phi \end{pmatrix} \tag{2.41}$$

There is no rotational moment applied by the gravitational force since it acts through the centre of gravity of the aircraft.

2.4.5.2 Aerodynamic Forces and Moments

The aerodynamic forces on an aircraft are induced by the flow of air around the airframe. In simplified terms; the wings generate most of the lift, drag is induced by the whole aircraft and rotational moments are modified by the control surfaces. The forces and moments can be stated as functions of their dominant variables, as described in the following two paragraphs.

Forces The aerodynamic forces acting on the airframe can be described by:

$$F_{drag} = F_x = \frac{1}{2}\rho V_T^2 S C_D(\alpha, q, \delta_e) \tag{2.42}$$

$$F_{side} = F_y = \frac{1}{2}\rho V_T^2 S C_Y(\beta, p, r, \delta_a, \delta_r) \tag{2.43}$$

$$F_{lift} = F_z = \frac{1}{2}\rho V_T^2 S C_L(\alpha, q, \delta_e) \tag{2.44}$$

where C_D, C_L and C_Y represent nondimensional coefficients which define the translational aerodynamic characteristics of the aircraft. These can be

implemented as single values or lookup tables to provide accurate data across the whole flight envelope. The coefficients are dimensionalised using the air density ρ, the planform area of the wing S and the true airspeed V_T. The overall force is a function of the angles of attack α and sideslip β, roll, pitch and yaw rates p, q, r and control surface angles δ_a, δ_e and δ_r (ailerons, elevators and rudder respectively).

The overall coefficients C_D, C_L and C_Y are formed from the combination of several static and dynamic coefficients:

$$C_D = \left[C_{D_0} + \frac{\partial C_D}{\partial \alpha}\alpha + \frac{\partial C_D}{\partial q}q + \frac{\partial C_D}{\partial \delta_e}\delta_e \right] \tag{2.45}$$

$$C_Y = \left[C_{Y_0} + \frac{\partial C_Y}{\partial \beta}\beta + \frac{\partial C_Y}{\partial p}p + \frac{\partial C_Y}{\partial r}r + \frac{\partial C_Y}{\partial \delta_a}\delta_a + \frac{\partial C_Y}{\partial \delta_r}\delta_r \right] \tag{2.46}$$

$$C_L = \left[C_{L_0} + \frac{\partial C_L}{\partial \alpha}\alpha + \frac{\partial C_L}{\partial q}q + \frac{\partial C_L}{\partial \delta_e}\delta_e \right] \tag{2.47}$$

The derivatives of p, q and r must then be nondimnensionalised using $\bar{c}/2V_T$ in the longitudinal direction and $b/2V_T$ in the lateral direction. The linear lift, drag and sideforce coefficients based on zero angle of attack (AOA) and sideslip are replaced with functions of the respective angles to highlight the use of nonlinear lookup tables. Partial derivatives are written in shorthand and the drag, side force and lift coefficients are written as:

$$C_D = \left[C_D(\alpha) + C_{D_q}\frac{\bar{c}}{2V_T}q + C_{D_{\delta_e}}\delta_e \right] \tag{2.48}$$

$$C_Y = \left[C_Y(\beta) + C_{Y_p}\frac{b}{2V_T}p + C_{Y_r}\frac{b}{2V_T}r + C_{Y_{\delta_a}}\delta_a + C_{Y_{\delta_r}}\delta_r \right] \tag{2.49}$$

$$C_L = \left[C_L(\alpha) + C_{L_q}\frac{\bar{c}}{2V_T}q + C_{L_{\delta_e}}\delta_e \right] \tag{2.50}$$

where b is the wingspan and $\bar{c}$ is the mean chord of the wing. The aerodynamic force vector in the body frame can then be formed:

$$\mathbf{F}_a^b = \begin{pmatrix} F_x \\ F_y \\ F_z \end{pmatrix} \tag{2.51}$$

Moments The aerodynamic moments applied to the airframe are described by:

$$L = \frac{1}{2}\rho V_T^2 S b C_l(\beta, p, r, \delta_a, \delta_r) \tag{2.52}$$

$$M = \frac{1}{2}\rho V_T^2 S \bar{c} C_m(\alpha, \dot{\alpha}, q, \delta_e) \tag{2.53}$$

$$N = \frac{1}{2}\rho V_T^2 S b C_n(\beta, p, r, \delta_a, \delta_r) \tag{2.54}$$

where b is the wingspan, $\bar{c}$ is the mean chord of the wing and S is the planform area of the wing. C_l, C_m and C_n represent nondimensional coefficients which define the rotational aerodynamic characteristics of the aircraft. These can also be implemented as single values or lookup tables to provide accurate data across the whole flight envelope.

The coefficients for the moment equations are also formed from partial derivatives of the relevant motion state. Using the same shorthand that is used for partial derivatives in the previous force section, the rotational

aerodynamic coefficients of the aircraft can be described by:

$$C_l = \left[C_l(\beta) + C_{l_p} \frac{b}{2V_T} p + C_{l_r} \frac{b}{2V_T} r + C_{l_{\delta_a}} \delta_a + C_{l_{\delta_r}} \delta_r \right] \tag{2.55}$$

$$C_m = \left[C_m(\alpha) + C_{m_q} \frac{\bar{c}}{2V_T} q + C_{m_{\delta_e}} \delta_e \right] \tag{2.56}$$

$$C_n = \left[C_n(\beta) + C_{n_p} \frac{b}{2V_T} p + C_{n_r} \frac{b}{2V_T} r + C_{n_{\delta_a}} \delta_a + C_{n_{\delta_r}} \delta_r \right] \tag{2.57}$$

Finally, the aerodynamic moment vector (in the body frame) can be formed:

$$\mathbf{M}_a^b = \begin{pmatrix} L \\ M \\ N \end{pmatrix} \tag{2.58}$$

2.4.5.3 Propulsive Forces and Moments

The forces and moments on the aircraft induced by the propulsion system can include parasitic characteristics besides the desired forward thrust. Single engine UAVs can suffer from a spiral instability caused by the roll moment induced by the propeller rotation. This effect is negligible on twin engine jets but the equations are formulated to allow 6-DOF behaviour - the level of fidelity depends on the engine model attached in each aircraft model. The

force and moment vectors are described by:

$$\mathbf{F}_p^b = \begin{pmatrix} F_{xp} \\ F_{yp} \\ F_{zp} \end{pmatrix} \tag{2.59}$$

$$\mathbf{M}_p^b = \begin{pmatrix} L_p \\ M_p \\ N_p \end{pmatrix} \tag{2.60}$$

The values can be as simple as linear relationships with throttle position to highly detailed models which include data on the thermodynamic behaviour inside the engines.

2.4.6 Aerodynamic Load Estimation

Aerodynamic load estimation can range from complex CFD simulation [141] to simple first order functions of control surface deflection. There is also DATCOM [142] and the slightly more complex vortice lattice method [143] which provides analytical techniques of producing hinge moment coefficients. The chosen method is to program lookup tables for estimating hinge moment coefficients online based on altitude and airspeed, as presented by Scholz [144]. This paper uses a method which is contained within DATCOM, but programming it directly provides a fast and reusable load estimation code.

When making this decision, a trade off is being made between accuracy and speed. Without real aircraft flight test data, wind tunnel data or an accurate 3D geometric model it is difficult to be precise. Functionally, there may not even be a definite need for high levels of accuracy since for this work, it is the relative power consumptions that are of interest not the actual

numerical value.

For more information this topic is covered further in section 3.7 on page 217.

2.5 Flight Control and Guidance

When conducting a forward kinematic and dynamic simulation of an uncontrolled aircraft the tasks are generally limited to analysing simple dynamic characteristics around steady state flight conditions. In order to execute advanced manoeuvres such as controlled heading, altitude or speed changes an FCS is required. This closes the loops between the aircraft control inputs and its output states in order to achieve the desired motion:

$$\text{Control Inputs} = \begin{pmatrix} \delta_e \\ \delta_t \\ \delta_a \\ \delta_r \end{pmatrix} = \begin{pmatrix} \text{Elevator angle} \\ \text{Throttle position} \\ \text{Aileron angle} \\ \text{Rudder angle} \end{pmatrix}$$

$$\text{Position States} = \begin{pmatrix} p_n \\ p_e \\ p_d \\ \phi \\ \theta \\ \psi \end{pmatrix} = \begin{pmatrix} \text{Inertial } n \text{ position} \\ \text{Inertial } e \text{ position} \\ \text{Inertial } d \text{ position} \\ \text{Euler roll angle} \\ \text{Euler pitch angle} \\ \text{Euler yaw angle} \end{pmatrix}$$

$$\text{Velocity States} = \begin{pmatrix} u \\ v \\ w \\ p \\ q \\ r \end{pmatrix} = \begin{pmatrix} \text{Longitudinal (forward) velocity} \\ \text{Lateral (transverse) velocity} \\ \text{Vertical velocity} \\ \text{Roll rate} \\ \text{Pitch rate} \\ \text{Yaw rate} \end{pmatrix}$$

There are many different forms of aircraft control systems which are far too extensive to cover in a thesis, so only those attempted in the progression of this work will be covered. This work mainly considers stable aircraft which do not require stability augmentation; this is generally true of transport aircraft in history, including the main case study aircraft. This simplification is becoming less applicable to modern aircraft such as the A380 which has relaxed stability margins to allow reduced stabiliser size and reduced drag [145].

This section will briefly describe initial control system design attempts using classic single input - single output (SISO) controllers, before explaining why they were replaced at an early stage of the integration work. Following on from this will be a more detailed description of the successful flight control algorithm, based on total energy control.

2.5.1 Classic Single Input - Single Output flight control algorithms

2.5.1.1 SISO Overview

A SISO control system design begins with models of the aircraft flight dynamics which have been linearised at specific flight conditions. These control loops are therefore optimised for that specific operating point. To provide good control across the whole flight envelope this process needs to be done for a wide range of linearised models, and then the controllers combined with logic switching or gain scheduling to adapt the SISO control laws to suit the current flight conditions. This is not exclusive to normal operating modes across the whole flight envelope, it also includes such instances as engine out failure modes, windshear handling and crosswind landings. In addition, a modern aircraft has tight integration between the flight management com-

puter (FMC) and flight controllers to provide top level mission planning, navigation and performance functions. This, combined with the fact that autopilot, autothrottle and yaw damping functions are designed and implemented separately leads to a complex FCS architecture with highly evolved subsystems and significant overlap in functions, as shown in Figure 2.18.

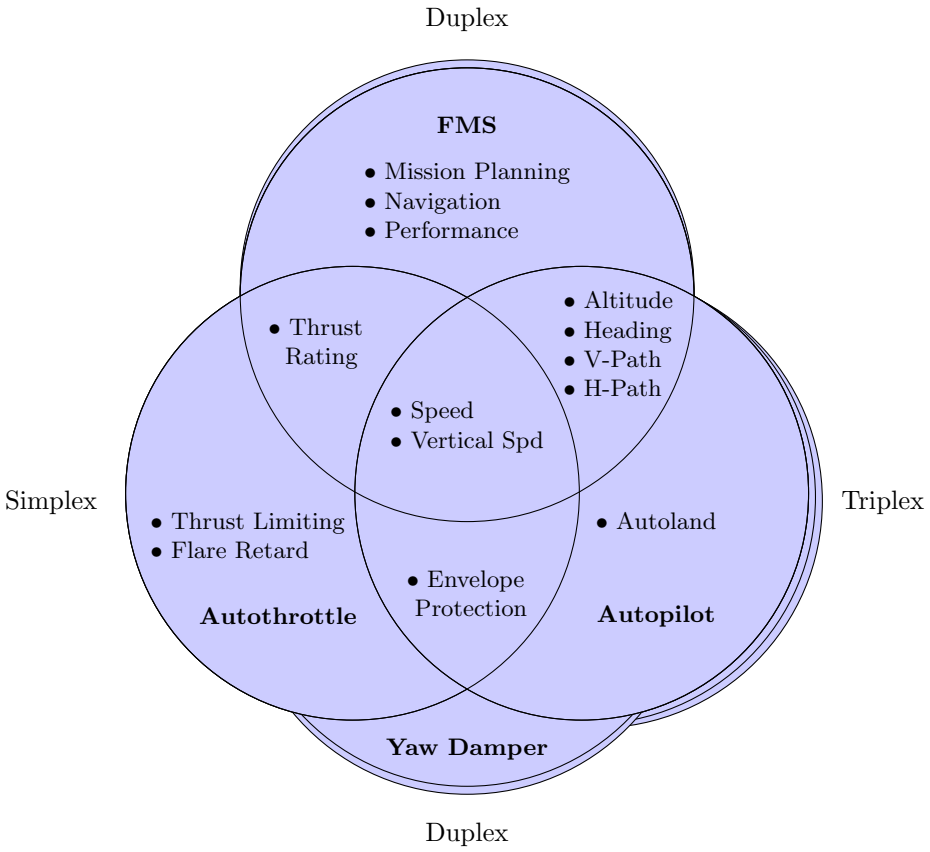

Figure 2.18: Current FCS architecture [146]

In a SISO FCS speed is typically controlled using the throttle and pitch angle is controlled by the elevators [146]. These two controllers act independently and are not aware of what each other are doing. Having the elevator control the pitch angle/angle of attack/lift in order to track a given flight path has the effect of converting flight path error into speed error. Since the

elevator has higher authority than the throttle, it puts the speed control loop in a troublesome situation in which it cannot control speed optimally. This has been described anecdotally by Lambregts [147] as

> *"Like giving the throttle to one pilot to control speed and the elevator to the other pilot to control flight path."*

which is clearly not a sensible cockpit workflow. Implementing control systems of this nature leads to fragmented systems which need many layers and interactions to enable all the modes required for a certified autopilot. Instead of continuously adding and adjusting the control loops to allow the simulation model to manoeuvre cleanly at all flight conditions, a novel and more integrated solution is described in section 2.5.2 on page 96.

All included, an SISO FCS for a modern aircraft is complex and does not guarantee safe control in every possible eventuality. For this reason the autopilot requires full time pilot monitoring, a fact that has lead to incidents in the past as described by Lambregts [148]:

- Pilot fails to monitor autopilot operation (Mexicana DC10) autopilot (A/P) stalls airplane.
- A/P roll control saturation, after engine out (China Airlines B747).
- Unexpected high altitude automatic disengage, out-of-trim, pilot over controls (MD11).
- Imperceptible aeroplane slow roll response, due to A/P sensor failure without proper alert (Evergreen 747).
- A/P reaches roll authority limit in icing, disconnects without timely warning, stall (Embrair Comair, Detroit).

- Pilot tries to take manual control, A/P remains engaged, overrides pilot (China Airlines A300, Nagoya).
- Pilot over controls rudder, after mild wake vortex encounter. Vertical stabilizer fails (AA A300, New York).

Perhaps the most significant long term drawback of a SISO FCS is that the designs are aircraft specific; it is generally not possible to reuse the code directly on another aircraft. This means longer development times and repeated costly certification programmes between subsequent aircraft design programmes.

2.5.1.2 SISO Implementation

Classic SISO controllers were found to not be robust in maintaining simulation stability when executing different manoeuvres at different flight conditions. Whilst it could be optimised for a given flight condition, for example at cruise altitude and speed, when the operating point was changed to landing approach, the controllers became suboptimal. Using gain scheduling of dynamic pressure only provided limited relief, in some situations Simulink's solver would take extremely small timesteps and cause the simulation to take orders of magnitude longer to complete.

The solution, if sticking with this control architecture is to iteratively refine the control loops at different operating conditions until they do not induce unnecessary oscillations at any point. This can take an unpredictable amount of time, depending mainly on the complexity of the flight dynamics model and the aerodynamic coefficients used within it.

An extra point worth noting is that the effect of poorly tuned PID control loops is likely to manifest itself as increased oscillations of the flight control

inputs. This has two effects; requiring smaller timesteps and increased actuator acceleration. Reduced timesteps cause longer simulation times and increasing the dynamic motion of the actuators causes increased (and unnecessary) power consumption.

To solve these issues, further research presented the more sophisticated control topology; the total energy control system (TECS).

2.5.2 Total Energy Control System

2.5.2.1 TECS Overview

The TECS is a method of controlling an aircraft which bears many resemblances to how pilots are taught to fly an aircraft. The technique was first written about by Lambregts while working for Boeing in 1983 [149]. In the longitudinal direction, the system controls the aircraft's total energy (kinetic + potential) using the throttle and the distribution of energy between the two forms using the elevator. An analogy of this is shown in Figure 2.19 using fluid flows to reservoirs. The control loop for each effector has a cross feed to the other which allows coordinated changes of the thrust and elevator commands. The concept has been validated using nonlinear simulation [150, 151] and secondly on test aircraft from Boeing 737 size [152] to UAVs [148], and general aviation aircraft [153].

Coordinating throttle and elevator control to manage aircraft energy is fundamentally different to how the previously mentioned SISO autopilots handle the aircraft. Shown in Figure 2.20 is the relationship between thrust and elevator control and how they affect altitude and speed. It is quite clear that to achieve a level acceleration, the control system needs to do more than just use the throttle to increase speed as this will also increase altitude. This

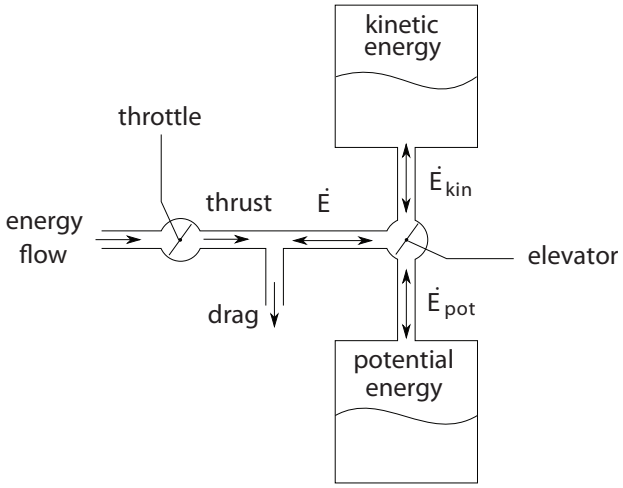

Figure 2.19: Reservoir analogy of the total energy control system - Throttle regulates total energy flow and the elevator controls the distribution of flow between the two forms [154]

figure shows explicitly the coupling between the two longitudinal controls and emphasises the need for coordination between thrust and pitch controls.

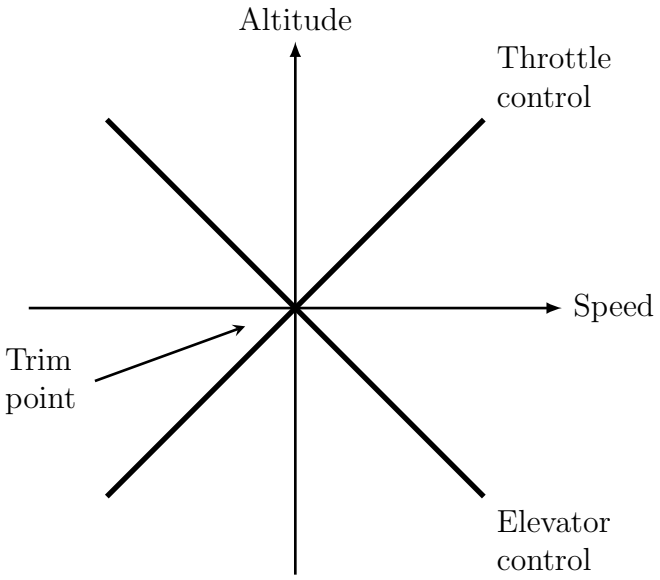

Figure 2.20: Longitudinal energy of an aircraft in trimmed flight [148]

One of the benefits of TECS is that the architecture is generalised and re-

quires little adjustment when moving from aircraft to aircraft; this has been demonstrated by a Federal Aviation Administration (FAA) study which applied an unmodified generic TECS controller to a Gulfstream jet with good success [155]. Only the inner loops are aircraft dependent; these loops function as the main controllers of the aircraft, providing stability augmentation functions if necessary and providing direct control over the elevators, throttle, ailerons and rudder.

The outer loops operate with a lower bandwidth and function to manage the energy states of the aircraft. At the top level inputs of TECS, the aircraft appears as a point mass which makes it ideally suited to integration with an FMC. The FMC handles top level aircraft functions such as navigation and path planning; when combined with a TECS autopilot the FCS is naturally segregated and does not have function overlap or segregated control systems as shown in Figure 2.21.

Once the main TECS architecture is functional in managing aircraft energy state, additional functionality is enabled by providing extra input processing. This may include selection between Mach/calibrated airspeed (CAS)/ground speed modes, glide slope and localiser tracking modes or altitude intercept modes as described by Bruce [151].

Besides safety, the other main benefit of TECS is the improved energy efficiency it achieves. As an energy based control technique it is inherently well suited to performing energy-optimal manoeuvres such as climbs, descents, level accelerations or constant speed altitude changes without unnecessary control effort. Since total energy (from fuel) is only added when required, the system is inherently energy optimal. This was put to good use by Kaminer [156] who developed 4D trajectory control functions which can ensure the aircraft arrives at specific locations at specified times in an energy optimal

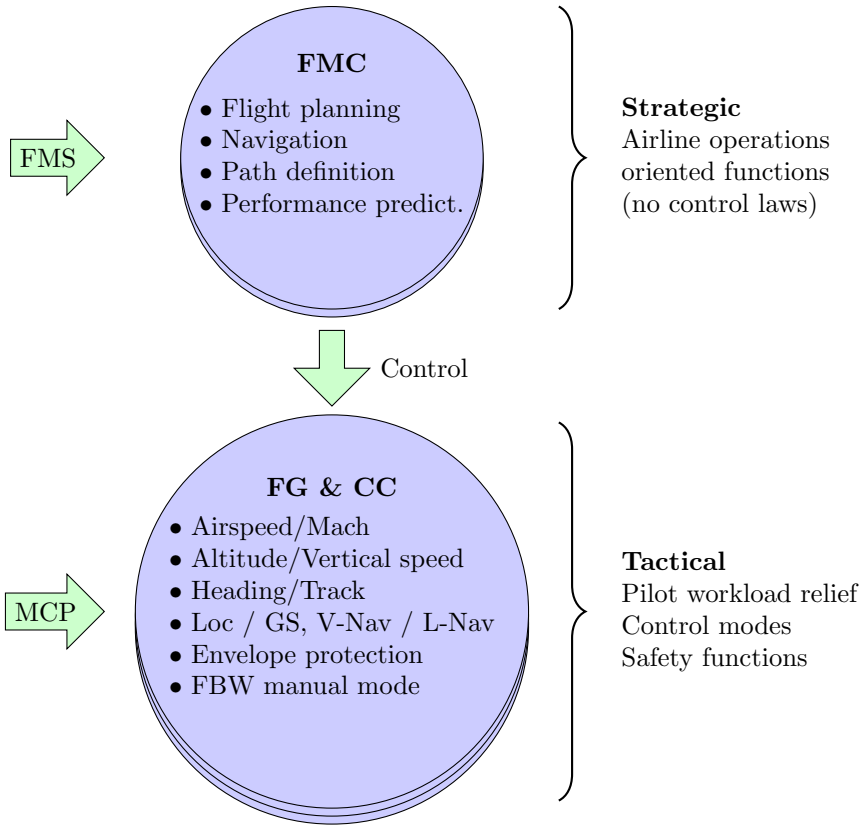

Figure 2.21: TECS architecture [146]

fashion. In order to develop these algorithms for aircraft use, automatic spoiler control had to be implemented to allow controlled energy dissipation in descents, although this was impoved upon by Srivatsan [157] to ensure reduced spoiler activity.

Importantly for the current work is the reduced control surface activity which TECS provides over SISO controllers; in previous work Bruce found [151], for example, a reduction in elevator activity in turbulence from 0.81° root mean square (RMS) to 0.16° RMS for a simulation of a Boeing 737 aircraft (without penalising velocity or altitude tracking). From an actuator power perspective this reduces control surface acceleration and hence power consumption.

This has notable advantages for high speed and robust simulations involving aicraft and actuator interactions; reduced control activity means reduced oscillations and likewise, reduced reliance on small timesteps for variable-step solver accuracy. This has the effect of reducing simulation times and most importantly, avoids situations where a simulation halts due to crossed minimum timestep constraints.

Further development of TECS has seen a variety of technologies implemented to improve reliability. Rysdyk used nonlinear adaptive control to augment TECS in order to achieve improved failure tolerance of the FCS [158] which was successful, although the author cites difficulty in getting such systems certified as a drawback of the system.

Various attempts have been made to improve the human - machine interface; noted to be one of major influences in the list of accidents quoted previously in this section. The concepts primarily attempt to quantify the energy state of the aircraft, instead of just considering speed and altitude separately as is commonplace currently. Before the publishing of TECS,

Honeywell developed a cockpit instrument in 1973 to display energy and energy rate [159] to assist pilots manually controlling an aircraft. Using modern technology, this functionality has evolved into digital displays which can integrate with current cockpit primary flight display (PFD) screens [160] or even a head up display (HUD) in order to display digitally generated, energy optimal 'tunnels in the sky' for the pilot to fly through [154].

2.5.2.2 TECS Implementation

The fundamental concept behind TECS is to control the total energy of the aircraft, including both kinetic and potential energies. The following method is summarised from [146] and [156], for greater depth refer to the referenced documents.

The total energy of an aircraft E can be expressed as:

$$E = Wh + \frac{1}{2}\frac{W}{g}V_T^2 \tag{2.61}$$

Where W is the aircraft weight, h is the aircraft altitude, g is the acceleration due to gravity and V_T is the aircraft velocity along the flight path (true airspeed). By differentiating this equation, a function for the total energy rate can be obtained. This is more usefully divided by weight and expressed as specific energy rate $\dot{E}_s$:

$$\dot{E}_s = \frac{\dot{E}}{W} = \dot{h} + \frac{V_T \dot{V}_T}{g} \tag{2.62}$$

Then, normalising by airspeed:

$$\frac{\dot{E}_s}{V_T} = \frac{\dot{h}}{V_T} + \frac{\dot{V}_T}{g} = \gamma + \frac{\dot{V}_T}{g} \tag{2.63}$$

where γ is the flight path angle with respect to the air mass.

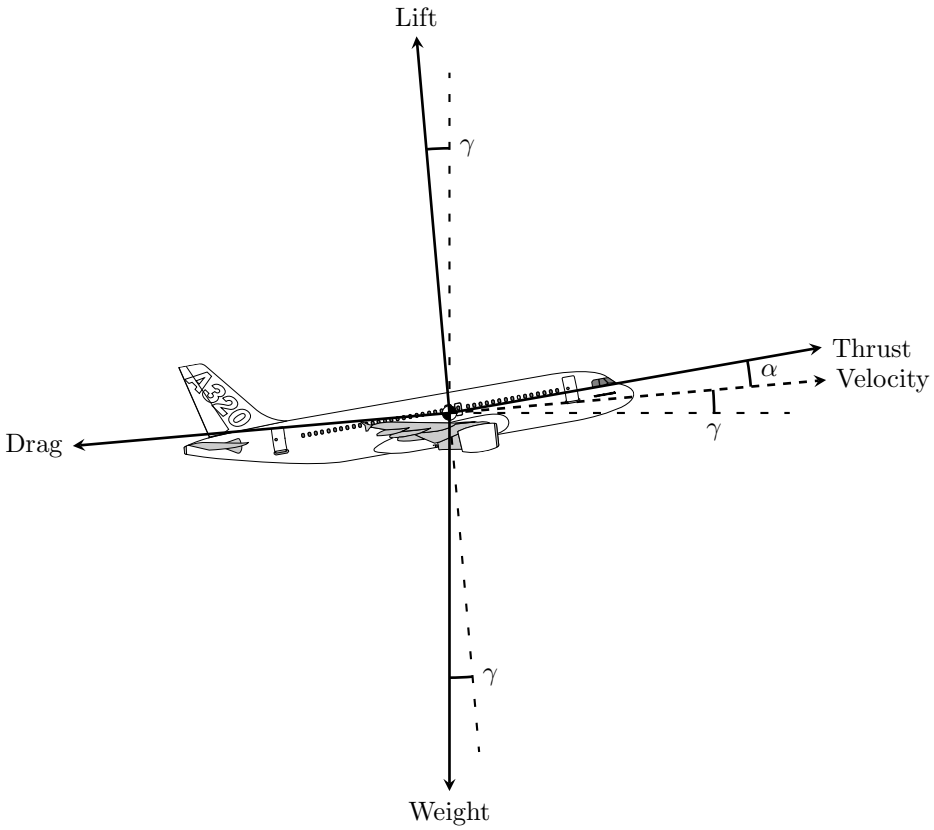

Figure 2.22: Forces on a point mass representation of an aircraft in flight

The acceleration of the aircraft along the flight path $\dot{V}_T$ is a function of thrust T, drag D, weight W and flight path angle γ and can be derived from the equation of motion:

$$T\cos\alpha - D - W\sin\gamma = m\dot{V}_T \tag{2.64}$$

Assuming α and γ are small, equation (2.64) can be rearranged using

$W = mg$ to form an expression for thrust required T_{req}:

$$T_{req} = W\left(\gamma + \frac{\dot{V}_T}{g}\right) - D \tag{2.65}$$

Physically, this is the thrust required to achieve a certain longitudinal acceleration at a given flight path angle. Considering the aircraft in steady flight, the initial thrust is trimmed against the drag. Assuming change in drag is slow, equation (2.65) can be adapted to compute incremental thrust from trim conditions,

$$\Delta T_{req} = W\left(\gamma + \frac{\Delta\dot{V}_T}{g}\right) \tag{2.66}$$

or the incremental thrust command T_{com} based on the flight path angle and longitudinal acceleration errors:

$$\Delta T_{com} = W\left(\gamma_e + \frac{\dot{V}_{Te}}{g}\right) \tag{2.67}$$

By comparing with equation (2.63) it can be seen that the parameters inside the parenthesis in equation (2.67) represent the error in normalised specific energy rate of the aircraft. From trim, a change in thrust will be met with a directly proportional change in total energy. **Therefore, it can be deduced that the throttles control the total energy of the aircraft.**

In order to form the control law for the throttle δ_{tc}, a proportional + integral (PI) structure is used. The proportion gain is fed using γ and $\frac{\dot{V}_T}{g}$ signals whilst the integral action minimises the error computed from $\gamma_c - \gamma$ and $\frac{\dot{V}_{Tc}}{g} - \frac{\dot{V}_T}{g}$. This accounts for errors downstream of the TECS control loop and ensures the throttle can be trimmed precisely. The control law is formed

as follows:

$$\delta_{tc} = K_{TP}\frac{\dot{E}_s}{V_T} + \frac{K_{TI}}{s}\frac{\dot{E}_{se}}{V_T} \tag{2.68}$$

where K_{TP} and K_{TI} are the proportional and integral controller gains of the throttle control loop.

Now that the total energy of the aircraft is controlled with the throttle, a control law needs to be derived which manages the transfer of energy between the two forms. The design is based on the specific energy rate of equation (2.63), but adapted to represent the energy distribution rate between kinetic and potential forms:

$$\frac{\dot{E}_d}{V_T} = \gamma - \frac{\dot{V}_T}{g} \tag{2.69}$$

and its error signal:

$$\frac{\dot{E}_{de}}{V_T} = \gamma_e - \frac{\dot{V}_{Te}}{g} \tag{2.70}$$

The distribution rate controller is required to have as similar dynamics as possible to the total energy controller. One part of this means using the same PI structure (and gains) as the total energy controller:

$$\delta_{ec} = -K_{EP}\dot{E}_d - \frac{K_{EI}}{s}\dot{E}_{de} + \text{damping terms} \tag{2.71}$$

where the damping terms represent aircraft specific functions to damp the short period modes and K_{EP} and K_{EI} are the proportional and integral controller gains of the elevator control loop. The elevator commands are inverted to align the direction of energy transfer of TECS with standard elevator convention; a positive deflection is downwards, causing a nose down attitude change and conversion of energy from potential to kinetic energy.

It should be noted at this point that the gain pairs must be numerically identical between the throttle and elevator loops to ensure coordinated

responses between the elevator and throttle. To this end, the inner pitch control loop must also be designed to give the aircraft a similar pitch response to the engine dynamics to further synchronise the total energy and energy distribution rates. Also, the aircraft dependent inner pitch and engine control loops require bandwidth separation from the TECS controller. This makes the inner loop design simpler and facilitates the representation of the aircraft as a point mass to the TECS controller. The block diagram for the controller is shown in Figure 2.23 where the interconnected multi input - multi output (MIMO) structure is clearly recognisable. The schematic of the control system has been simplified from the source document to remove envelope protection functions. This is considered acceptable since the scope of the work only includes normal flight conditions.

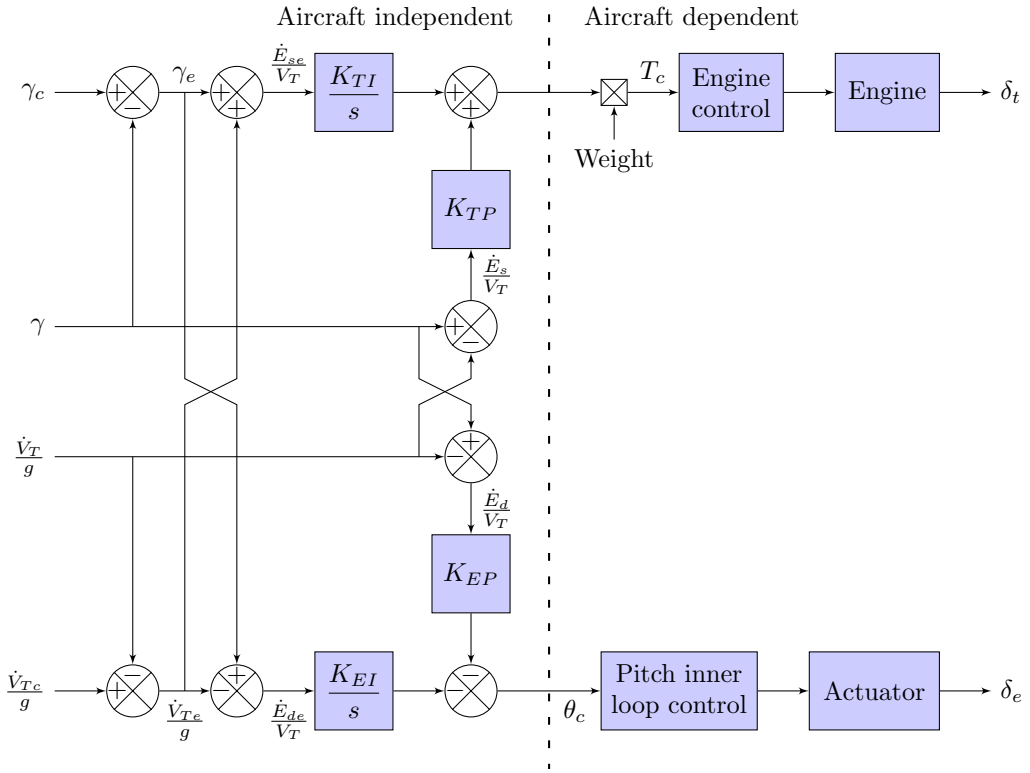

Figure 2.23: Block diagram of TECS. Modified from: [146]

The engine and pitch inner loop controllers can be designed using any preferred technique; in this case using PI control with pitch rate feedback for the pitch loop and thrust feedback for the engine loop. In reality, thrust is not directly measurable and would have to be estimated using some other quantities such as engine pressure ratio. For the purpose of this simulation this accuracy is not required and has therefore been omitted.

Tuning the TECS can be challenging due to its MIMO structure. For this work the gains were tuned manually, using the gains published for the Boeing 737 as a starting point. This is considered acceptable since the purpose is only to achieve fast simulations for actuator power estimation, rather than to achieve a flightworthy design. If a design of this nature was to be undertaken, several works have been published which use eigenstructure analysis and assignment [161, 162] or optimisation [163, 164] to achieve improved gain selection.

2.5.2.3 Performance Demonstration

This section is intended to demonstrate the operational behaviour of the TECS while it executes a series of manoeuvres. Figure 2.24 shows the A320 aircraft starting from a trimmed operating point in cruise at 10000 m altitude and 233 m/s true airspeed (Mach 0.78). Trimming is achieved using the Matlab function `trim`, which acts to find a steady state operating point (within some error bounds) of a system which satisfy some user defined constraints. The function is given the commanded altitude and airspeed while having the throttle, elevator and angle of attack as free variables which are optimised to satisfy the constraints.

There is an initial step command to climb to 10200 m, while maintaining a constant airspeed, once the commanded altitude has been reached there is

a demanded speed increase by 5 m/s to 238 m/s at constant altitude. Lastly, both variables are commanded to return to initial values but timed such that the speed decrease command is initiated during the descent. The aim of the plot is to show the good accuracy of TECS at handling coupled elevator + throttle manoeuvres; the synchronisation between the two controls during constant speed climbs (100 s - 300 s) and level accelerations (400 s - 500 s) is clearly visible.

One weakness in the current FCS tuning can be seen in the throttle plot which shows evidence of damped oscillatory behaviour. This is put down to a poorly tuned engine inner control loop, but has been left in the figure for one good reason: to demonstrate that throttle oscillations do not induce elevator oscillations. This highlights why a TECS controller has been used; because the TECS loop operates at a lower bandwidth than the inner loops, oscillatory behaviour like this does not get transmitted to the commands for the coupled controller. With a regular SISO FCS the oscillation of the throttle would induce pitch oscillations in the aircraft which the elevator would then try to cancel out. This would cause a severe decrease in simulation speed which is avoided by using TECS.

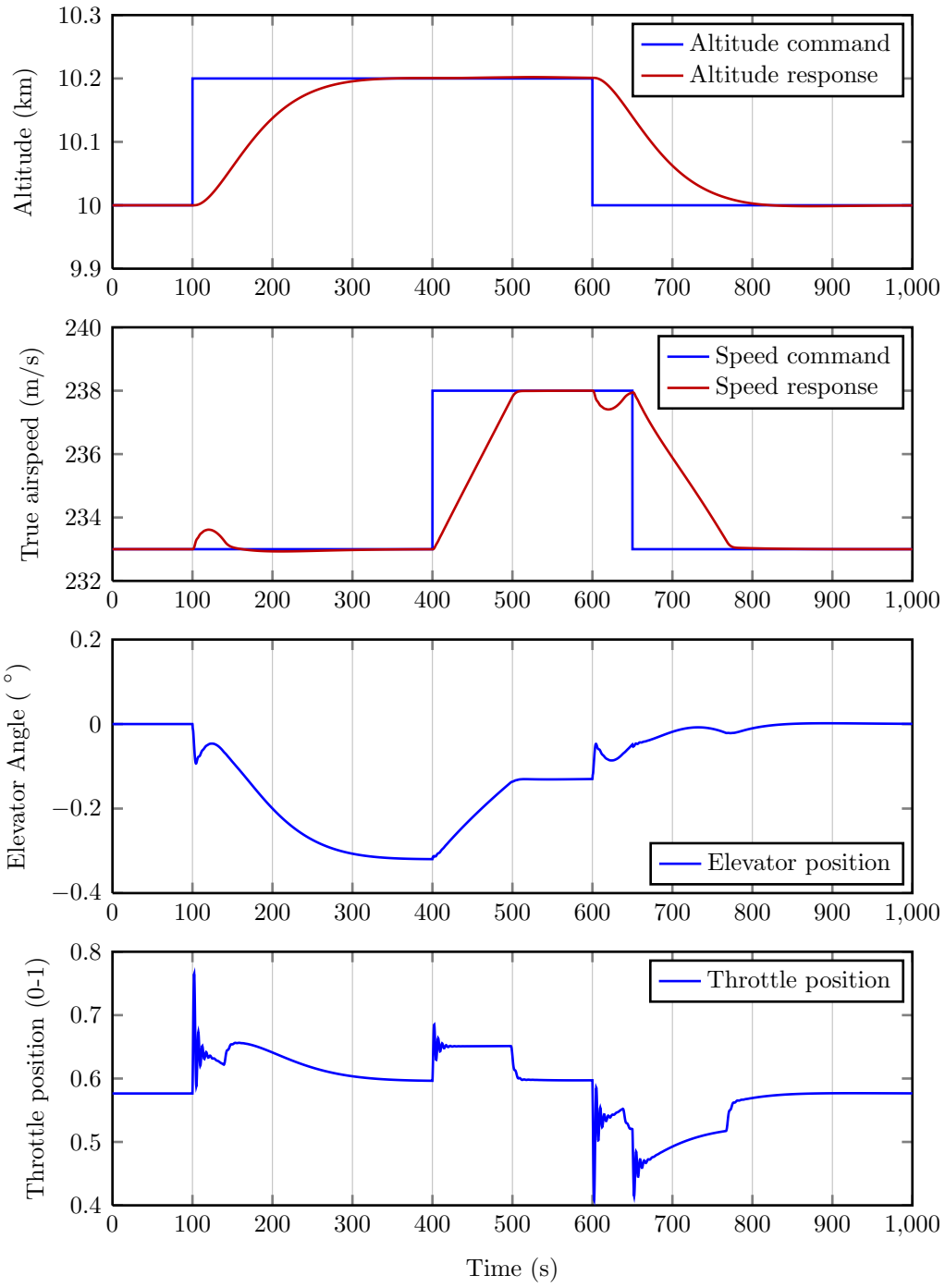

Figure 2.24: TECS controlled climb, descent and speed change

2.5.3 Total Heading Control System

2.5.3.1 THCS Overview

The total heading control system (THCS) is a natural evolution of the TECS described in section 2.5.2, applying energy balanced control techniques to the roll and yaw motions of an aircraft. Since it is a natural extension and functionally very similar to the TECS described previously the same benefits apply and so they will not be repeated in this section.

The concept of THCS was first published by Bruzzini when he applied it to a simulation of an F-15 Eagle [165], seeking to coordinate the roll and yaw controls to achieve coordinated turns. The work was a success and it inspired further development and flight trials on the Condor UAV [148] and general aviation aircraft [153, 166, 167].

2.5.3.2 THCS Implementation

The principles behind the THCS controller will be summarised in this chapter from [146, 165], for a more detailed description the reader should refer to these documents.

Similarly to TECS, the derivation of the THCS control law stems from first principles. From the body axis equations of motion in chapter 2.4 (page 73), the lateral force equation is [168]:

$$\dot{v} = \frac{F_y}{m} + g \sin\phi \cos\theta + pw - ru \tag{2.72}$$

By assuming the pitch and roll angles, ϕ, θ are small and that the aircraft is in a steady coordinated turn ($F_y = p = 0$), equation (2.72) can be

simplified.

$$\dot{v} = g\phi - ru \tag{2.73}$$

Normalising by the true airspeed V_T and considering the side slip angle rate $\dot{\beta}$ as $\dot{v}/V_T$, the equation can be approximated by:

$$\frac{\dot{v}}{V_T} = \dot{\beta} = \frac{g\phi}{V_T} - r = 0 \tag{2.74}$$

Now, rearranging to give the relationship between roll angle and yaw rate in steady state:

$$\phi = \frac{V_T}{g} r \tag{2.75}$$

To deduce the final THCS equation describing the lateral energy control algorithm, equation (2.75) is broken into incremental steps:

$$\Delta\phi = \frac{V_T}{g}\left(\dot{\beta} + \Delta r\right) \tag{2.76}$$

This equation implies several things; firstly, the roll angle ϕ produced by the ailerons can be used to control yaw rate if the side slip angle rate is held at zero (coordinated turn), or it can be used to control side slip angle rate if the yaw rate is held at zero. Conversely, the yaw rate produced by the rudder can be used to coordinate a turn if sideslip angle rate is held at zero or to control sideslip angle rate if the roll angle is held constant.

It is therefore possible to control the heading angle ψ and sideslip angle β by using an aileron control command proportional to $(\dot{\psi}_e + \dot{\beta}_e)$. In order to control the distribution between the two (i.e. zero sideslip to coordinate a turn or maintain constant heading to perform a crosswind landing) by commanding a yaw rate proportional to $(\dot{\psi}_e - \dot{\beta}_e)$.

The error signals are computed by simple subtractions between com-

manded rates and measured rates; $\dot{\psi}_e = \dot{\psi}_c - \dot{\psi}$ and $\dot{\beta}_e = \dot{\beta}_c - \dot{\beta}$.

In order to generate rate commands, an error signal is computed between the commanded and actual heading angle and sideslip angle before being multiplied by a gain which controls the rate of error nulling:

$$\dot{\psi}_c = K_\psi \left(\psi_c - \psi\right) \tag{2.77}$$

$$\dot{\beta}_c = K_\beta \left(\beta_c - \beta\right) \tag{2.78}$$

Like all gains in TECS/THCS controllers, it is imperative that the gain pairs have the same value to ensure matched energy transfer dynamics between the two forms.

The commands can either be fed into a PI control structure similarly to TECS as shown by Bruzzini [165], or a simpler integral only form as used by Lambregts [146]. The latter has been used in this work for simplicity; the proportional gains offer most benefit when considering asymmetric flight such as single engine failure which is beyond the scope of this work.

The aileron and rudder control signals are described as follows:

$$\delta_a = \frac{V_T}{g} K_a \left(K_{RP} + \frac{K_{RI}}{s}\right)\left(\dot{\psi}_e + \dot{\beta}_e\right) \tag{2.79}$$

$$\delta_r = K_r \left(K_{YP} + \frac{K_{YI}}{s}\right)\left(\dot{\psi}_e - \dot{\beta}_e\right) \tag{2.80}$$

The block diagram of the general THCS structure is presented in Figure 2.25.

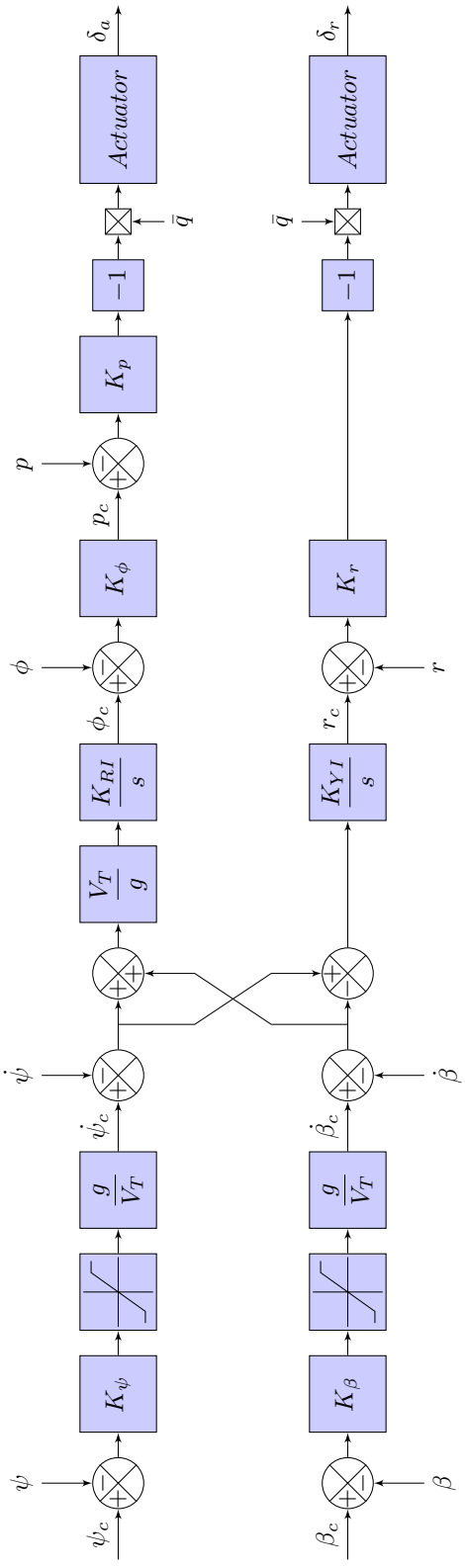

Figure 2.25: Block diagram of THCS. Modified from: [146]

2.5.3.3 Performance Demonstration

This section seeks to demonstrate the behaviour of THCS in controlling lateral motion; both heading change and sideslip angle control. This is achieved by applying a selected set of manoeuvres to the FCS and observing the response in the key state variables. The manoeuvres of interest are shown in Figure 2.26 (and Figure 2.27) and include an initial heading change of 60° with zero commanded sideslip, followed by a 200 second long constant 2° sideslip flight at constant heading. These two manoeuvres represent a coordinated banked turn and a crosswind landing respectively. In order to conduct this experiment, the longitudinal direction must be controlled by TECS; Figure 2.27 is included to show the effect on the major longitudinal parameters during lateral manoeuvres.

The results show that THCS provides smooth control over both heading angle and sideslip angle in a coordinated fashion. There are no significant oscillatory motions induced in the control surface demands, which ensures maximum simulation speed when actuator models are included. The control surface plot demonstrates the synchronisation between aileron and rudder movements used to distribute energy between the roll and yaw axes of motion.

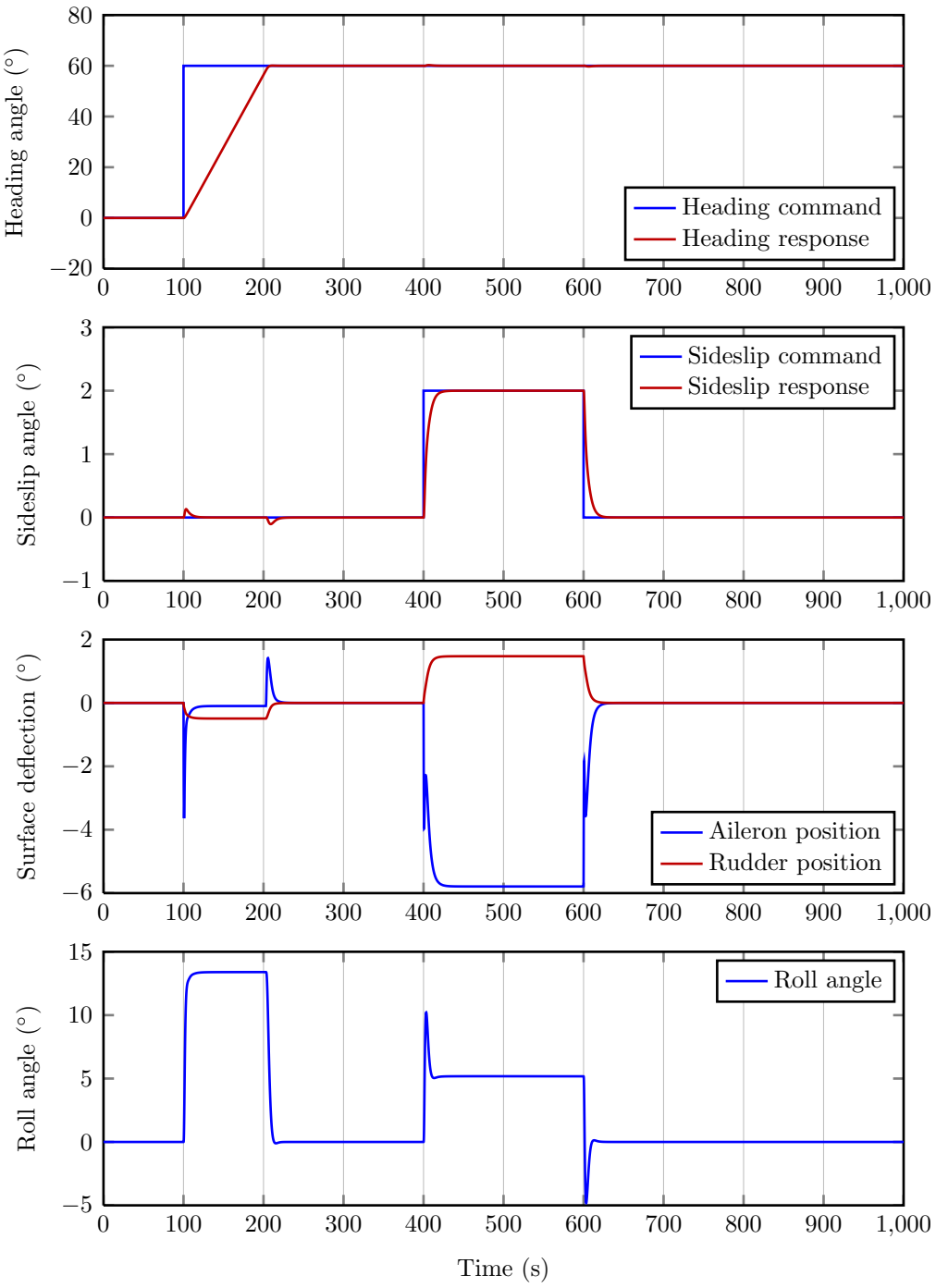

Figure 2.26: THCS controlled heading change and constant sideslip flight

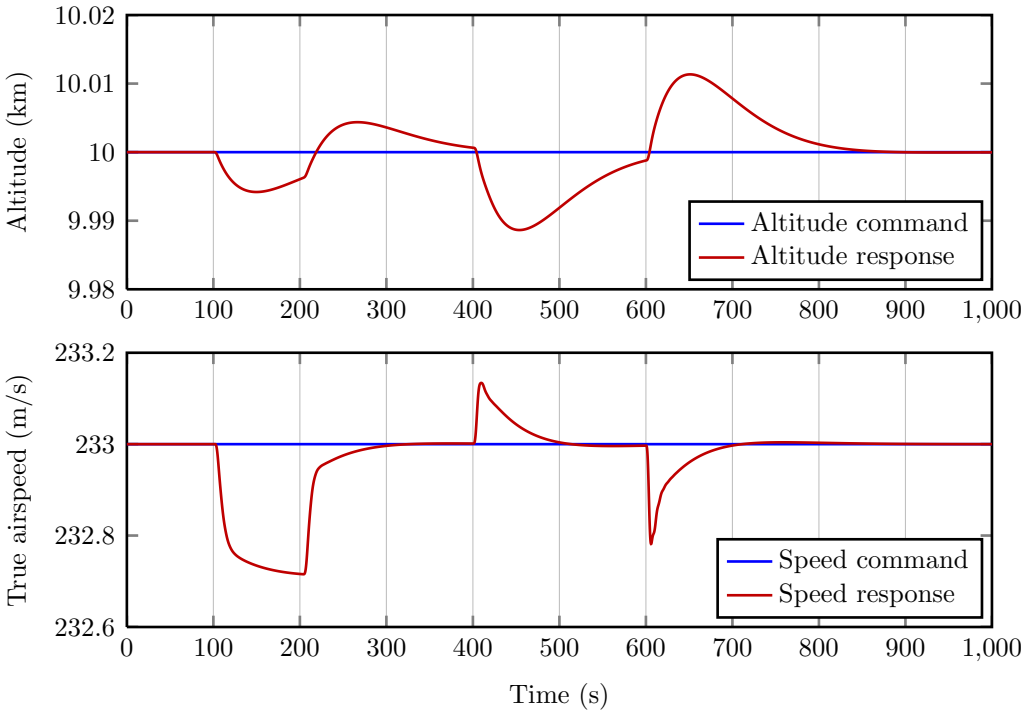

Figure 2.27: THCS controlled heading change and constant sideslip flight - longitudinal effects

2.5.4 Guidance Algorithm

The guidance function for the aircraft in this thesis requires only basic functionality; flight plan segment tracking, turn anticipation and waypoint switching. These are typically provided by the FMC on a commercial aircraft, allowing a list of waypoints to be programmed into the computer to define the planned trajectory. FMCs on a modern aircraft provide an outer loop to the autopilot, issuing heading and pitch commands to make the aircraft follow the specified lateral and vertical flight path. Extra functions often include performance calculations to assist with climb and descent, fuel burn and range estimation, centre of gravity calculations and different waypoint tracking modes.

Only a small subset of the full FMC functions are required, at the present time only lateral guidance is desired since all manoeuvres shall be flown at constant altitude and airspeed. A basic guidance algorithm that enables most of the path tracking and filleted 'fly-by' waypoint manoeuvre functions is provided by Allerton [169] in section 4.13 of his textbook. The minimisation of error between flight path segment and aircraft course angle technique shown in Figure 2.28 for straight line segment tracking is adequate for large aircraft in simulations, but it does not work well on small UAVs in unsteady air. This is because micro-electromechanical compasses may not possess the fidelity to measure the small error angles when tracking towards a distant waypoint.

Instead a more robust vector field technique provided by Beard [139] is shown in Figure 2.29, which generates a heading command for the aircraft depending on the cross track distance error e_{py}. This is the error on the y axes of a Cartesian coordinate system; oriented with its positive x direction

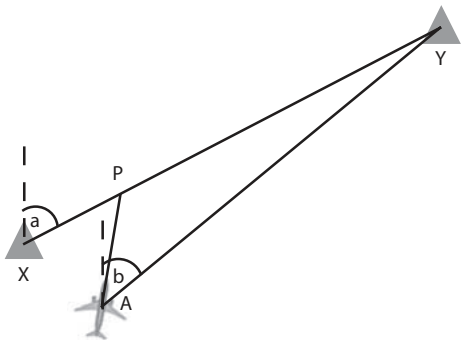

Figure 2.28: Flight plan segment tracking using bearing error [169]

parallel to the flight path segment and the y direction being horizontal to the flat Earth plane. The heading command is computed using Equation (2.81) where χ_q is the vector field heading (normalised to $\pm 180°$ from the current heading) and k_{path} is the sharpness of the vector field course correction slope, which is set as 1E-4 for both aircraft types tested in this thesis.

$$\chi_c(t) = \chi_q - \chi^{\infty} \frac{2}{\pi} \tan^{-1}(k_{path} e_{py}(t)) \tag{2.81}$$

A linear proportional control law minimises the error between the vector field heading command χ_q and the aircraft heading χ to keep the aircraft on course. Since this technique is robust for both large and small aircraft it is considered a good candidate for use in this thesis, which seeks to model both transport aircraft and UAVs with minimal reprogramming.

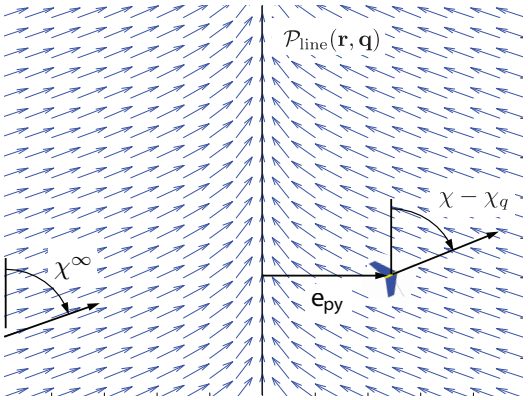

Figure 2.29: Vector field of heading commands which guide the aircraft back towards the flight path [139]

Turn Anticipation Turn anticipation is achieved by first estimating the turn initiation distance PY in Figure 2.30 using equation (2.82):

$$d = \frac{V^2}{g \tan(\phi) \tan(\Delta\psi)} \tag{2.82}$$

where g is the gravitational constant, ϕ is the Euler roll angle and $\Delta\psi$ is the change in heading angle PYO. The derivation for this function can be found in the previously mentioned reference to Allerton.

The geometric problem of turn anticipation is shown in Figure 2.30. The guidance algorithm checks to see when the distance from the aircraft to the waypoint becomes less than d; when this condition is true the aircraft begins a turn to towards the waypoint Z. The segment tracking controller is switched so that a is computed using the new waypoint Z.

Waypoint crossing detection can be achieved using numerous techniques; commonly a radius type is used which detects when an aircraft flies within a certain distance of a waypoint. This is not very robust, particularly in the case of small UAVs where gusts can significantly affect the position of the aircraft. A more robust technique is to detect when the aircraft crosses the

half space defined between vectors $\vec{XY}$ and $\vec{YZ}$ at the coordinate Y [139]. Computationally, this is relatively simple to calculate by detecting when the magnitude of the vector between the aircraft and a perpendicular point on the plane changes sign [170].

Overall, the turn is triggered by offsetting the half plane $\mathcal{H}_1$ by d to $\mathcal{H}_2$ (Figure 2.31). When the aircraft crosses this, the next waypoint is switched directly to Z and the a maximum rate turn is executed between the two bearings.

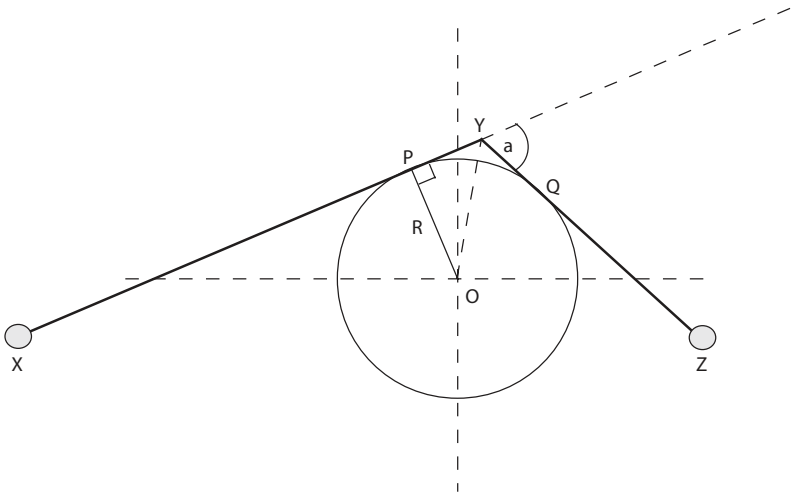

Figure 2.30: Turn anticipation schematic [169]

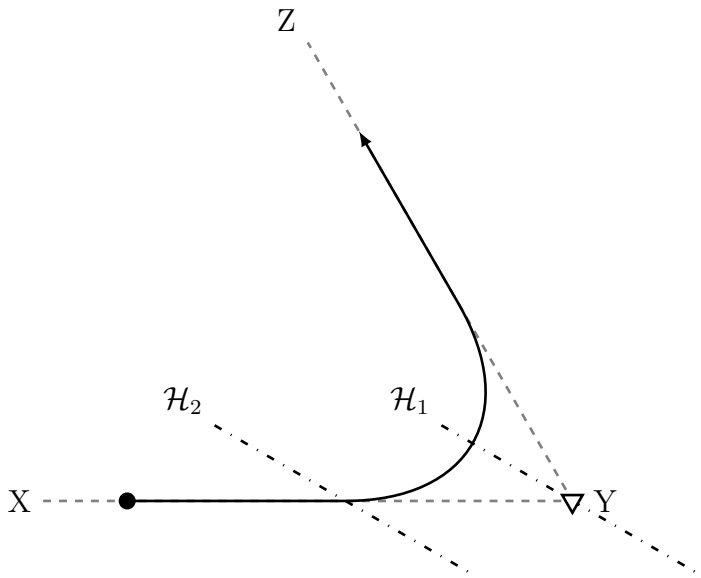

Figure 2.31: Diagram showing offset half plane flight plan segment switching

Software Implementation of Guidance Algorithm The guidance algorithm is implemented using a state machine in Simulink's Stateflow software for two reasons; it naturally handles complex route management functions and compiles into a fast executing binary file. This makes it more optimal for high speed simulation compared to embedded Matlab files. A reduced pseudo-code version of the guidance algorithm is shown in Figure 2.32, where the general structure and operation is presented but not the explicit code because it is not compact and fairly unreadable to none-Stateflow users.

The general operation is as follows. Stateflow enters the chart at the top and performs some initialisation, working out the number of waypoints in the list and setting a flag based on the result. The main body of the chart is then entered and the Waypoint_Select subchart executes first. This extracts the position and direction of the vectors which define the current and next flight path segments and the angle between them. Secondly the Path_Manager

subchart is entered and the halfplane which triggers the turn to the next waypoint is defined, and the aircraft position is checked to see whether it has crossed into the triggering halfspace. If the check returns true, the waypoint counter index is increased and both Waypoint_Select and Path_Following advance to the next position in the waypoint list. The straight line path tracking is performed in the Path_Following subchart, where it computes the bearing of the current waypoint segment and normalises the heading command so the heading command is within $\pm 180°$ of the current heading. The crosstrack position error is calculated, that is the lateral distance error in the horizontal plane between the aircraft and the flight path segment. This value is then used to generate a heading command for the FCS to follow.

It should be noted that at every time step each subchart is executed once; the general work flow is to retrieve the current waypoints, check whether the half plane is triggered and then to continue tracking the current straight line path. If a half plane is crossed, it will not change to follow the next waypoint until the next time step

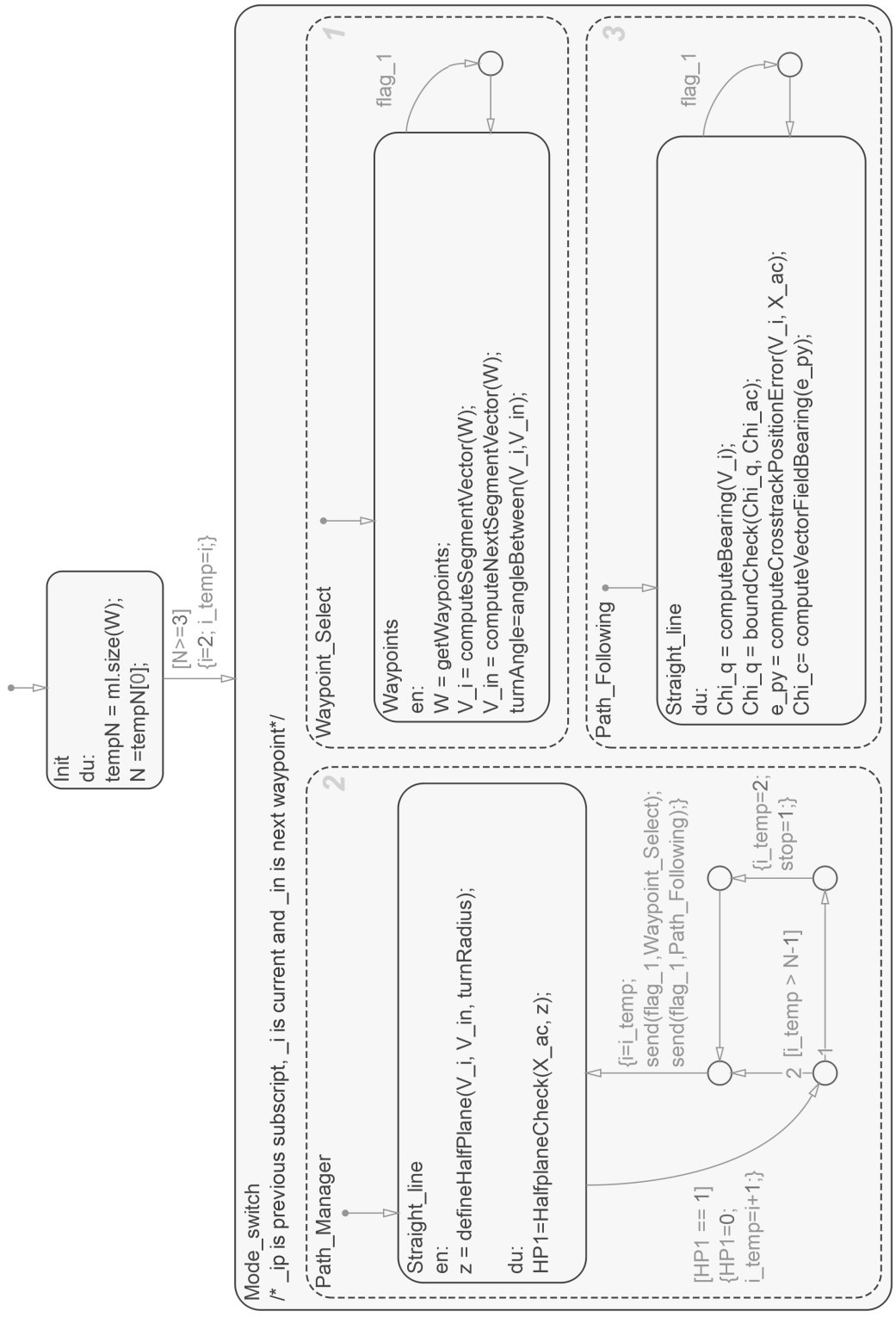

Figure 2.32: Route management and waypoint following state machine, showing pseudo-code indicating the functions which are performed in a readable format

2.5.4.1 Performance Demonstration

The end result can be seen in Figure 2.33 which shows multiple trajectories of an aircraft executing a 150° heading change at a range of turn rates. The aircraft is initialised at $(0, 0)$, heading directly towards waypoint 1 (marked with an orange triangle). As the aircraft approaches the waypoint, the guidance algorithm is constantly checking whether the aircraft has entered the half-plane defined for waypoint switching. When this condition becomes true, the aircraft turns at the predefined turn rate for that instance towards waypoint 2 (off the page). If the turn is initialised at the correct distance from waypoint 1, a neat filleted turn is achieved with no under/overshoot.

The plot 2.33 shows a slight undershoot, but considering no special consideration has been made towards compensating for the non-zero time to bank it is quite acceptable. A worse situation is to have overshoot leading to oscillations as the aircraft tracks the exit path - this causes more heading changes and a considerably higher actuator energy usage.

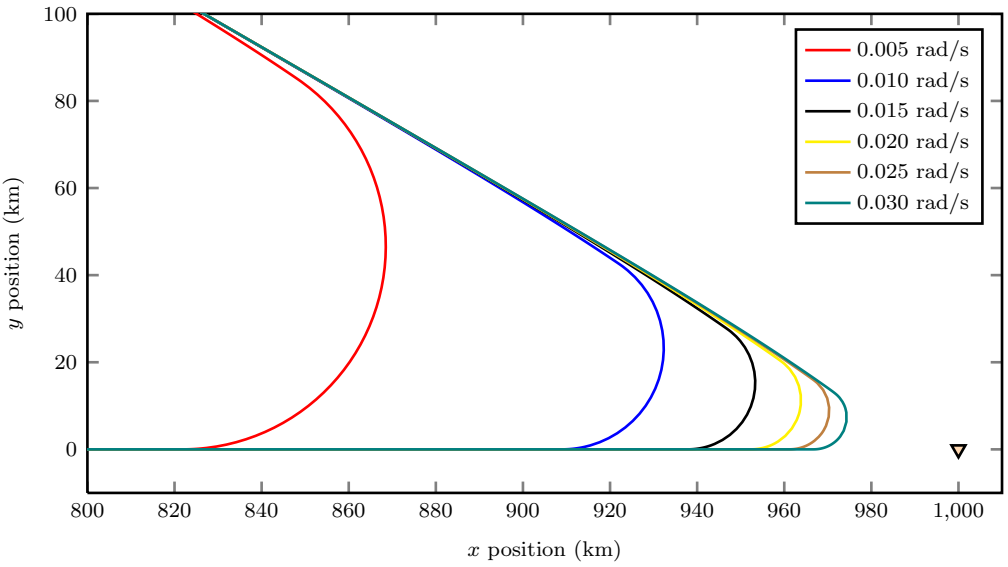

Figure 2.33: Demonstration of guidance algorithm, with aircraft executing a 150° turn at six different turn rates

Chapter 3

Actuation System Modelling

The models described in this thesis are designed to represent the dynamic position performance and instantaneous power consumption demands of an aircrafts primary flight control actuation system. The models include three actuation technologies; the classical centralised hydraulic system (ESHA) and also the modern electromechanical (EMA) and electro-hydrostatic (EHA) power-by-wire (PBW) actuators.

Each model takes a control surface position command and applied load force as inputs and provides the achieved control surface deflection and instantaneous power consumption as outputs. The power consumption estimates are given in terms of fluid power for the hydraulic system and electrical power for the EMA and EHA.

Each system is currently tailored to model the aileron, elevator and rudder actuators of the Airbus A320 aircraft, but they can be adapted to represent the performance of another aircrafts actuation system, given the required performance data is known.

Specific modelling characteristics of the actuators installed on real aircraft are generally not available in the public domain, so the actuator models can be scaled from known data [12] or created using preliminary design tech-

niques to size the major components [144, 171]. Tuning the models to the performance of the desired aircraft is achieved using no load speed, stall force and stroke length characteristics which, for the A320, have been sourced from prior works [1, 172]. Other characteristics which are unique to the different technologies (such as hydraulic cylinder leakage coefficients, ball screw efficiency and pump leakage) are sourced from similar commercially available product datasheets for the individual components.

The actuation system models are intended to represent the main components of the primary flight control suite which are used during a flight. As such, redundant actuators are not modelled because only those which are typically active have a power demand requirement. The number of active actuators and performance characteristics for the A320 actuators are shown in Figure 3.1.

Combining Table 3.1 and the schematic in Figure 2.4 (on page 18), it is possible to see the locations of the actuators which are active and being powered at any one time. The surfaces marked L.AIL, R.AIL, L.ELEV, R.ELEV each have one active actuator and the rudder has three. The spoiler, horizontal trim and yaw damper actuators are not modelled to reduce complexity. In total, seven actuators are represented, but where possible symmetry is used to reduce duplication. An example of this is the two elevator actuators which typically experience similar force and velocity demands. This is also used on the rudder where the simplification is made that each actuator applies a third of the force required for the whole rudder. In both of these cases the power consumption data is multiplied by the number of active actuators on those surfaces.

	Aileron	Elevator	Rudder
Purpose	Roll control / Load alleviation	Pitch control	Yaw control
Actuators	2 total 1 normally active 1 in damping mode	2 total 1 normally active 1 in damping mode	3 total 3 normally active (+2 yaw dampers)
Maximum Control Surface Deflection	± 25°	30° up, 17° down	± 25° at/below 160 kts ± 3.5° at/above 380 kts
Actuator Stroke	44 mm	60 mm	110 mm
No Load Rate	90 mm/s	60 mm/s	110 mm/s
Max Extend Force	48.0 kN	27.7 kN	44.3 kN
Max Retract Force	48.0 kN	27.7 kN	44.3 kN

Table 3.1: Airbus A320 control surfaces and actuator characteristics [1, 172]

3.1 Hydraulic actuation system

The primary components represented by the hydraulic system model consist of linear hydraulic cylinders attached to the primary flight control surfaces through moment arms. The cylinders have a servo-valve local to the cylinder controlling the flow from the main hydraulic pumps. The pumps are located in the engines and are driven by the power off-take shaft; they function to convert rotational shaft power to hydraulic fluid power which is delivered to the actuators using long lengths of high pressure hydraulic tubing.

On a certified commercial aircraft there will be multiple hydraulic systems for redundancy, duplicating the 3000 psi supply and 50 psi return lines needed to complete the hydraulic circuit (in the A320 case). The provided model assumes there are no failures along the trajectories to be simulated by the tool, for this reason the power losses in the redundant hydraulic systems are neglected.

Pressure lost in the transmission tube is neglected since the system is assumed to be well designed with a minimum loss due to optimum pipe diameter, flow rate, pipe surface finish and joint fixing layout. It is decided to keep the estimation as simple as possible and focus solely on the servo valve and cylinder because a lack of data makes the transmission losses difficult to quantify. There is however a provision to use it in the model should proprietary data become available by changing the input from the default of 0 psi.

The basic pump data is obtained from an Eaton Aerospace document [41] which specifies the model as a Vickers PV3-240-10C. This pump can supply 141.95 L/min at a pressure of 3000 psi. The pumps have a maximum rotation

rate of 3750 rpm and are implemented as variable displacement piston (VDP) pumps with automatic pressure compensation. For the purpose of this model it is assumed that the hydraulic load is distributed equally between the two engine driven pumps.

Given that technical details of the real actuators are not available, a preliminary design is carried out for sizing the hydraulic cylinders.

Taking the system design pressure P and actuator stall force F_s the piston surface area A_c can be calculated using equation (3.1),

$$A_c = \frac{kF_s}{P} \tag{3.1}$$

where k is an oversizing factor which gives some headroom to ensure the stall force requirements are met in the presence of pressure loss due to leakage and pipe flow. This has a value of 1 when there is no loss and must increase as the losses increase. This form of the equation is useful when a specific safety factor is desired, but can be written in an alternative form which accounts for the losses analytically:

$$A_c = \frac{F_s}{P - P_{Loss}} \tag{3.2}$$

where P_{Loss} is the pressure lost due to internal and external cylinder losses.

The flow rate at the cylinder Q_c which is required to achieve the no load rate $\dot{x}_{NL}$ is calculated using equation (3.3),

$$Q_c = \dot{x}_{NL} A_c \tag{3.3}$$

Once the flow rate to each cylinder is known, the sum can be calculated to

give the total flow rate required for the whole primary flight control system:

$$Q_{total} = Q_{L.AIL} + Q_{R.AIL} + Q_{L.ELEV} + Q_{R.ELEV} + Q_{RUD} \tag{3.4}$$

At this point the total flow rate required (assuming the system has the capacity to move all primary control surfaces at their no load rates at the same time) can be checked against the specifications for the PV3-240-10C to give confidence whether the cylinder designs are realistic or not. Using the assumption that the flow is split equally between the engines, the fluid power $P_{fluid(pump)}$ required from each pump is:

$$P_{fluid(pump)} = \frac{Q_{total} P_s}{2} \tag{3.5}$$

where P_s is the pressure generated across the output ports of the pump (i.e. system operating pressure). $P_{fluid(pump)}$ represents the fluid power output by the pump and does not include the efficiency of the pumps themselves. This work does not seek to exhaustively compute the power consumption at every conversion from the engine, instead leaving this for separate architectural level simulation exercises.

The pump generates excess internal pressure above the system operating pressure to overcome internal leakage flows, but this is excluded from the analysis in a similar fashion to the exclusion of electrical generation losses for the EMA and EHA.

There are two main techniques to maintain a setpoint pressure in a hydraulic circuit; using a fixed displacement pump with a pressure release valve set to system pressure or a variable displacement type with a closed loop pressure regulation system. The former means the excess pressure that is generated by the constant displacement pump must be wasted through leak-

age from the pressure release valve. In modern aircraft a pressure regulated pump is used which only provides the flow that is required to maintain the system pressure at setpoint. If there are no fluid flow demands, the pressure across the output ports of the pump remains at setpoint, but the pump only has to deliver enough flow to overcome system leakages. Quantifying power consumption at engine level would require a more detailed representation of the pump and its losses, but this is out of scope for this thesis.

3.1.1 Dynamic hydraulic cylinder model

The modelling in this section is conducted with reference to Pastrakuljics thesis [104] and uses the diagram for the hydraulic cylinder shown in Figure 3.1. Taking the loading condition in the diagram, chamber 1 is at high pressure and chamber 2 is at return pressure.

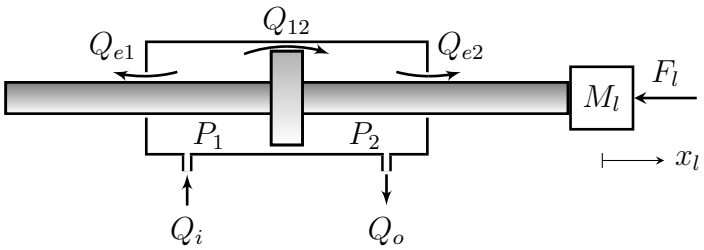

Figure 3.1: Modelling diagram of a hydraulic cylinder

The equations which describe the cylinder flow are given below:

$$\frac{dV_1}{dt} = +Q_i - Q_{e1} - Q_{12} \tag{3.6}$$

$$\frac{dV_2}{dt} = -Q_o - Q_{e2} - Q_{12} \tag{3.7}$$

Where Q_i is the cylinder inlet volume flow rate, Q_o is the cylinder outlet volume flow rate, Q_e is the external leakage flow and Q_{12} is the leakage past

the piston. The volumes introduce nonlinear behaviour to the model as they include the dead volume in the pipes V_{01} and V_{02}. They are described as:

$$V_1 = V_{01} + A_C x \tag{3.8}$$

$$V_2 = V_{02} + A_C(L_c - x) \tag{3.9}$$

where L_c is the actuator stroke length. Using the continuity equation for compressible flows, the hydraulic transmission lines can be described using equation (3.10):

$$\sum Q_{in} - \sum Q_{out} = \frac{dV_0}{dt} + \frac{V_0}{\beta_e}\frac{dP}{dt} \tag{3.10}$$

where Q_{in} is the flow into the cylinder chamber, Q_{out} is the flow out of the cylinder through piston movement and leakages. V_0 represents the fluid volume and β_e is the fluid bulk modulus (the inverse of compressibility coefficient). Assuming the transmission lines are rigid and do not expand under pressure, equation (3.10) simplifies to:

$$\sum Q_{in} - \sum Q_{out} = \frac{V_0}{\beta_e}\frac{dP}{dt} \tag{3.11}$$

By applying equations (3.6) - (3.9) to (3.11) the following are obtained, which describe the flow on each side of the cylinder.

$$Q_i - Q_{12} - Q_{e1} - \dot{x}A_c = \frac{V_{01} + A_c x}{\beta_e}\frac{dP1}{dt} \tag{3.12}$$

$$-Q_o + Q_{12} - Q_{e2} + \dot{x}A_c = \frac{V_{02} + A_c(L_c - x)}{\beta_e}\frac{dP2}{dt} \tag{3.13}$$

Once implemented in the model, equations (3.12) and (3.13) allow the calculation of pressure difference across the piston. The force balance of the

mechanical model of the piston is given in equation (3.14):

$$A_c(P_1 - P_2) = M\ddot{x} + B_v\dot{x} + F_L \tag{3.14}$$

where M is the mass, B_v is the viscous friction coefficient and F_L is the load force. Equations (3.12), (3.13) and (3.14) represent a non-linear model of a hydraulic cylinder. For the best accuracy the model can be implemented in this form, but the model becomes slow to solve due to its stiff nature (hydraulic pressure oscillations occur at high frequency while the piston motion is slow).

An idealised model can be formed which combines equations (3.12) and (3.13), and a significant reduction in computation effort is gained. Firstly, by considering the actuator starting position (and x zero location reference) to be the centre of travel, i.e. the neutral position, equation (3.13) can be rewritten to give the volume due to piston position in an alternative form:

$$-Q_o + Q_{12} - Q_{e2} + \dot{x}A_c = \frac{V_{02} - A_c x}{\beta_e}\frac{dP_2}{dt} \tag{3.15}$$

Equations (3.12) and (3.15) can be linearised and rearranged to give the equations for pressure change in the system:

$$\frac{dP_1}{dt} = [Q_i - Q_{12} - Q_{e1} - \dot{x}A_c]\frac{\beta_e}{V_{1c}} \tag{3.16}$$

$$\frac{dP_2}{dt} = [-Q_o + Q_{12} - Q_{e2} + \dot{x}A_c]\frac{\beta_e}{V_{2c}} \tag{3.17}$$

where V_{1c} and V_{2c} are the volumes displaced by the piston movement, excluding the dead volumes V_{01} and V_{02}. Assuming the motion is modelled around the neutral point, the volumes can be considered as equal; i.e. $V_{1c} = V_{2c}$. Assuming also that the supply and return flows to the pump are equal: $Q_i = Q_o$,

equations (3.16) and (3.17) can be combined to form a single equation that represents the pressure difference across the piston:

$$\frac{d\left(P_1 - P_2\right)}{dt} = \left[2Q_i - 2Q_{12} - 2\dot{x}A_c\right]\frac{\beta_e}{V} \tag{3.18}$$

The compressibility now represents the entire cylinder volume and as such $V_{1c} + V_{2c} = V$. Assuming laminar flow past the piston between the two chambers, Q_{12} can be represented using a leakage coefficient C_{12}:

$$Q_{12} = C_{12}(P_1 - P_2) \tag{3.19}$$

and substituted back into equation (3.18) to form the final linearised hydraulic cylinder equation:

$$\frac{d\left(P_1 - P_2\right)}{dt} = \left[2Q_i - 2C_{12}\left(P_1 - P_2\right) - 2\dot{x}A_c\right]\frac{\beta_e}{V} \tag{3.20}$$

When integrated, equation (3.20) provides the pressure difference across the cylinder to the mechanical model of the piston in equation (3.14).

3.1.2 Dynamic Pump Model

The centralized hydraulic system is powered by an engine driven variable displacement hydraulic pump (VDP), which spins at a constant speed and has a pressure compensation controller to adjust the displacement and maintain 3000 psi in the system. Also installed are pressure release valves which bleed oil back to the reservoir if the pressure exceeds 3000 psi due to excess load.

The pump is modelled using the continuity equation (3.11) where the pump flow Q_P, load flow Q_L and the volume of trapped fluid between the pump and servo valves is V_t [173]. By saturating the integrator used to find

P_s in equation (3.21) at 3000 psi, the pump will maintain 3000 psi until the load flow becomes larger than the pump output flow, at which point the pressure will start decreasing. In the case of the A320 where there are two pumps there is a choice of implementing equation (3.21) twice, or simply setting Q_P to a value which represents both pumps. In this instance, the latter is chosen as it reduces the computational effort and the accuracy that modelling each pump individually brings is not required.

$$\frac{dP_s}{dt} = [Q_P - Q_L]\frac{\beta_e}{V_t} \tag{3.21}$$

Although equation (3.21) represents the characteristics of the pressure compensated variable displacement hydraulic power supply, it does not provide a means of relating the hydraulic power required to the shaft power required of the pump. This is straightforward if the system is to be considered in normal flight conditions only because the hydraulic pumps should never enter a flow saturation state.

The performance curves for commercial VDP pumps (such as the Vickers PV3-240 series [174]) show the typical overall efficiency η_{vdp} is in the range 80-90%. If the mechanical shaft power from the engine is required, a lookup table can be produced from the referenced datasheet which converts hydraulic power to shaft power.

Care should be taken when integrating the models for different control surfaces to ensure that there is a single pump model for the whole system. When using a single instance of equation (3.21) to represent two pumps, Q_L must be the sum of the load flows from each actuator, and thus the mechanical shaft power (for two engines) is the power from the pump divided by η_{vdp}.

3.1.3 Servo Valve Model

The valve used to control flow to the cylinder is a two stage nozzle-flapper servo valve which is commonly used for aerospace primary flight control applications due to its high dynamic performance. This valve primarily consists of an electrical torque motor, a hydraulic amplifier and a precisely machined valve spool assembly. Each component will be briefly described but for an expanded understanding the user should refer to [45] or any hydraulic control system text book.

The power source for the spool positioning system is a torque motor as shown in Figure 3.2. The function of this device is simple; when a current is passed through the purple coils, the dark grey armature becomes polarised. The armature is pivoted in the centre and its ends rest between two permanent magnets (shaded white); the armature becomes attracted to one pole and repelled from the other when a current is applied. This induces a torque on the armature and the flapper which is rigidly connected to it.

The electrical characteristics of the torque motor can be modelled as a series LR circuit if the back e.m.f generated by the load is neglected. The transfer function of a series LR circuit is given by equation (3.22).

$$\frac{I(s)}{V(s} = \frac{1}{sL_t + R_t} \tag{3.22}$$

where L_t is the inductance of the coil and R_t is the total resistance in the coil and drive circuit. The torque exerted by the motor is proportional to the current flowing through the coils.

The flapper does not drive the spool directly; instead it controls a hydraulic amplifier which provides the power to move the spool. There are two common methods of achieving this, either using a jet valve or the flapper

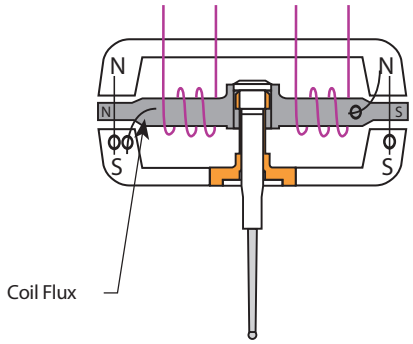

Figure 3.2: Diagram showing basic torque motor layout [45]

type which is used here. The flapper valve operates by having two nozzles supplied by the supply pressureP_s, mounted on opposite sides of the previously mentioned torque motor flapper. When in a neutral position (i.e. zero current and zero torque) each nozzle emits an equal flow and the pressure on either side of the spool is equal. When an electrical input is given to the torque motor it applies a torque to the flapper which causes an angular deflection and reduces the flow at one of the nozzles.

In Figure 3.3 this has occurred and the nozzle on side B is blocked, forcing more flow to the spool on side B and thus a deflection of the spool. This opens one control port to the supply pressure P_s and the other to the tank pressure P_t. The movement of the spool also moves the ball end of the flapper feedback spring which induces a restoring torque on the flapper and armature assembly, eventually leading to the balancing of the applied magnetic torque with the feedback torque.

The location at which the spool stops depends on the magnitude of the magnetic torque and thus, the spool position is proportional to the input current. It can also be said that when the supply and load pressures are constant, the flow to the load is proportional to the spool position.

With reference to the Moog servo valve transfer functions [175], it is

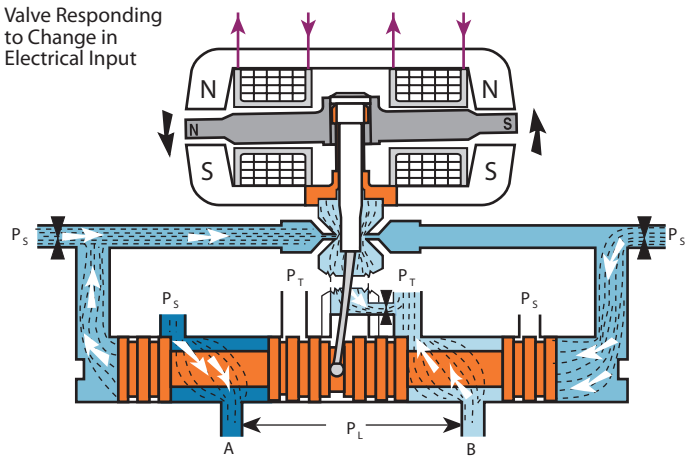

Figure 3.3: Diagram of torque motor and spool when responding to a change in electrical input [45]

decided to model the spool dynamics using a second order transfer function of the form:

$$\frac{Q(s)}{I(s)} = \frac{\omega_n^2}{s^2 + 2\zeta\omega_n s + \omega_n^2} \tag{3.23}$$

where ω_n is the undamped natural frequency and ζ is the damping ratio. Both of these values are estimated from the manufacturers datasheet frequency response bode plots such as that shown in Figure 3.4. The value ω_n comes from the -3dB or 90° phase point and ζ is estimated from the peak amplitude ratio M_v using equation (3.24).

$$M_v = \frac{1}{2\zeta\sqrt{1-\zeta^2}} \tag{3.24}$$

The transfer function given in equation (3.23) is valid when the load is constant at the rated pressure drop. This occurs when the actuator is experiencing a load force that generates a pressure across the cylinder that equals ⅔ of the supply pressure P_s. In order to adjust the flow output from the servo valve according to a varying load, equation (3.25) is used. This

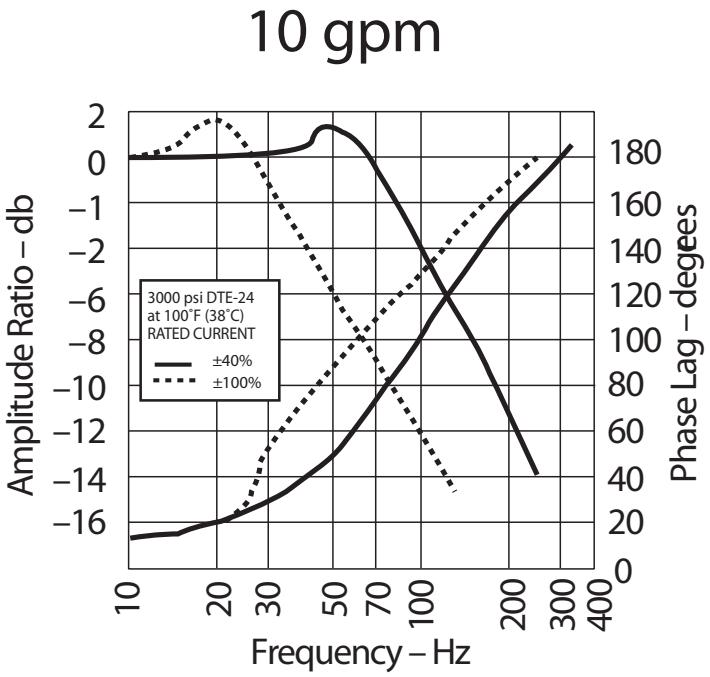

Figure 3.4: Magnitude Phase frequency response plot of Moog G77x series servo valves [176]

relates load flow Q_L to rated flow Q_R using the square root of the pressure dropped across the valve (normalised by the rated pressure) and I_V^*, the current flow to the torque motor normalised by the saturation current.

$$Q_L = Q_R I_V^* \sqrt{\frac{\Delta P_v}{\Delta P_r}} \tag{3.25}$$

The pressure drop across the valve ΔP_v is calculated using $\Delta P_v = P_s - P_t - P_l$ where P_s is the supply pressure, P_t is the tank pressure (return line) and P_l is the pressure dropped across the load. The maximum power is transferred to the load when $P_l = {}^2/_3 P_s$ and most systems operate at a pressure of 3000 psi. Therefore, the rated pressure drop across the servo valve ΔP_r is 1000 psi and this is the pressure at which the rated flow occurs.

The relationship between the load flow and pressure drop across the valve can be represented using equation (3.25) and plot as in Figure 3.5. The horizontal axis is the pressure dropped across the load as a percentage of the supply pressure (with 66% being optimum for power transfer), while the vertical axis represents the load flow as a percentage of the rated flow.

3.1.4 Steady State Behaviour

Dynamic models of actuators deliver high fidelity simulation and give information about transient effects such as voltage spikes, pressure oscillations, and time delays. This lends itself neatly to integration with a 6-DOF flight dynamics model in order to generate estimates of the power peaks that will be required of the power supply. Not only that but it gives a realistic estimation of dynamic performance, above that of simple transfer function models.

There are however drawbacks, mainly in the computation required to

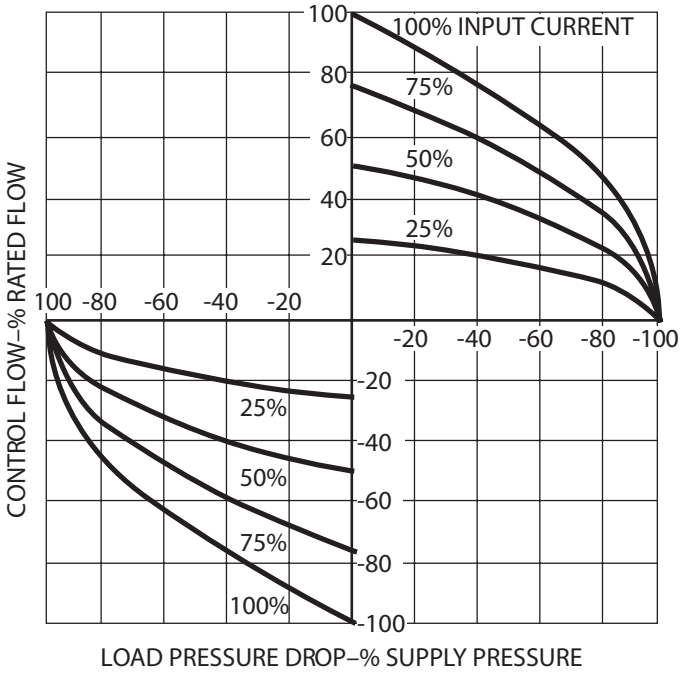

Figure 3.5: Change in load flow with current and load pressure [45]

execute the models. If the user does not require dynamic simulation and instead seeks code which will produce a final estimate in a single model iteration, a steady state model must be used. When fed with a step input, a dynamic model will exhibit a finite rise time before settling at a steady state value. A steady state model however will ignore the dynamics and output the same steady state values of the dynamic model but with no rise time. Thus, the model needs to be executed once to provide an estimate of power consumption instead of at a series of time steps.

It should be noted however that actuators do not typically lend themselves to steady state simulation. By their very nature they are dynamic machines which use power to apply force and achieve motion. Whilst they do have steady state operating conditions on an aircraft (i.e. holding the surfaces in position during straight and level flight) which can be simulated

using steady state models, caution should be used if trying to mimic aircraft manoeuvres using steady state actuator models. When executing a manoeuvre, an actuator will experience transient load force and be expected to move at varying velocities, drawing a distinctly transient power flow. For this reason it is presumed that the steady state models are to be used for steady state flight conditions and the dynamic models used when manoeuvres are of interest.

It is anticipated that the main use of the steady state actuator models is to generate estimates of the power required to hold the surfaces in their steady state trimmed flight positions. They can also be used as simple performance estimators to plot the open loop steady state performance data that will be presented in section 3.1.7 on page 147. They will not however be used directly in this thesis, but are provided for reference.

The steady state hydraulic cylinder is built using equation 3.20 with the dynamic part set to zero, leading to the equation for steady state velocity:

$$\dot{x} = \frac{1}{A_c} \left[Q_i - C_{12} \left(P_1 - P_2 \right) \right] \tag{3.26}$$

Equation (3.26) needs the pressure across the cylinder as an input, which is calculated from the applied load force using equation (3.14) by setting the acceleration term to zero.

$$P_1 - P_2 = \frac{1}{A_c} \left(B_v \dot{x} + F_L \right) \tag{3.27}$$

When connected in Simulink, equations (3.26) and (3.27) form an algebraic loop which is solved using a memory block between the $\dot{x}$ output of (3.26) and input of (3.27). This has the effect of requiring the model to be executed across two time steps to correctly include the viscous friction.

The hydraulic power supply is modelled using a constant value for supply pressure P_s.

The servo valve is converted to steady state form by ignoring the inductance term in equation (3.22) to give the steady state current of the torque motor:

$$I = \frac{V}{R_t} \tag{3.28}$$

Then, by setting the transfer function of the spool dynamics in equation (3.23) to 1 and using the same flow reduction equation described in equation (3.25), the steady state flow rate out of the valve is calculated.

3.1.5 Power Consumption

Calculation of power consumption in the hydraulic system needs to be handled carefully to ensure the correct measurements are taken to produce valid results. The complexity arises from the servo valve and the pressure lost by it which changes with load pressure across the cylinder. When measured across the cylinder control ports, the fluid power follows the piston mechanical output power closely, but with a value proportionally higher due to the leakage past the piston. When measured across the supply pressure, the fluid power vs. cylinder force function becomes nonlinear with an optimum power transfer occurring when the cylinder pressure is ⅔ the supply pressure. At zero load, the entire supply pressure is dropped across the valve and the leakage flow through it to the tank becomes significant. When moving very low forces, the power transfer from hydraulic supply to cylinder becomes very inefficient; in flight control surface applications this can cause inefficient operation of the hydraulic system due to the frequent low load usage.

Equations (3.29) to (3.33) show how the powers are calculated for the

various components, from the engine shaft power drawn by the all the actuator models in (3.29), to the power drawn by a single actuator and servo valve in (3.30). This power consumption is broken down into the fluid power lost in the servo valve and cylinder individually in (3.31) and (3.32). Finally, the mechanical power delivered by the output piston is shown in (3.33).

$$P_{engine} = \frac{P_{fluid(total,all)}}{\eta_{vdp}} \tag{3.29}$$

$$P_{fluid(total)} = P_s Q_L \tag{3.30}$$

$$P_{fluid(valve)} = (P_s - \Delta P)\, Q_L \tag{3.31}$$

$$P_{fluid(cylinder)} = \Delta P Q_L \tag{3.32}$$

$$P_{piston} = F\dot{x} \tag{3.33}$$

3.1.6 Position Control

In order to track a time varying position command under variable load the hydraulic actuators need a closed loop controller. Several options are available to control hydraulic actuators from simple PID linear disturbance rejection algorithms to complex nonlinear techniques such as neural networks or fuzzy logic. PID controllers provide acceptable performance at a single operating point but the response becomes suboptimal or even oscillatory as the load force varies.

To overcome this issue, a variant linear disturbance rejection algorithm is used; the proportional + integral + velocity (PIV) controller (Proportional position loop, proportional and integral velocity loop) with load force feedforward which is shown in Figure 3.6. The feedforward is a bias voltage which is applied directly to the servo valve, proportional to the load force applied.

Essentially, the feedforward compensator directly opposes the applied force with an applied voltage and importantly, does not rely on an error signal. As soon as the force changes, the voltage applied (and thus flow rate) changes. In some systems this technique can achieve zero tracking error.

The benefit of the feedforward path is that the PIV controller becomes independent of the load applied and the response will remain stable across the load range. The feedforward component is outside the feedback loop and thus cannot cause instability of the control system. The feedforward gains are provided in lookup table form in Figure 3.7, after gathering the data by running the models in a position holding mode with monotonically increasing load forces. The voltage required for the servo valve to oppose the load force is measured when steady state has been achieved. For more information on the algorithm please refer to the source material from Parker in [177].

The PIV technique is used for two reasons; one is that a hydraulic cylinder is inherently a velocity controlled actuator and better velocity tracking is achieved with PIV over PID, secondly PIV provides greater control over the tuning. This can make them more difficult to tune but their greatest strength over PID is that the rise time and overshoot are strongly decoupled. With PID it is difficult to achieve fast response with minimum overshoot because the parameters are tightly linked to the proportional term of the controller.

The controller takes feedback signals from the piston position (or control surface angular deflection δ if using the control surface model) and velocity. To simplify the tuning of the loop gains, the feedback signals are normalised to ± 10 V and all computation is conducted in this range. At the output of the control circuit the command signal is attenuated to the ± 2 V required to power the servo valve.

The gains are selected using a simple gradient descent based tuning

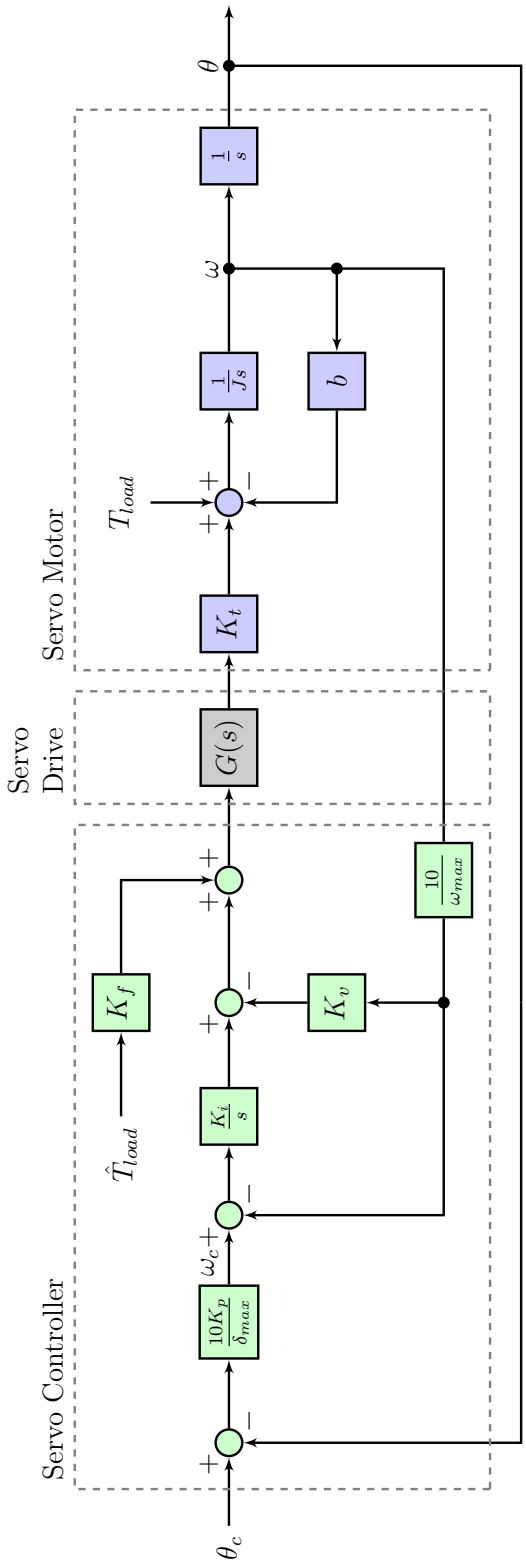

Figure 3.6: PIV controller block diagram [177]

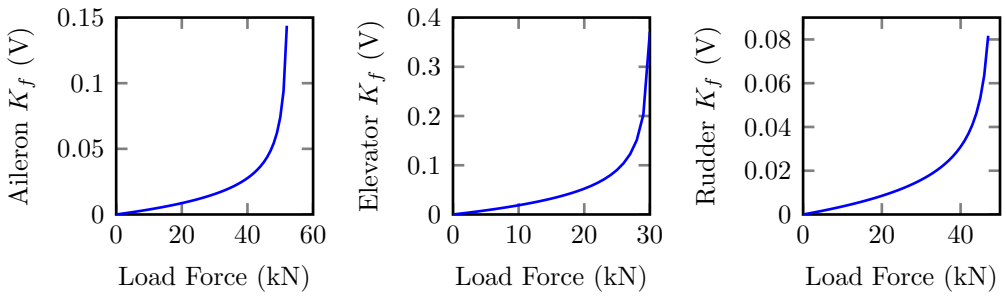

Figure 3.7: Feedforward gain lookup tables for the ESHA PIV controllers

method that is built into Simulink; this provides a graphical response which updates as the gains are changed, allowing straightforward loop tuning. The gains which parametrise the controller are presented in Appendix B. Clamping is used to prevent integrator windup which is required as the controller is designed to push the output to saturation on a regular basis; without this characteristic the actuator will not achieve its open loop linear speed when subject to a step input. To demonstrate the capability of the controller, a randomly varying input signal and sinusoidal load force are applied to the actuator and the response is shown in Figure 3.8.

The frequency response of the complete actuator is shown in Figure 3.9, the -3 dB bandwidth occurs at around 4 Hz and the third order model exhibits a 60 dB/decade roll off.

3.1.7 Model Validation

Validation of the ESHA models breaks down to two distinct parts; verifying the speed-force capabilities against the specifications and secondly analysing the efficiencies of the energy conversion throughout the actuator and servo valve.

The first task is normally satisfied using a speed-force graph which provides data on the no load rate, stall force and an indication of the performance

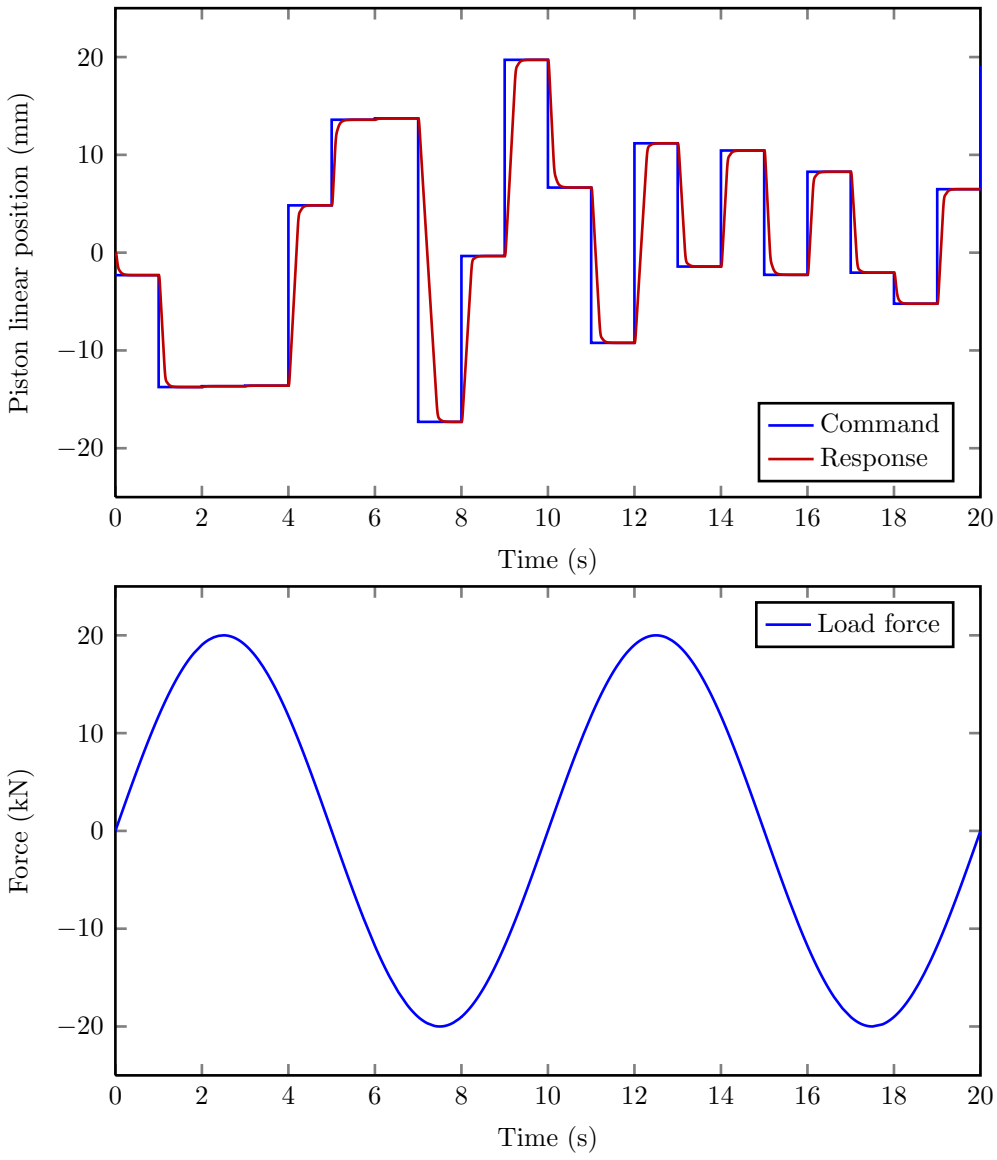

Figure 3.8: Position control of ESHA with pseudo-random input commands and 20 kN, 0.1 Hz sinusoidal load force

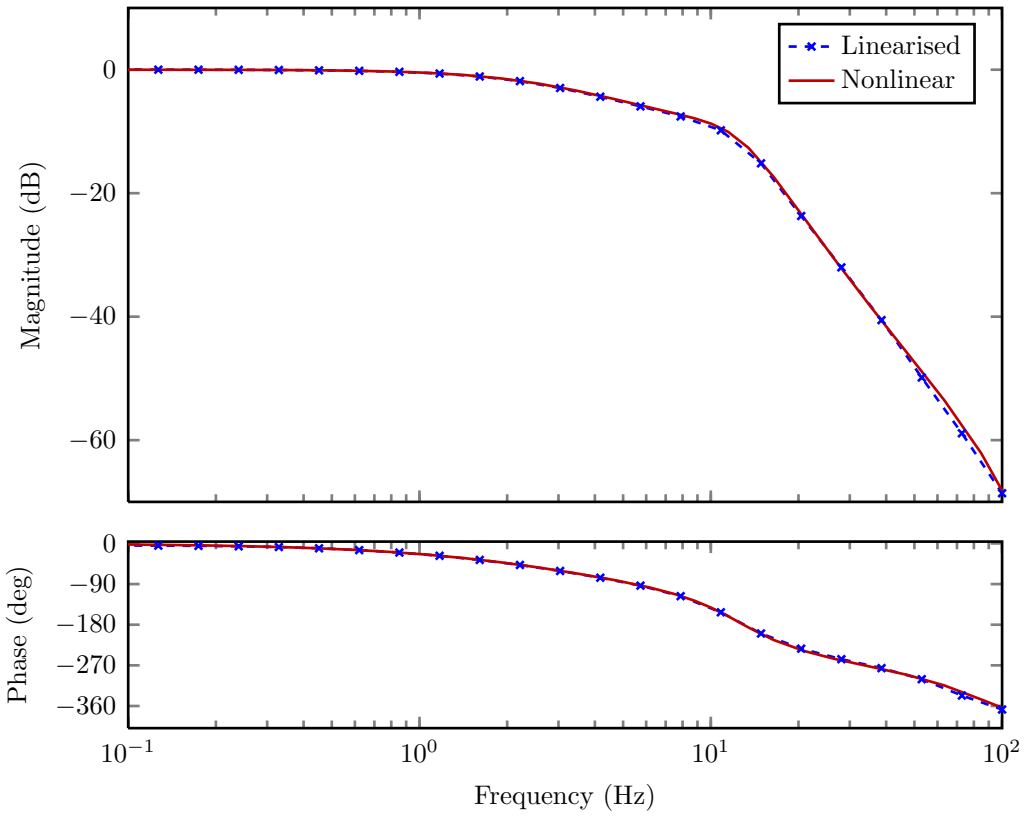

Figure 3.9: Closed loop frequency response of ESHA with a ±1 mm sinusoidal position command

in between these two key points. Since the ESHA is controlled using a flow control valve whose flow rate varies according to the function $\sqrt{1 - P_l/P_s}$, it would be expected to see this behaviour in the speed-force plot as the load force is directly proportional to the load pressure.

The speed-force graphs are generated by writing a script which iterates the model with a constant torque motor voltage and increasing force. The model has the limits removed from the piston position integrator so the piston is free to travel any distance to achieve steady state; then the model is configured to run for long enough to ensure steady state is achieved in all steps. The script records the piston linear rate output from the model and monitors it to check for stall (velocity less than 0); if this occurs, the loop is terminated and the data is ready to be plot.

The output from this step is shown by the blue line in Figure 3.10 and as expected, it shows the $\sqrt{1 - P_l/P_s}$ shape. This curve is used to calculate the mechanical power curve (product of force and velocity) which shows the optimum power transfer occurring at ⅔ of the stall force. This agrees with the Moog literature discussed in section 3.1.3 on page 136. The final curve of interest is the efficiency curve, which shows maximum efficiency to occur just before stall. This is because the efficiency curve is generally formed from the function:

$$y = \frac{x\sqrt{1-x}}{\sqrt{1-x}} \tag{3.34}$$

which follows the function $y = x$ until x approaches 1. As x approaches 1, y rapidly tends towards 0. Relating this directly to the hydraulic circuit in question, the value of 1 would be replaced by the stall pressure (or force) and x becomes the load pressure (or force). Thus, the efficiency of the hydraulic circuit increases linearly until the load force reaches over 90% of its maximum

before rapidly decreasing as it approaches 100% of the stall force.

To investigate the relationship between efficiency and actuator force and speed individually, the model is closed loop controlled and given ramp position commands with gradients equal to the desired linear velocity. A script with a for loop is used again to cycle through the force and velocity inputs, at each stage the steady state power consumption and efficiency is recorded. An alternative method is to use the steady state models from section 3.1.4 (on page 140) which do not need trimming. This is easier, but it is preferred to validate the dynamic models which will be used in the rest of the simulation.

The expected response for the power-speed behaviour is a linear plot due to equation (3.30). Since P_s is a constant 3000 psi, the power from the supply varies linearly with velocity and will reach a maximum when the servo valve reaches its maximum flow rate given by equation (3.25). When the power against force relationship is considered, the expected behaviour is to see an almost flat gradient for most of the force range; again due to equation (3.30) and because the supply pressure P_s is constant. For a constant velocity, the load flow Q_L does not change much; only the leakage flow component of the load flow increases due to the increased pressure across the piston caused by an increasing load force. Thus, a small gradient is expected to be evident with increasing force up until a point where the flow rate capacity of the servo valve decreases to zero as a result of equation (3.25) equating to zero. When a range of linear speeds (i.e. flow rates) are studied and plot on the same axes, a front is expected to form which follows the form of the valve flow rate.

The results of the closed loop tests can be seen in Figure 3.13, where the relationships described in the previous paragraph manifest themselves. This demonstrates the expected operation of the model up until the stall force.

The second closed loop plots in Figure 3.14 show the relationship between force, velocity and the overall efficiency. The efficiency-velocity graph shows a constant efficiency with increasing speed which seems counter intuitive, but can be explained using the efficiency calculation:

$$\eta = \frac{F_L \dot{x}}{P_s Q_L} \tag{3.35}$$

Since F_L and P_s are constant and the velocity $\dot{x}$ and steady state load flow Q_L form a constant ratio related by the piston area, efficiency remains constant as velocity (and load flow) increase.

The second plot in Figure 3.14 shows a linear increase in efficiency as the applied force increases, which can again be explained using equation (3.35). Given that the velocity and flow rate are linked by the piston area as in equation (3.3), equation (3.35) can be rewritten as follows:

$$\eta = \frac{F_L}{P_s A_c} \tag{3.36}$$

The efficiency at constant velocity effectively becomes a ratio between the applied force and the maximum theoretical force, and as such should follow the trend shown in the velocity plot.

The final part of the validation aims to demonstrate the power consumption and efficiencies of the internal energy conversions (discussed in section 3.1.4 on page 140) in the simulated actuator. Using closed loop control to make the actuator maintain a commanded linear velocity; a load force can be applied, to the input which, (providing the commands fall within the force-speed envelope) will effectively set the piston mechanical power to a known value. Once the actuator achieves this steady state condition, the powers can be sampled and the efficiencies compared with those of typical

values from commercially available products where possible. Unfortunately efficiency curves are seldom provided in manufacturer datasheets and as has been demonstrated in the previous open loop graphs; efficiency varies widely with operating point. For this reason, singular quotes of efficiency by manufacturers stating "over 90% efficient" on their products marketing literature are not of much value for quantitative validation.

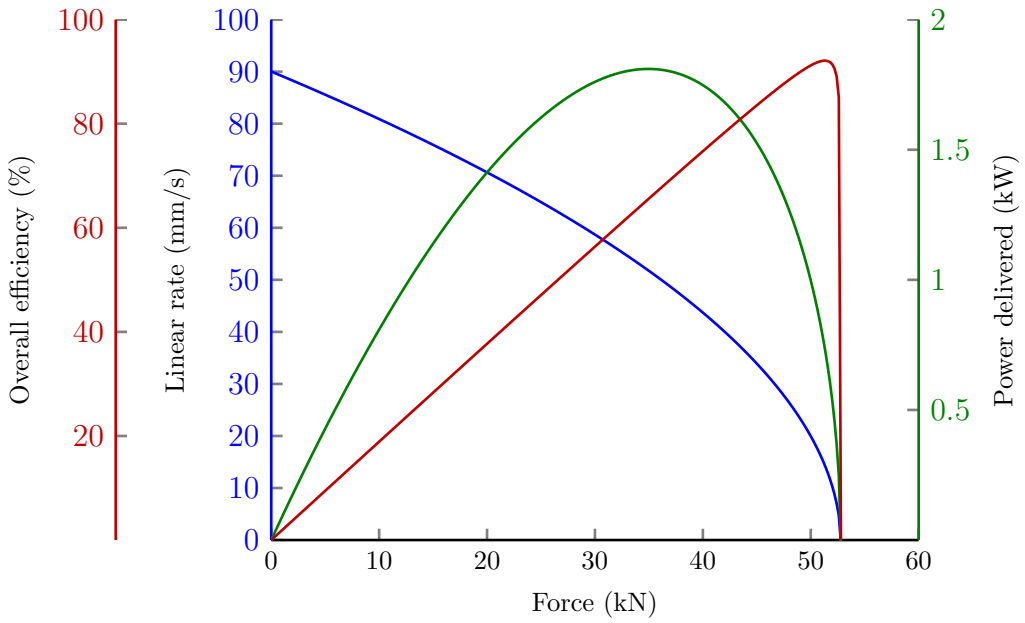

Figure 3.10: Open loop performance characteristics of the aileron ESHA

Indeed, the ideal validation would be to construct a full size 'iron bird' actuation rig with the same cylinders and pumps used in the model. This has inherent cost and complexity issues so a scaled down version is a second option, but the main sources of energy loss (valve and cylinder leakage and cylinder friction coefficients) do not necessarily scale well and is still costly.

The decision is to use a combination of datasheet parameters and papers published on actuator system identification and friction model identification as a basis for leakage coefficient and Coulomb friction estimates. The val-

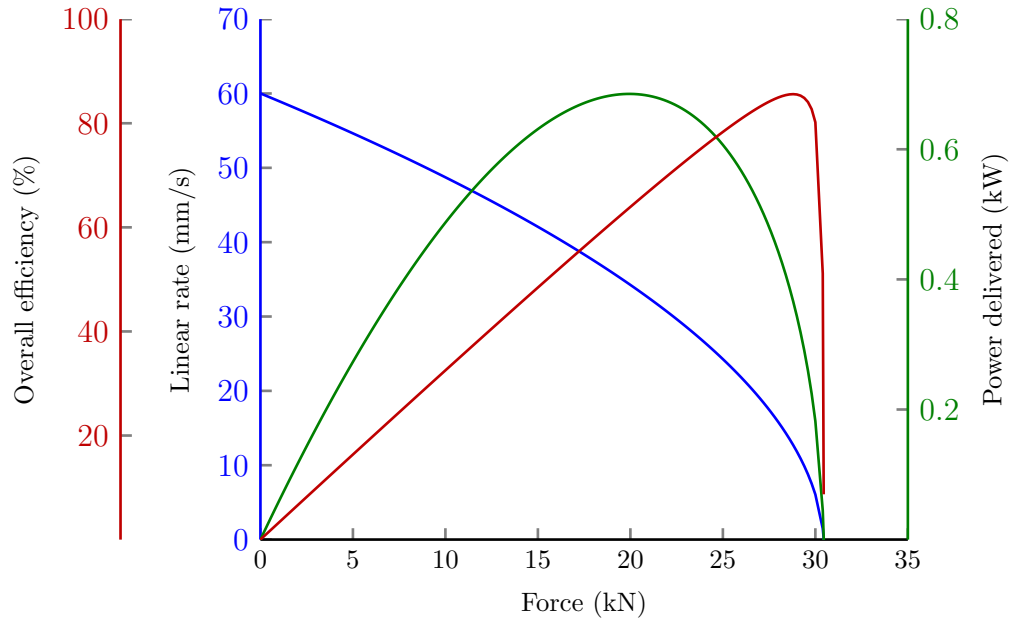

Figure 3.11: Open loop performance characteristics of the elevator ESHA

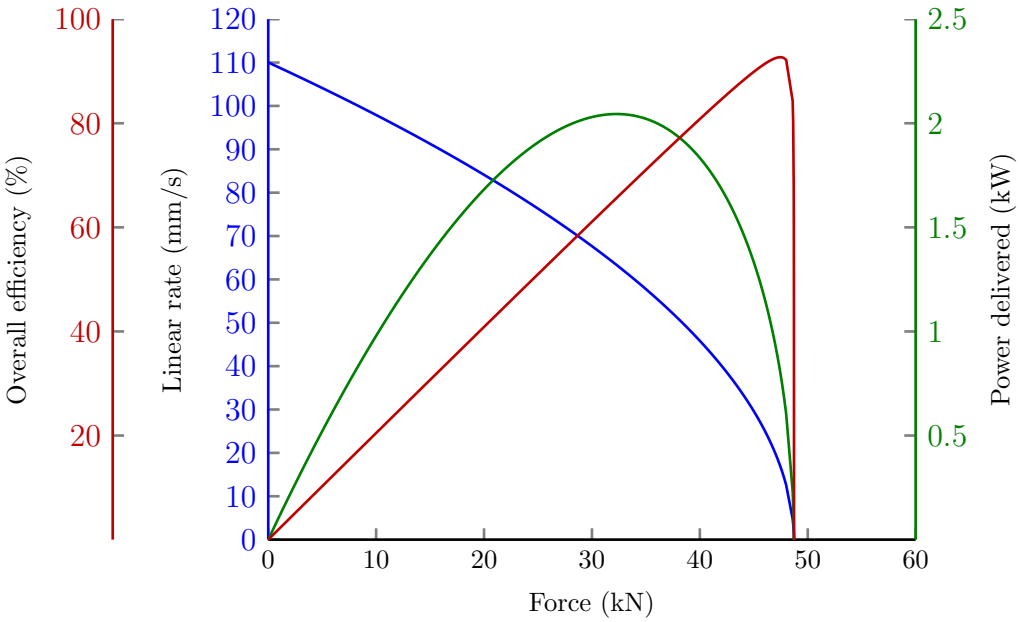

Figure 3.12: Open loop performance characteristics of the rudder ESHA

ues used are purposely configured as external inputs which can easily be substituted if more accurate data becomes available.

The results from the test are compiled in tables 3.2 - 3.4, with the highest efficiencies evident at the highest loads as discussed previously.

Table 3.2: Table showing the power consumption and efficiency for the aileron ESHA at a range of operating points

Inputs			Model outputs			Efficiency		
Linear speed (m/s)	Load force (N)	$P = F\dot{x}$ (W)	Mechanical piston power (W)	Fluid power through piston (W)	Hydraulic power input (W)	Fluid to piston (%)	Supply to cylinder fluid (%)	Overall (%)
0.000	10000	0	0.00	1.53	8.10	-	18.89	-
0.001	10000	10	10.00	11.53	60.90	86.73	18.93	16.42
0.050	10000	500	500.00	501.91	2648.11	99.62	18.95	18.88
0.040	40000	1600	1600.00	1624.80	2144.42	98.47	75.77	74.61
0.010	50000	500	500.00	538.38	568.52	92.87	94.70	87.95

Table 3.3: Table showing the power consumption and efficiency for the elevator ESHA at a range of operating points

Inputs			Model outputs			Efficiency		
Linear speed (m/s)	Load force (N)	$P = F\dot{x}$ (W)	Mechanical piston power (W)	Fluid power through piston (W)	Hydraulic power input (W)	Fluid to piston (%)	Supply to cylinder fluid (%)	Overall (%)
0.000	10000	0	0.00	4.61	14.04	-	32.83	-
0.001	10000	10	10.00	14.61	44.51	68.45	32.82	22.47
0.040	10000	400	400.00	404.85	1232.85	98.80	32.84	32.45
0.020	25000	500	500.00	528.87	644.51	94.54	82.06	77.58
0.010	29000	290	290.00	328.77	345.42	88.21	95.18	83.96

Table 3.4: Table showing the power consumption and efficiency for the rudder ESHA at a range of operating points

Inputs			Model outputs			Efficiency		
Linear speed (m/s)	Load force (N)	$P = F\dot{x}$ (W)	Mechanical piston power (W)	Fluid power through piston (W)	Hydraulic power input (W)	Fluid to piston (%)	Supply to cylinder fluid (%)	Overall (%)
0.000	10000	0	0.00	1.80	8.78	-	20.50	-
0.001	10000	10	10.00	11.80	57.51	84.75	20.52	17.39
0.050	10000	500	500.00	502.18	2445.29	99.57	20.54	20.45
0.040	40000	1600	1600.00	1629.08	1984.32	98.21	82.10	80.63
0.020	45000	900	900.00	936.55	1014.11	96.10	92.35	88.75

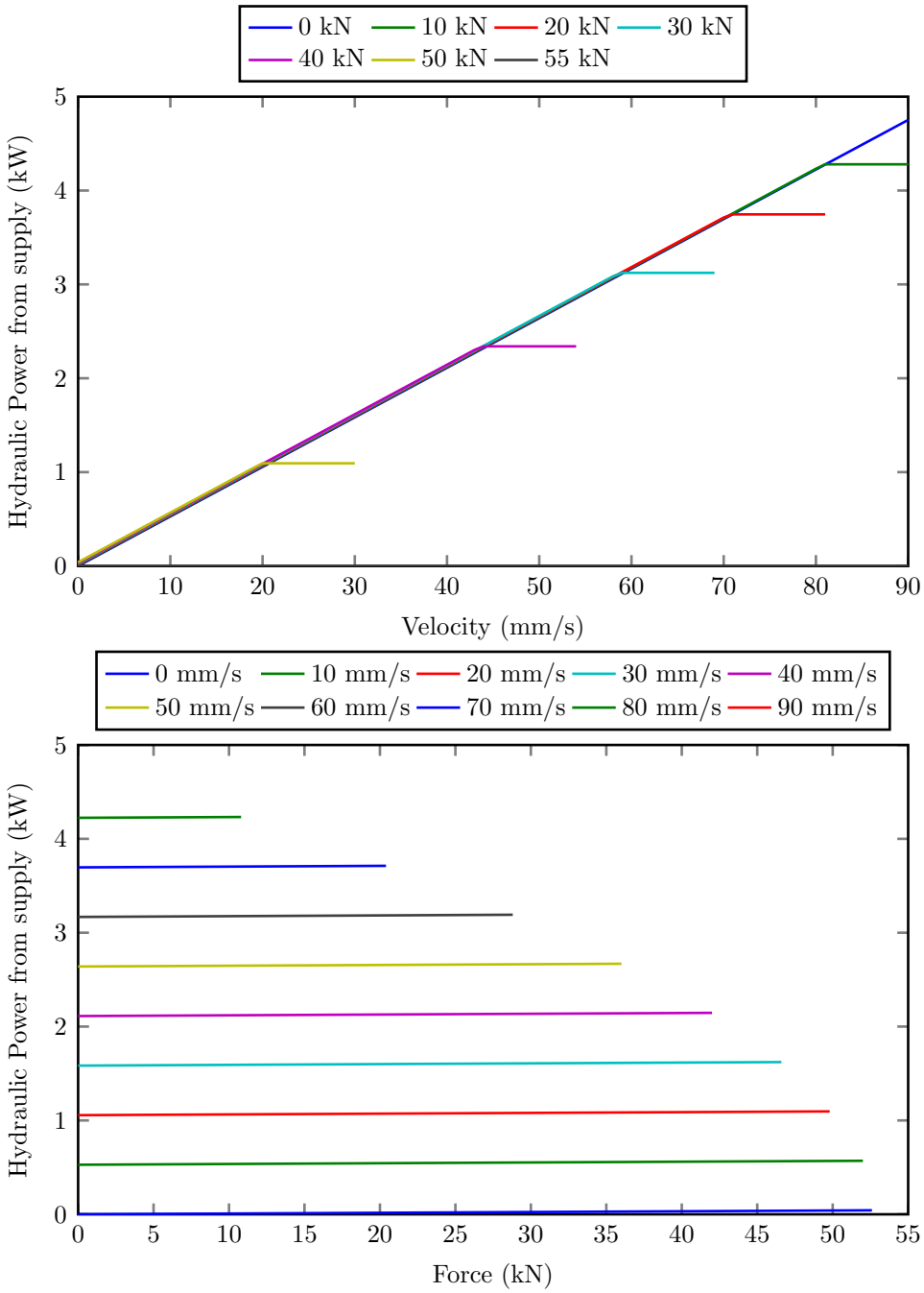

Figure 3.13: Total steady state hydraulic power of the aileron ESHA measured at pump (excluding pump efficiency), as a function of force and velocity

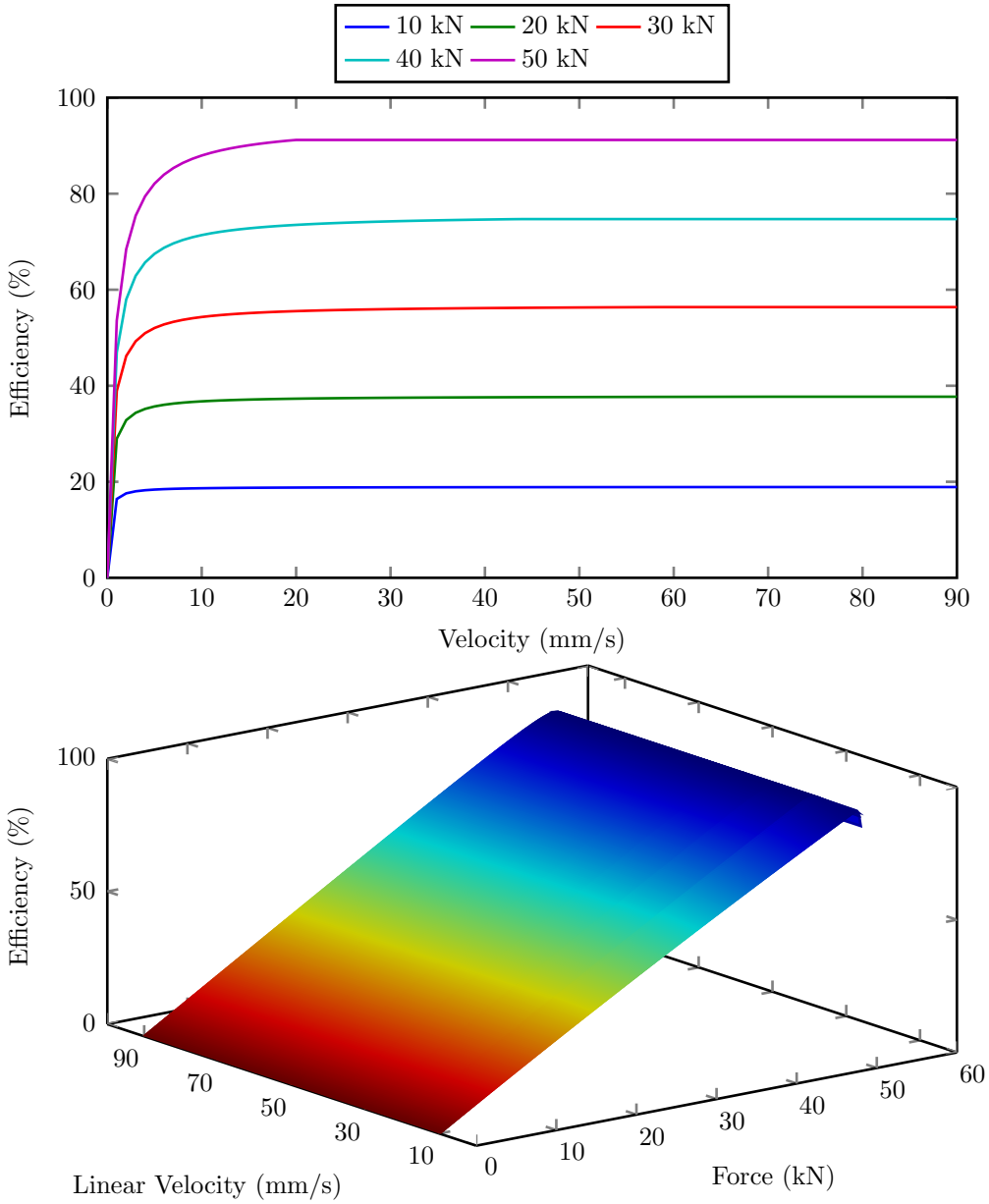

Figure 3.14: Efficiency curves (output mechanical power/input hydraulic power) as a function of load and speed for the aileron ESHA

3.2 Electromechanical Actuation System

Electromechanical actuators take electrical energy from an electric power bus and convert it using a motor to rotational mechanical energy, in this case a BLDC permanent magnet motor. This energy is then delivered to a ball screw which converts it to linear mechanical power. Each component has its own sources of power loss; mainly through friction but also electrical effects such as heating and magnetic flux leakage. This model seeks to provide an estimate of the electrical power consumption and position response when a load force and position is demanded of it.

3.2.1 DC Motor Model

Any power-by-wire actuator requires a means of converting electric energy from the power bus to mechanical energy to enact the motion required; although there are other methods (e.g. piezo electric actuators), the most common of which is from an electric motor. There are several viable motor options which each have unique benefits and drawbacks, from the type of bus the actuators are supplied by (AC or DC) to the ease and accuracy of control or the overall weight (permanent magnet or field wound). In the case of this thesis, the motor model represents a BLDC type with a trapezoidal back EMF profile.

Modelling a DC motor requires both the electrical and the mechanical characteristics to be represented through differential equations which will be derived in this section.

Physically, a brushless DC motor is constructed of two main components; the rotor and the stator. The rotor in its most elementary form is a north – south magnet arrangement which is free to spin on bearings. The stator has

electromagnets located at different angular positions (poles) of the annulus, which when switched in a square step pattern provide a rotating magnetic field around the rotor. The only difference between this and a brushless AC motor is that the stator poles must be switched more precisely to create a sinusoidal rotating magnetic field in a brushless AC motor.

In simple brushed DC motors, a two pole stator requires the voltage polarity applied to the rotor to be reversed every 180°. This is classically handled by carbon brushes and a split ring commutator, but in modern motors commutation is handled electrically in order to improve efficiency, reliability and to reduce electromagnetic noise due to electric arcing. From a functional modelling perspective a BLDC motor can be considered to be equivalent to a brushed DC, when only the major motion and losses are required. Detailed three phase models are only required when detailed interactions between the servodrive and motor are required.

The aim of the motor model is to simulate the angular velocity, torque and induced current flow when a voltage stimulus and load torque is applied to the inputs. The product of the input voltage and current will produce a value for input electrical power, which must be translated to mechanical shaft power (the product of torque and angular velocity). The model must have the ability to take load torque as an input in order to model the changes in electrical power consumption as the load on the actuator changes. This is fundamental to modelling the power consumption and in turn, analysing flight trajectories to minimise actuator energy usage. Two differential equations will be derived to model the electrical and mechanical responses to the applied inputs as described in the following sections.

Electrical Characteristics

The electrical properties of a permanent magnet DC motor can be repre-

sented with an equivalent circuit of the armature winding as shown in Figure 3.15. The applied voltage V_a is connected across the terminals of the armature coil which is represented by a series connected resistance R_a, inductance L_a and opposing voltage source V_{emf}. This voltage source is caused by the armature coil passing through the stationary magnetic flux lines, which induces a current flow and hence voltage in the coil. It is most frequently known as the back electromotive force or back e.m.f. for short.

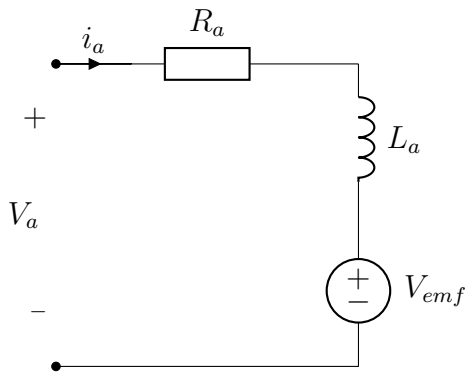

Figure 3.15: Equivalent circuit of DC motor

The sum of the voltages around the circuit according to Kirchoff's voltage law must equal zero, in mathematical notation:

$$V_a - V_{Ra} - V_{La} - V_{emf} = 0 \tag{3.37}$$

The components V_{Ra} and V_{La} represent the voltages that appear across the resistor and inductor. Using Ohms law it can be stated that:

$$V_{Ra} = i_a R_a \tag{3.38}$$

where i_a is the armature current. The voltage that is induced across the inductor is proportional to the rate of change of current flow through it,

correctly notated as:

$$V_{La} = L_a \frac{di_a}{dt} \tag{3.39}$$

Finally, the current flow induced in a wire which travels through a magnetic field varies with the velocity at which the wire passes through the magnetic flux lines. In rotational motor systems the back e.m.f. voltage generated is proportional to the angular velocity of the rotor:

$$V_{emf} = K_v \omega_a \tag{3.40}$$

where K_v is the velocity constant of the motor and ω_a is the angular velocity of the rotor. The constant K_v is derived from the magnetic flux density, the reluctance of the armature iron core and the number of turns of the armature coil.

By substituting the equations (3.38)-(3.40) into (3.37), the following differential equation is derived:

$$V_a - i_a R_a - L_a \frac{di_a}{dt} - K_v \omega_a = 0 \tag{3.41}$$

To put equation (3.41) into the required format to program the model in Simulink, the differential term is isolated from the other terms as follows:

$$\frac{di_a}{dt} = \frac{1}{L_a}(V_a - i_a R_a - K_v \omega_a) \tag{3.42}$$

Mechanical Characteristics

By considering the motor in dynamic equilibrium, the net torque on the motor must equal zero:

$$T_e - T_{\dot{\omega}} - T_\omega - T_L = 0 \tag{3.43}$$

where T_e is the generated electromagnetic torque, $T_{\dot{\omega}}$ is the torque required to accelerate an inertia, T_ω is the torque required to overcome viscous friction and T_L is the load torque.

The electromagnetic torque is proportional to the current flow through the armature:

$$T_e = K_t i_a \tag{3.44}$$

where K_t is the torque constant of the motor. This constant is also a function of magnetic flux density, the reluctance of the armature iron core and the number of turns of the armature winding. When using S.I units the velocity and torque constants are numerically equal.

The torque that appears at the motor shaft due to an accelerating inertia is described as follows:

$$T_{\dot{\omega}} = J\frac{d\omega_a}{dt} \tag{3.45}$$

where J is the total inertia of the motor and load, as it appears at the motor through any gearing. The calculation of this inertia is detailed in the next section (3.2.2 on page 166).

Assuming viscous and Coulomb frictions are modelled, the torque as a function of angular velocity is:

$$T_\omega = B_v\omega_a + C_{coul}\tanh\left(K_{cm}\omega_a\right) \tag{3.46}$$

where B_v is the damping coefficient of the motor's mechanical components, C_{coul} is the Coulomb friction coefficient and K_{cm} is the crossover curve sharpness. Since the motor speed will frequently cross through zero, the viscous friction is coupled with a Coulomb friction model which is based on a $\tanh\left(K_{cm}\omega_a\right)$ function. This represents the Coulomb friction with a continuous function to allow fast execution. Modelling these additional details

typically adds a discontinuity in the modelling equations where ω_a crosses through 0. This causes a severe slowdown in the simulation speed which is avoided by using a continuous function, as discussed in section 2.3.5 on page 64.

By substituting equations (3.44) - (3.46) into (3.43), the following differential equation is derived which describes the motor's mechanical behaviour:

$$K_t i_a - J\frac{d\omega_a}{dt} - B_v\omega_a - C_{coul}\tanh(K_{cm}\omega_a) - T_L = 0 \tag{3.47}$$

Rearranging to the format required to input into Simulink:

$$\frac{d\omega_a}{dt} = \frac{1}{J}\left(K_t i_a - B_v\omega_a - C_{coul}\tanh(K_{cm}\omega_a) - T_L\right) \tag{3.48}$$

3.2.2 Gearbox and Ballscrew Model

The dynamic model for the mechanical sub system can be approached from several angles; one option is to take the outputs of the motor model and use steady state equations to calculate the linear velocity and force output of the ball screw. The limitation this has is that the efficiency is generally modelled as a single constant and therefore does not represent the variation in efficiency across the force-velocity envelope that is exhibited by the real system.

The second option is to model the ball screw using Newtonian mechanics which simulates the dynamic behaviour of the power transfer from motor input to linear piston output much more accurately. This method allows separate friction models to be implemented for the ball screw and motor and can thus generate realistic estimates of power flow and efficiency at each stage of the actuator.

The second option is chosen because the dynamic motion is a key interest of this work.

With reference to Du *et al.* [178], the ball screw can be modelled using two masses, one representing the screw and the second representing the rod end and load mass combination M_l. Between the two masses is a spring-damper pair which models the material and structural properties of the lead screw. This makes the model more accurate in the high frequency range but adds little to the power consumption simulation. Additionally, the use of a 2-DOF model increases the computational complexity and reduces the simulation speed noticeably. This method was used initially, but when integrated with the full aircraft model it was found that the simulation would not significantly exceed real time speed. To overcome this, the ball screw model is reduced to a 1-DOF simulation which represents only the low frequency dynamics and frictional losses.

The actuator modelling diagram is shown in Figure 3.16; the motor is connected to the ball screw nut through a gearbox which is constrained to rotational motion only. The rotation of the nut causes translation of the lead screw, which is constrained to disallow rotation.

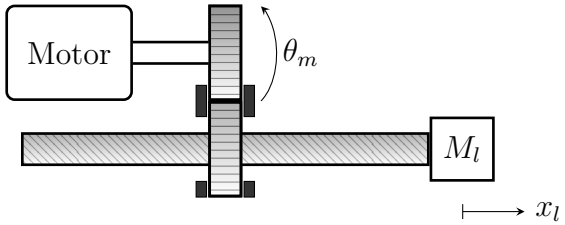

Figure 3.16: Diagram of motor, ball screw and load mass configuration of EMA

The materials used in the construction of the ball screw have a very high, but finite stiffness (K_m) which is exploited to model Newton's 3rd Law of equal and opposite reaction forces between the motor output and load mass.

This stiffness (modelled as a spring) allows an angular displacement of the motor θ_m to be converted to a force on the screw.

The schematic representation of the actuator shown in Figure 3.17 depicts the mechanical model as a 1-DOF mass-spring-damper system. Position x_m represents the theoretical linear position of the nut as the product of the motor shaft position and the lead screw pitch, but it does not represent the location of a mass like x_l does.

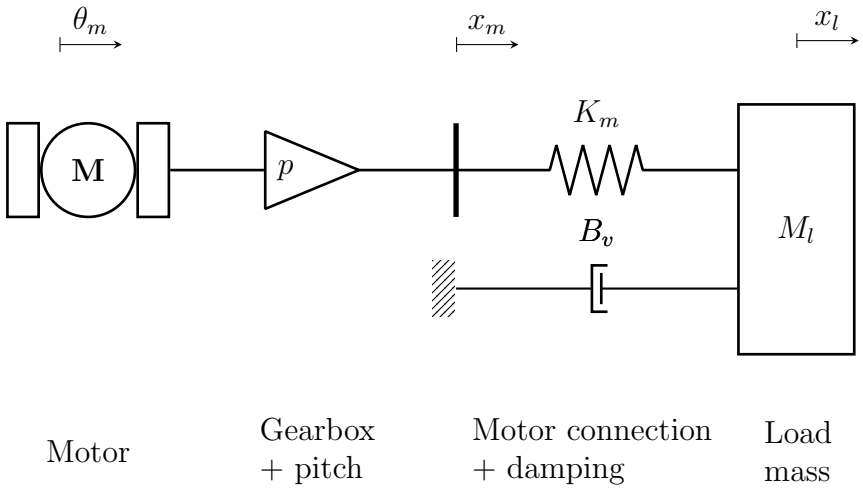

Figure 3.17: Equivalent schematic diagram of EMA

Transferring the schematic into a free body diagram, the forces which define the dynamic behaviour of the mass are shown in Figure 3.18.

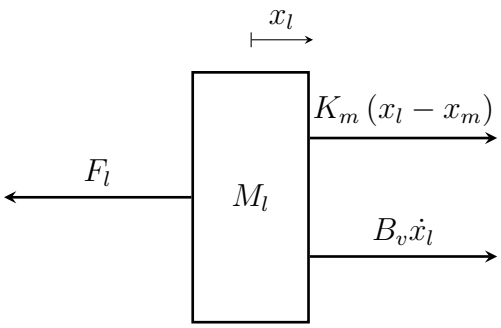

Figure 3.18: Free body diagram of the ball screw

Once a free body diagram of the system is obtained, the differential equation for the load mass can be formed:

$$M_l\ddot{x}_l - B_v\dot{x}_l - K_m\left(x_l - x_m\right) + F_l = 0 \tag{3.49}$$

Equation (3.49) is rearranged for entry into Simulink:

$$\ddot{x}_l = \frac{1}{M_l}\left(B_v\dot{x}_l + K_m\left(x_l - x_m\right) - F_l\right) \tag{3.50}$$

The term $B_v\dot{x}_l$ represents the viscous friction in the system, but can more generally be referred to as the friction force F_C. This model also includes Coulomb friction, but this is left off the free body diagram for clarity. Coulomb friction is often modelled using a function of the form:

$$F_C = C_C\left(\frac{\dot{x}_l}{|\dot{x}_l|}\right) \tag{3.51}$$

where C_C is the Coulomb friction coefficient. This function is discontinuous at $\dot{x}_l = 0$, which forces a decrease in simulation speed as the solver attempts to keep the error in the solution within tolerance. Another method of representing Coulomb friction is used in this model which is based on a continuous $\tanh(\omega)$ function. This is less realistic because at $\dot{x}_l = 0$ the friction force should equal the applied force as the breakaway force has not been reached yet, but the $\tanh(\omega)$ model gives zero friction force in this condition. This means the model will not simulate the peaks in power consumption required to start the actuator moving from stationary accurately, but for the benefit in overall simulation speed this is considered a fair trade off.

In order to match the speed and torque of the motor to the linear velocity and force specifications, the gear ratio and screw pitch need to be consid-

ered. To simplify the problem, the gear ratio between the motor and nut is combined with the screw pitch; the value of pitch p required to match the no load speed of the motor to the required no load linear speed of the actuator is then calculated using:

$$p = \frac{\dot{x}_{NL}}{\omega_{NL}} \tag{3.52}$$

To conclude the ball screw model, the load torque on the motor needs to be calculated using:

$$pK_m \left(p\theta_m - x_l\right) \tag{3.53}$$

Inertia Considerations

In the case where a non-unity gearbox is used between the motor and ball screw, the inertia of the rotating components J are reflected to the motor shaft. In general it can be stated that:

$$\bar{J} = \frac{J}{\tau^2} \tag{3.54}$$

where $\bar{J}$ is the reflected inertia and τ is the gear ratio. There are two rotating masses which are directly connected to the motor shaft, there is the motor rotor J_m and ball screw J_{bs}. The total inertia referred to the motor shaft can be calculated using the summation of the directly connected inertias and reflected inertias:

$$J = J_m + \frac{1}{\tau^2}\left(J_{bs}\right) \tag{3.55}$$

3.2.3 Steady State Behaviour

With reference to the purpose and limitations of steady state modelling covered previously in the ESHA section 3.1.4 (page 140); the electromechanical actuator is converted to steady state form by firstly setting the dynamic

component of the motor electrical equation (3.41) to zero. The motor modelled in this work uses permanent magnets to generate the magnetic field so the motor can be represented using just the electrical circuit. Since only steady state behaviour is considered, the $\tanh(K_{cm}\omega_a)$ term is replaced by a function $sign(x)$ which produces a value of +1 when the input voltage is positive, 0 when there is 0 Volts applied and -1 when the voltage is negative. This removes the dependency on ω_a.

$$V_a = i_a R_a + K_v \omega_a \tag{3.56}$$

Substituting i_a using equation (3.44) and rearranging to give the angular velocity as an output:

$$\omega_a = \left(\frac{V_a}{K_v}\right) - \left(\frac{R_a}{K_t K_v}\right) T \tag{3.57}$$

where T is the total torque on the motor, including the load torque T_L and friction torques T_{coul}, T_ω:

$$T = T_L + C_{coul} sign(V_a) + B_v \omega_a \tag{3.58}$$

Current flow is also calculated using equation (3.44).

The next component of the EMA is the gearbox, which in steady state is based purely on the gear ratio; the output of the gearbox is an angular velocity fed forwards to the ball screw and a load torque fed back to the motor.

$$\omega_{gearbox} = \frac{\omega_a}{\tau} \tag{3.59}$$

$$T_L = \frac{T_{gearbox}}{\tau} \tag{3.60}$$

Finally, the ball screw velocity is represented by equation (3.52) since all dynamic characteristics have settled.

$$\dot{x} = p\omega_{gearbox} \tag{3.61}$$

The load torque fed back to the gearbox is calculated by combining the load force and friction forces. In this component the velocity signal must be fed through a memory block to avoid an algebraic loop.

$$T_{gearbox} = p\left(F_L + B_{vs}\dot{x} + C_{coul}\tanh(\dot{x})\right) \tag{3.62}$$

3.2.4 Power Consumption

The EMA model provides values of instantaneous power for all stages of energy transfer in the actuator. This begins with the electrical power consumed from the power supply, then moves to the power delivered at the motor's output shaft and finishes with the linear mechanical power of the piston.

$$P_{electrical} = VI = \frac{P_{motor}}{\eta_m} \tag{3.63}$$

$$P_{motor} = T\omega = \frac{P_{piston}}{\eta_{bs}} \tag{3.64}$$

$$P_{piston} = F\dot{x} \tag{3.65}$$

These values should reflect the efficiency of power conversion of each stage in the actuator. For example, with correct operation it would be anticipated that the piston power would be a factor equal to η_{bs} smaller than the motor's mechanical shaft power and the shaft power would be a factor η_m smaller than the electrical power supplied. These simple relations allow the user to

verify the correct operation of the model in a straightforward way.

The overall power consumption charts for the range of load speeds and velocities are given in chapter 3.2.6 (starting from page 179), along with data from the model which gives the intermediate power consumptions. Such data provides insight into where the power is lost rather than just giving an overall efficiency figure.

3.2.5 Position Control

The overall structure of the controller is the same PIV with load force feedforward used for the ESHA in section 3.1.6 (page 144). For a detailed overview refer to that chapter, only the differences are listed in this section.

The main change to the control system stems from the change of plant from a servo valve to a DC motor. The best control performance is achieved when the velocity loop is connected to the fastest loop in the system; i.e. controlling the velocity of the motor rather than the output piston. Hence, the feedback signals taken are the piston position (or control surface angular deflection δ if using the control surface model) and motor velocity. When changing between the control surface output and linear output models, only the outer position loop gain needs re-tuning.

The signals are again normalised to ± 10 V and all computation is conducted in this range. At the output of the control circuit, the command signal is amplified to the ± 270 V required to power the motor.

Tuning is conducted using Simulink's built in PI tuning blocks to achieve a trade off between fast response and disturbance rejection, the end result of which can be seen in Figure 3.19. The linear region where the actuator achieves its steady state speed is evident, followed by a well damped response with zero overshoot.

The frequency response of the complete actuator is shown in Figure 3.20, the -3 dB bandwidth occurs at around 2.5 Hz and the model exhibits a 40 dB/decade roll off in the frequency range of interest.

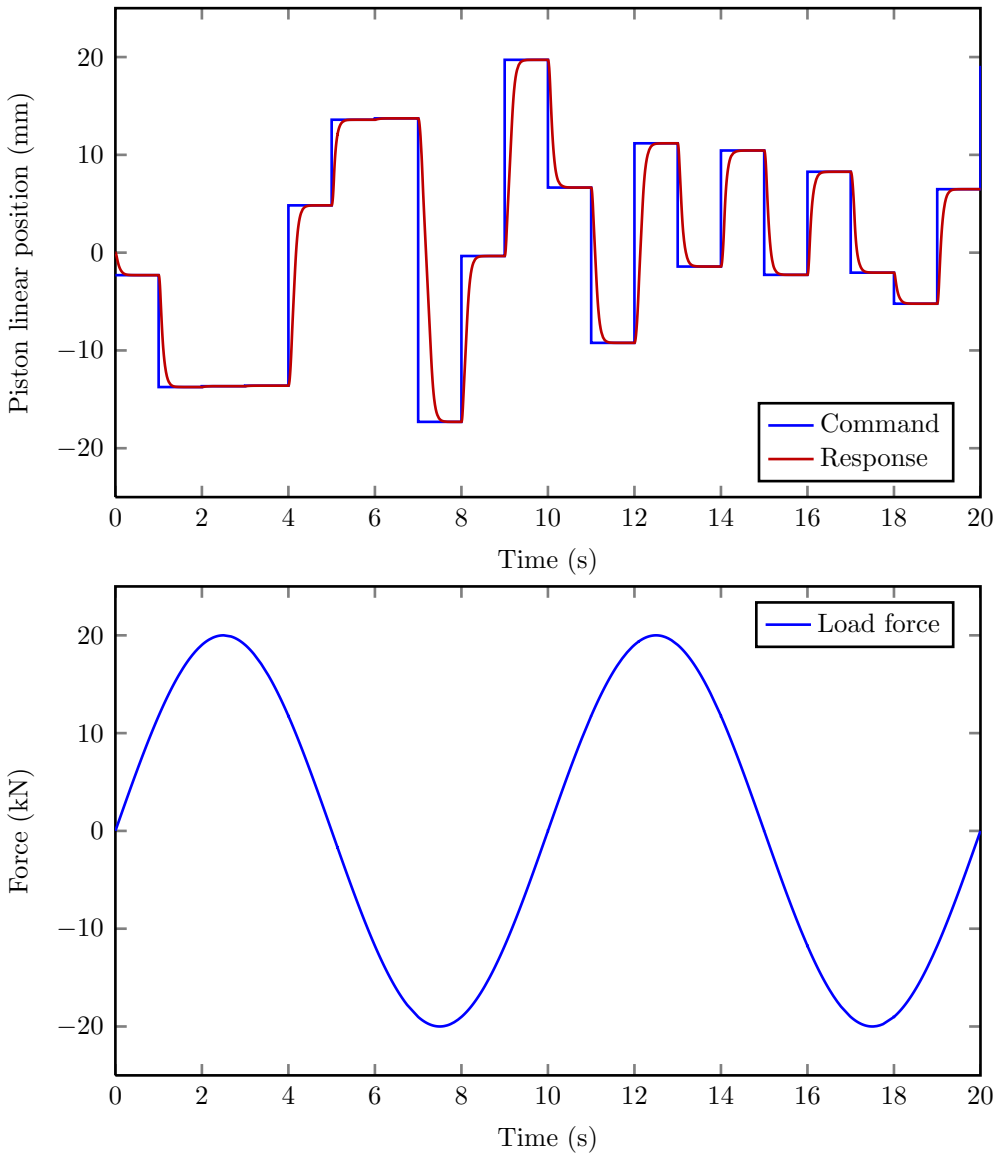

Figure 3.19: Position control of aileron EMA with pseudo-random input commands and 20 kN, 0.1 Hz sinusoidal load force

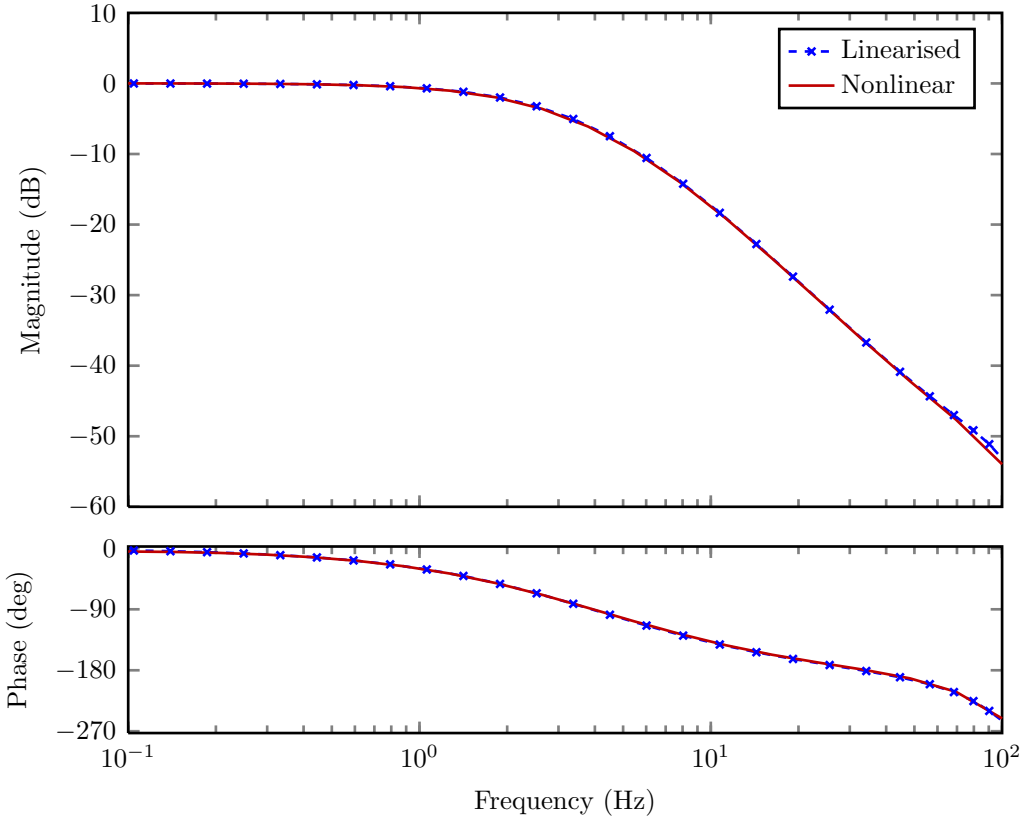

Figure 3.20: Closed loop frequency response of EMA with a ±1 mm sinusoidal position command

3.2.6 Model Validation

This section demonstrates the ability of the EMA model to simulate the dynamic position and power performance of a ball screw based electromechanical actuator. The aim is to lend credence, to the estimates produced by the models in a clear and straightforward manner using diagrams wherever possible.

Since experimental data for the specific actuators modelled is not available, the validation is mostly qualitative with reference to typical performance of other commercially available components.

The open loop performance plots of the three actuators (Figures 3.21 to 3.23) show particular resemblance to the speed-torque curves in the datasheet of the DC motor model [179], with a relatively small linear decrease in speed up to the stall force. The EMA and motor graphs are expected to be similar shapes since the ball screw model is essentially just a gearbox; the speed and force performance of the linear actuator is mostly dependent on the motor's speed and torque performance.

Referring to Table 3.1 in chapter 3 (page 125), the speed-force performance profiles of the actuators in Figures 3.21 to 3.23 meet the specifications required, achieving (in the case of the aileron) a no load linear rate of 90 mm/s and a stall force of 48 kN. The model simulates the nonlinear effect of field saturation as can be seen from the corner around 42 kN, where the limited torque forces a decrease in linear rate as the load force increases beyond saturation. The power curve (product of speed and force) shows the peak power delivered to the load occurs at the point of saturation at 42 kN; correspondingly, the efficiency curve shows the maximum efficiency occurring at the point of stall.

Figures 3.21, 3.22 and 3.23 are generated using a script which executes the dynamic models multiple times while incrementing the load force and recording the achieved steady state linear velocity, current and efficiency. The model is configured with no controller, a fixed input voltage of 270 VDC and is set to run for long enough to allow all transients to settle during each run. The limits on the ball screw position integrator are removed to allow the system to reach steady state without the obstruction of the end stops. Since no post processing is used and the figures are generated from the actual output of the models, Figures 3.21 to 3.23 are considered the basis of the validation.

It can be seen that the actuators meet the no load speed requirement precisely and the stall force exceeds the requirements. This is a result of selecting the closest Parker M series motor which can deliver the required shaft power, which, in the case of the elevator leads to overrating the stall force by a factor of 2. Ideally a motor with a closer power capacity match would be substituted if the electrical and mechanical variables of a suitably high performance motor become available.

The same steady state technique is used to generate the power and efficiency plots in Figure 3.24 and Figure 3.25 which show the closed loop performance across a range of forces and velocities. Inputs to the model are a ramp command with gradient equal to the desired linear velocity (fed in to the position controller) and the load force applied to the actuator.

The field saturation characteristics are visible in Figure 3.25, where the actuator can deliver no extra power at the higher load forces. The closed loop figure also shows the same efficiency curve behaviour as in the open loop model of Figure 3.21, where the highest efficiency occurs at the field saturation point.

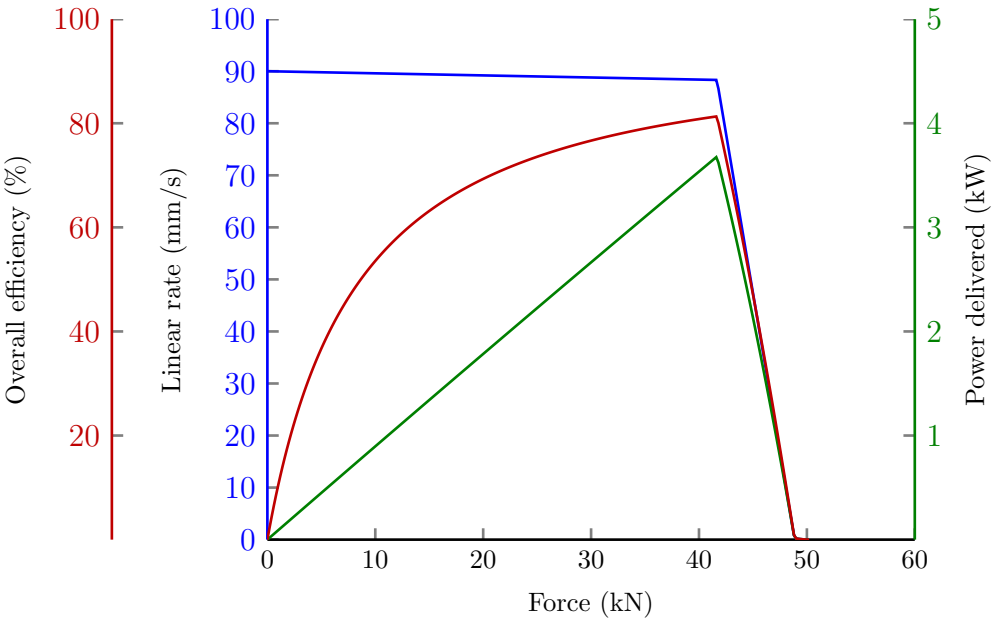

Figure 3.21: Open loop performance characteristics of the aileron EMA

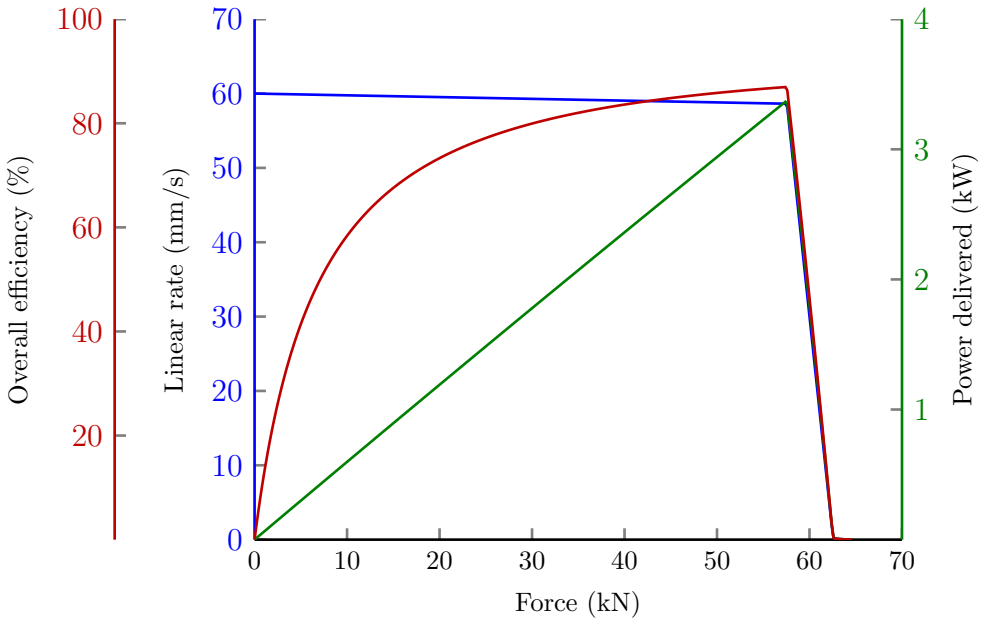

Figure 3.22: Open loop performance characteristics of the elevator EMA

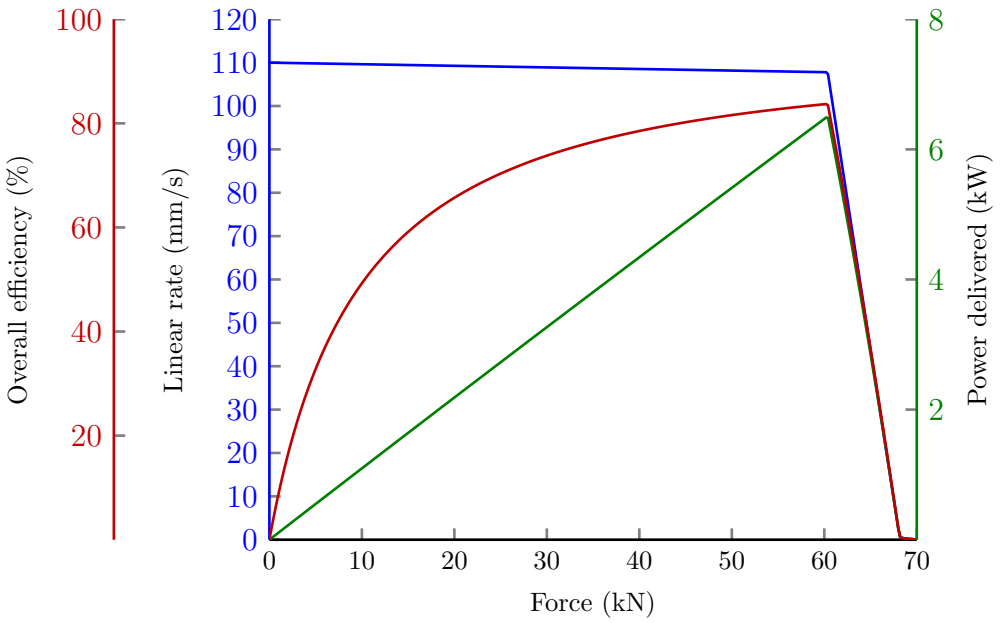

Figure 3.23: Open loop performance characteristics of the rudder EMA

The final part of the validation involves showing some data which demonstrates the ability of the model to calculate intermediate power consumptions as discussed in chapter 3.2.3 (page 170). The closed loop model is used, such that specific linear velocities can be given as an input. When combined with a known load force, the mechanical power at the piston can effectively be specified. This allows an easy comparison of power consumption at each stage of power conversion, originating from a known reference. Tables 3.5 – 3.7 show the results of this experiment at a variety of operating points, with the values taken after all transients have settled.

The last row of each sub table represents an operating point just below the stall condition; the values are selected from the open loop performance charts to ensure the controller output remains unsaturated.

The continuous approximation used to model Coulomb friction shows its weakness in the 1 mm/s case, where the very high ball screw efficiency is

a result of the of the $\tanh(x)$ function crossing through zero at $x = 0$ and giving an abnormally low friction at low speeds.

The results from the table show the EMA reflecting typical efficiencies of the real components, with a high quality ball screw being up to 95% efficient and a precision DC motor between 90-95% efficient. In the case where the user knows specific modelling constants for an actuator (particularly including the friction coefficients), the accuracy could be increased.

Table 3.5: Table showing the power consumption and efficiency for the aileron EMA at a range of operating points

Inputs			Model outputs			Efficiency		
Linear speed (m/s)	Load force (N)	$P = F\dot{x}$ (W)	Mechanical piston power (W)	Power output on motor shaft (W)	Electrical power input (W)	Shaft to piston (%)	Electrical to shaft (%)	Overall (%)
0.000	10000	0	0	0	4.03	-	-	-
0.001	10000	10	10	10.07	16.43	99.30	61.29	60.86
0.050	10000	500	500	676.44	774.05	73.92	87.39	64.60
0.050	40000	2000	2000	2176.4	2347.63	91.89	92.71	85.19
0.080	40000	3200	3200	3651.5	3911.54	87.64	93.35	81.81

Table 3.6: Table showing the power consumption and efficiency for the elevator EMA at a range of operating points

Inputs			Model outputs			Efficiency		
Linear speed (m/s)	Load force (N)	$P = F\dot{x}$ (W)	Mechanical piston power (W)	Power output on motor shaft (W)	Electrical power input (W)	Shaft to piston (%)	Electrical to shaft (%)	Overall (%)
0.000	10000	0	0	0	2.38	-	-	-
0.001	10000	10	10	10.07	15.43	99.30	65.26	64.81
0.050	10000	500	500	676.44	815.21	73.92	82.98	61.33
0.050	50000	2500	2500	2676.4	2884.65	93.41	92.78	86.67
0.058	57000	3306	3306	3543.4	3801.81	93.30	93.20	86.96

Table 3.7: Table showing the power consumption and efficiency for the rudder EMA at a range of operating points

Inputs			Model outputs			Efficiency		
Linear speed (m/s)	Load force (N)	$P = F\dot{x}$ (W)	Mechanical piston power (W)	Power output on motor shaft (W)	Electrical power input (W)	Shaft to piston (%)	Electrical to shaft (%)	Overall (%)
0.000	10000	0	0	0	3.68	-	-	-
0.001	10000	10	10	10.07	17.82	99.30	56.51	56.12
0.050	10000	500	500	676.44	801.28	73.92	84.42	62.40
0.050	40000	2000	2000	2176.4	2369.52	91.89	91.85	84.41
0.100	60000	6000	6000	6705.2	7124.6	89.48	94.11	84.22

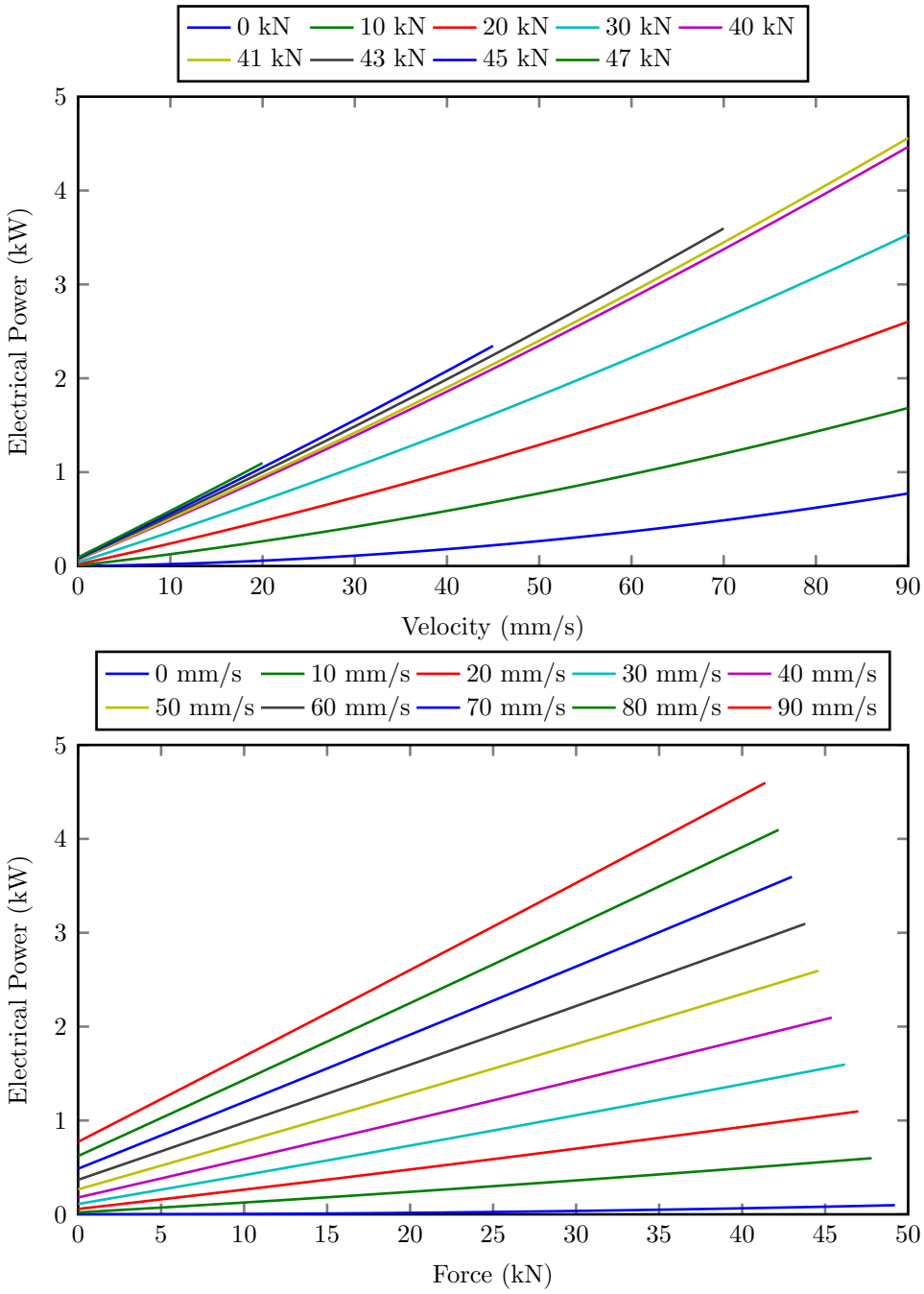

Figure 3.24: Total steady state electric power of the aileron EMA measured at power supply (excluding supply efficiency), as a function of force and velocity

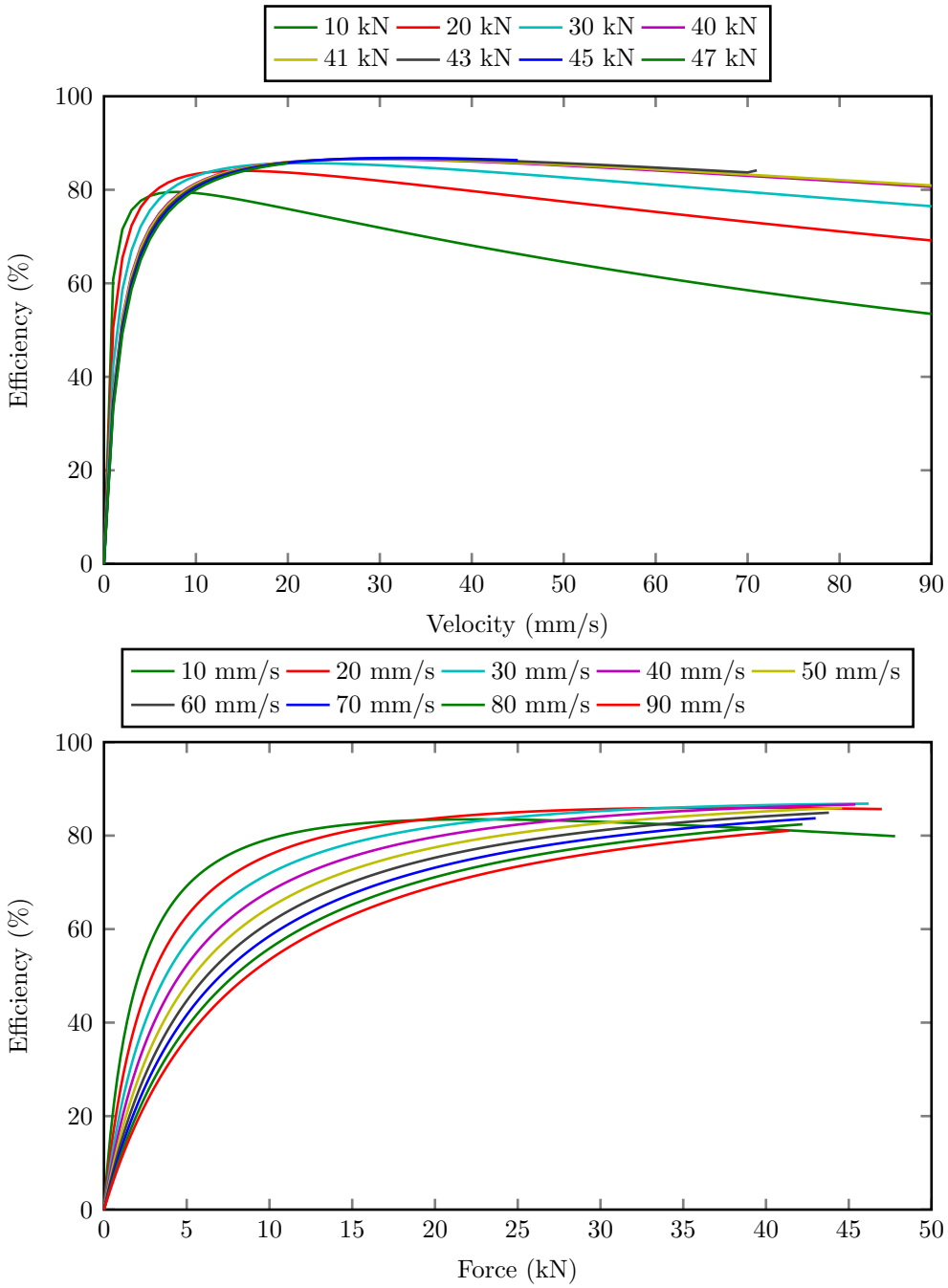

Figure 3.25: Efficiency curves (output mechanical power/input electrical power) as a function of load and speed for the aileron EMA

3.3 Electro-hydrostatic Actuation System

Electrohydrostatic actuators (EHAs) take electric energy from an electrical power bus and convert it to hydraulic energy by using a directly connected motor (in this case a permanent magnet DC motor) and (most commonly) a fixed displacement hydraulic pump. Due to the physical connection between the motor and pump, both components rotate at the same speed and thus flow rate is controlled by the angular velocity of the motor. By controlling the motor speed and torque, the actuator can follow time varying position commands with time varying load forces.

There is a significant advantage to this; when servo valves are used a significant amount of pressure is lost across the valve, meaning a larger piston area is required to achieve a given force than it would be from an EHA. This is because the EHA can receive the full 3000 psi at the cylinder, while the hydraulic system works most efficiently when ⅔ of the supply pressure is dropped across the cylinder.

Each component has its own sources of power loss; in common with the EMAs are the electrical effects such as heating and magnetic flux leakage, but also included are fluidic losses such as the viscosity of the fluid and leakages around the pump and cylinder moving parts. This model seeks to provide an estimate of the electrical power consumption when a time varying load force and position response is demanded of it.

The model is constructed by reusing the DC motor of section 3.2.1 (page 161) with some slight changes to how the load inertia is handled, combined with the hydraulic cylinder model in section 3.1.1 (page 3.1.1). Only the relevant parts of these components will be described in this section which highlight the changes made for the EHA, for more detail the user should

refer to the previous chapters as mentioned.

3.3.1 DC Motor Model

To allow easy comparisons to be made between the EMA and EHA technologies, it is chosen to construct both actuators around the same DC motors where possible. The motor model used for the EHA is identical to the model derived in section 3.2.1 (page 161), except that the inertia in equation (3.48) is chosen to include only the rotor inertia of the motor J_m. In this model the acceleration of the load mass is handled separately to the inertia of the motor and thus does not need to be included in the motor model. The load torque on the motor due to linear acceleration of the load mass is fed back to the motor through the counter torque input from the hydraulic circuit model.

3.3.2 Fixed Displacement Pump

Unlike the classical hydraulic actuators of chapter 3.1 (from page 128), EHAs have a small localised pump which directly controls the fluid flow to the cylinder via a hydrostatic transmission. It is possible to use either fixed or variable displacement pumps in this situation but most common EHA designs use a fixed displacement pump attached to a variable speed servo motor. This method requires precision control of the motor but has the advantage of reducing the complexity of the actuator and reducing power consumption. This is particularly evident at low load because the motor does not have to spin at a constant velocity at all times to maintain the system pressure.

Since the motor is rigidly connected to the pump the torque on the pump due to the pressure difference across it must equal the torque on the motor.

The fixed displacement pump flow rate is modelled as a linear function of the angular velocity ω_a (with no losses):

$$Q_p = D\omega_a \tag{3.66}$$

where D is the pump displacement. The pump will have a leakage flow caused by the pressure differential that the pump induces. This is modelled using equation (3.19):

$$Q_{12} = C_{12}(P_1 - P_2) \tag{3.67}$$

To reduce duplication in the model, the coefficient C_{12} is chosen to be the sum of the pump and piston leakage coefficients as they are both functions of the pressure difference:

$$C_{12} = C_{pump} + C_{piston} \tag{3.68}$$

3.3.3 Hydraulic Cylinder Model

The hydraulic cylinder and piston models are functionally identical to the model described in chapter 3.1.1 (on page 131), with an additional function to calculate the load torque on the motor due to the pressure in the cylinder.

The cylinder equation (3.20) is applicable with minor modification to the EHA cylinder. Given that the cylinder is now powered directly from a pump the input flow at the cylinder Q_i in equation (3.20) can be replaced with the equation for pump flow in (3.66) and combined leakage coefficients in equation (3.68):

$$\frac{d\left(P_1 - P_2\right)}{dt} = \left(2D\omega_a - 2C_{12}\left(P_1 - P_2\right) - 2\dot{x}A\right)\frac{\beta_e}{V} \tag{3.69}$$

Once integrated, equation (3.69) gives the pressure difference across the cylinder; which also induces a torque on the pump and motor, calculated using the pump displacement and pump efficiency η_p:

$$T_L = \frac{D}{\eta_p}\Delta p \tag{3.70}$$

3.3.4 Steady State Behaviour

The steady state model of the EHA has the same purpose and limitations as those discussed for the ESHA in chapter 3.1.4 (page 140). The motor model is identical to that used in the EMA defined in chapter 3.2.3 (page 170) and will not be repeated here.

The fixed displacement pump output flow rate is calculated using the same equation (3.66) as the dynamic model. The load torque on the motor is calculated using equation (3.70).

The hydraulic cylinder is the same as the ESHA cylinder covered in equations (3.26) and (3.27).

3.3.5 Power Consumption

The EHA model allows for the calculation of power at every stage of energy conversion, from electrical input to linear mechanical output using

the equations given below.

$$P_{electrical} = VI = \frac{P_{motor}}{\eta_m} \tag{3.71}$$

$$P_{motor} = T\omega = \frac{P_{fluid}}{\eta_p} \tag{3.72}$$

$$P_{fluid} = \Delta P Q_L = \frac{P_{piston}}{\eta_c} \tag{3.73}$$

$$P_{piston} = F\dot{x} \tag{3.74}$$

where η_m is the efficiency of the motor, η_p is the efficiency of the pump and η_c is the efficiency of the hydraulic cylinder.

The main value of interest is the electrical power, but the other values give a valuable verification of the correct functioning of the model. Equations (3.71) – (3.74) are listed in the direction of power flow, so if the actuator is dissipating a known power (e.g. moving 1000 N at 1 mm/s, i.e. 1 Watt), the powers back through the system should increase by the typical efficiency factor of that particular conversion. The difference between the electrical power in and the mechanical power out will represent the efficiency of the whole actuator.

3.3.6 Position Control

The controller used for the EHA is identical to that used for the ESHA so it will not be covered in detail again. Simply stated, the actuator employs a PIV controller with load force feedforward, as detailed in the ESHA and EMA control sections 3.1.6 (page 144) and 3.2.5 (page 173). The position response achieved under sinusoidally varying loads can be seen in Figure 3.26.

The frequency response of the complete actuator is shown in Figure 3.27, the -3 dB bandwidth occurs at around 3.5 Hz and the model exhibits a 40

dB/decade roll off in the frequency range of interest.

3.3.7 Model Validation

The validation for the electro-hydrostatic actuator begins with testing the open loop speed-force performance of the motor at a fixed supply voltage of 270 VDC. The results can be seen in Figures 3.28 to 3.30; the actuators behave as expected, with a linear decrease in achieved linear velocity as the load force increases (due to leakage). The instant drop at around 52 kN on the aileron is caused by the hydraulic circuit saturating at 3000 psi; the pressure release valves open and discard all excess fluid back to the tank.

Initially the aileron EHA actuator was given the same motor (M1054K) as the aileron EMA, but due to the increased losses in the hydraulic circuit the actuator did not meet the stall torque requirements. For this reason, the next size up motor (M1453L) has been substituted to obtain the capacity required.

Comparing Figure 3.28 with the requirements in section 3 (page 125), the aileron EHA can achieve a load rate of 90 mm/s and exceeds the required stall torque of 48 kN. The peak efficiency occurs at the stall force (and maximum output power point), in this case 52 kN.

Figure 3.29 and Figure 3.30 show the open loop performance of the elevator and rudder actuators which can be compared to the A320 specification in chapter 3 (page 125) to verify the models meet the requirements.

Once the open loop performance is known, the position controller is enabled and graphs of how power consumption varies with the speed of travel and load applied are generated. Figure 3.28 shows the performance of the aileron EHA up until stall; in the linear region before stall the behaviour is similar to the EMA of chapter 3.2 (page 161). After stall, the actuators be-

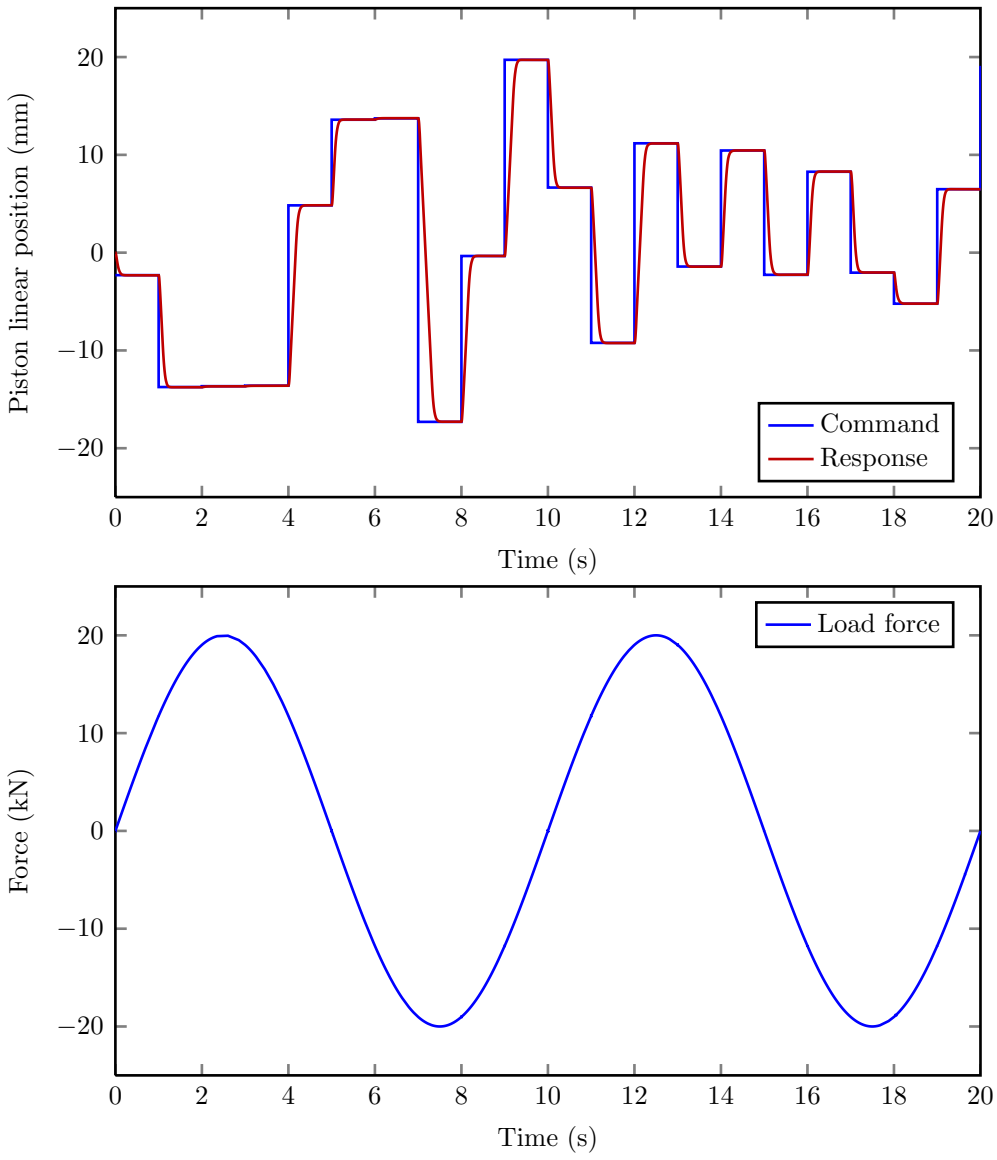

Figure 3.26: Position control of the aileron EHA with pseudo-random input commands and 20 kN, 0.1 Hz sinusoidal load force

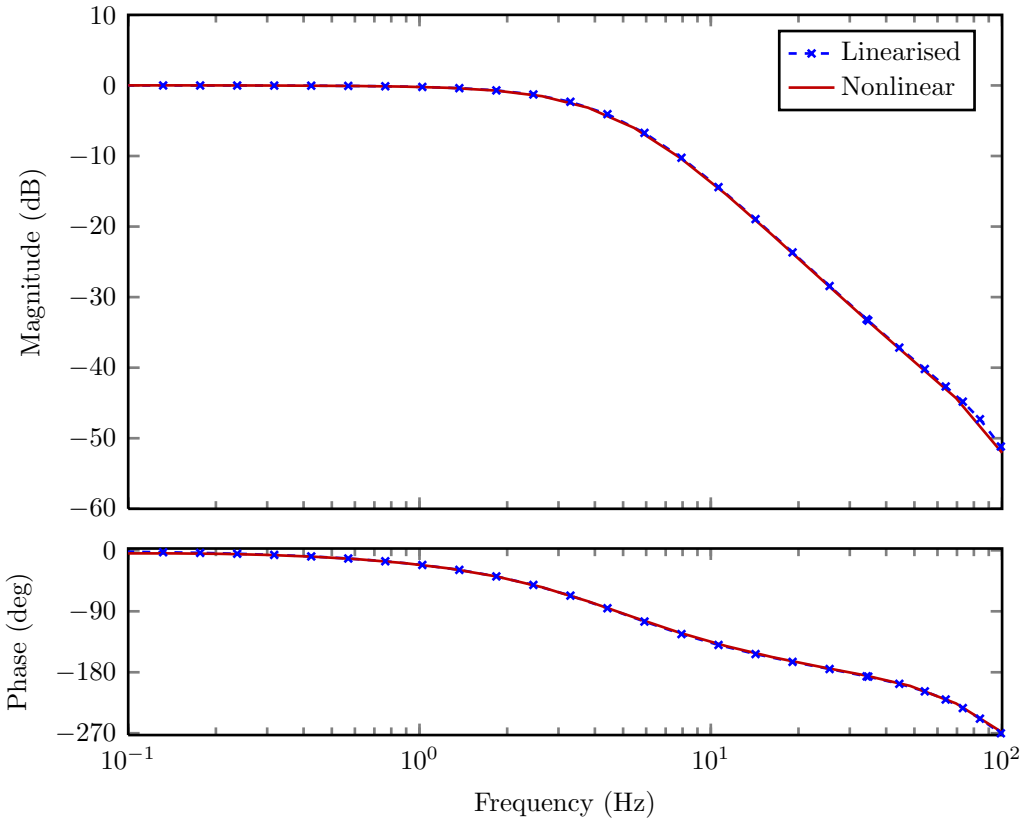

Figure 3.27: Closed loop frequency response of EHA with a ±1 mm sinusoidal position command

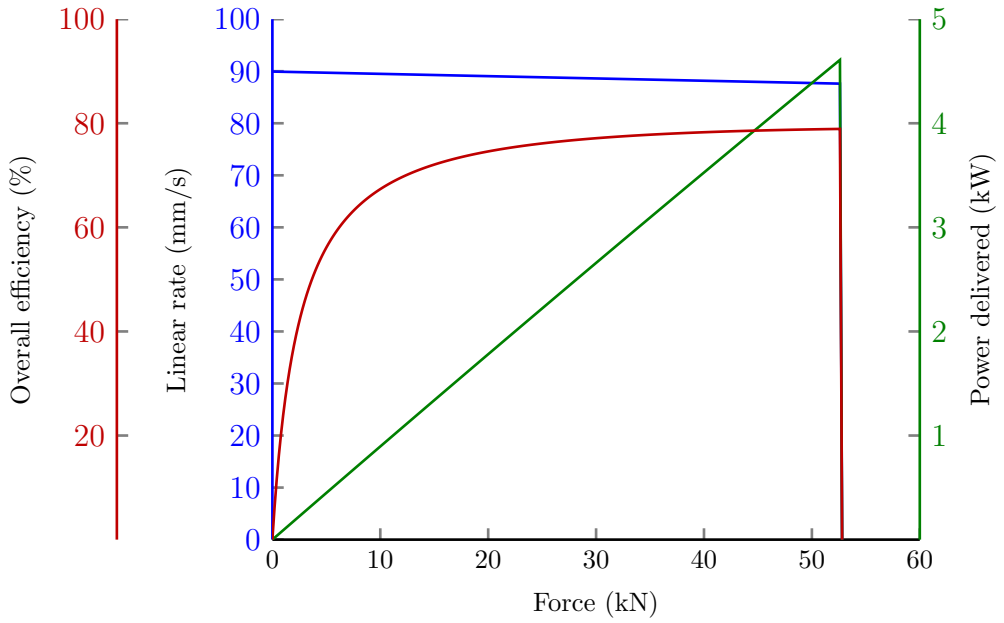

Figure 3.28: Open loop performance characteristics of the aileron EHA

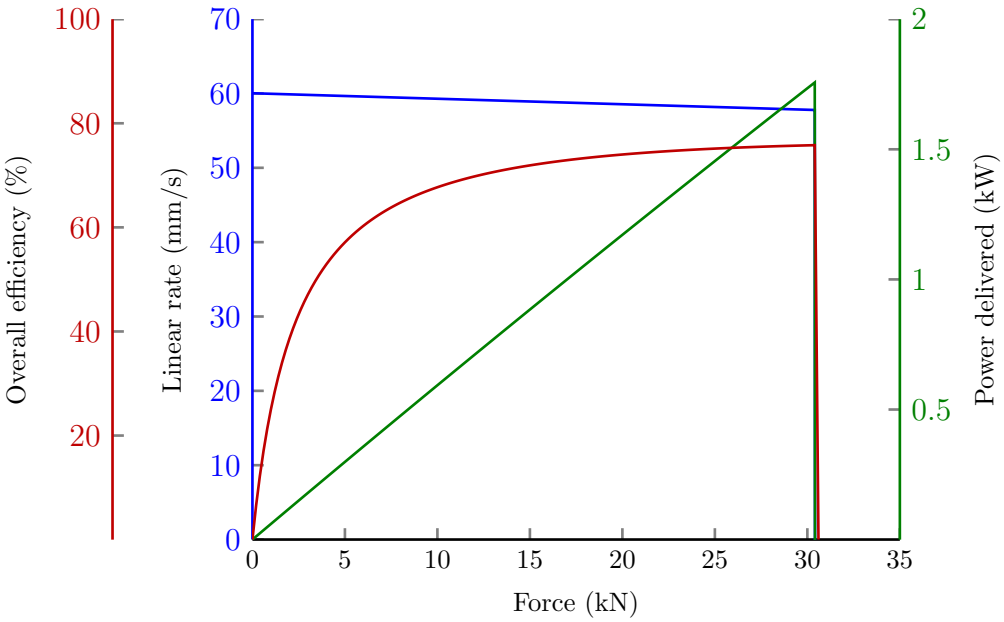

Figure 3.29: Open loop performance characteristics of the elevator EHA

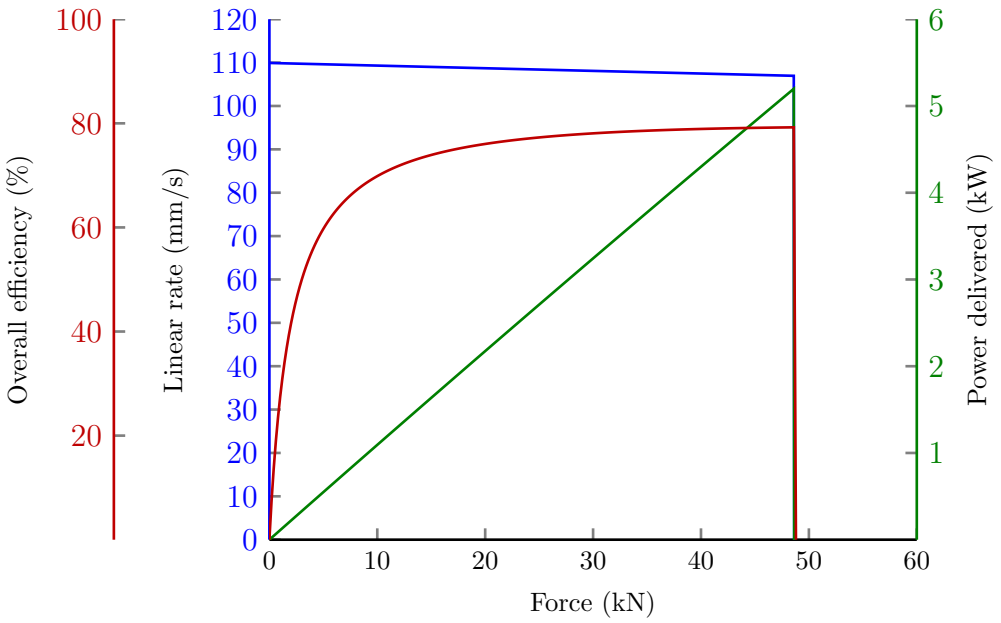

Figure 3.30: Open loop performance characteristics of the rudder EHA

have differently; the EHA only stalls because the hydraulic circuit is limited to 3000 psi. Since the counter torque on the motor is directly proportional to the pressure in the system, it follows that the counter torque is also limited by the pressure limit.

In the case of the oversized motor used for the aileron EHA, the maximum load torque that can be applied by the hydraulic circuit is below the stall torque of the motor. The force response in Figure 3.31 shows the stall point for all velocities occurring at almost the same value, which is consistent with the hydraulic pressure saturation explanation given above. Since the pressure in the cylinder is generated by the load force (and vice versa), it is expected to see this common stall force at all velocities for a particular cylinder.

Figure 3.32 shows how the efficiency of the actuator changes across its operational envelope, highlighting the optimum efficiency at the stall force as seen in the open loop response (although it does vary with speed). Coupling

this with the increasing efficiency as velocity increases, it can be deduced that the EHA is most efficiently operated at a high linear rate and high load. This is attributed to the motor used, which sees a particularly low reduction in speed throughout its torque range. If a lower quality cylinder with greater leakages is used, it is possible for the efficiency plot to reach a maximum somewhere in the middle of the force range and to be decreasing again by the time the stall force is reached.

The final part of the validation involves demonstrating the ability of the EHA model to produce realistic estimates of intermediate power conversions between the input and output stages. For the EHA, this means tabulating the output from four power flows at several operating points to see if the estimated efficiencies are realistic. The data given in Tables 3.8 – 3.10 show how the power loss is distributed between the components.

Table 3.8: Table showing the power consumption and efficiency for the aileron EHA at a range of operating points

Inputs			Model outputs				Efficiency			
Linear speed (m/s)	Load force (kN)	$P = F\dot{x}$ (kW)	Mech. piston power (W)	Fluid power at cylinder (W)	Mech. power at motor shaft (W)	Elec. power input (W)	Fluid to piston (%)	Shaft to cylinder fluid (%)	Elec. to shaft (%)	Overall (%)
0.000	10	0	0	2	2	6	0.00	84.53	28.37	0.00
0.000	40	0	0	25	29	91	0.00	84.98	31.73	0.00
0.001	10	0.01	10	12	14	22	86.73	84.97	62.16	45.81
0.050	10	0.5	500	502	590	739	99.62	85.00	79.87	67.63
0.050	45	2.25	2250	2281	2684	2906	98.62	85.00	92.37	77.43
0.080	50	4	4000	4039	4752	5085	99.03	85.00	93.46	78.67

Table 3.9: Table showing the power consumption and efficiency for the elevator EHA at a range of operating points

Inputs			Model outputs				Efficiency			
Linear speed (m/s)	Load force (kN)	$P = F\dot{x}$ (kW)	Mech. piston power (W)	Fluid power at cylinder (W)	Mech. power at motor shaft (W)	Elec. power input (W)	Fluid to piston (%)	Shaft to cylinder fluid (%)	Elec. to shaft (%)	Overall (%)
0.000	10	0	0	5	5	11	0.00	85.06	50.37	0.00
0.000	30	0	0	41	49	84	0.00	85.00	57.77	0.00
0.001	10	0.01	10	15	17	24	68.45	84.99	70.22	40.85
0.050	10	0.5	500	505	594	733	99.01	85.00	81.01	68.18
0.050	20	1	1000	1019	1199	1351	98.15	85.00	88.72	74.02
0.040	30	1.2	1200	1242	1461	1600	96.64	85.00	91.32	75.02

Table 3.10: Table showing the power consumption and efficiency for the rudder EHA at a range of operating points

Inputs			Model outputs				Efficiency			
Linear speed (m/s)	Load force (kN)	$P = F\dot{x}$ (kW)	Mech. piston power (W)	Fluid power at cylinder (W)	Mech. power at motor shaft (W)	Elec. power input (W)	Fluid to piston (%)	Shaft to cylinder fluid (%)	Elec. to shaft (%)	Overall (%)
0.000	10	0	0	2	2	9	0.00	84.91	24.91	0.00
0.000	40	0	0	29	34	124	0.00	85.02	27.32	0.00
0.001	10	0.01	10	12	14	24	84.75	85.01	58.69	42.28
0.050	10	0.5	500	502	591	714	99.57	85.00	82.69	69.98
0.050	45	2.25	2250	2287	2690	2920	98.39	85.00	92.13	77.05
0.100	40	4	4000	4030	4742	5076	99.25	85.00	93.42	78.81

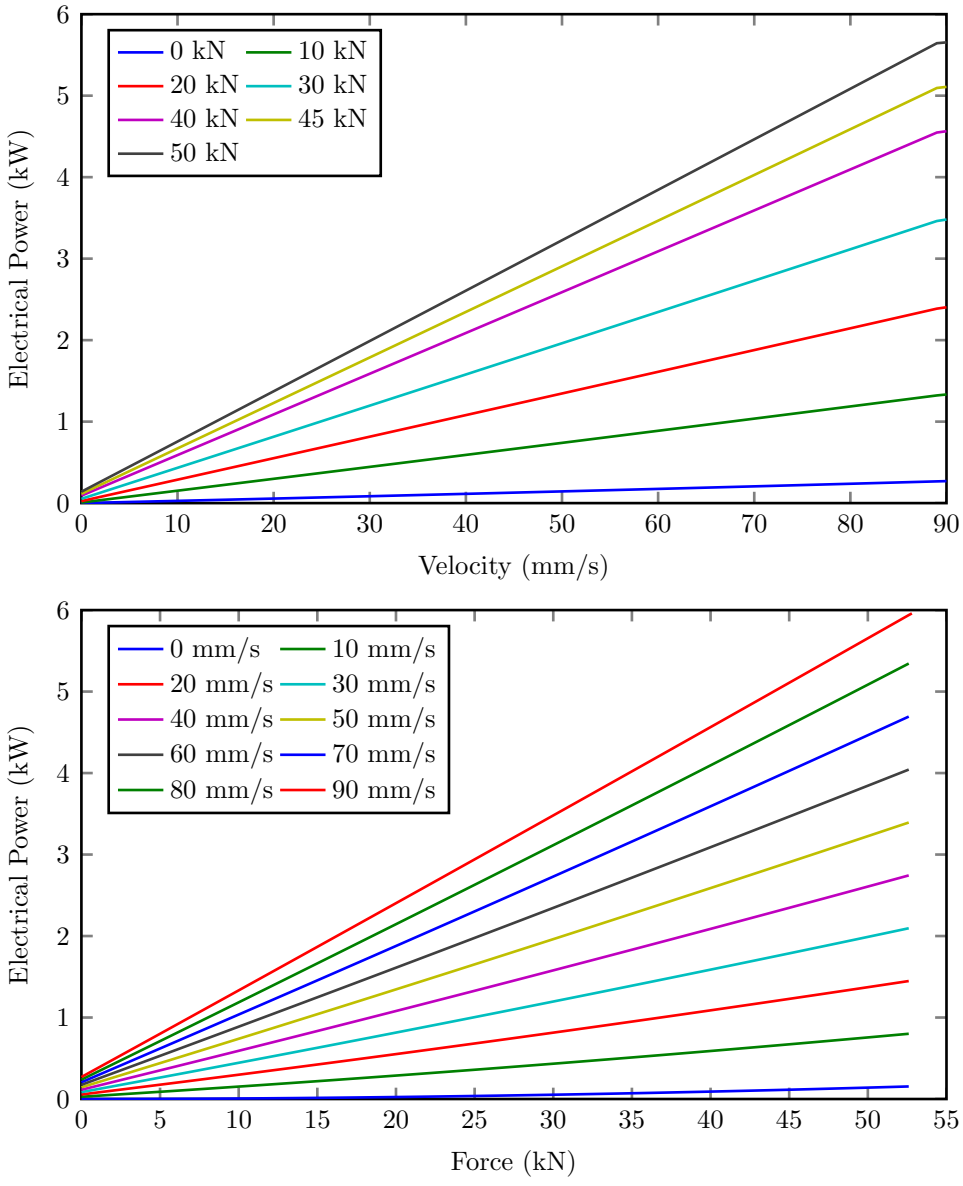

Figure 3.31: Total steady state electric power of the aileron EHA measured at the power supply (excluding supply efficiency), as a function of force and velocity

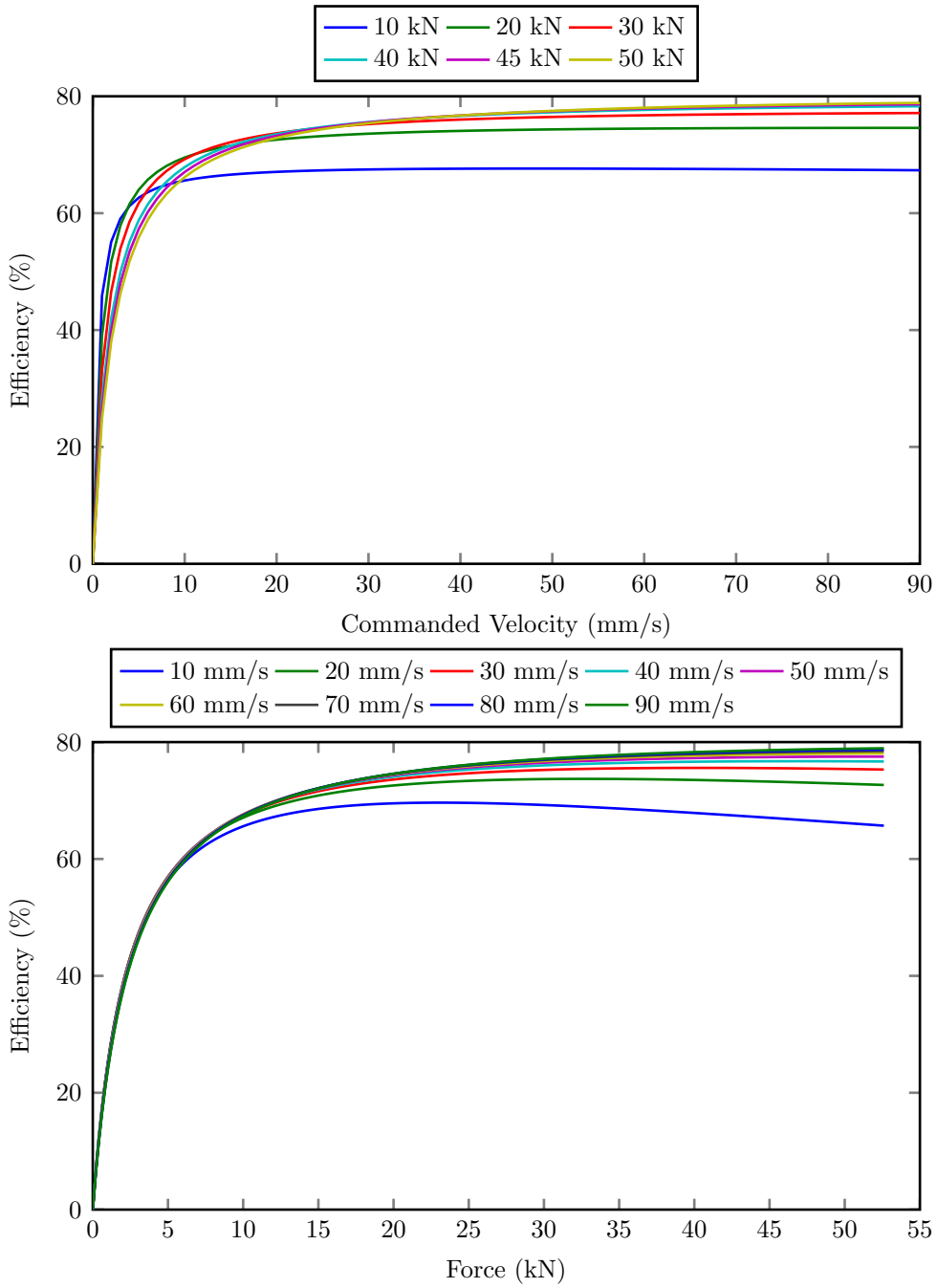

Figure 3.32: Efficiency curves (output mechanical power/input electrical power) as a function of load and speed for the aileron EHA

3.4 Role of the Servo Valve and Power Electronics

This work considers the hydraulic actuator as a complete system consisting of the cylinder and hydraulic servo valve. On the other hand, the electric actuators model the motor and the cylinder/roller screw, but do not include the power electronics. The power electronics perform the same function as the hydraulic servo valve; it regulates a 115 V, 400 Hz three phase AC bus into a three phase variable voltage signal which controls the speed and torque of the motor. This also translates into velocity and force control at the linear output of the actuators.

Hydraulic servo valves regulate a (for example) 3000 psi supply pressure into a flow rate through a cylinder and through fluid compressibility, pressure across the cylinder. The most significant performance difference between the fluidic and electric converters in flight control applications is the off state losses. Servo valves require a minimum amount of clearance and lubrication between the spool and the case to ensure a long mechanical lifetime, meaning a constant leakage flow when blocking 3000 psi. Additionally, there is a constant leakage flow due to the pilot flow in the flapper-nozzle spool position controller. Conversely, power electronic converters have very low current leakage during the off state, meaning power is only consumed when necessary to move the control surfaces.

The lack of a servo drive in the electric actuator models can affect the results considerably; depending on the on state resistance, current flow through the device and switching losses, the power losses in the servo drive can be significant. To quantify the potential losses in the power electronics, the design tool IPOSIM provided by IGBT manufacturer Infineon is used to compute the losses in the three phase inverter. IPOSIM is used to specify an inverter

which can supply 30 A from a 600 VDC bus; the results for the Infineon FP40R12KE3 three phase inverter are shown in Figure 3.33.

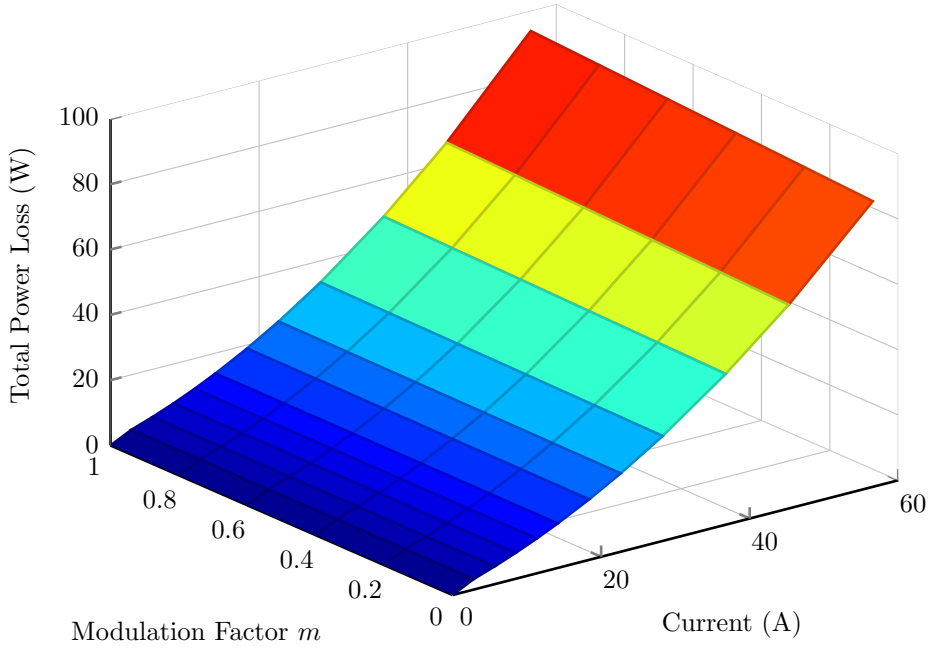

Figure 3.33: Power losses of an Infineon FP40R12KE3 three phase IGBT inverter with flyback diodes. DC link voltage = 600 V, Switching frequency = 2 kHz, Current phase lag $\cos(\phi) = 0.8$

The rectifier that converts the three phase AC aircraft supply to a DC bus contains six diodes and is included in the same package as the inverter switches and diodes in the Infineon FP40R12KE3. The three phase rectifier loss computations include the forward voltage drop and i^2r heating losses and is computed using:

$$P_{Dr} = 6\left(\frac{V_F}{3} I_{DC} + \frac{R_F}{3} I_{DC}^2\right) \tag{3.75}$$

where P_{Dr} is the power loss in the rectifier bridge, V_F is the forward voltage drop, I_{DC} is the current required on the DC bus and R_F is the on-state resistance of the diodes and connecting leads. The power loss of the rectifier

is shown in Figure 3.34. The combined power loss of the complete power electronics including rectifier and inverter is shown in Figure 3.35.

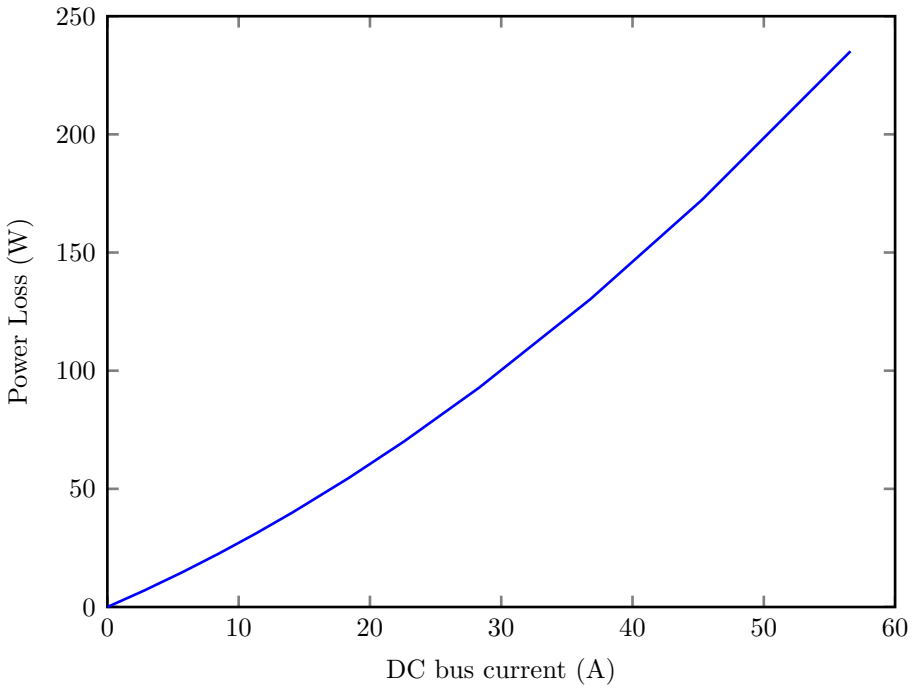

Figure 3.34: Power losses of an Infineon FP40R12KE3 three phase bridge rectifier. Forward voltage drop = 1.2 V, Diode + lead resistance = 15.5 mΩ

The lookup table method is used here to give a quick estimate of power converter losses; using a manufacturer provided tool is a reliable method to obtain correct results. However, the Excel based tools do not lend themselves to easy integration with a Simulink model. To program a native language version, the equations can be sourced from the work presented by Maré [3].

The results in this section are intended to give some quantification of the change in results that may be evident if the electric power converters were included in this work. At high currents the power converter losses can be high, at 30 A the total power loss is around 150 W. Any future work should seek to include these major losses either through the lookup table method used here or by explicit modelling of the dominant physical effects.

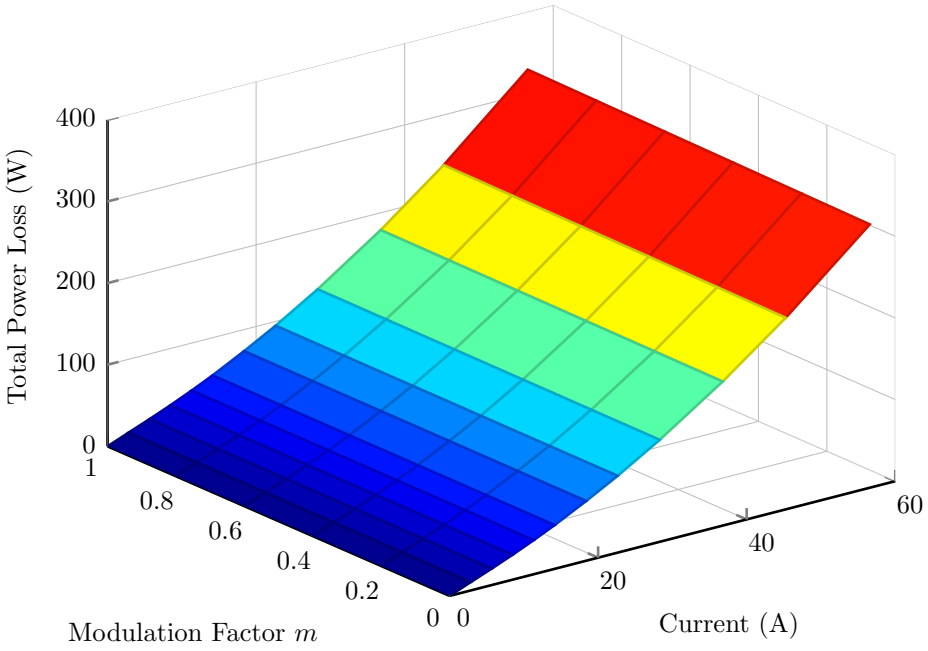

Figure 3.35: Total power losses of an Infineon FP40R12KE3 inverted + rectifier operating with a current phase lag of 0.8

3.5 Sensitivity Analysis

The mathematical models of the actuators contain a significant amount of uncertainty which can only be reduced by validating against experimental data. Uncertainty can never be reduced to zero since even the measurements of a hardware system contain error related to the tolerance of their components. What is important is knowing where the uncertainty lies and to what degree the output error depends on each unknown.

This section investigates the effect uncertainty in the parameter variables has on the power consumption estimates that are used in this thesis. Some parameters are taken from manufacturer datasheets which do not always state the tolerance of the data, others are derived from approximations of friction which are not necessarily true to the real world physics.

This section performs a parameter sweep on the component data such as

resistance and friction coefficients, varying each value by ±10% and recording the power output for the complete actuator. The aileron actuators are commanded to extend at 45 mm/s while exposed to a 24 kN load force; the stroke limit is removed to allow the models to be run for long enough that the transients subside. The power consumptions using unmodified parameters are plot as the baseline and the ±10% parameters presented as error bars in Tables 3.11 - 3.16 and Figures 3.36 - 3.41.

3.5.1 ESHA Parameter Sensitivity

The first two figures show the sensitivity of the aileron ESHA power consumption estimate to variations in the servo valve (Figure 3.36) and hydraulic cylinder parameters (Figure 3.37). The simplicity of the servo valve model means there is only one parameter which can be varied to assess its effect on the power consumption, the return pressure. Varying this parameter has no effect on the actuator level power consumption however, as shown in Table 3.11 and (Figure 3.36).

The cylinder has much more scope for variation with five variables, listed in Table 3.12. The fluid compressibility B_e has no effect on the steady state power consumption since it affects the properties of the oil spring and therefore manifests itself in dynamic motion only. C_{12} creates a 0.08% error in the system since it directly modifies the amount of leakage flow past the piston; if the actuator was to hold a constant position a 10% increase in leakage coefficient would lead to a 10% increase in total power consumption. However, when the actuator is commanded to have a none-zero linear velocity the leakage flow effect is significantly reduced. The piston area A_c has the most significant effect on the overall power consumption, driving a 9.84% increase in total power consumption. An increase in piston area leads to an

Table 3.11: Sensitivity of ESHA servo valve power consumption estimate to variation in parameter P

Parameter	Power (W)	Abs. Error (W)		Max. Error (%)
		+10% P	-10% P	
P_r	2395.45	0.00	0.00	0.00

Table 3.12: Sensitivity of ESHA cylinder power consumption estimate to variation in parameter P

Parameter	Power (W)	Abs. Error (W)		Max. Error (%)
		+10% P	-10% P	
B_e	2395.45	0.00	0.00	0.00
C_{12}	2395.45	1.95	-1.95	0.08
A_c	2395.45	235.83	-235.44	9.84
M	2395.45	0.00	0.00	0.00
$B_{v_{cyl}}$	2395.45	0.00	0.00	0.00

increase in losses in this experiment because the amount of fluid flow required to achieve a specified piston velocity increases; this leads to greater losses in the actuator.

The piston mass M also only affects power consumption during dynamic motion since it is only during acceleration that the actuator experiences an additional force due to mass. The friction in the cylinder $B_{v_{cyl}}$ does however affect the power consumption, but it is insignificant and does not register any change when presented to two decimal places.

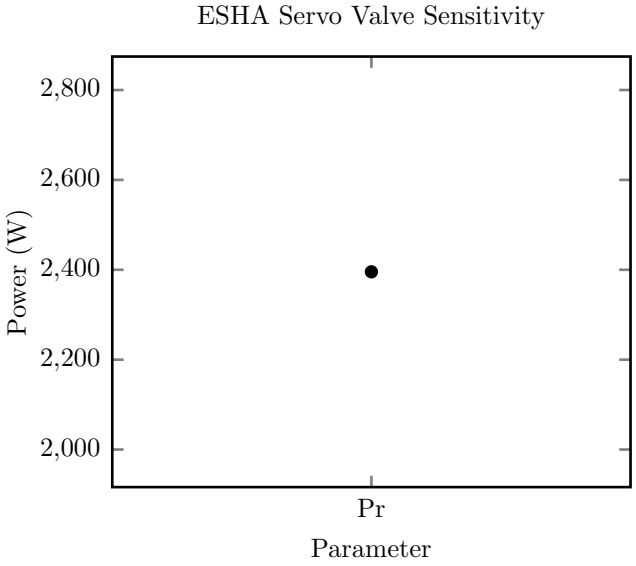

Figure 3.36: Parameter sensitivity of aileron ESHA valve model

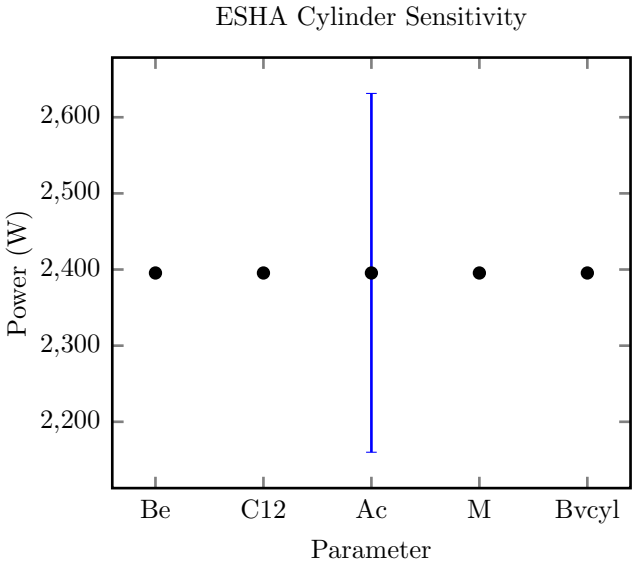

Figure 3.37: Parameter sensitivity of aileron ESHA actuator model

3.5.2 EMA Parameter Sensitivity

The motor powering the EMA has six parameters which are examined in Table 3.13 and Figure 3.38. Variance in the winding resistance R of 10% causes a 0.25% change in power consumption estimate. The viscous friction B_v and Coulomb friction C_{oul} combined have a greater effect on power loss at 0.18% and 0.43% respectively, which increase with increasing actuator velocity. The greatest effect on power consumption is produced by the torque constant K_t (and also the numerically equal back e.m.f constant) at 11.42%. The dynamic parameters L and J_m have no effect on the steady state power consumption estimation since they require a changing current or accelerating motor to produce none-zero power losses.

Table 3.14 and Figure 3.39 present the results of the parameter sweep on the ball screw. Again, several parameters only have an influence during dynamic motion, namely the screw material spring constant K_m and the screw and load masses M_S and M_L. The change in power consumption estimate from these variables is therefore zero.

The friction components B_{vs} and C_{oul} are the dominant sources of power loss estimation error in the moving actuator, contributing 0.81% from viscous friction and 0.32% from Coulomb friction coefficients. The lead screw gearing ratio or pitch p introduces a 0.4% error to the actuator level power consumption estimate assuming a 10% error in the characterising input variable.

Table 3.13: Sensitivity of EMA motor power consumption estimate to variation in parameter P

Parameter	Power (W)	Abs. Error (W)		Max. Error (%)
		+10% P	-10% P	
R	1333.56	3.36	-3.36	0.25
L	1333.56	-0.00	-0.00	0.00
B_v	1333.56	2.36	-2.36	0.18
K_t	1333.56	-124.01	152.33	11.42
J_m	1333.56	-0.00	-0.00	0.00
C_{oul}	1333.56	5.72	-5.72	0.43

Table 3.14: Sensitivity of EMA screw power consumption estimate to variation in parameter P

Parameter	Power (W)	Abs. Error (W)		Max. Error (%)
		+10% P	-10% P	
p	1333.56	-2.32	5.38	0.40
K_m	1333.56	-0.00	-0.00	0.00
M_S	1333.56	-0.00	-0.00	0.00
M_L	1333.56	0.00	-0.00	0.00
B_{vs}	1333.56	10.82	-10.82	0.81
C_{oul}	1333.56	4.21	-4.21	0.32

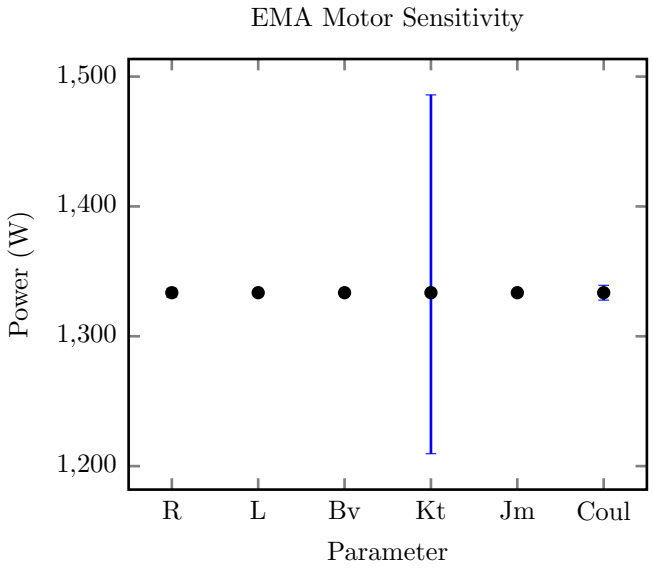

Figure 3.38: Parameter sensitivity of aileron EMA motor model

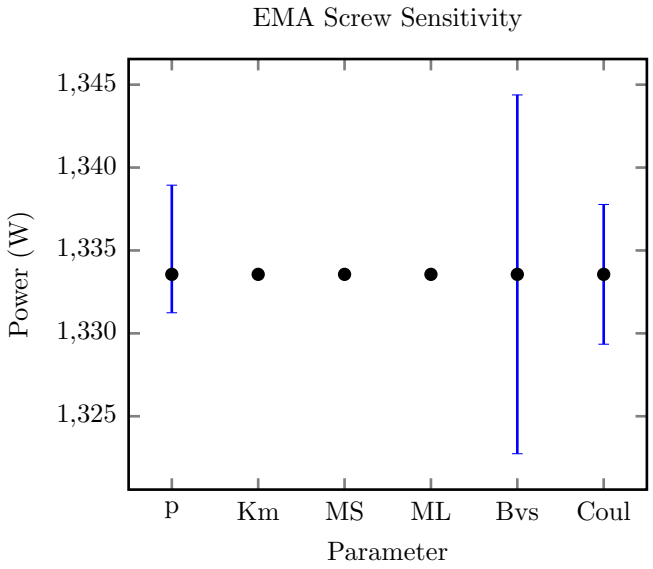

Figure 3.39: Parameter sensitivity of aileron EMA screw model

3.5.3 EHA Parameter Sensitivity

The EHA aileron motor sensitivity analysis shows a different response to the EMA motor. This is because the EHA aileron motor is over-motored and therefore operates at a relatively low load torque compared to its operating envelope. As seen in the electric actuator efficiency plots in sections 3.2.6 and 3.3.7, the efficiency of a DC motor is low at low load forces. This is because Coulomb friction C_{oul} and resistance R have a strong effect on the losses compared to higher loads, where the torque/back e.m.f. constant K_t plays a dominant role.

In this operating condition the EHA power consumption estimations experience a 0.16% error due to uncertainty in the motor winding resistance R, a 0.04% error due to the viscous friction parameter B_v and 0.89% contributed by the Coulomb friction C_{oul}. As discussed previously, these loss values are significantly higher than those seen in Figure 3.38 because of the oversized motor in the aileron EHA; on the other hand the induced error on the power consumption by the torque/back e.m.f. constants is a comparatively low 0.39%.

As mentioned previously in the EMA section, the motor winding inductance and rotor inertia have a zero contribution to power consumption error, because their values equate to zero in steady state. In dynamic motion the power consumption error added by the inductance L and inertia J_m would become none-zero.

The largest contributor to error in the EHA pump and cylinder power consumption estimate is the pump displacement D_p at 0.77%. The cylinder area is the second largest contributor to error at 0.55% while the leakage past the piston C_{12} is the third with 0.08%.

Table 3.15: Sensitivity of EHA motor power consumption estimate to variation in parameter P

Parameter	Power (W)	Abs. Error (W)		Max. Error (%)
		+10% P	-10% P	
R	1434.15	2.36	-2.36	0.16
L	1434.15	-0.00	0.00	0.00
B_v	1434.15	0.64	-0.64	0.04
K_t	1434.15	-4.10	5.54	0.39
J_m	1434.15	0.00	-0.00	0.00
C_{oul}	1434.15	12.71	-12.70	0.89

Table 3.16: Sensitivity of EHA pump and cylinder power consumption estimate to variation in parameter P

Parameter	Power (W)	Abs. Error (W)		Max. Error (%)
		+10% P	-10% P	
D_p	1434.15	-7.79	11.04	0.77
C_{12}	1434.15	1.15	-1.15	0.08
A_c	1434.15	7.86	-5.82	0.55
B_e	1434.15	0.00	0.00	0.00
$B_{v_{cyl}}$	1434.15	0.04	-0.04	0.00
M	1434.15	-0.00	0.00	0.00

The pump and cylinder models show a negligible error induced by the cylinder viscous friction $B_{v_{cyl}}$ because of the low friction of the oil lubricated piston seal at nominal conditions. The fluid compressibility B_e and piston mass M have the expected zero contribution to steady state power consumption estimation.

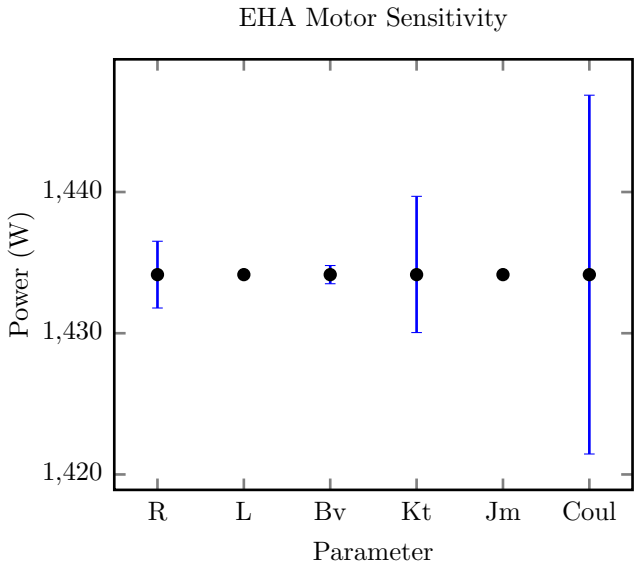

Figure 3.40: Parameter sensitivity of aileron EHA motor model

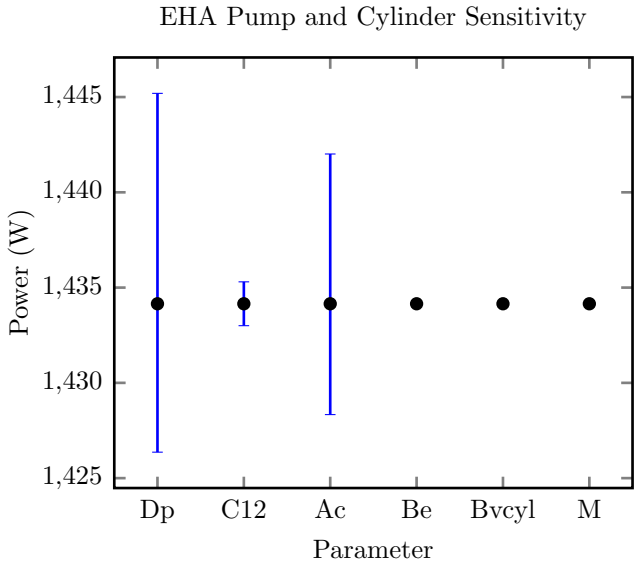

Figure 3.41: Parameter sensitivity of aileron EHA pump and cylinder model

3.6 Control Surface Geometric Model

The control surface model's sole purpose is to calculate the deflection angle δ from the input actuator displacement x. It is not required to calculate the load force fed back to the actuator, as this is estimated separately using the aeroload estimator (section 3.7 on page 217). The linear motion of the actuator is converted to rotational motion of the control surface using a moment arm configuration, as shown in Figure 3.42.

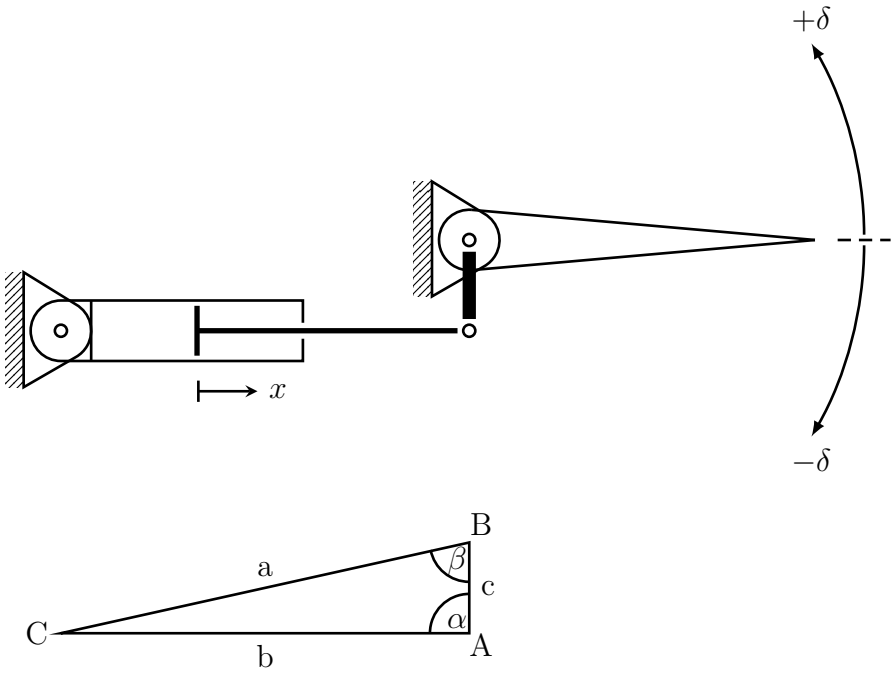

Figure 3.42: Diagram showing the notation for actuator - control surface installation.

All lengths must be calculated or measured before using the following equations, which implement the control surface using the cosine rule. The lengths and angles of the installation when the control surface is in a neutral position ($\delta = 0$) are denoted with a subscript 0. The distance b from actuator mount pivot (C) to rod pivot (A) is calculated using the actuator

displacement x and neutral position length b_0 in equation (3.76):

$$b = x + b_0 \tag{3.76}$$

Since length a and c are fixed, the cosine rule can be used to calculate the angle β:

$$\beta = \cos^{-1}\left(\frac{b^2 - c^2 - a^2}{-2ac}\right) \tag{3.77}$$

Once β is known it can be combined with the neutral position angle to produce the change in surface angle from neutral, δ:

$$\delta = \beta - \beta_0 \tag{3.78}$$

For the steady state models the previous equations do not apply, since the output provided by the actuator models is the piston velocity. The control surface assembly reduces to a straightforward rotational motion problem to calculate the angular velocity of the control surface:

$$\omega = \frac{\dot{x}}{c} \tag{3.79}$$

3.7 Aerodynamic Load Estimation

Estimating the loads applied to flight control surfaces can be an extremely complex task, depending on the detail required. The simplest first estimations can be as rudimentary as using spring-damper approximations, whilst at the other end of the scale more accurate simulations can be achieved using detailed three dimensional software models and computational fluid dynamics software. Although very high fidelity, this method is slow and does not lend itself to high speed simulation and optimisation tasks; instead a simpler

method which still retains the flexibility to estimate the loads at different airspeeds and altitudes is required.

The method chosen is derived from Roskam's Airplane Design [180] and referenced in Airbus' notes on initial actuator sizing [144]. This document seeks to derive the hinge moment coefficients based on basic knowledge of 2 dimensional wing geometry and lookup tables of empirical test data. This data is presented in graph form in the two references; the graphs are digitised using Engauge Graph Digitiser and a curve fitting tool is used to find a polynomial function which approximates the curve accurately. This step requires more work initially than having interpolation based lookup tables, but a reduction in computation time should be evident with less calculations required per lookup.

Most of the variables used in the hinge moment equations can be pre-calculated, since they are dependent only on wing and control surface geometry. Only the variables which depend on the flight condition and angular deflection need to be evaluated during a coupled 6-DOF and actuator simulation. This again lends itself to faster execution by repeating only the lookups that change during a flight.

The software implementation is intended to be as generic as possible to make modification of the aeroload estimator to another aircraft as easy as possible. Characterising the estimator to a particular aircraft or surface requires information on the aerofoils and surface areas of the aircraft of interest, but is handled entirely through the inputs to the model.

Although more flexible and complete than simple spring-damper models, this method does have its limitations. Firstly, the estimations are based on 2D aerofoils so any cross span components are ignored. Secondly, Roskam's lookup tables only provide data for three symmetrical NACA aerofoils (0009,

0015 and 66009) in the subsonic speed regime, so the accuracy when considering a supercritical transonic wing such as the A320 is reduced. Finally, the methods provided by Roskam are only valid for the for linear range of surface travel which is, at best, around 20° and an angle of attack up to 12°. For a transport aircraft this is more than acceptable.

This chapter looks first at estimating the surface areas of the control surfaces of the A320 aircraft, using scale drawings provided by the manufacturer. Secondly, the hinge moment coefficients are calculated based on the A320 geometry, which are then used to calculate the hinge moments on the control surfaces due to aerodynamic loads.

The end result will be a collection of equations suitable for programming into Matlab; which model the force applied to the actuators attached to the ailerons, elevators and rudder (as a function of the control surface deflection, altitude and airspeed).

3.7.1 Control Surface Geometry Estimation

Measuring and calculating the surface areas using Figure 3.43 is conducted using trapezoidal and triangular area calculation techniques which are trivial and will not be discussed in this document. Instead, just a table of results is provided in Table 3.17, which are directly used by the aeroload estimator.

Table 3.17: Surface areas and chords for the A320 control surfaces

Surface	**Surface area (m^2)**	**Chord (m)**
Aileron	1.676	0.63
Elevator	3.962	0.76
Rudder	7.447	1.338

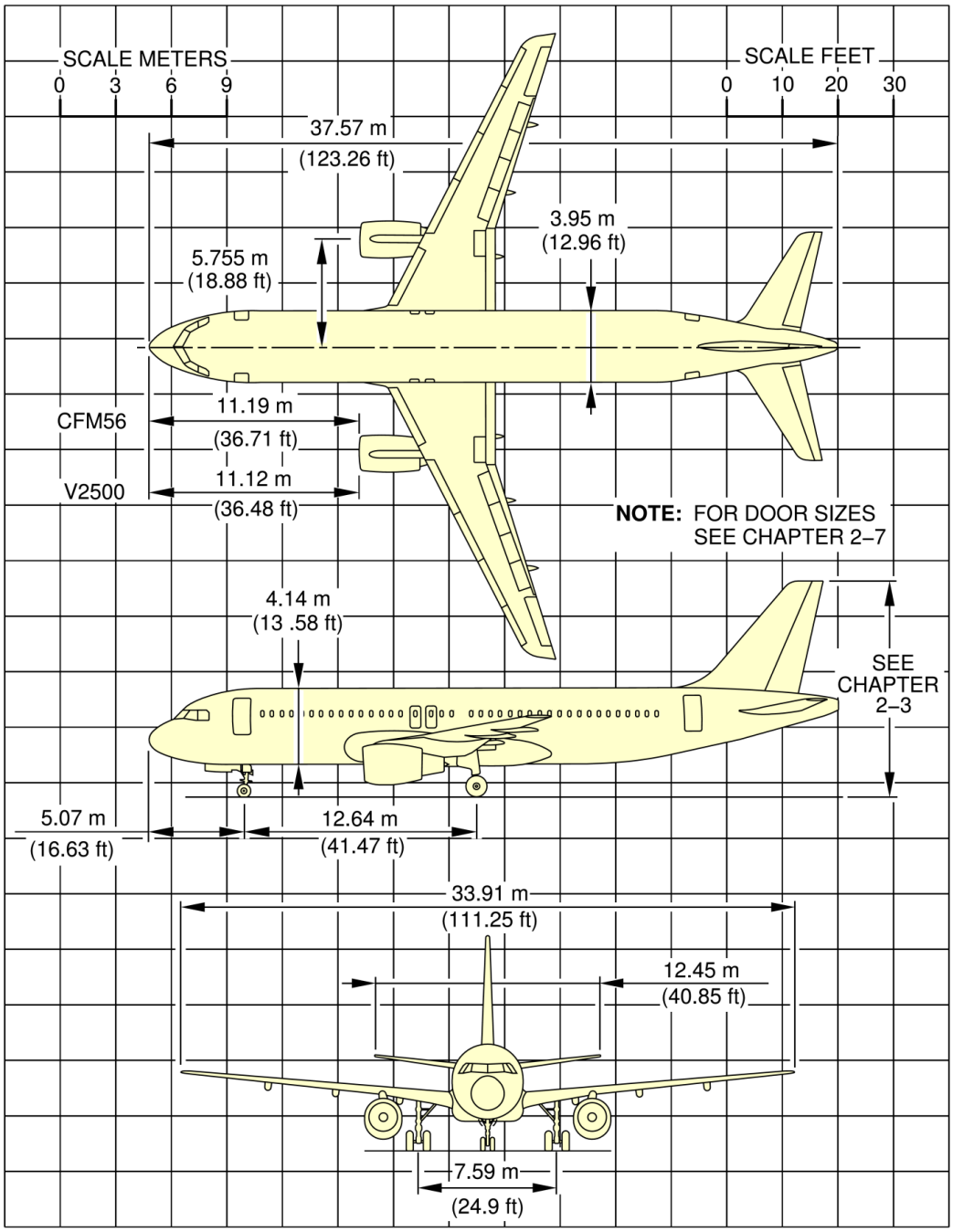

Figure 3.43: Scale diagram used to estimate control surface areas for the Airbus A320 [14]

3.7.2 Hinge Moment Derivatives

The method for calculating the hinge moments is well documented in reference [144], so only a brief summary will be provided here. Each factor in the equations below are taken from lookup tables provided in both Roskam part VI [180], chapter 10.4 and duplicated online in Sholz' actuator sizing work; for reference please see either of these two sources.

The 2D control surface hinge moment derivative due to angle of attack is represented by $c_{h\alpha}$:

$$c_{h\alpha} = \left\{ \frac{c_{h_\alpha}'}{(c_{h\alpha})_{theory}} \cdot (c_{h\alpha})_{theory} + 2\,(c_{l\alpha})_{theory} \cdot \left[1 - \frac{c_{l\alpha}}{(c_{l\alpha})_{theory}}\right] \cdot \left[\tan\frac{\Phi''}{2} - \frac{t}{\bar{c}}\right] \right\} \cdot \frac{(c_{h\alpha})_{bal}}{c_{h_\alpha}''} \cdot \frac{1}{\sqrt{1-M^2}} \tag{3.80}$$

and the 2D control surface hinge moment derivative due to control surface deflection is modelled by $c_{h\delta}$:

$$c_{h\delta} = \left\{ \frac{c_{h_\delta}'}{(c_{h\delta})_{theory}} \cdot (c_{h\delta})_{theory} + 2\,(c_{l\delta})_{theory} \cdot \left[1 - \frac{c_{l\delta}}{(c_{l\delta})_{theory}}\right] \cdot \left[\tan\frac{\Phi''}{2} - \frac{t}{\bar{c}}\right] \right\} \cdot \frac{(c_{h\delta})_{bal}}{c_{h_\delta}''} \cdot \frac{1}{\sqrt{1-M^2}} \tag{3.81}$$

where Φ'' is the trailing edge shape factor [see [144] for definition], $\frac{t}{\bar{c}}$ is the aerofoil thickness ratio and M is the Mach number.

3.7.3 Hinge Moment

Once the hinge moment derivatives have been calculated for the aerofoil and flight conditions, they can be combined to produce an overall hinge

moment coefficient; used to calculate the actual hinge moment c_h.

$$c_h = c_{h_\alpha}\alpha_w + c_{h_\delta}\delta \tag{3.82}$$

where α_w is the angle of attack of the wing (or fin) that the control surface is mounted to and δ is the control surface deflection angle. The hinge moment is calculated by dimensionalising the coefficients using:

$$HM = c_h q A_w \bar{c}_c$$

where the dynamic pressure q is equal to $\frac{1}{2}\rho V_T^2$, A_w is the control surface area and $\bar{c}_c$ is the mean chord of the control surface.

3.7.4 Model Verification

Quantitative validation of aerodynamic load estimates requires privileged information. Without flight test (or validated CFD) data, the verification must remain qualitative and related to the actuator performance. Figure 3.44 shows the load forces on the actuators as a function of control surface deflection at three flight phases. The three conditions are used throughout the A320 case study; they have different trim airspeed, altitude (and thus dynamic pressure), angle of attack and Mach numbers. Dashed grey lines are added to show the stall forces given in Table 3.1 on page 127.

It is expected that the range of deflections achievable without stalling are greater at lower dynamic pressures (descent and approach) than at cruise. Because the angle of attack is non-zero, the aerodynamic force at zero deflection is also not zero (except for the rudder which is symmetrical). The figure demonstrates the ability of the aerodynamic load estimator to provide

hinge moment values across the flight envelope without modification. As with much of the work in this thesis, the absolute numerical value of the aeroload is not of primary importance; instead it is the relative change in force as the manoeuvres change that is important. As long as the estimates remain constant throughout the turn rate analysis, the patterns obtained will be valid.

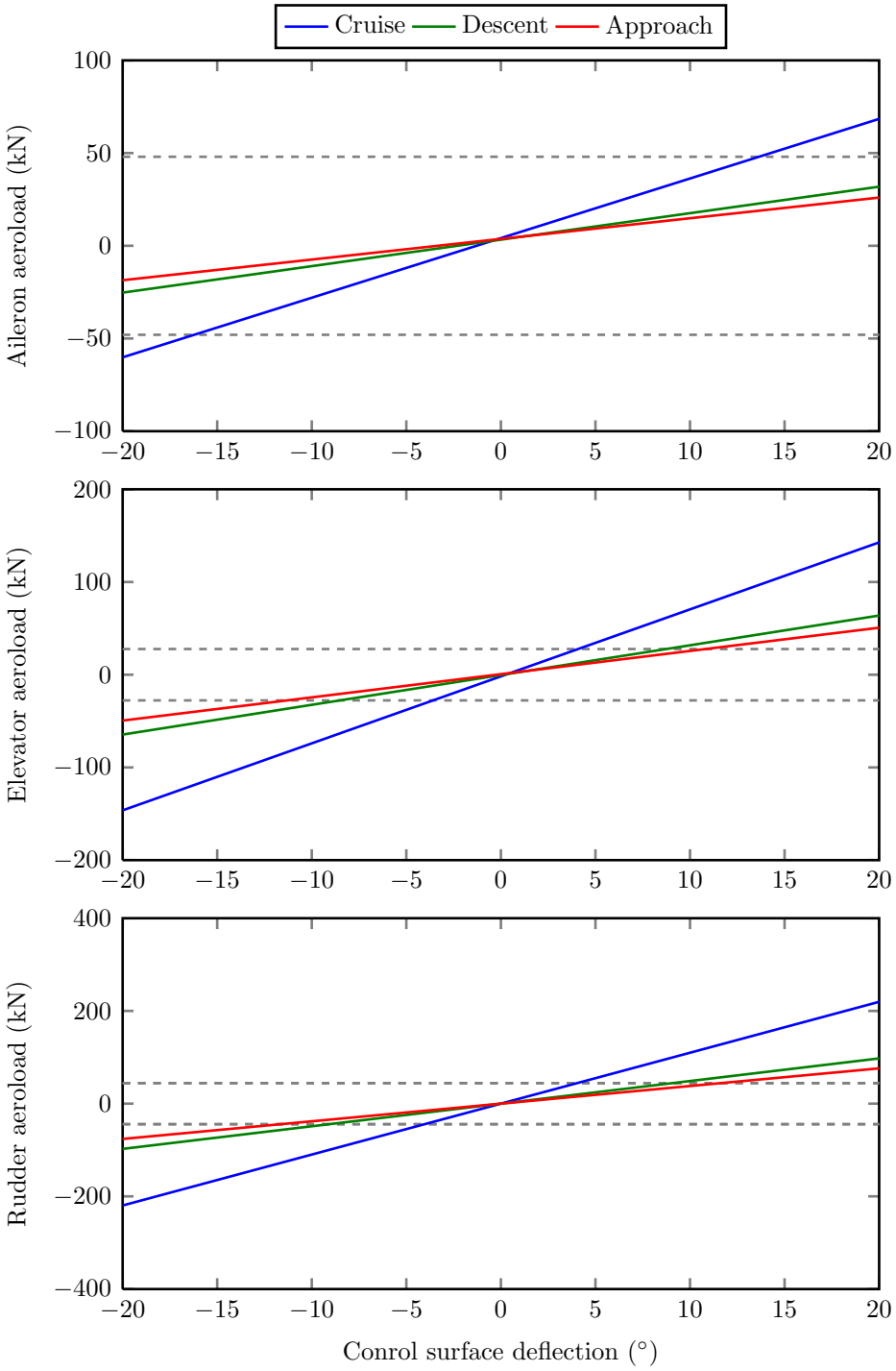

Figure 3.44: Aerodynamic load forces estimated using analytical method [144]

Chapter 4

Experimental Validation

4.1 Experiment Aims

The intention of the experimental validation is to perform a system identification experiment in which a variety of input signals are fed into the actuators and the resulting motion and power signals are used to estimate internal parameters which are not published by the manufacturer. The end result should be to estimate all parameters which directly affect the dynamic power consumption estimation of the simulated actuators.

To perform a useful system identification experiment it is important to operate the device under conditions which are as close to the real world situation as possible. This includes both joint kinematics and load forces. Therefore, the test rig was designed to achieve motion which is as similar to the mechanics of a flight control surface as possible.

The data sought from the experiment includes factors such as friction coefficients, motor inductance and resistance which will be used to characterise simulation models. Once real data is obtained by experiment, the dynamics and power consumption estimates from the simulation model should be close to the real world unit, with the exception of unmodelled characteristics.

Certain parameters can be estimated through steady state means such as

viscous friction, while others such as inertia and inductance require dynamic motion. The key consideration is that when using system identification to parametrise dynamic simulation models, dynamic system identification experiments must be conducted to capture information during acceleration as well as steady state velocity.

It is unfortunate that the experiment did not proceed as planned for a number of factors which will be discussed in this section. Although some results are obtained, the fidelity falls far short of expectations and for this reason this chapter will focus on the reasons for the failure, the lessons learnt and what would be improved if the work was to be repeated.

4.2 Test Hardware

4.2.1 Electrohydrostatic actuator

The Parker Compact EHA is a self contained and sealed unit which is purchased off the shelf (see image in Figure 4.1). It is designed to provide high power density for a relatively low cost, with simple installation and with zero maintenance. It features a 245 W permanent magnet DC motor connected to a reversible gear pump and hydraulic cylinder; maximum stall force is 12.5 kN and the no load rate is 28 mm/s. Also included are the direction control and pressure regulating valves shown in Figure 4.2, to manage the flow of fluid and limit the pressure developed across the hydrostatic transmission.

The actuator velocity can be controlled continuously in both directions by varying the input voltage in the range ±24 V. The valves labelled 'RV' ensure the maximum pressure between the high side and tank is constrained. The value of this release valve is not known, but presumed to be 3000 psi. The check valves between the pump and tank allow fluid to enter the hydrostatic

circuit, necessary because of the asymmetric piston. The check valves located next to the cylinder act to block fluid flow from the cylinder chambers when the motor is off. This acts as a load holding mechanism that ensures the piston can oppose external load forces when powered off. As will later become clear, these check valves have a serious impact on the closed loop control of the actuator under load.

Servo control of the EHA was intended to be achieved using an Electrocraft SCA-SS-70, a four quadrant PWM servo amplifier [181]. This drive can supply 30 A at 24 V. Control is achieved using a preconfigured PID controller which can be adjusted by means of a single overall gain. Feedback can either be provided using a motor shaft encoder (ideally) or an analogue voltage comparison input. Since the Parker Compact EHA does not have an encoder on the shaft, analogue positioning was the only option. Here, a voltage command is compared against a user supplied feedback; in this case a linear potentiometer attached to the moving beam of the test rig. The command signals are calibrated to the range of mechanical travel to ensure maximum control resolution.

Figure 4.1: Photograph of the Compact EHA [182]

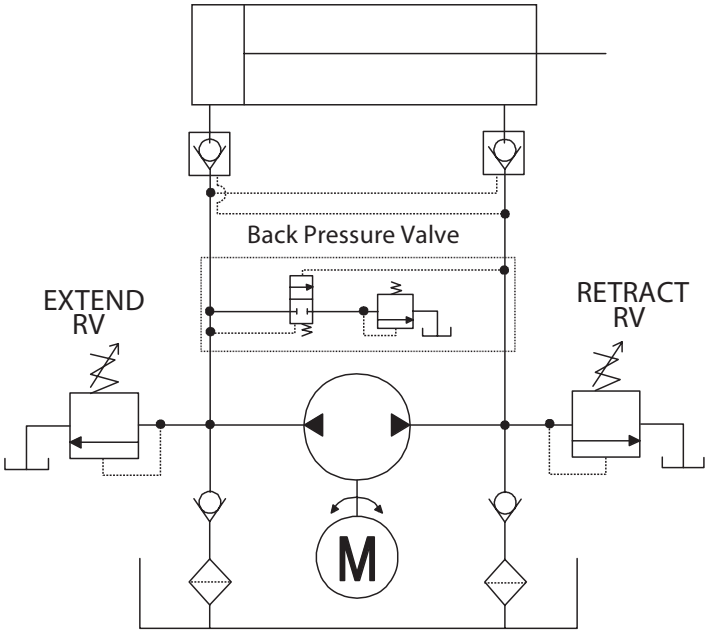

Figure 4.2: Schematic of hydraulic circuit in the Parker Compact EHA [182]

4.2.2 Electromechanical actuator

The MecVel actuator is a commercial off-the-shelf EMA for light duty actuation tasks [183]. It features a permanent magnet brushed DC motor, worm gearbox and a ball screw to convert rotary motion to linear. A parallel motor version is shown in Figure 4.3; the actuator used in this work had the motor mounted perpendicular to the ball screw shaft, but a good quality photograph could not be found. The actuator is capable of achieving a maximum force of 1600 N (at 25 mm/s) and a no load speed of 50 mm/s.

Control was achieved using a RoboteQ AX1500 servo drive [184], capable of pulse width modulating up to 60 A at 24 V. The unit provides closed loop control using a PID algorithm with an encoder input to obtain feedback from the motor shaft. The device is configurable, but was tuned for the MecVel actuator by a previous student. No adjustments were made for the course

of this experiment since time was not available to learn the programming required.

Figure 4.3: Photograph of MecVel EMA [185]

4.3 Test Rig

4.3.1 Source of load force

An important aspect of the experiment is how to generate load forces, since this decision will affect the design choices of the test rig significantly. Solutions exist which span the accuracy and cost scales and a decision must be made which is ultimately affordable. Low cost options are generally passive and include fixed masses combined with gravity (by mounting the actuator vertically), high force springs and dampers (with the actuator mounted horizontally to exclude effects due to gravity) or a rotational inertial load which is also mounted horizontally. High cost methods are inevitably more desirable and can be summarised as any active load generation system, for example a hydraulic or electric actuator with a closed loop force control system. Not

only does this have the benefit of being able to apply time varying load forces, but can also ensure special characteristics such as zero mean force. This is a statistical property which means the average force applied over time is zero; useful when using open loop control since it avoids the tendency of the piston position to diverge from the central displacement under an asymmetric load force.

Given the complexity of active load generation, external parties are often contracted to design and install a force generating actuator, control system and power supply. This results in a highly reusable test rig, but it is beyond the scope of this work to produce apparatus with these features (and cost). It has instead been decided to pursue a technique using variable masses which can be installed on the rig incrementally to study the actuator's full load range. This has a significant drawback; the load force is asymmetric with gravity aiding downwards motion.

4.3.2 Control

The requirement for dynamic motion poses a problem for short stroke actuators since it is inherently easy for saturation to occur as the end stops are reached in a short period of time. System identification is usually performed with small signals, in the range of about 1% of the maximum input voltage. This helps prevent saturation occurring with potentially damaging force as metal contacts impact each other. One problem with conducting small signal analyses is that it is difficult to accurately capture all phases of friction since full sliding modes may not occur with small signal stimulation. This poses a real problem when validated power consumption estimation is the top level objective since friction is of prime importance.

In an attempt to deal with the asymmetric load force, a closed loop

system identification method was to be used in order to maintain control of the system. A servo-drive was purchased with the intention of providing both control and power supply functions in a single, safe unit. The closed loop controller measures the control surface position and provides input voltages to the actuator motor with the aim of maintaining a commanded position (or time series positions). Ideally this would be independent of the load force but as will be shown in the results and discussion section, the linear PID control algorithm which is implemented in the COTS servo drive cannot cancel out the asymmetric load force applied by gravity.

4.3.3 Mechanical apparatus

The most straightforward method of presenting the test rig is to first show a diagram of the complete apparatus, followed by an explanation of the key components. The design rendering of the rig is shown in Figure 4.4 and the photograph of the manufactured apparatus in Figure 4.5.

The apparatus consists of the moving load beam (mounted centrally) which represents the control surface; this is attached to the wall using a bracket and bushing to allow rotation. The actuator is connected using a pin and bushes to allow rotation on both ends. The bracket which the actuator is mounted on is sized to ensure the actuator is vertical when the load beam is in a neutral position (as shown in the figures). The bottom bracket holds a potentiometer (thin blue cylinder in Figure 4.5) which senses the position of the main beam for control and data logging. The bracket at the top supports two safety harnesses which limit the travel of the main beam in the event of uncontrolled motion. On the left hand side of the photograph the servo-drive is visible which was intended to provide closed loop control of the actuators.

In Figure 4.4 half of the load masses are shown to convey how the rig is

loaded. The weights are barbell type fitness weights which can be securely attached by placing a large collar onto the load bar after the masses have been installed. These collars (one on each side) have bolts in them which can be tightened against the load bar to prevent movement.

4.4 Results and discussion

Although there was some success from the experiments on the two types of actuator, overall the aims were not met for a couple of reasons which are discussed in this section.

4.4.1 Electrohydrostatic actuator

The EHA suffered from not having direct feedback of motor shaft velocity to the controller; the feedback loop from control surface position to servo-drive had a low bandwidth and a significant backlash. The mechanical play around the mounting pins is amplified by the leverage created by the locations of the main beam pivot, actuator and position sensing potentiometer. Combined, the position control of the servo loop was reasonably good with no extra mass on the load bar, but as the load progressively increased the control accuracy worsened.

When the maximum load available was applied, the EHA exhibited another major problem. The Parker Compact EHA is not specifically designed for servo-control, instead being optimised for on-off control using a relay. When sourcing the actuator this was understood, but it was suspected that the main reason for this was the lack of any motor shaft feedback. When operating the actuator in a negative power quadrant (lowering the main beam, assisted by the load force) severe pressure oscillations occurred; caused by

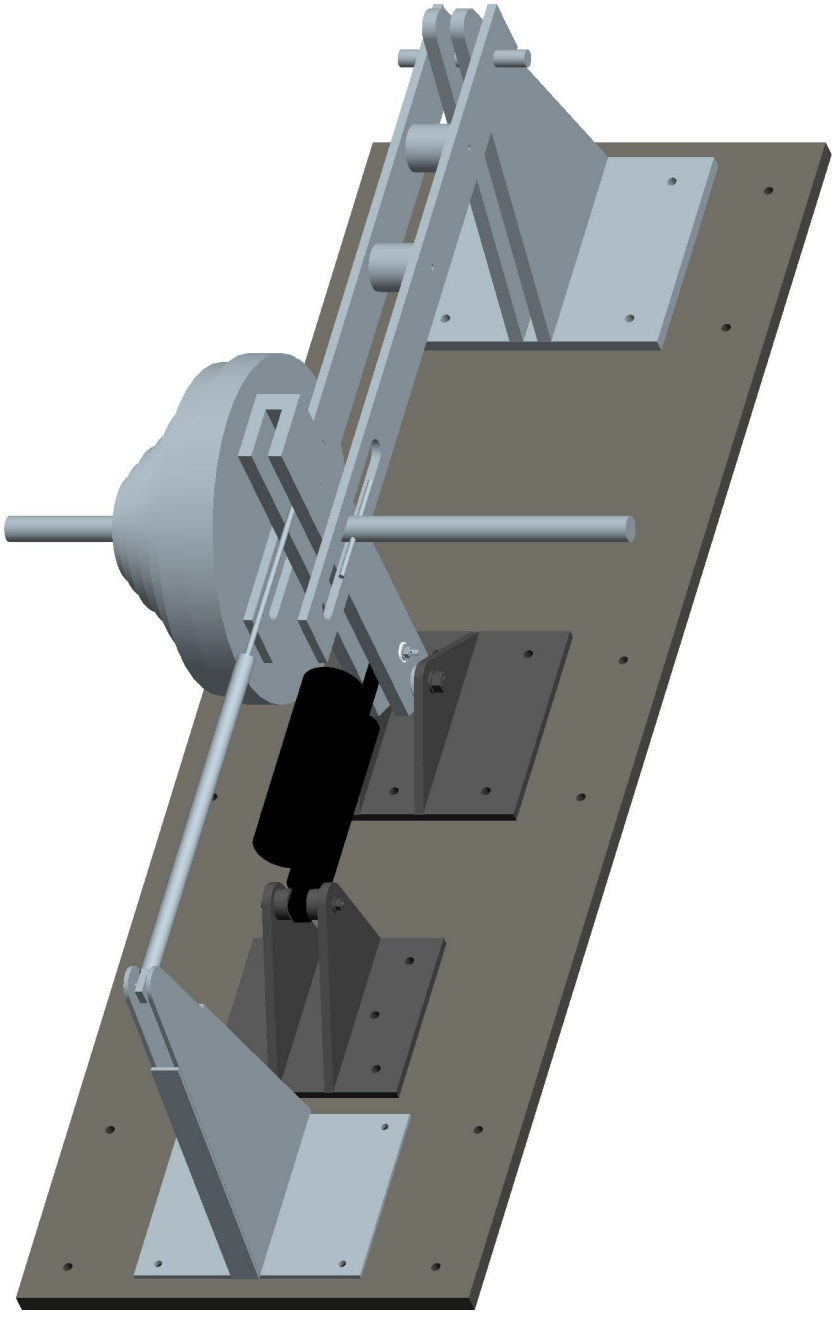

Figure 4.4: Overview of test rig with half the load masses hidden for clarity

Figure 4.5: Photograph of installed test rig

rapid opening and closing of the load holding pilot-operated check valves.

When the main beam was at the top of the range of travel, the EHA would comfortably hold the load stationary when no power was applied. When the motor was powered to lower the load, the high pressure caused by the pump rotating would open the pilot operated check valve to allow reverse flow through. However, once the load begins to move and the flow rate increases, the pressure across the valve becomes high enough to force it closed and the flow ceases. The end result is violent vibration as the load is lowered; followed by a loud crash as the main beam impacts the bottom of the safety harness. Consultation with the manufacturer revealed the only way to remedy the situation is to return the actuator to have a metering orifice installed; allowing flow to bypass the check valves as the load is lowered. This required the specification of the operating load to correctly size the orifice, meaning the actuator would still be suitable for operation at a single load force. Considering time, cost and minimal benefit; the actuator was not returned for modification and the experiment reduced to performing open loop on-off experiments when raising the load only.

The time series data sampled during the open loop experiment is shown for the no load case in Figure 4.6 and for the maximum load (130 kg) in Figure 4.7. There are also experiments performed using masses of 20 kg, 40 kg, 60 kg, 80 kg and 100 kg. Data on the actuator velocity, power delivered and efficiency is computed towards the end of the lifting phase when steady state has been achieved. The results are combined into a force-speed plot to show the characteristics of the EHA in Figure 4.8.

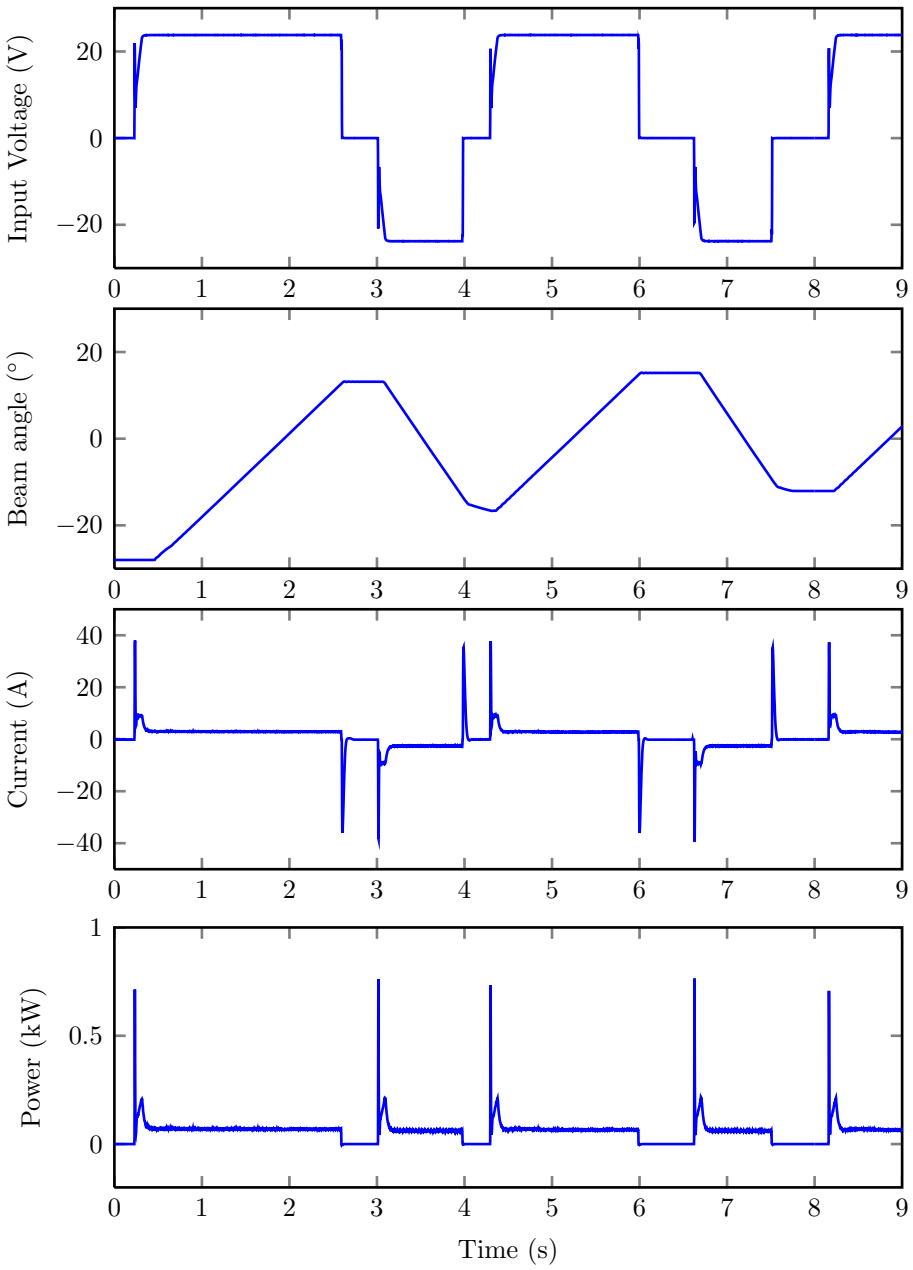

Figure 4.6: Supply voltage, control surface angle, motor current and power for an EHA on test rig with 0 kg load mass

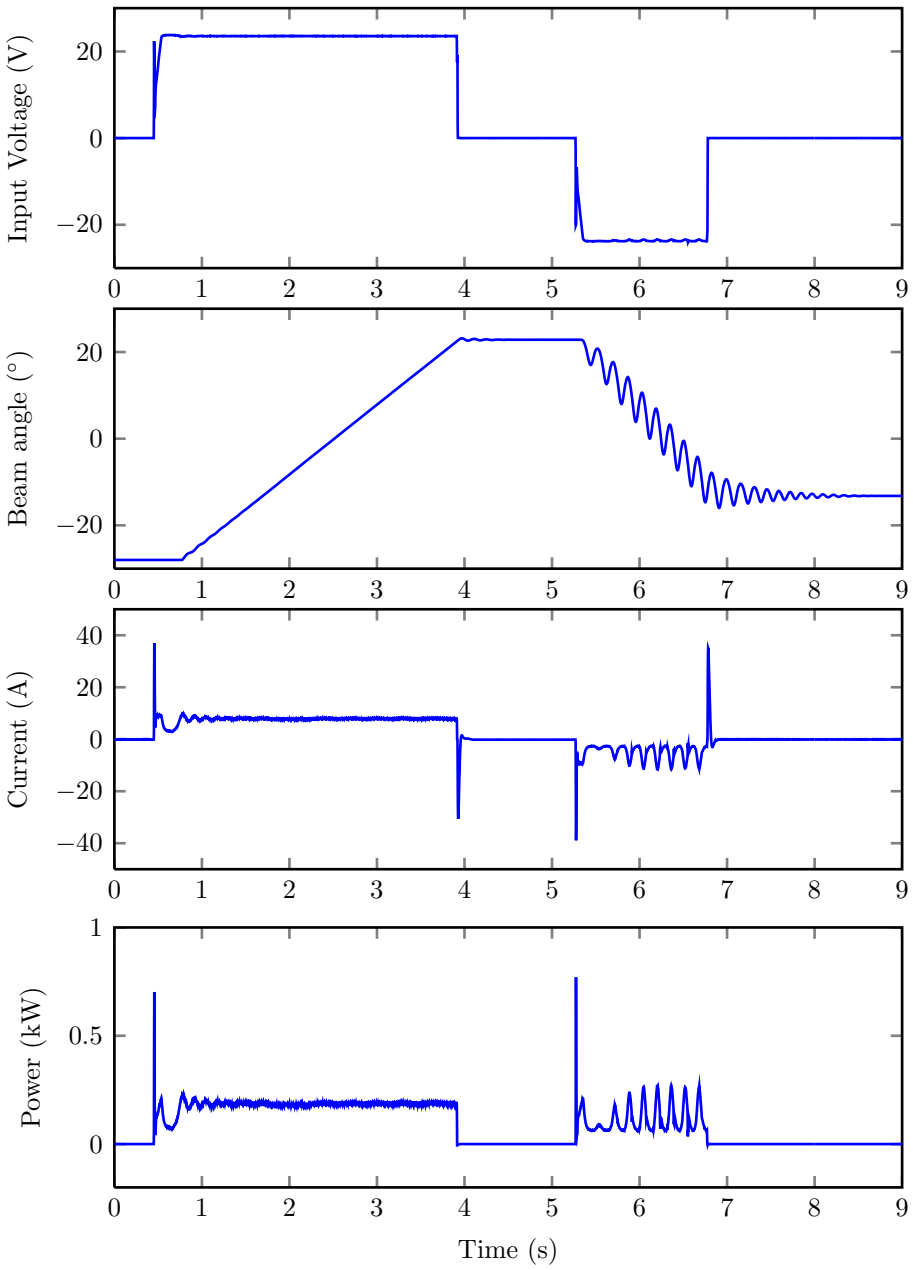

Figure 4.7: Supply voltage, control surface angle, motor current and power for an EHA on test rig with 130 kg load mass

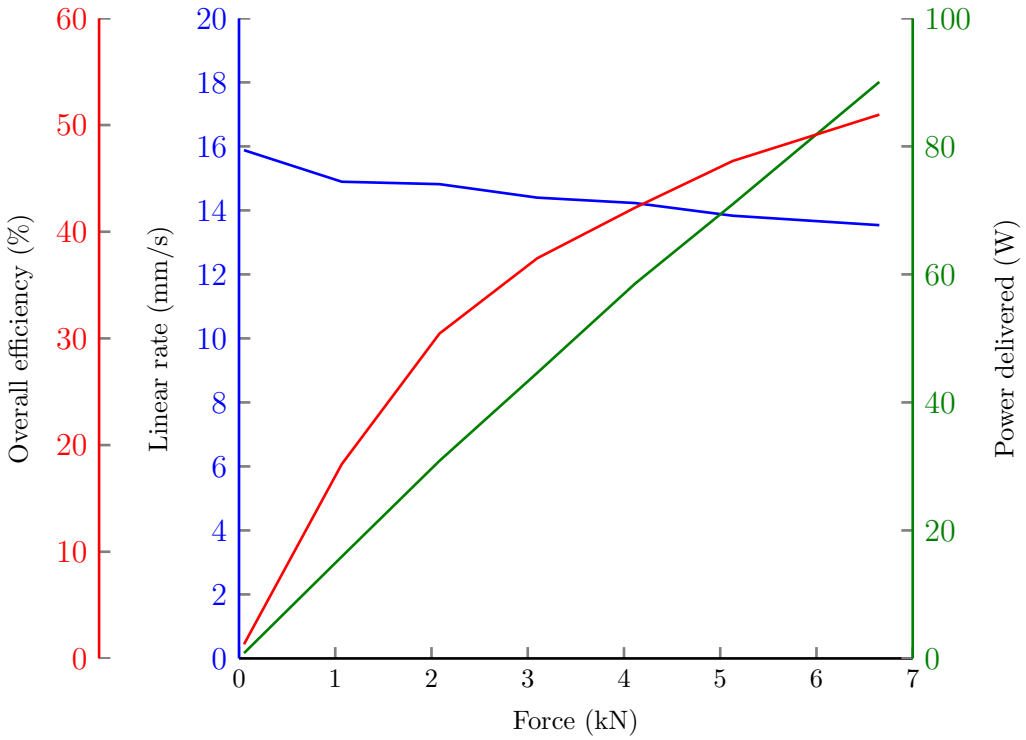

Figure 4.8: Open loop performance of Parker Compact EHA on test rig

4.4.2 Electromechanical actuator

The EMA experiment had its own problems which also limited the usefulness of the results obtained from it. The control system had much better position accuracy compared to the EHA which is attributable to the encoder fixed to the rotor shaft.

The first problem which manifests itself is caused by the linear PID control algorithm not taking into account the load force. The speed of extension and retraction is vastly different which, in itself is to be expected. The difficulty occurs at the end of the downward motion when the load needs to be decelerated, reversed and accelerated again. Because the control algorithm has no additional information provided to it such as a force feedforward, it has no concept of the additional power (or time) that is required to achieve this. What occurs is a large overshoot, sometimes causing an impact against the safety harness. Conversely, a noticeable undershoot occurs as the load reaches the top of travel when it is being raised. When the load increases to near maximum, it becomes impossible to stop the load falling because there is just not enough excess power or time to decelerate the falling mass before the end stop is hit.

The second and more significant trouble that was encountered was the limited data logging and computer interface facilities. The actuator, power supply and controller were purchased for prior work where data output was not a motivating factor. While the control loop had a high enough bandwidth to provide good control of the actuator, the data which was returned to the host computer was at a far lower resolution and sample rate than was adequate for conducting accurate power consumption validation. Initial power spikes when accelerating the motor were lost and so conducting a dynamic

analysis again became impossible.

Open loop results are flawed for two reasons; the very low sample rate (90 ms sample time) and the erroneous resetting of the datalogged results file. For the first problem the actuator position was sampled using the internal EMA potentiometer and recorded by the servo-drive and hardware interface unit. This came prepackaged and was not modifiable in the time available, making it impossible to reverse engineer it in order to sample piston position with the National Instruments data acquisition hardware.

The second problem was a fault of the interface software which caused the results file to be cleared every time the actuator reached a steady state resting position. This would require the source code to be modified to fix the problem, which was not available. The solution would be as above, to replace the entire presupplied servo-drive and hardware interface with the same relay and data acquisition solution that was used in the EHA experiment.

To make the best of a bad situation, only the closed loop data can be used since the open loop data is too short to obtain any reliable piston velocity data. In this case however the servo-drive PWM power output induces high frequency current oscillations at the switching frequency and above (from harmonics). These are above the sample rate of the National Instruments data acquisition device, causing under sampling of the signal and therefore making it impossible to retrieve useful current data using filtering or smoothing. This does not occur in the open loop case because the output of the servo-drive is operating at a 100% on duty cycle.

With these problems in mind, the EMA validation is left in a difficult situation; in the closed loop experiment there is usable data for the piston position, but the current and power data is very poor. In the open loop tests the current and power are good because they are sampled using National

Instruments hardware, while the piston position is unusable. The only real solution is to mix the data from the open and closed loop tests; this is hardly ideal because it cannot be guaranteed that the closed loop controller saturates the input voltage at 24 V when lifting the load. To provide some backup to this merging of data is the fact that for both experiments the voltage signal (sampled using National Instruments hardware) is usable after filtering; this allows the cross verification of supply voltages during steady state load lifts whether open or closed loop controlled.

The power signals in Figure 4.9 and Figure 4.10 are taken from the provided hardware interface; both plots show a power consumption of around 0.1 kW. However, the current in the no load case is around 1.2 A and 4.7 A when lifting 30 kg (measured at the steady state horizontal section of the current plot); the supply voltages are 24 V and 23 V respectively, suggesting the power data is inaccurate. For the open loop performance data in Figure 4.11 the power is calculated from the product of voltage and current during the rising edge instead of the unreliable power signal. This figure suffers from there only being two load forces applied to the actuator in the experiment; each parameter is therefore represented by a linear trend. The results would benefit from a finer granularity of load forces but not enough small masses were available to mount on the load bar.

4.5 Conclusion

It became evident at this stage that much greater consideration (and cost) must be afforded to high power actuator system identification; the actuators themselves, the servo controls and the data acquisition must all be of a very high standard. They must also be specifically designed and tuned together; with retrospect it would have been wise to make a purchase *only*

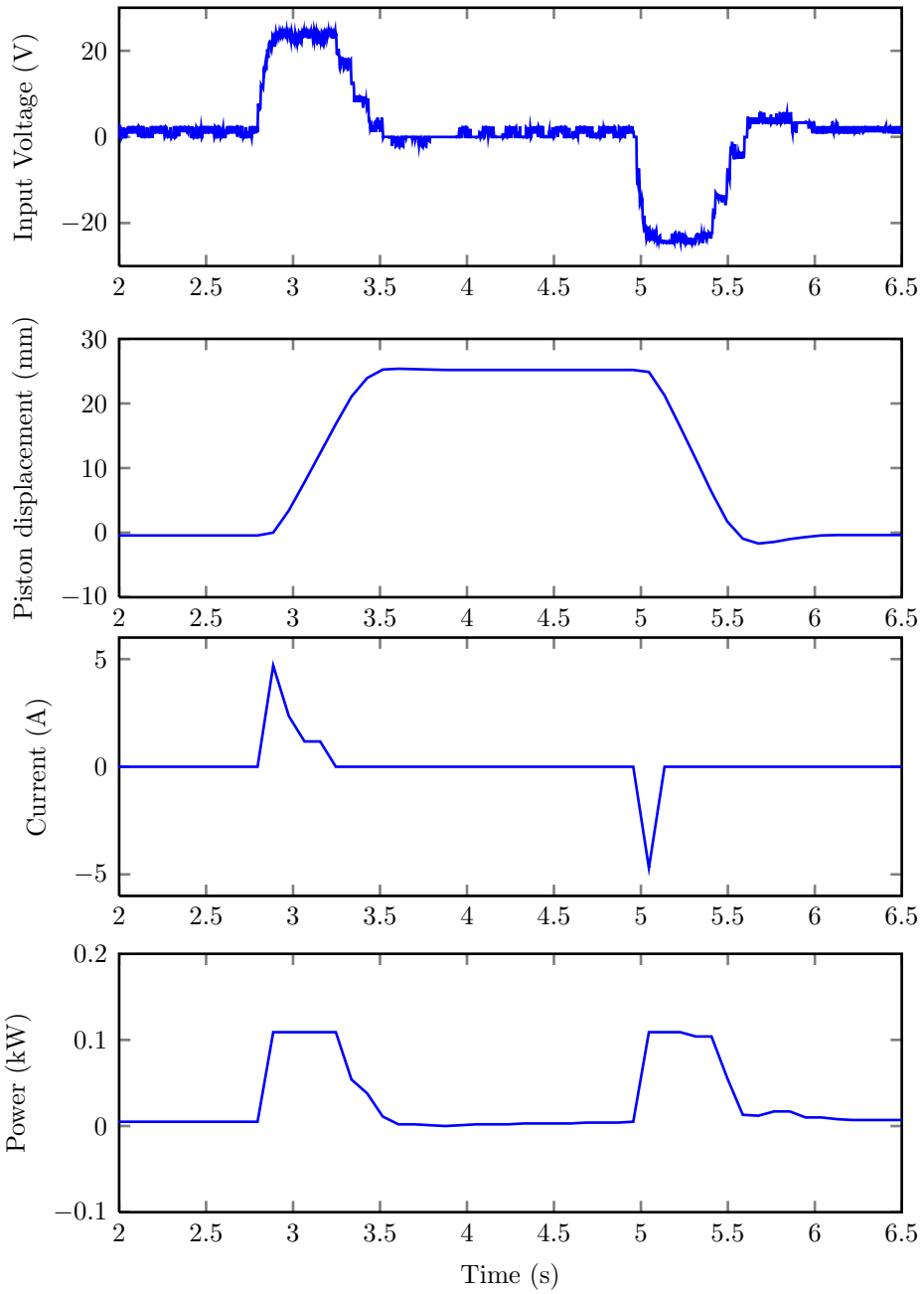

Figure 4.9: Closed loop step response of MecVel EMA with 0kg load on test rig

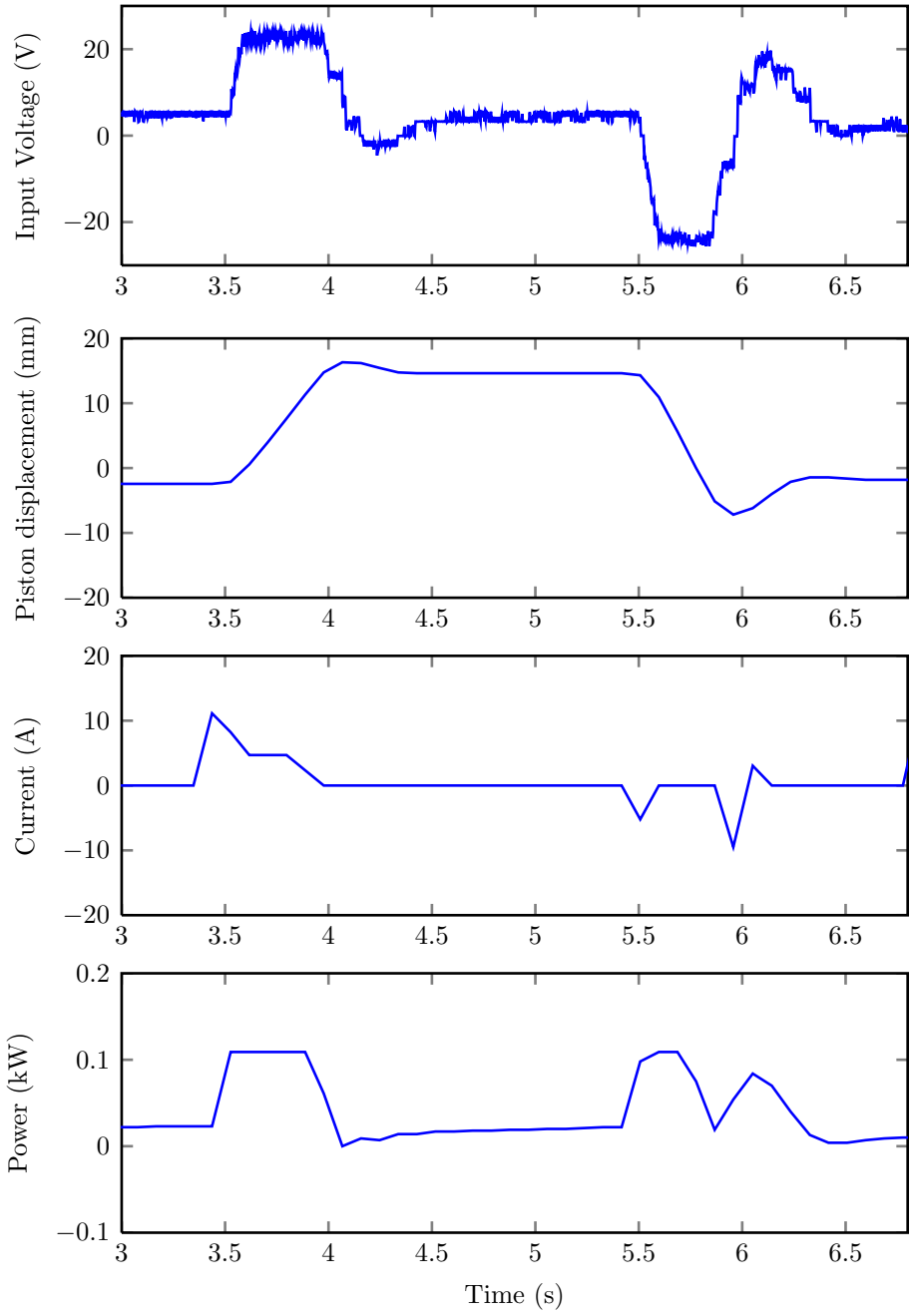

Figure 4.10: Closed loop step response of MecVel EMA with 30kg load on test rig

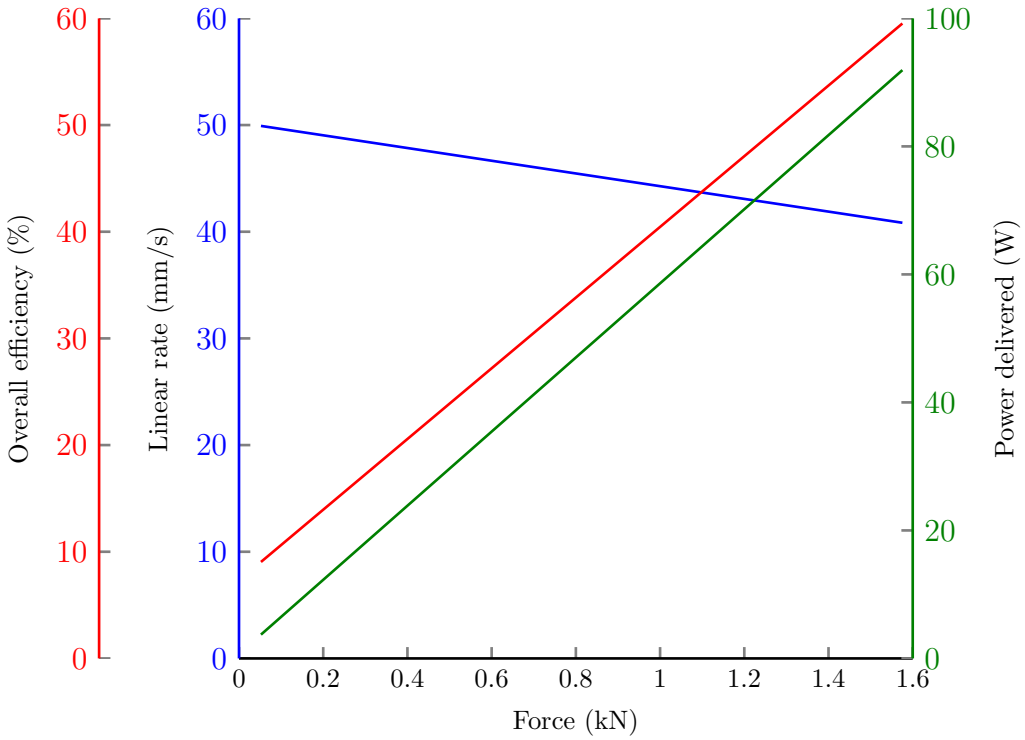

Figure 4.11: Characteristics of MecVel EMA as a function of load

if an actuator and servo-drive are made by the same manufacturer (Parker Hannifin are one example) or are *explicitly* compatible. This experience was derived from the EHA experiment and given as advice to the colleague who procured the EMA; the improvement in closed loop control accuracy is evident between the two experiments. The weakness in hardware interfacing experienced with the EMA is a result of both cost limitations and the poor availability of high performance, COTS actuation hardware which can be purchased as single units. To obtain actuators which are of the performance and quality that might be expected of aerospace grade actuators requires the commitment to a contract to purchase hundreds of actuators per year (or more). The cost of developing single high performance actuators is in the remit of dedicated research programmes involving companies such as Moog, Parker, Lucas or Liebherr.

Chapter 5

Integration

This chapter describes the integration of the different components; the aircraft model, actuators, flight control and guidance systems into a complete model which represents the aircraft and its actuation systems.

The most appropriate means of presenting the structure of the model is through the flowchart shown in Figure 5.1. The actuators and their controllers form the inner most loop, sending control surface positions to the inputs of the aircraft model. The TECS/THCS FCS closes the next loop around both aircraft and actuators, while the guidance controller forms the outer most loop. Integration is performed in stages, with the model being tested after each significant step.

While there are several ways of achieving integration, the most successful for this work is described as follows:

1. Design actuator position and force controllers
2. Trim aircraft model
3. Combine actuator models with aircraft model
4. Incorporate aeroloads
5. Connect and tune TECS inner loops first followed by THCS

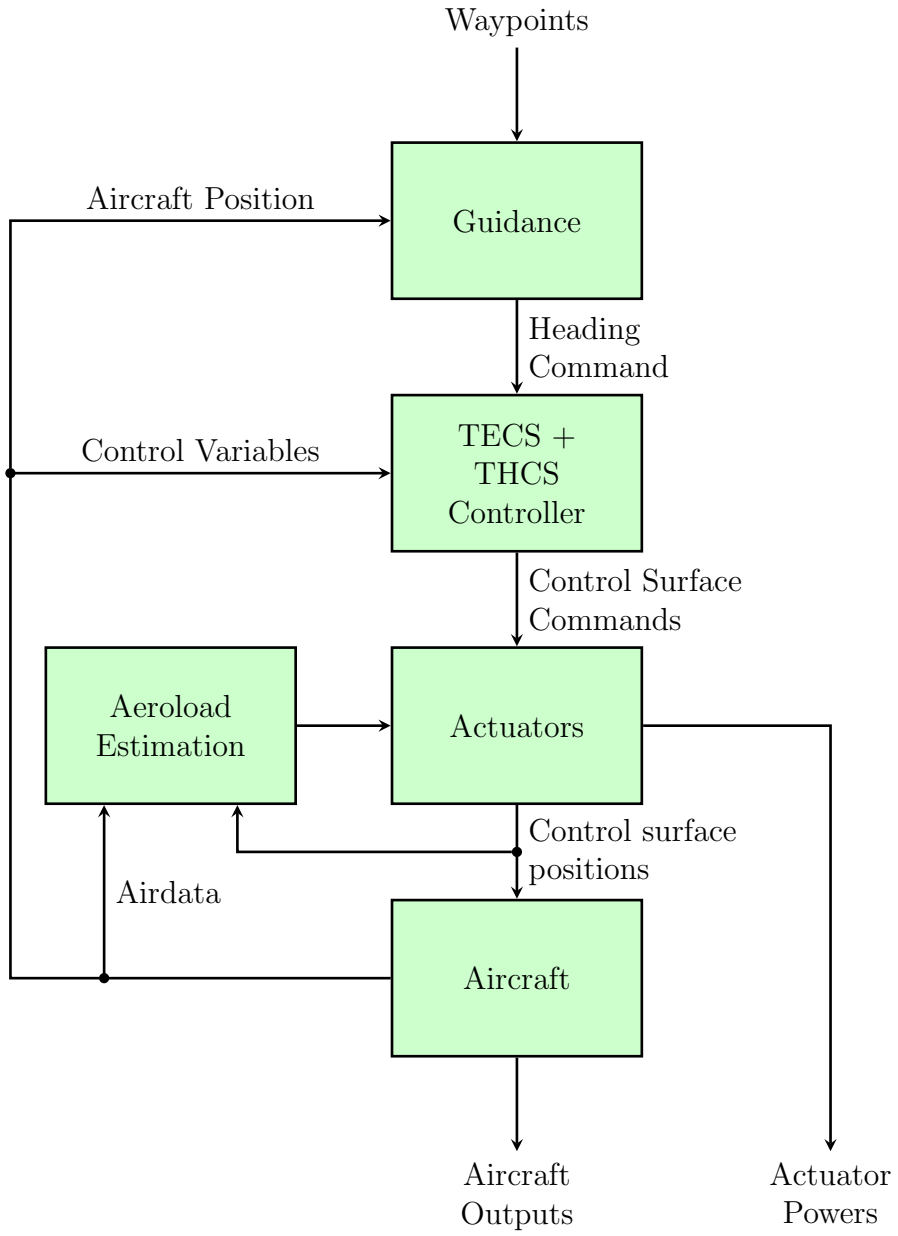

Figure 5.1: Functional model schematic

6. Enable TECS (first) and THCS outer loops (second)

7. Install guidance algorithm

Another possible technique is to design and test the FCS on the aircraft model after trimming and before adding the actuators. However, once the actuators are installed the control gains must be retuned to reduce the bandwidth of the FCS control loops. This is to ensure loop stability with the lag induced by the actuators.

This method has the benefit of making it more straightforward to apply classical design techniques such as root locus or Bode plots when designing the FCS. Matlab does have the capability of linearising complex models (i.e. including actuators), so tuning the FCS with the dynamic actuator models in the loop is the preferred method.

5.1 Actuators

The prerequisite for integration is that the actuator models must have already been equipped with robust position and force controllers. These must not cause a drastic slow down of the variable step solver since they operate on the lowest layer of the simulation and have the highest bandwidth signals. Slow simulation of the isolated actuator models will be magnified many times over in the integrated model so this is a *key* requirement.

By applying control techniques which are optimised for motor control such as PIV, it is possible to reduce oscillations in the actuator response to a minimum. When a step command is issued to the PIV controller it should move the actuator at high speed towards the commanded position, before decelerating as it approaches the setpoint in order to stop precisely on the setpoint. This is not achievable using PID since the response rate (initial

speed) is directly related to the amount of overshoot and settling time. In order to have zero overshoot, the gains must be set very low and the response rate is correspondingly very slow. For more information on the control design used for the actuators in this work, please refer to sections 3.1.6, 3.2.5 and 3.3.6 (on pages 144, 173 and 191).

The reason control quality is of utmost importance is because oscillatory motion requires small timesteps to ensure the numerical error remains below the solver error tolerance. Compounding this is the fact that the actuators form part of the inner most loops of a highly cascaded design; incorporating actuator control, aircraft dynamic controllers, TECS and THCS loops and a guidance system. If oscillations are induced at the actuator level then every closed loop above it will be affected in the simulation.

The next step in preparing the actuator models for efficient simulation in Simulink is to vectorise the model and its controller. The aircraft requires multiple actuators; instead of duplicating the same model (i.e. duplicating the equations) to represent the different control surfaces, it is far more efficient to vectorise a single instance of the model. The equations will not be repeated from the actuator section 3 (page 125) since they do not change, the only difference is that each model parameter is entered into Simulink as a vector of all the actuators. Taking the motor current as a simple example; to calculate the current, Ohm's law can be applied to a single resistance:

$$I = \frac{V}{R} \tag{5.1}$$

This form of the equation is acceptable if a single motor is to be simulated, but if four are to be modelled then it becomes inefficient for Matlab to solve equation (5.1) four times. Implementing the equation (and all others) in vector form takes advantage of Matlab's optimised matrix algebra capabilities

(as noted in the Mathworks' '*Tips for improving performance*' [140]).

$$\boldsymbol{I} = \boldsymbol{V} \oslash \boldsymbol{R} \tag{5.2}$$

where $\oslash$ is a Hadamard division (element-wise division). On a processor level, this has the effect of solving the equations of four motors in parallel instead of serially and has a significant improvement in simulation speed.

Once the actuator models are converted to this format, a single model will exist which communicates through input and output vectors. The length of these vectors is equal to the number of actuators represented.

Aerodynamic loads are typically added after the actuators since it adds an extra layer of complexity to the control system above that of just position control. At the start of the iterative design process, simple linear PID controllers were used; load forces caused unwanted tracking error and reductions in simulation speed. In some cases (at particularly high forces) the control loops would even become unstable; for this reason a two step design process makes it simpler to deduce whether the control lacks robustness in either position or force control.

At this level of integration, the aircraft and actuation systems function together to estimate dynamic power consumptions as an aircraft flies and manoeuvres. It has no autopilot, so it requires manual control or it is limited to simulating the response to small amplitude control inputs from a trimmed flight condition.

5.2 Flight Control System

In order to conduct repeatable experiments relating actuator power to trajectory, the aircraft needs an automatic control system. To integrate

TECS and THCS with the aircraft model, the first task is to tune the inner loops to control the elevator, throttle, ailerons and rudder. This process can be achieved with any method that suits the aircraft and inner loop controls of choice.

For the first case study aircraft; the A320, this consisted of using Matlab's Control Design Toolbox to perform graphical tuning of cascaded PID controllers through root locus and Bode plots.

Once the inner loops are installed and capable of executing simple manoeuvres, the TECS and THCS outer loops are connected, debugged and tuned until the aircraft is able to execute manoeuvres robustly. At this stage, it is important to check the FCS at a range of flight conditions and while executing different manoeuvres to verify that the simulation is robust. If anything is found to 'freeze' the solver (as the timesteps automatically adjust and approach zero) the design must be iterated, most likely by loosening the controller gains in the component causing the problem.

5.3 Guidance Algorithm

Once the integrated model satisfactorily passes the robustness check the guidance algorithm can be connected. Tuning this component is undertaken manually since its design is fairly basic; the gains are chosen at a level which is just below the onset of course tracking oscillations. If the aircraft has to 'hunt' for the correct trajectory, then power is being wasted by the actuators as they have to induce the unnecessary accelerations. At the end of this stage it is again important to verify the robustness of the simulation by executing different manoeuvres at different flight conditions. While it is expected to see a reduction in simulation speed during manoeuvres compared to straight segments, care should be taken to ensure it does not occur to a level where

the simulation stops. In the author's experience this occurs most frequently during sharp turns; where large bank angles, control surface deflections and forces are required. This induces strong cross coupling between the axes of motion. For this reason, these areas should be tested in particular detail.

At the end of this process the aircraft can be initialised in specific locations, given a list of waypoints and it will fly the trajectory defined by them. While it does this, it will provide transient actuator power consumption estimates and when these signals are integrated, estimates of energy consumed.

5.4 Simulation Settings

The final note on integration relates to the solver type and configuration settings used to simulate the model. If chosen poorly, these can have dramatic consequences on simulation speed.

The key point is that a *stiff* solver must be used. Generally speaking, stiffness concerns ordinary differential equations which model a mixture of fast and slow dynamics. While the slow trend is the property of interest (e.g. the roll motion of the aircraft), the dynamics of the fast motion (e.g. the aileron actuator motor) are important to estimate the change in the roll rate.

Most solvers are likely to be able to tackle this problem but the question regards the efficiency with which they do it. By using a specially designed *stiff* solver such as *ode23tb*, the simulation can proceed orders of magnitude faster than when using *non-stiff* solvers such as Simulink's default *ode45*.

The final settings worth drawing attention to are the maximum timestep, and the absolute and relative error tolerances. The purpose of this work is to simulate manoeuvres between straight flight path segments. During the

straight segments, the aircraft is flying in trim and there will be no motion from any of the actuators (assuming the aircraft is stable and winds are zero). During these phases it is acceptable for the solver to take large steps since the errors induced will be small. Maximum timesteps of between 1 s and 10 s have been used successfully with 1 s providing a good tradeoff between speed and accuracy.

The problem with increasing the maximum timestep is that it becomes possible for the solver to 'miss' the command from the guidance algorithm and execute the turn late. To avoid this, the absolute and relative error tolerances need to be adjusted; these will differ from aircraft to aircraft and from one FCS to another, but values of 1E-3 worked well for the simulations in this work.

Chapter 6

Method of Actuator Simulation

This chapter describes the methodology used to investigate the actuator power consumptions as a function of aircraft turn rate. It covers the techniques used to achieve the parameter sweep which quantifies the power consumption across the problem space. Secondly, the methods of optimising the experiment for speed are presented.

6.1 Parameter Sweep Automation

After the aircraft model is integrated with the airframe systems and the controllers have been verified for robust operation, it is ready to conduct trajectory sweep investigations. The intention of this is to map time variant performance data of the aircraft as it flies through a parameter sweep of some particular variable. It could for example be used to investigate how the handling qualities of the aircraft change with varying actuator motor parameters or failures.

To demonstrate the abilities of the simulation framework, a case study is conducted which investigates the effect that turn rates have on actuation system energy consumption. This is the primary focus of the exercise; it will of course also produce auxiliary data of interest such as the trajectories of

the aircraft and fuel burn, if a suitable engine model is used.

The principle is that a set of three waypoints are generated which define a single heading change manoeuvre; the aircraft is initialised at the first coordinate (A) with the second waypoint (B) directly in front. The third coordinate (C) is offset by the heading change angle, an example of which is shown in Figure 6.1 for a 150° turn.

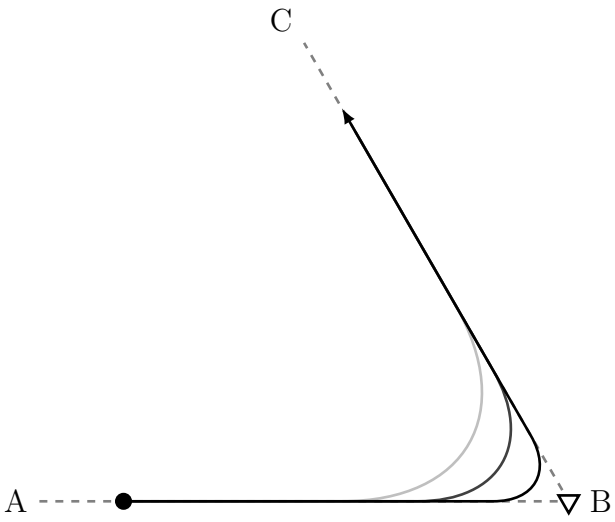

Figure 6.1: Heading change with varied turn rates

These waypoints are loaded into the guidance system and by default, the aircraft will execute the maximum rate turn allowed by the THCS. The turn rate is limited by the saturation blocks in Figure 2.25 (on page 112), which are typically used to ensure the aircraft remains within its lateral manoeuvre envelope. This functionality is adapted in order to limit the turn rate used between segments 1 and 2 of the predefined trajectory. Thanks to the structure of THCS, the saturation is placed outside the high bandwidth aircraft inner control loops and so it does not affect the stability of the control systems.

Since the integrated aircraft model simulates a single aircraft, with a sin-

gle model run representing a single 'flight'; simulating groups of trajectories requires multiple executions of the model. To do this by hand would be laborious and error prone; the number of manoeuvres needed to completely map the space of solutions may be several hundred. The data storage space required to save the results array can swell to a gigabyte, depending on the fidelity of the simulation.

Instead, a program is created which automates the process of selecting waypoint and turn rate limit inputs, executing the model and storing output data. This program is simple in concept; a `for` loop iterates over the Matlab command to run the Simulink model the desired number of times to cover all turn rates. Input and output to the model is very simple since the variables are designed to be stored in the Matlab Workspace; here they can be accessed by both the Matlab program and the Simulink model. This allows the controlling program to select the desired turn rate from a vector, indexed by the `for` loop counter, and save it to a variable which is accessed by the Simulink model on execution.

The above description will execute a case study of multiple turn rates at a single heading change. To build up a complete picture of the full scope of manoeuvres, multiple heading changes must be investigated. More manoeuvres obviously means more simulations and more time spent, while doing too few makes it harder to visualise patterns in the results. The selected manoeuvres are in steps of 30°, from 0° to 150°. A zero degree turn case is used as a baseline to compare the results against a straight and level flight.

In order to incorporate the different heading changes into the case study automation program, another `for` loop must be used which encloses the previous loop. Descriptively, the software will select a heading change (e.g. 30°) and execute a turn rate sweep study, then increment the heading change

to 60° before repeating the turn rate sweep. This is repeated until all heading changes have been run.

By this point, it is easy to appreciate the growing number of model runs which are necessary to implement this procedure. Assuming 10 turn rates are being investigated at 6 heading changes, 60 model runs are needed. This is a fairly low resolution experiment and the output figures will have noticeable granularity, but increasing the completeness of the results requires more model runs. Consider also that three actuation technologies are being investigated and that other uses of this technique may wish to simulate complete flight trajectories; the computational workload is appreciably large. It should become clear now why such stress was implied on the importance of robust and fast simulation speeds of the individual models.

By design, Simulink implements centralised solvers which numerically integrate the differential equations of the entire model at each timestep. Currently, these do not lend themselves to multithreaded execution in the same way that the distributed solvers studied by other authors do [14].

A single Simulink model cannot be modified in order to run efficiently on a multicore computer. In order to take advantage of the multiple processors in modern computers, the Matlab Parallel Computing Toolbox is used to execute the previously mentioned `for` loops in parallel; using the specially designed parallel-for loop `parfor`. This can be used on certain types of loops in which each iteration is independent of each other and do not require sequential execution of the loop.

The general behaviour is best described by an example; assuming a `parfor` loop is going to iterate over some code 8 times, and is given a 4 core machine (called the *matlabpool*). The `parfor` function distributes the entire piece of code to each processor core (called a *worker*), along with the index

for that particular loop iteration. The distribution of work packages is somewhat arbitrary and the time at which each worker finishes a job depends on how long a particular loop iteration takes. Conveniently, regrouping data at the end is handled by `parfor`, so once the code has been modified to allow for parallel computing it is easy to distribute the various model runs between a multicore processor or even a networked cluster of machines. Scalability is one of the key benefits of the Parallel Computing Toolbox.

The functionality of the program is best described with the following section of skeleton code, which shows the key operations:

```
1                   parfor i = 1:number_Psidots
2                       for j = 1:number_turnAngles
3                           Results(i,j) = sim(Model);
4                       end
5                   end
```

The `parfor` loop is on the top level and iterates over the turn rates. The second level is a regular `for` loop, which iterates over the turn angles and executes a run of the model at each iteration (on a single processor core). The results are gathered in an array called 'Results' which stores large numbers of time varying signal data. It is not shown in the code, but the results array is created and stored in the main instance of Matlab; its elements are filled as and when the parallel workers finish their particular jobs. Using this technique, the solving of multiple Simulink simulations can be accelerated significantly.

6.2 Optimising for Speed

Throughout this document, many comments have been made about how to ensure fast simulation using Simulink. For clarity, this information is

gathered into its own section here in order to make a neat, collated 'checklist' of things that must be taken into account to ensure efficient models.

- Use of solvers for stiff systems; the bandwidth of the actuator motor controls are significantly higher than that of the slow aeroplane dynamics.
- Long maximum timesteps for the variable step solver (*ode23tb* with a 1 second max. timestep is used).
- Careful adjustment of solver absolute and relative tolerance to allow automatic adjustment to long timesteps in periods of low activity (straight segments) and suitably small timesteps during periods of high activity (during manoeuvres).
- Vectorised actuator models.
- Minimum control oscillations from well tuned controllers.
- Use of Matlab's Parallel Computing `parfor` loop in the main control loop, so one complete model/trajectory can be computed on each processor core / computer.
- Initialise model from a trimmed operating point for *all* states.

The final point is of particular interest here as it has not been appropriate to discuss it anywhere else, yet it can have a significant effect on simulation times - in some cases doubling it. The aircraft model has been trimmed on its own to assist with the integration of the control systems and actuators. Once integration is complete however, it alone does not suffice to initialise the complete model from a steady state operating point. The reasoning behind

this is that even though the aircraft [airspeed, altitude, attitude, control inputs] is trimmed for the current flight condition, the actuators are not.

In this condition, the actuators initialise at the position defined by the aircraft trim condition with motors stationary and no torque being generated. At the start of the simulation ($t = 0$), the aeroload estimator will compute a load force which in most cases is not equal to zero. This is instantaneously applied to the actuator; causing a deflection from the initialisation position, a corrective effort from the actuator controller and an associated reduction in timestep and simulation speed. After a few seconds (in the simulation timebase) the actuators will return to an equilibrium position with a constant torque opposing the aerodynamic force. By avoiding this, the results data contains less spurious initialisation transients and the overall simulation speed for a single run is increased significantly.

The method used to avoid this is by re-trimming the fully integrated model using Matlab's *Operating Point Search* function. This creates an operating point from which to initialise the model on subsequent runs, where the actuators are in equilibrium with the aeroload at ($t = 0$). The *Operating Point Search* function can trim a model using optimisation algorithms, but the integrated model is complex with many states (66 in the integrated EMA) so trimming this way can be difficult. The preferred option is to let the model run for a prescribed amount of time to allow all transients to die out, before sampling the values of all inputs and states. This needs to be done with the guidance system disconnected and with fuel mass held constant (if a variable mass aircraft model is used) to obtain valid trim data. The operating point gathered is valid for all runs using the same type of actuator at the current flight condition. By taking the time to trim the model this way once saves a worthwhile amount of time in the main parameter sweep program.

Chapter 7

Case Studies

7.1 Airbus A320 - Transport Aircraft

7.1.1 Aircraft Description

The aircraft used throughout the development of the models in this thesis has been the Airbus A320 type; a twin turbofan, single aisle, medium range transport aircraft (shown in Figure 7.1). It is a proven design and is used as the baseline aircraft for many research projects. Its relatively small size and simple flight controls make it an ideal candidate for a case study aircraft. Larger aircraft require split control surfaces and multiple actuators which complicates the model, but achieves no material benefit. The platform is however large enough for it to be feasible to implement all three actuation technologies; when an aircraft is too small it is not practical to suggest any type of hydraulic power because the forces are too low.

The aircraft model is derived from DATCOM [142] and Tornado [143] and combined with flight control actuators that are sized using preliminary design methods to achieve the performance specified in Table 3.1 (page 127). The flight control actuators and their mechanical installations are checked to ensure the aircraft meets the basic handling requirements defined on page 451

Figure 7.1: Airbus A320 aircraft [186]

in [187]. The FCS is designed and tuned to control all the degrees of freedom of the model, but makes no attempt to relate exactly to the real aircraft because this performance data is not known. The result is a simulation of an aircraft that behaves *similarly* to an A320 or Boeing 737.

7.1.2 Results and Discussion

By the very nature of the experiment it is possible to produce massive amounts of data. There are three actuator technologies being flown through five different heading change manoeuvres, at three flight conditions and six turn rates; the full experiment involves 270 model executions. Each execution produces over thirty outputs, each consisting of thousands of datapoints. Clearly the results need to be grouped together and presented in a way that conveys the most important data, without inundating the reader with hundreds of pages of time series plots. It is decided to combine the results and discussion section, so the description and analysis is located close to the figures which they describe.

The chosen method is to present the time series data for a single manoeuvre with a single actuator technology, to demonstrate the behaviour of the

aircraft and actuator models during that manoeuvre. Because of the space required to show this data only one manoeuvre is shown, but the collated results from multiple experiments are presented afterwards. These show the overall energy consumed by the actuation systems as a function of turn rate and preliminary comparisons between the actuator technologies are drawn.

Finally, examples of the load-speed data generated by the model are presented. These have uses in the design and specification stages of actuator development. Only a small subset of the 45 total figures are presented; showing how the load-speed envelopes of the actuators change with actuator technology, flight condition and turn angle in a representative fashion. When presenting results for different flight conditions, the EHA will be used.

When presenting results comparing actuator technologies, the approach flight condition and the 150° turn will be used, because the results are the most clear to visualise.

It helps to study the initial approach flight phase when the aircraft is at around 200 knots; at this velocity the flaps are retracted which avoids the issue of flap modelling on the aircraft model, while still allowing high turn rates to be achieved. In cruise (233 m/s), expecting a 0.03 rad/s heading rate requires a bank angle of over 40° which is clearly not realistic, so the range of plausible turn rates reduces.

The order of plots in this section is:

Time series plots of EHA at approach:

- xy trajectory plot of all experiments in one
- xy trajectory plot of 150° turn, EHA at approach
- Euler angles

- Altitude and airspeed
- Control surface deflections
- Aerodynamic load forces
- Electrical power consumption
- Mechanical power delivered

Energy plots:

- Mechanical energy delivered at approach
- Efficiency of energy conversion at approach
- Total energy consumed by the 3 technologies at approach [3 figures]

- Mechanical energy delivered at descent
- Efficiency of energy conversion at descent
- Total energy consumed by the 3 technologies at descent [3 figures]

- Mechanical energy delivered at cruise
- Efficiency of energy conversion at cruise
- Total energy consumed by the 3 technologies at cruise [3 figures]

Actuator force-speed plots:

- Force-speed plots of 3 technologies at approach [3 figures]
- Force-speed plots of EHA at 3 flight phases [2 figures (+1 previously shown)]
- Force-speed plots of EHA executing 3 heading changes [2 figures (+1 previously shown)]

7.1.2.1 Time series results

Trajectory The first plot in Figure 7.2 shows the superimposed trajectories of the aircraft at all turn rates and every heading change. It is intended merely to give the reader a clear picture of the experiment and what the autopilot, guidance algorithm and external scripting achieves. In every case the aircraft starts at (0,0) and flies parallel to the x axis, entering the figure at (200,0). When the aircraft is some distance from the waypoint at (300,0), a turn is initiated towards the new heading and throughout data is logged about the aircraft states and actuator power consumption.

To make the figure more clear for the single 150° turn case, the trajectories for other heading changes are removed in Figure 7.3. Although the plot does not provide results directly useful to the power consumption quantification, it sets the foundation for the following figures; it helps bring understanding to what may otherwise be somewhat abstract and difficult to visualise data.

The FCS and guidance system are shown to be effective at managing the manoeuvre. They maintain straight flight until the point of turn, hold a steady, constant radius turn before levelling off and continuing on the second leg of the route. A slight undershoot is evident on all turn rates, but is emphasized in the 0.005 rad/s case. This is acceptable since the aircraft smoothly intercepts the desired ground track without oscillation; this must strictly be avoided to minimise actuator power consumption.

To improve the turn anticipation function, a time-to-bank (TTB) estimation algorithm can be implemented which predicts how long (in time or distance) the aircraft will take to reach the desired bank angle (to achieve a specific radius turn). This is necessary since the assumption made in the guidance algorithm is that the aircraft achieves an instantaneous bank an-

gle at a set distance from the waypoint, which is clearly not true for a real aircraft.

Attempts were made to incorporate this into the guidance algorithm but two problems were uncovered: first is the complexity required to program a robust TTB estimator for all flight conditions, turn angles and rates. Second is the affect it has on the results; the most successful estimator (for a single flight condition) was found to be a nonlinear function which skewed the power consumption figures which will be presented later. The decision was made to implement a guidance algorithm which is as simple as possible to avoid confusing the results of the actuators and manoeuvre with those that are influenced by the guidance system.

One argument may be, why use a guidance algorithm at all? Using an open loop navigation mode, i.e. triggering all turns at a specific time or position causes the aircraft to exit the manoeuvre flying on separate but parallel ground tracks. This makes quantifying and comparing the results of different trajectories more difficult, so a compromise was made by using the simplest guidance control which achieved filleted waypoint transitions.

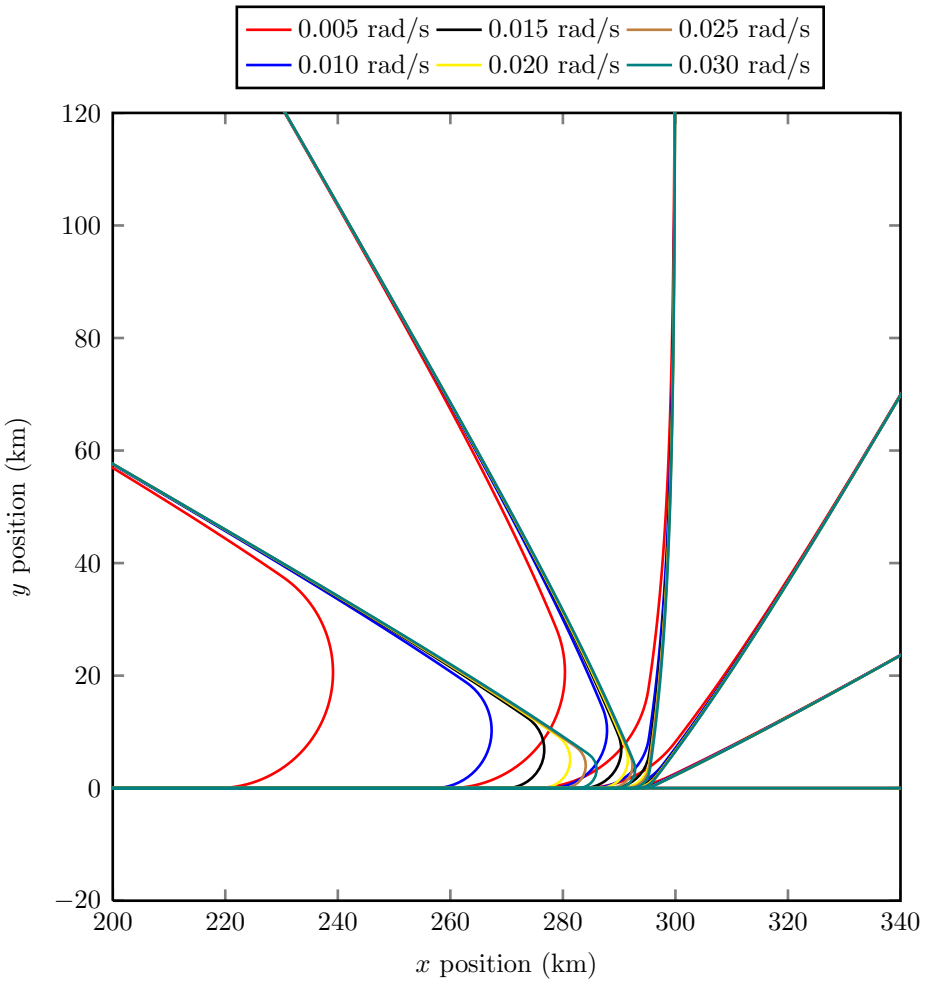

Figure 7.2: xy trajectories of heading and turn rate sweep for a EHA, at approach condition (102.9 m/s, 1000 m)

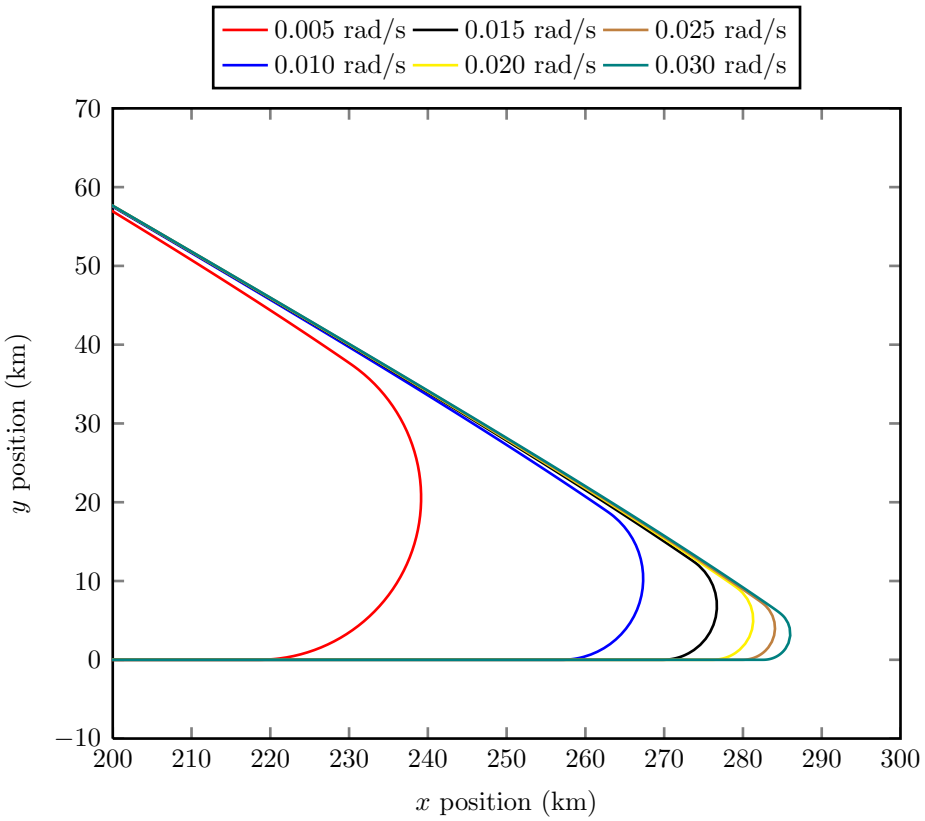

Figure 7.3: xy trajectories of turn rate sweep for a 150° turn, using EHAs at approach condition (102.9 m/s, 1000 m)

Euler angles The next figure 7.4 shows the Euler angles of the aircraft during the turn. This figure is useful to show how the three axes of motion interact during the manoeuvres, highlighting weaknesses in the control system if there are any. The expected behaviour is of course to see higher bank angles for higher turn rate cases, with a corresponding increase in pitch angle to maintain altitude.

The model produces the expected response, but with some problems at high turn rates. The turn rates from 0.005 rad/s to 0.015 rad/s achieve a constant roll angle during the turn with a relatively small increase in pitch angle. The pitching motion in well controlled for the slower turn rates but is diverging for the whole time the aircraft is banked for the 0.020 rad/s to 0.030 rad/s cases. This suggests the validity of the assumptions made in deriving longitudinal TECS reduces at high bank angles. During these cases the roll angle fails to reach a steady state value during the turn. The diverging pitch angle suggests the cross coupling between longitudinal and lateral motion is not well controlled by the functionally separate TECS and THCS algorithms. Some potential improvement could be made by including a crossfeed from THCS to TECS so that it is specifically aware of the bank angle and the effect this has on the longitudinal energy states through changing lift force direction.

Finally commenting on the heading angle plot; the gradient of the yaw angle is constant during the turns which shows that the aircraft is executing a continuous steady state turn. Given that for the three highest turn rates, the roll angle is not constant so it would be reasonable to assume there is a slight change in the gradient of the heading angle plot. However, this is difficult to perceive in Figure 7.4 because of the timescale used.

The yaw angles corroborate the trajectories presented in Figure 7.3, with

the constant radius turns (therefore constant gradient heading angle) and no overshoot or oscillatory motion when reaching the setpoint.

Altitude and Airspeed To demonstrate the problems with high turn rates further, the true airspeeds and altitudes of the aircraft during the manoeuvres are shown in Figure 7.5. Once again, for the lowest three turn rates the setpoint tracking is good, maintaining airspeed to within ± 1 m/s and altitude to within ± 5 m. However, for the three highest turn rates the tracking is not acceptable as there is a significant deviation from setpoint, as much as 40 m from the desired altitude and 8 m/s airspeed loss. Additionally, the aircraft states are diverging from the setpoints during the turn and only begin to correct themselves after the aircraft has levelled out. This again suggests a problem with TECS at high bank angles which is worthy of further study since a continuous turn at these angles would lead to a stall.

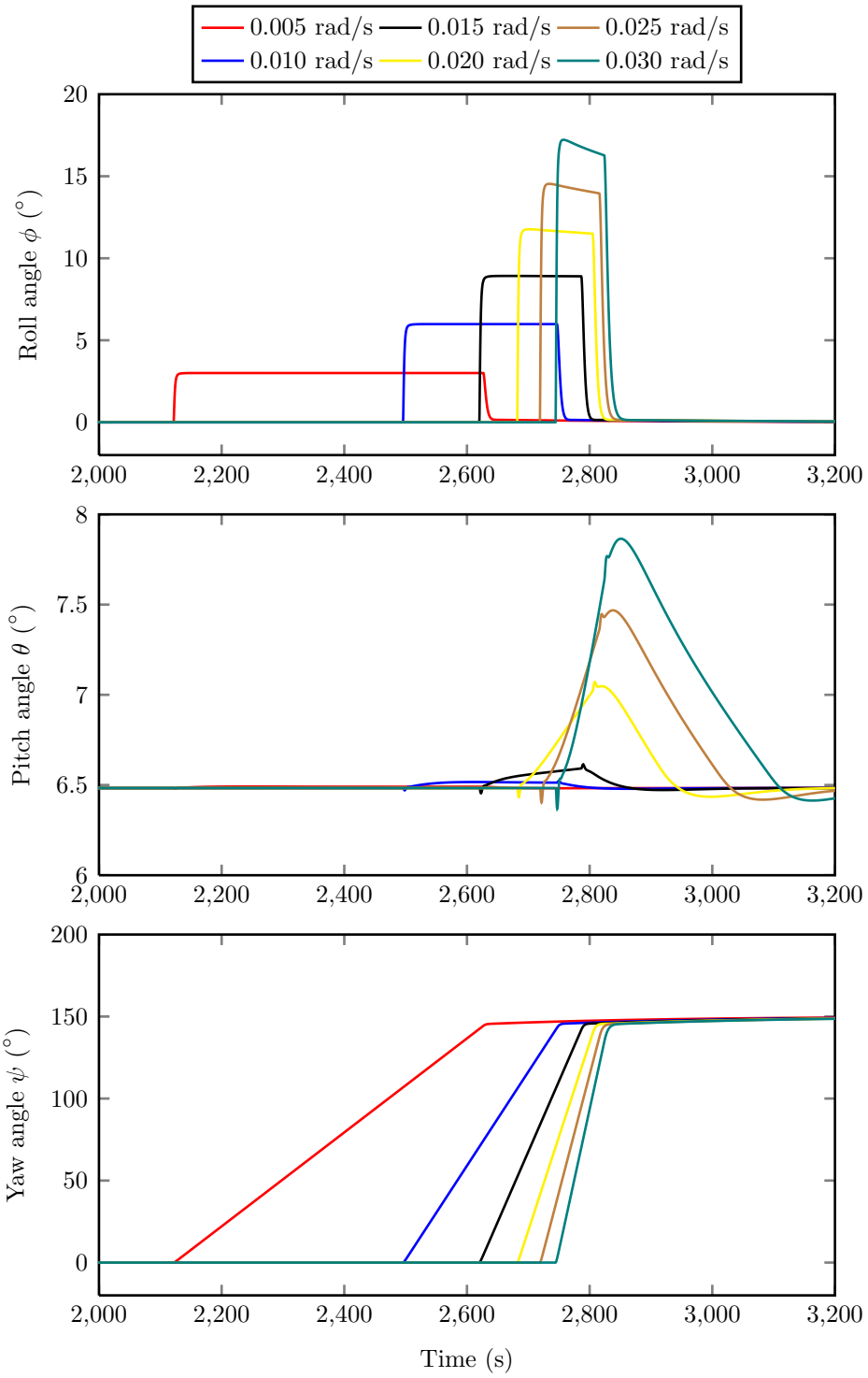

Figure 7.4: Euler angles during turn rate sweep, required to achieve a 150° turn using EHAs at approach condition (102.9 m/s, 1000 m)

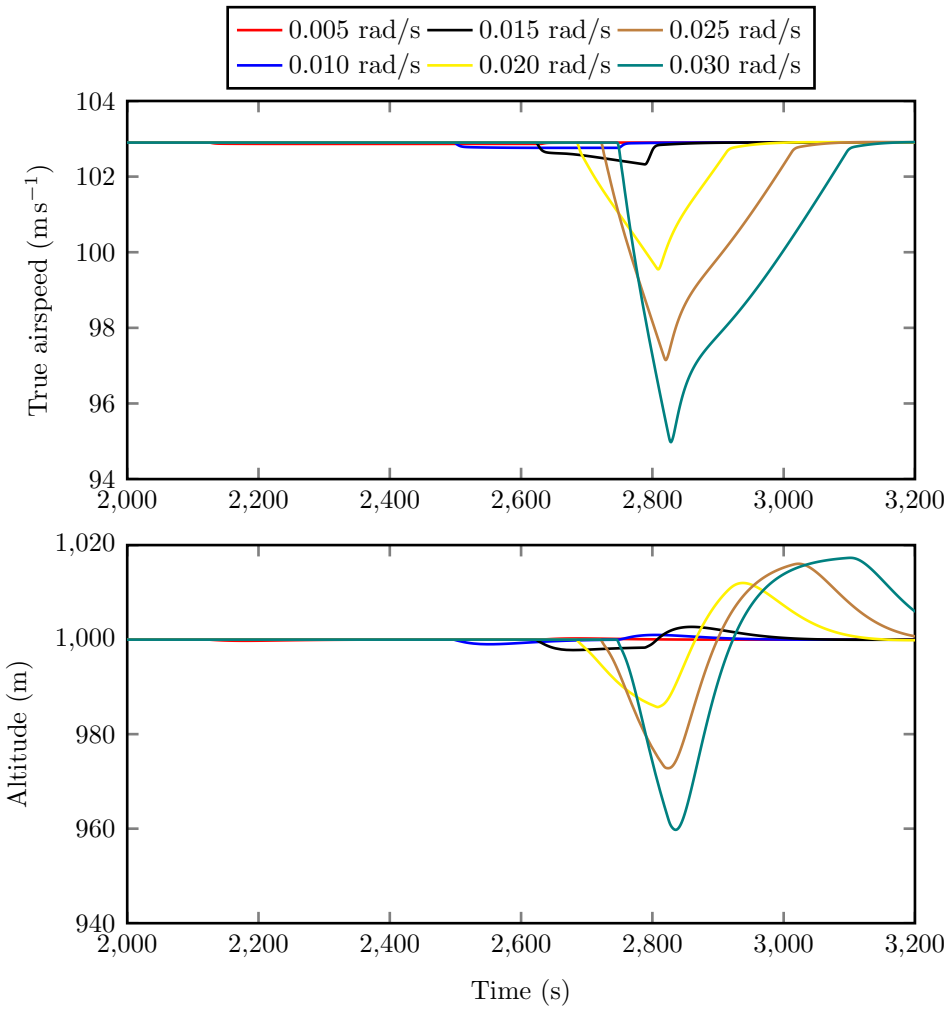

Figure 7.5: Altitude and airspeed during turn rate sweep, achieving a 150° turn using EHAs at approach condition (102.9 m/s, 1000 m)

Control surface deflection Perhaps a look at the control inputs in Figure 7.6 (the outputs of TECS and THCS) will provide a better understanding of the problem. The lateral controls are as expected; there is coordination between the ailerons and rudder, with an initial spike in aileron deflection to overcome the aircraft's moment of inertia and aerodynamic stability. It then decreases to a steady state value to maintain bank angle and turn rate. The rudder is moved smoothly into a position which provides the yaw moment required to coordinate the turn, before returning to a centred position when the aircraft levels out.

The longitudinal controls are not so neat however; as before, the three lowest turn rates show neat controlled motions in the elevator and throttle commands which become significantly more extreme for the highest three turn rates. A negative elevator deflection acts to raise the nose of the aircraft so the basic behaviour is correct to maintain altitude during a banked turn.

The throttle control is less ideal; for the low turn rates there is a initial decrease in throttle position (i.e. total energy) before increasing to a steady state position of increased total energy of the aircraft. For the three highest turn rates the TECS does not increase the throttle position fast enough to increase the total energy of the aircraft to maintain stable flight. Since published literature on TECS and THCS integration does not present time series control inputs it is difficult to problem solve the issue. One possibility that cannot be excluded is problems with the 6-DOF aircraft model and most likely, the merging of coefficients from DATCOM and Tornado. To be sure, more work needs to be undertaken to verify the aircraft model and FCS, or better to use a validated aircraft model if possible.

The throttle is limited to a minimum value of 0.2 which causes oscillations of the throttle control integrators which do not sufficiently manage wind-up.

Once the oscillations are damped out, a clear pattern is evident between the three highest turn rates so the saturation is not thought to have a serious effect on control performance. In the full TECS algorithm presented by Lambregts (see section 2.5.2 on page 96), an explicit method of handling control saturation is used to ensure safe flight. In the full design, when the throttle saturates the TECS reduces to control pitch angle only to ensure the aircraft speed does not decrease below stall or manoeuvring speed. This is not implemented in the model since envelope protection was not thought to be of interest to the work, but if it was, it is anticipated that the throttle saturation would be handled much more smoothly.

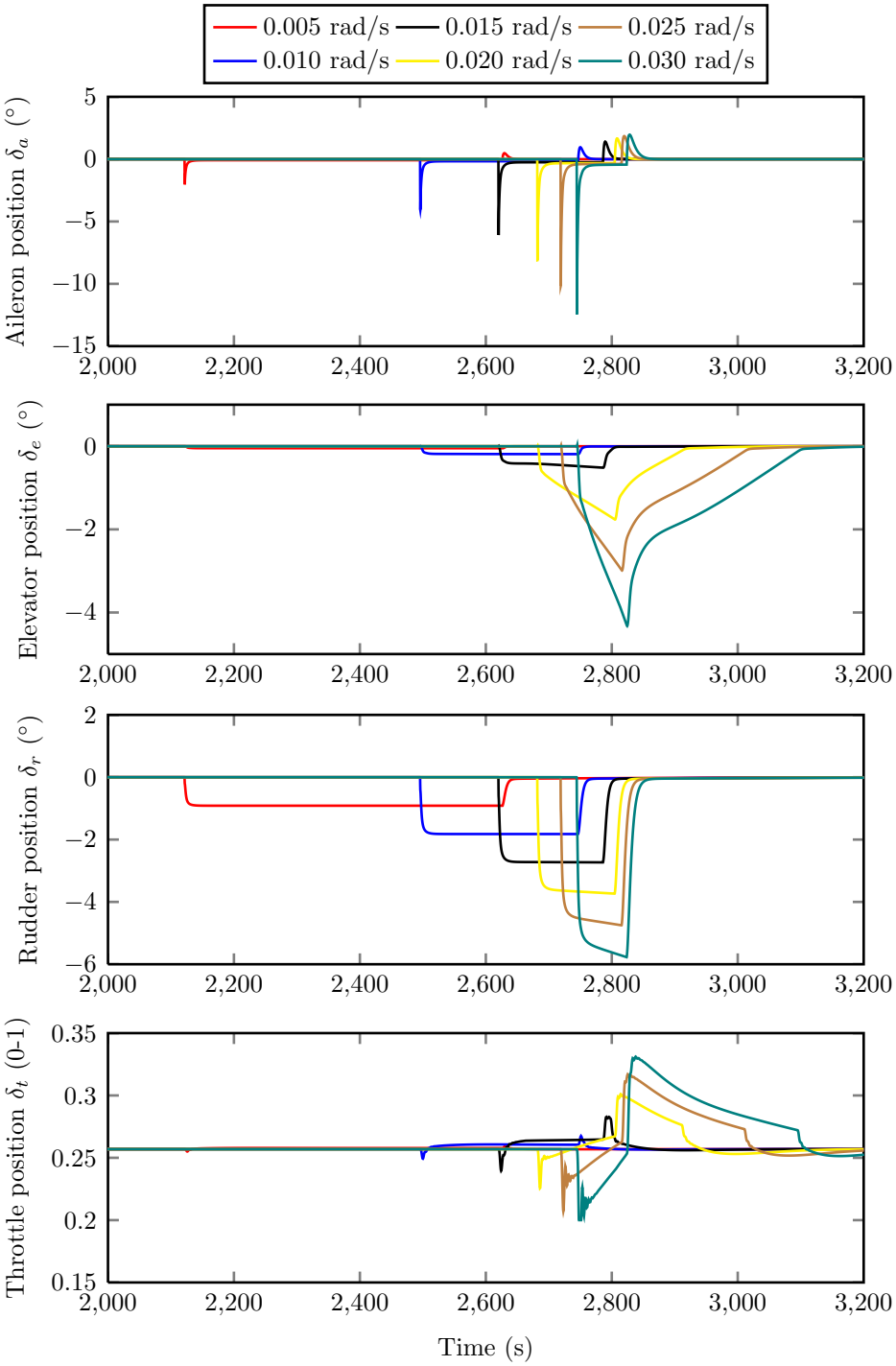

Figure 7.6: Control inputs during turn rate sweep, required to achieve a 150° turn using EHAs at approach condition (102.9 m/s, 1000 m)

Aerodynamic load force The primary mode of operation for flight control actuators is zero velocity, high force conditions. This means that when estimating power consumption in flight, the aerodynamic force on a control surface has a dominating effect compared to, for example, inertial acceleration which only occurs for very short periods in a flight. The model used to estimate aerodynamic force in this work uses a linear function of deflection at any given flight condition, therefore the shape of the plots in Figure 7.7 are expected to be the same as the deflections in Figure 7.6.

While it is impossible to validate quantitatively against real aircraft data without access to privileged information, it is possible to qualitatively verify the estimates. This is achieved by checking that the range of load forces is both within the specification in Table 3.1 and of the correct magnitude (it is expected to see forces in the kN range rather than MN or N). Aside from this, the actual values estimated do not have to be precise representations of the real aircraft. As long as they are consistent throughout the analysis, the numerical value is not so important.

Power consumption The final time series plots are the electrical or hydraulic power required from the aircraft in Figure 7.8, with the mechanical power of the output piston in Figure 7.9 to give an idea of the efficiency. The input and output power is presented in two figures as opposed to being combined into a single efficiency plot because of the problem of dividing zero when the mechanical power is zero at zero velocity. Efficiency will be presented again in the next section 7.1.2.2, regarding the overall energy used throughout the manoeuvre sweep.

Some interesting points about the plots are firstly that it is very difficult to see exactly what is happening on linearly scaled plots. An initial spike is

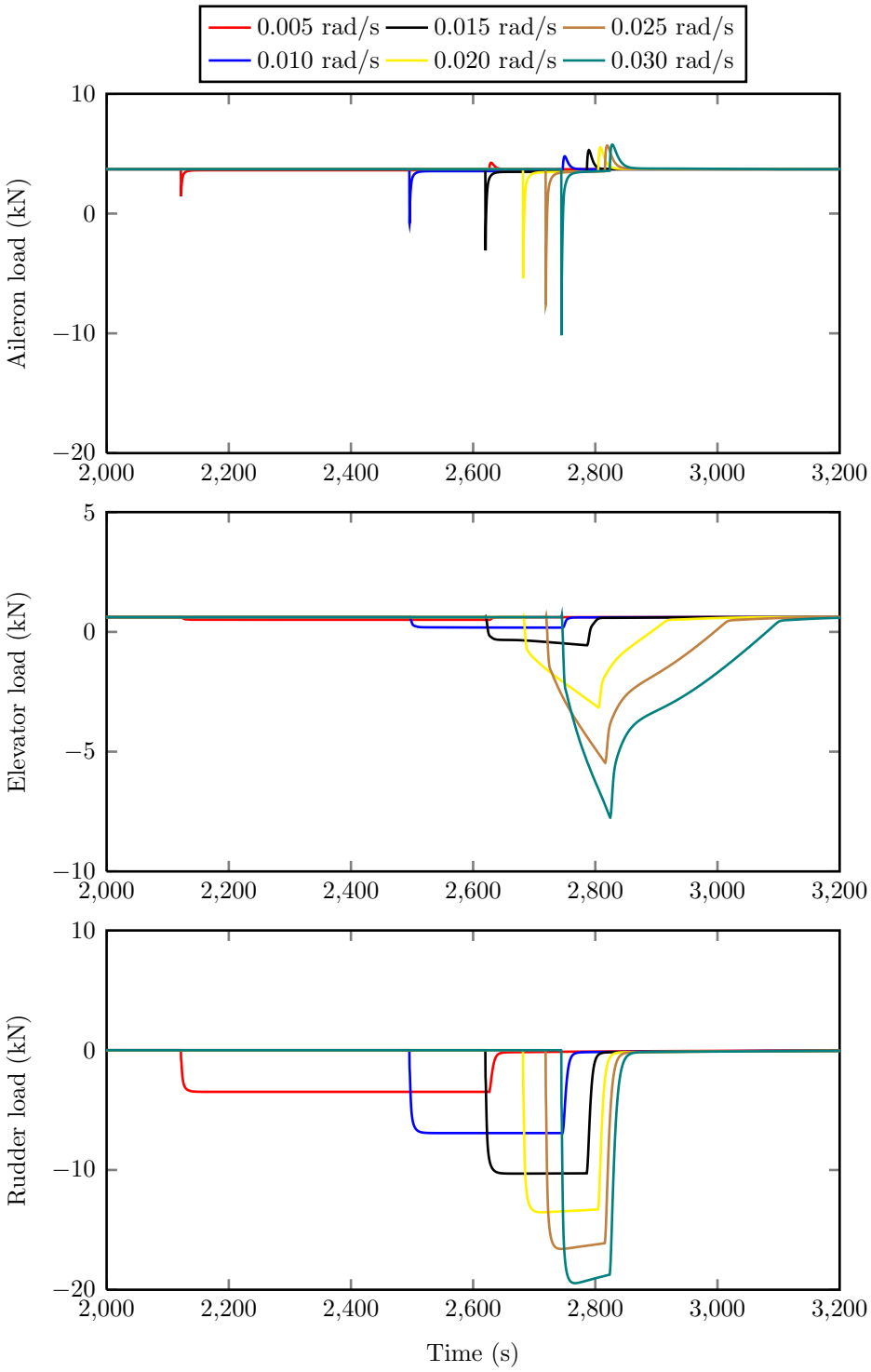

Figure 7.7: Aerodynamic load forces during turn rate sweep, required to achieve a 150° turn using EHAs at approach condition (102.9 m/s, 1000 m)

evident when the banked turn begins, which then reduces to an imperceptible steady state value during the turn. Although the plots are not useful to quantify the power consumption, they do highlight the benefit of using dynamic models for estimating power consumption compared to steady state duty cycle methods. By simulating the peak power flows, it aids the designers of power systems in sizing the system for both peak and RMS loads.

Also useful is the representation of the quadrant of operation - any time the power flow becomes negative it means the actuator is being aided by the load. Although not included in the simulation, these periods can be used to regenerate power to improve net efficiency. By storing the regenerated energy, less waste power needs to be dissipated through a resistor and therefore it can have a lower mass penalty on the aircraft.

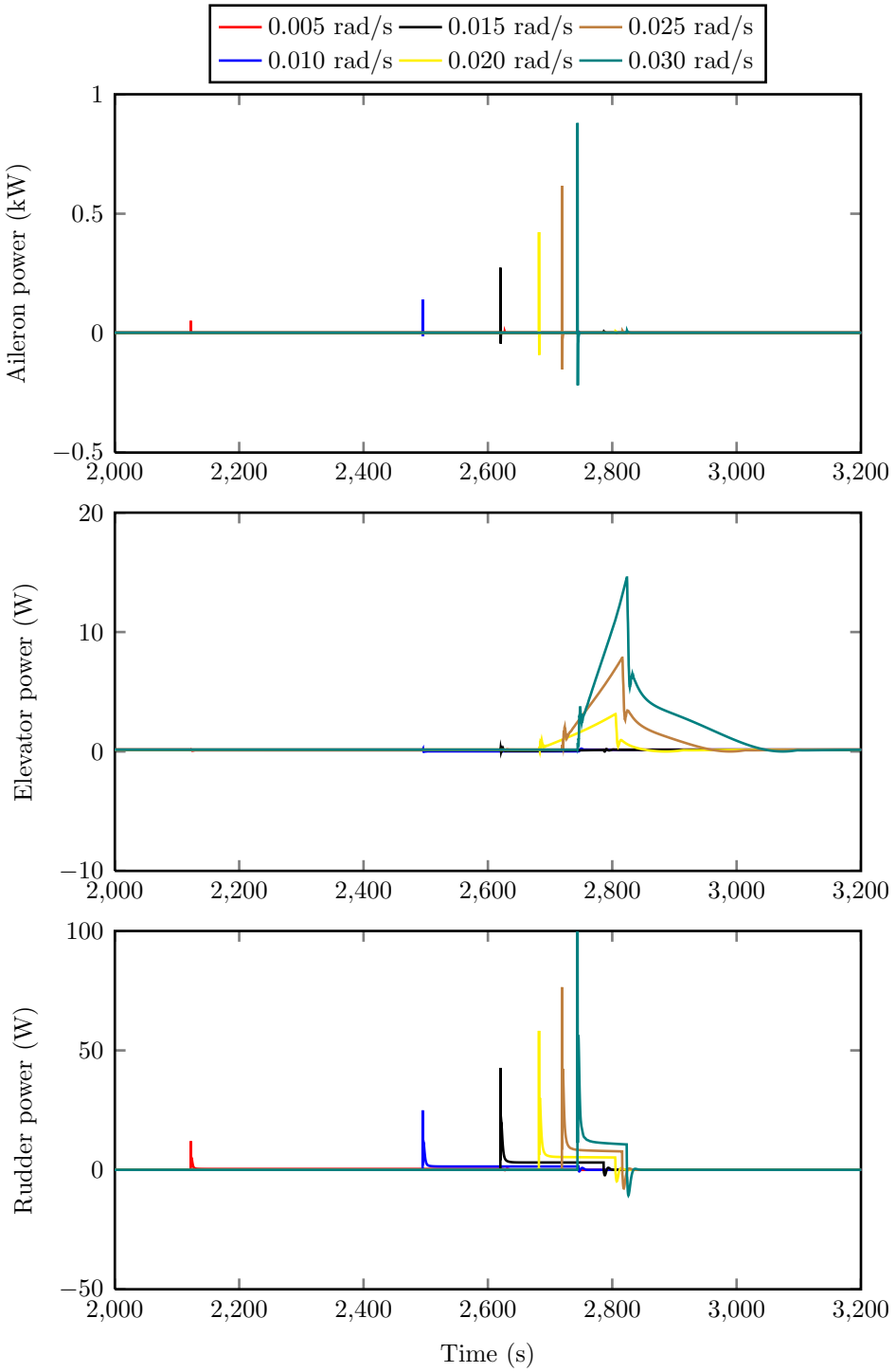

Figure 7.8: Electric power required during turn rate sweep, required to achieve a 150° turn using EHAs at approach condition (102.9 m/s, 1000 m)

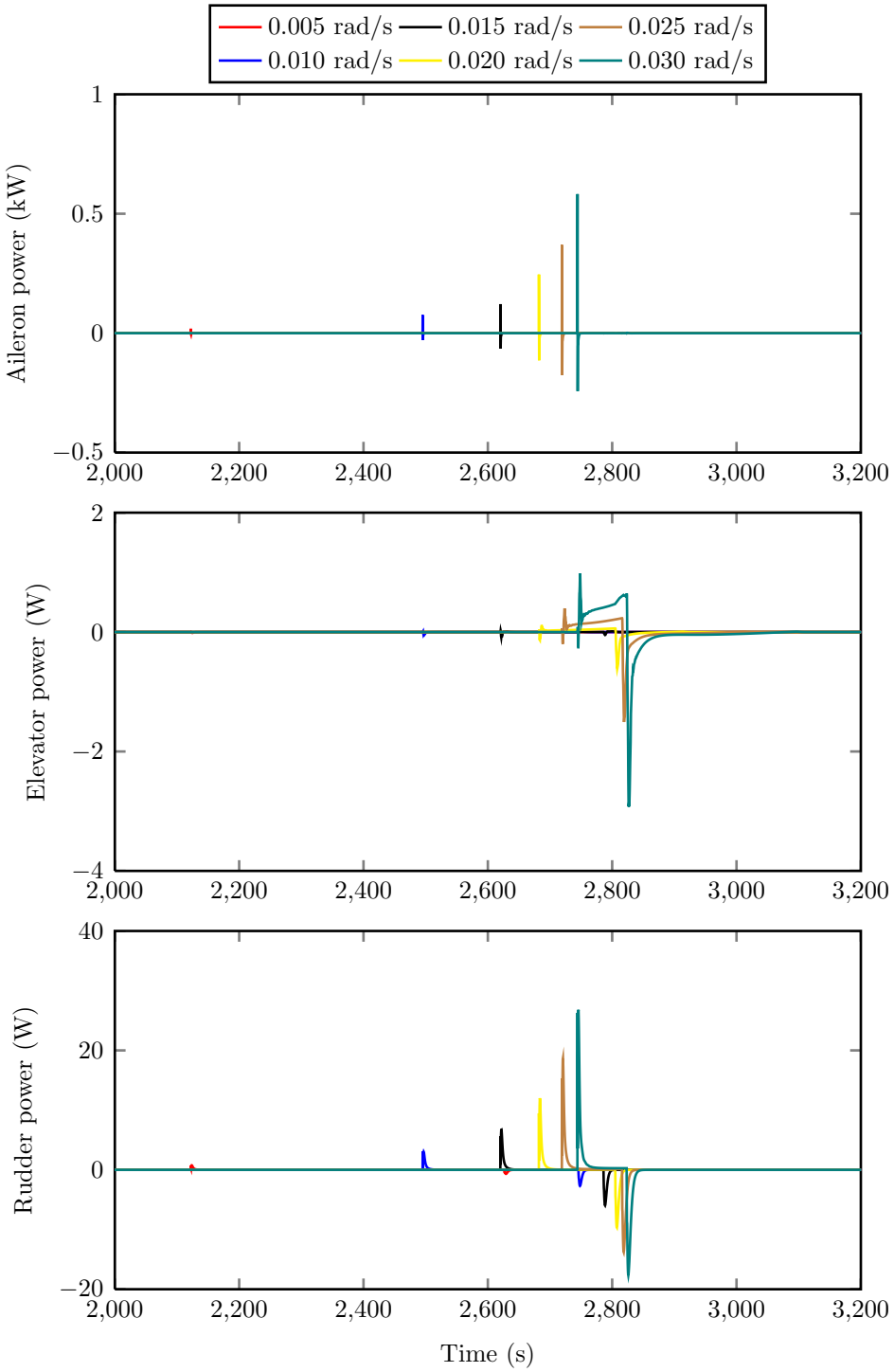

Figure 7.9: Mechanical power delivered during turn rate sweep, required to achieve a 150° turn using EHAs at approach condition (102.9 m/s, 1000 m)

7.1.2.2 Total energy consumed

The results presented in the previous section (7.1.2.1) show the time series data from a single heading change manoeuvre. To combine the results of all the flights shown in Figure 7.2, the time component must be removed from the results. To achieve this, the power consumption signals are integrated to find the energy consumed. This can be achieved using post processing but is easier to do inside the Simulink model; outputting time series energy data. The power signal is limited before the integrator to allow only the positive power flow to be included, this means there is no regeneration and all negative power flows are dissipated using a resistor. By taking the final value from the integrator, each flight can be reduced to a single value of energy consumed during that trajectory.

One problem that must be dealt with is the fact that each turn rate flight for a single heading change will take a different amount of time since they cover different distances. To make the results comparable they are averaged by the total distance flown during that particular flight. The end result is a value of energy per metre.

This data is plot on figures which combine data for the three actuator technologies, at a specified flight condition. Also presented are the energy consumptions for each of the three control surfaces: ailerons, elevators and rudder.

Approach - 102.9 m/s, 1000 m The first case to be presented is the approach phase for the ailerons (Figure 7.12), elevator (Figure 7.13) and rudder (Figure 7.14). The mechanical energy delivered to the load is shown in Figure 7.10 and the efficiency of the actuators calculated using mechanical power out divided by electrical or hydraulic power in and shown in Figure

7.11.

The mechanical energy figure is shown first because this directly enacts the manoeuvres by exerting work on the airflow around the control surfaces. It only includes positive energy flow and assumes all regenerative energy is wasted. It can be seen from the aileron plot in Figure 7.10 that the three technologies deliver different amounts of mechanical energy to the control surface; this is because of differences in the controllers for each actuator and not a reflection of the technologies themselves. When regenerative energy is captured with 100% efficiency, these plots lie almost exactly on top of each other. The plots for the elevator and rudder mechanical energy have this characteristic too but the difference is so small it makes it impossible to see on the plots in Figure 7.10.

Plotting the mechanical energy delivered with the energy drawn from the supply on the same figure is difficult because the range between them makes them both appear horizontal. A better option is to combine them to show the efficiency of energy conversion such as that shown in Figure 7.11. This figure shows the relative efficiencies of the actuators to be, in decreasing order EMA, EHA and finally the ESHA.

The efficiency of all the actuators increases as the turn rate goes up, because the average load force increases. With reference to the actuator performance validations in sections 3.1.7, 3.2.6 and 3.3.7 (on pages 147, 177 and 192) it can be seen that the efficiency of all technologies increases with load force.

The aileron exhibits a parabolic increase in efficiency which follows the pattern of the mechanical energy increase in Figure 7.10. This is because of the parabolic increase in the initial aileron deflection peak seen in Figure 7.6. This is a result of the FCS generating larger commands to roll the aircraft

faster as the turn rate increases. At maximum turn rate, the efficiency of the EMA is 2.2%, 1.5% for the EHA and 0.4% for the ESHA.

A significant increase in efficiency is seen from the electrical elevator actuators in Figure 7.11, particularly the EMA and to a lesser degree the EHA. This occurs from a turn rate of 0.015 rad/s and higher; it is caused by the excessive elevator deflection seen in Figure 7.6 at the higher turn rates. During the highest turn rate manoeuvres, the force on the elevator increases significantly which leads to the efficiency climbing to 10% for the EMA, 1.7% for the EHA and 0.3% for the ESHA at the maximum turn rate.

The rudder actuators see a linear increase in efficiency which is attributed to the linear increase in deflection angle (and therefore aerodynamic load force) seen in Figure 7.6. For this control surface the loading is higher, as a proportion of stall force, compared to the aileron and elevators. Because of this the rudder actuators see the highest efficiency of all: 23% for the EMA, 13% for the EHA and 4% for the ESHA (at the maximum turn rate).

Finally, the results which show how much energy is drawn from the aircraft power supply buses are shown for the full heading and turn rate sweep (shown in Figure 7.2) in Figures 7.12 to 7.14. The figures are divided into three; the first, Figure 7.12 shows the average energy consumed by the three actuation technologies on the ailerons. The second, Figure 7.13 shows the elevator data for each technology and Figure 7.14 shows the rudder data for the three technologies.

The overall power supplied to the aileron actuators is as expected; more power is required to enact higher turn rates since a higher force is required. Executing a longer turn at the same turn rate only requires a small increase in average power since the majority of the energy is used to roll the aircraft to begin and end the turn (see figures 7.6, 7.7 and 7.8). The power required

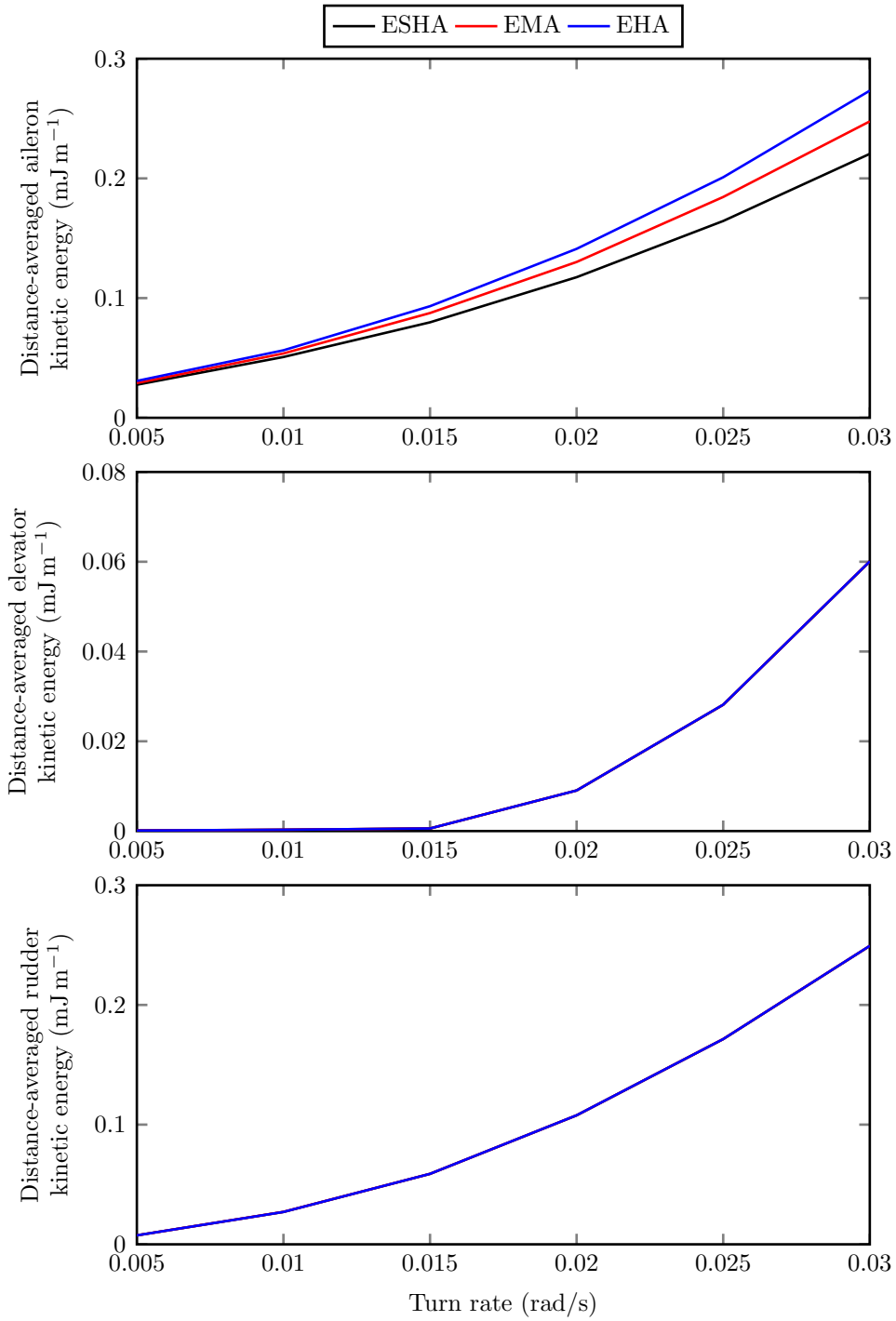

Figure 7.10: Distance-averaged mechanical energy of output piston for all technologies during a 150° turn, at approach condition (102.9 m/s, 1000 m). Top figure: Aileron, Middle: Elevator, Bottom: Rudder

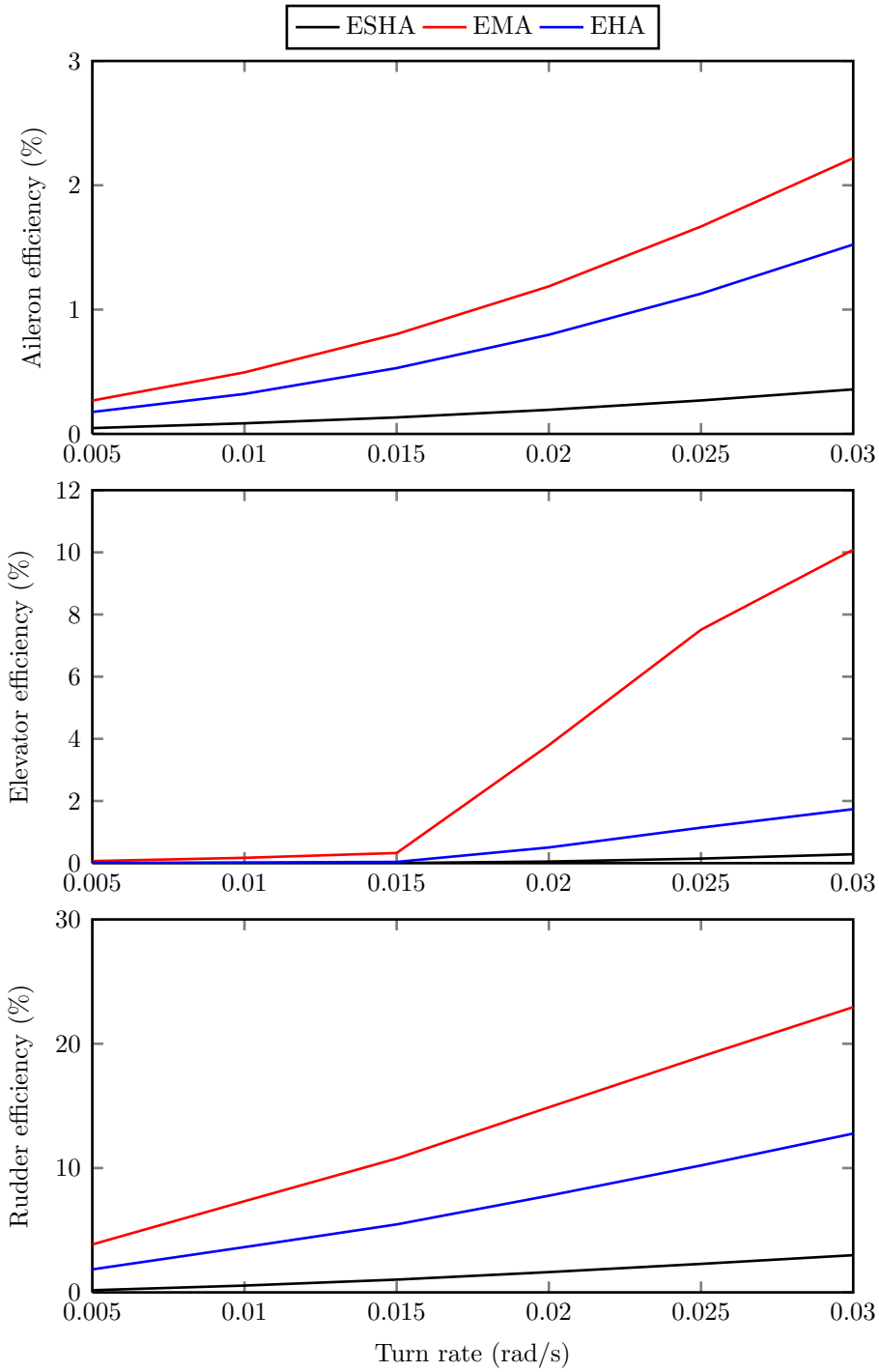

Figure 7.11: Efficiency of actuation technologies (average mechanical energy delivered to load / average energy from supply) during a 150° turn, at approach condition (102.9 m/s, 1000 m). Top figure: Aileron, Middle: Elevator, Bottom: Rudder

by the ailerons during a steady state banked turn is only slightly higher than that when flying straight and level.

The difference in curvature between the actuation technologies in Figure 7.12 is attributed to the combination of the different shape efficiency and energy delivered plots in Figures 7.10 and 7.11. The electric actuators appear to have greater variance between different heading changes at high turn rates. This is just because of the relative scales of the y axes; the ESHA has a 0.15 mJ/m difference between the 30° and 150° turns. The EMA has a 0.06 mJ/m range and the EHA has 0.1 mJ/m.

Considering the 150° turn during the approach condition in Figure 7.12, the ESHA uses 4.23% more energy to achieve a turn at a turn rate of 0.03 rad/s compared to a 0.005 rad/s manoeuvre. The EMA uses 1.67% more and the EHA uses 1.54% more to achieve the same turns. It can therefore be concluded that implementing some scheme of reduced turn rate turns in appropriate situations would have the largest benefit for current hydraulically powered aileron systems, compared to the electrical actuators.

The elevator data in Figure 7.13 shows a slightly different trend; the mean energy supplied initially decreases with increasing turn rate, before increasing parabolically beyond 0.01 rad/s turn rate. The initial decrease occurs because the elevator deflection in steady level trimmed flight is not equal to the position of zero hinge moment. An unpowered elevator will trail a few degrees upwards of its trim position, forced by the oncoming airflow. In a typical transport aircraft the horizontal stabiliser provides a downwards force to counteract the nose down pitching moment of the wings and fuselage. When the aircraft banks, the downwards force of the horizontal stabiliser must increase to raise the angle attack and maintain constant altitude. For small bank angles this means the elevator deflects upwards into a position of

lower hinge moment. When the bank angle increases more, the aerodynamic load begins to increase again as the surface deflects up into the airflow.

In this instance, the actuator requiring the most power to complete the manoeuvre is the ESHA and the least is the EMA. This continues the pattern seen throughout the results.

Finally, the rudder energy consumption is shown in Figure 7.14. The most notable difference in this figure from the aileron and elevator data is the difference in energy consumption due to the turn angle. The rudder response does not have an initial spike when deflected to coordinate the turn (see Figure 7.6) and the force increases linearly with deflection. In this situation the duration of the turn has a slightly more noticeable effect on energy consumption, but mainly the large increases between different heading changes is due to the substantially increased load force due to sideslip angle.

One point to notice from the results of all three control surfaces is the increased energy demands of the ESHA at low turn rates. This is caused by the servovalve optimum power transfer point discussed in section 3.1.3, where maximum power transfer occurs when ⅔ of the supply pressure is dropped across the load. When the load is below this, or very low in the case of the 0.005 rad/s turn rates, the efficiency decreases substantially.

Therefore, it can be concluded that if the duty cycle is going to involve continuous operation at low load then electrical actuators may be more power efficient. This depends of course on the reliability of the modelling of losses in the actuator models - something which has definite room for improvement.

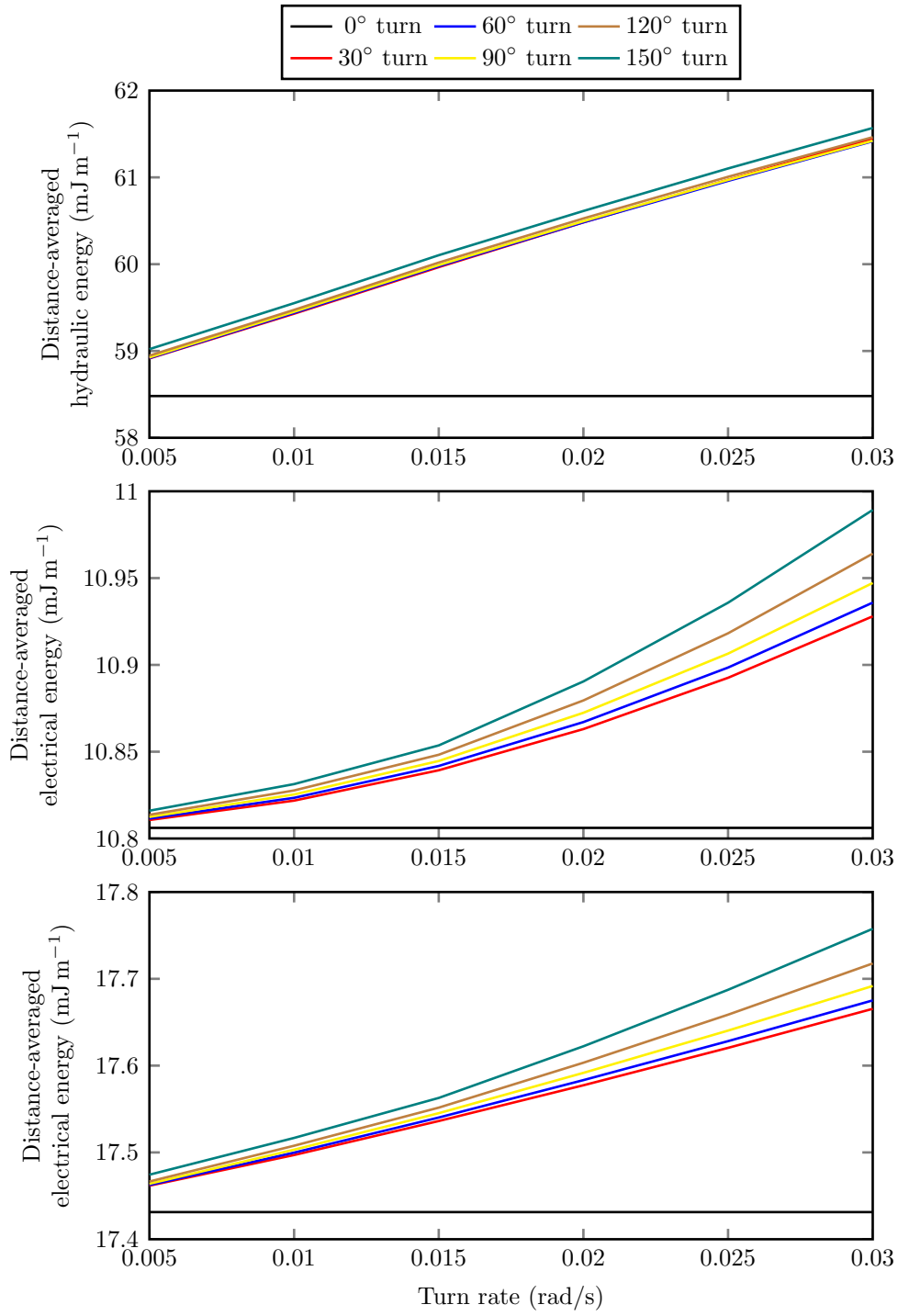

Figure 7.12: Distance-averaged energy demands from ailerons during turn rate sweep of all heading changes, using three actuation technologies at approach condition (102.9 m/s, 1000 m). Top figure: ESHA, Middle: EMA, Bottom: EHA

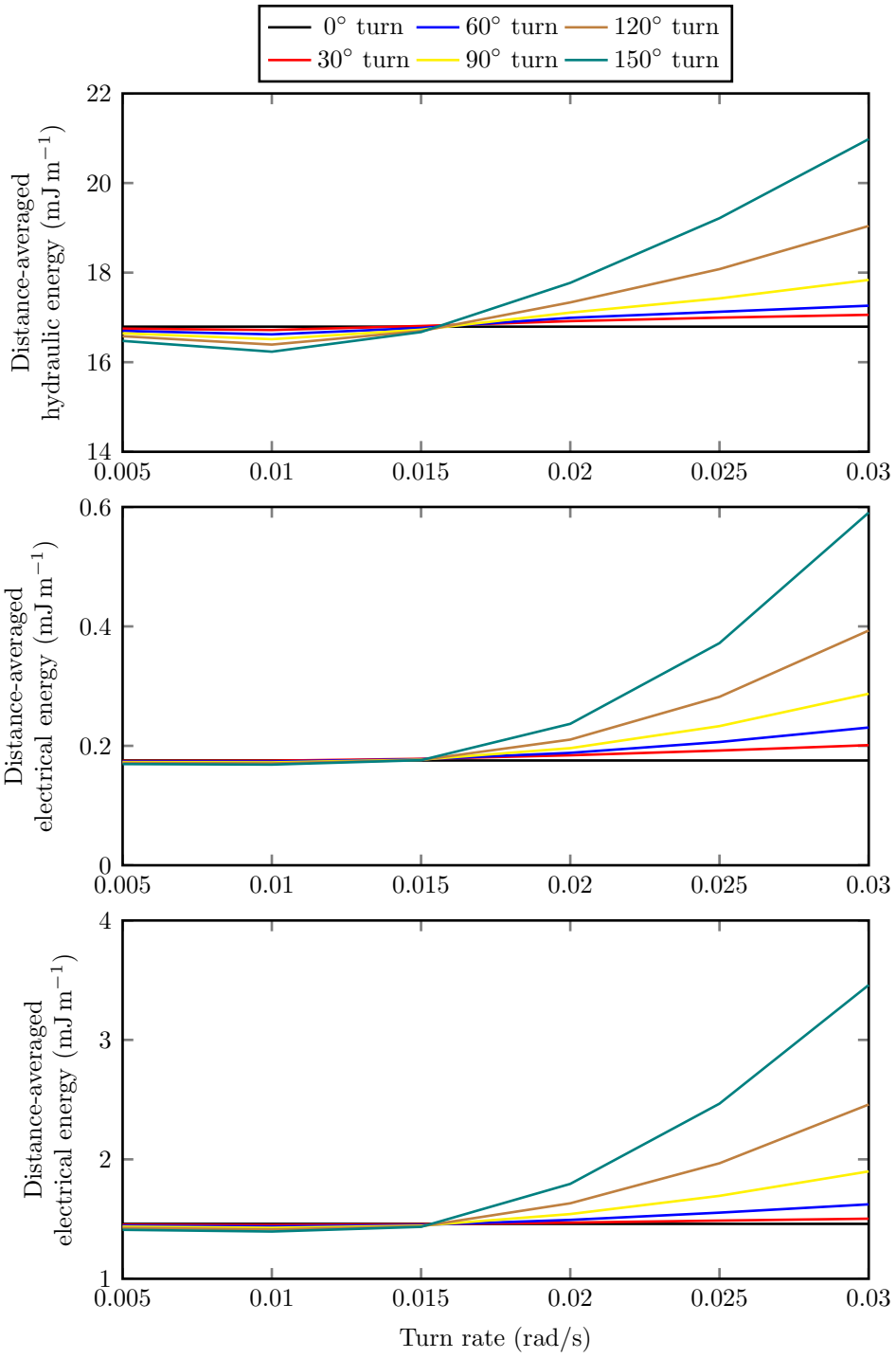

Figure 7.13: Distance-averaged energy demands from elevators during turn rate sweep of all heading changes, using three actuation technologies at approach condition (102.9 m/s, 1000 m). Top figure: ESHA, Middle: EMA, Bottom: EHA

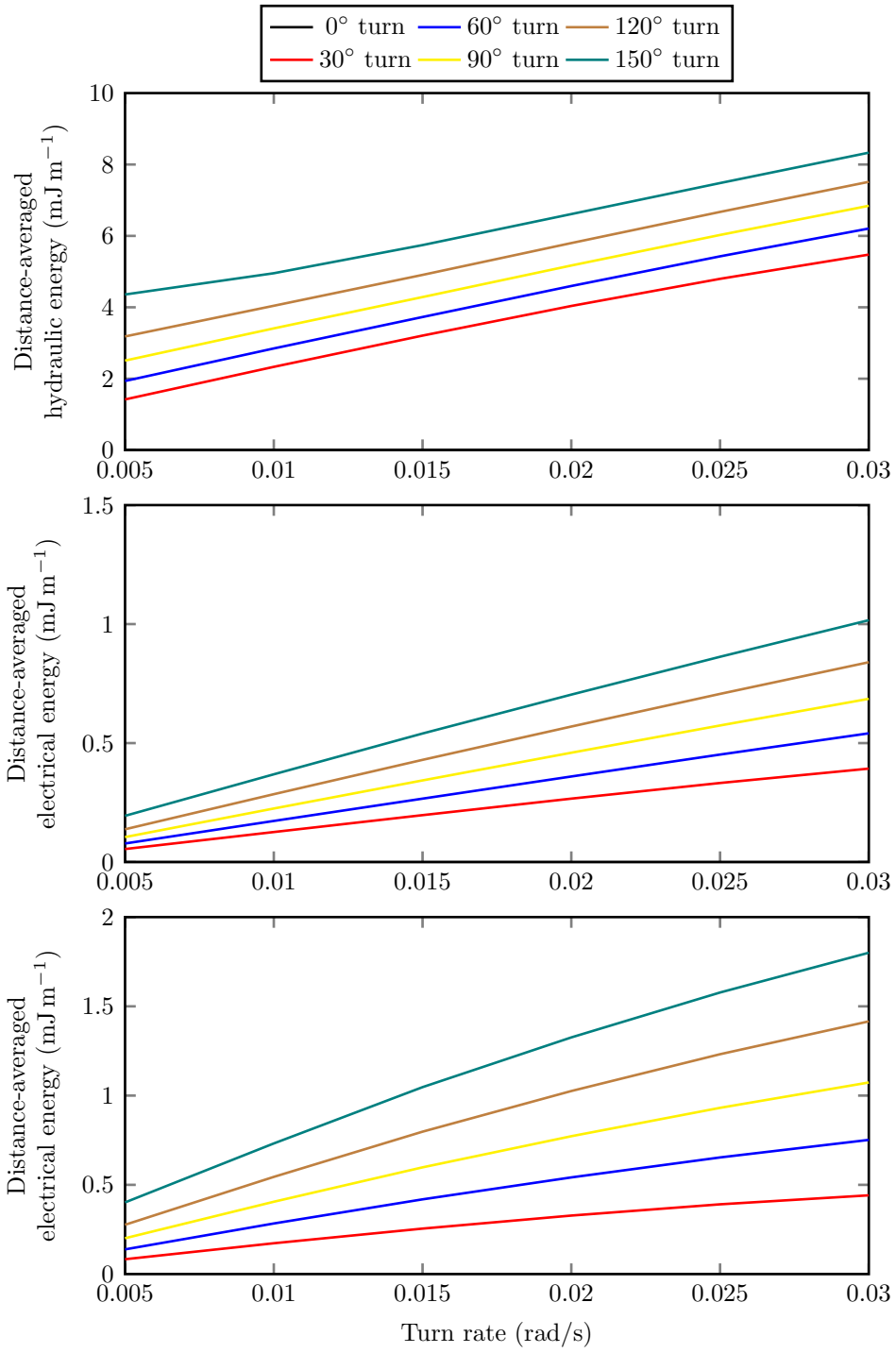

Figure 7.14: Distance-averaged energy demands from rudder during turn rate sweep of all heading changes, using three actuation technologies at approach condition (102.9 m/s, 1000 m). Top figure: ESHA, Middle: EMA, Bottom: EHA

Descent - 129 m/s, 3333 m The aircraft in the descent phase is travelling faster and higher than the approach. The dynamic pressure has increased and so an equal deflection causes a higher aerodynamic hinge moment on a control surface. Likewise, a smaller deflection angle will induce the same body angular acceleration as a large one during the approach condition.

The results in this section are conducted at the same turn rates which are used in the approach phase; since the speed is now different each turn rate will correspond to a different bank angle and turn radius to the previous section. Although more convenient for compatibility with the FCS, the downside is that the energy consumptions of manoeuvres executed at the different flight conditions are not directly comparable.

The general patterns seen in the approach phase are also exhibited in the descent results; the higher the turn rate, the more energy is used. The magnitude of energy consumption does vary from the previous flight condition however. Since the turn rates are equal to the approach case but the aircraft is now flying faster, the bank angle and turn radius must increase to achieve an equal turn rate.

As seen in Figure 7.15, the mechanical energy delivered by the ailerons is slightly greater than for the approach phase (Figure 7.10 on page 286), but the efficiency doubles from around 2% to about 4% for the EMA in Figure 7.16. This is a result of the aileron actuators experiencing a higher average load force during the trajectory. The effect is to actually reduce the amount of power demanded from the aircraft power supply (Figure 7.17), because the efficiency gain outweighs the increased energy requirement.

The elevator energy consumption in Figure 7.18 shows much the same behaviour at the descent condition as it does during approach (Figure 7.13 on page 291). The only difference is that at low turn rates, the elevator

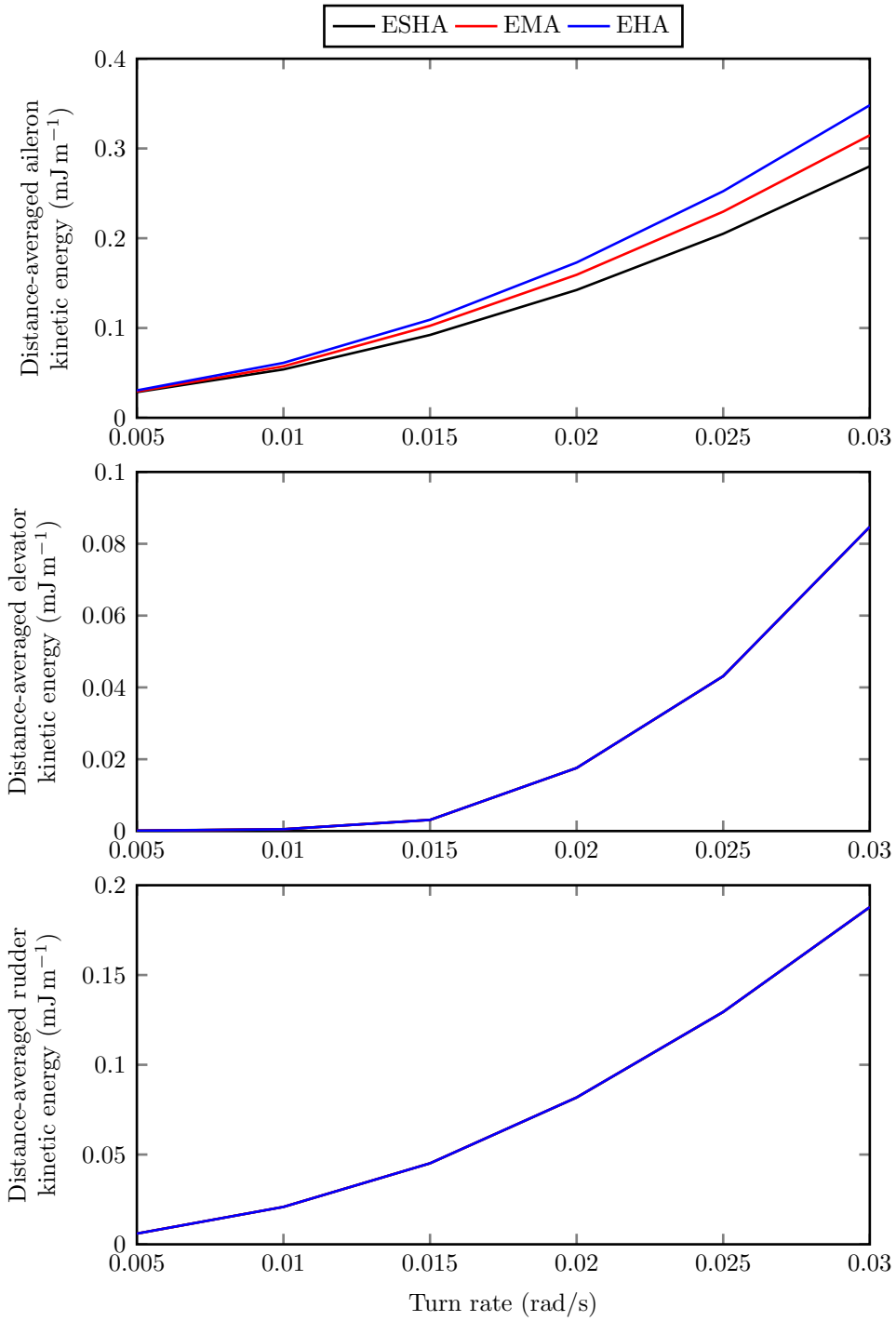

Figure 7.15: Distance-averaged mechanical energy of output piston for all technologies during a 150° turn, at descent condition (129 m/s, 3333 m). Top figure: Aileron, Middle: Elevator, Bottom: Rudder

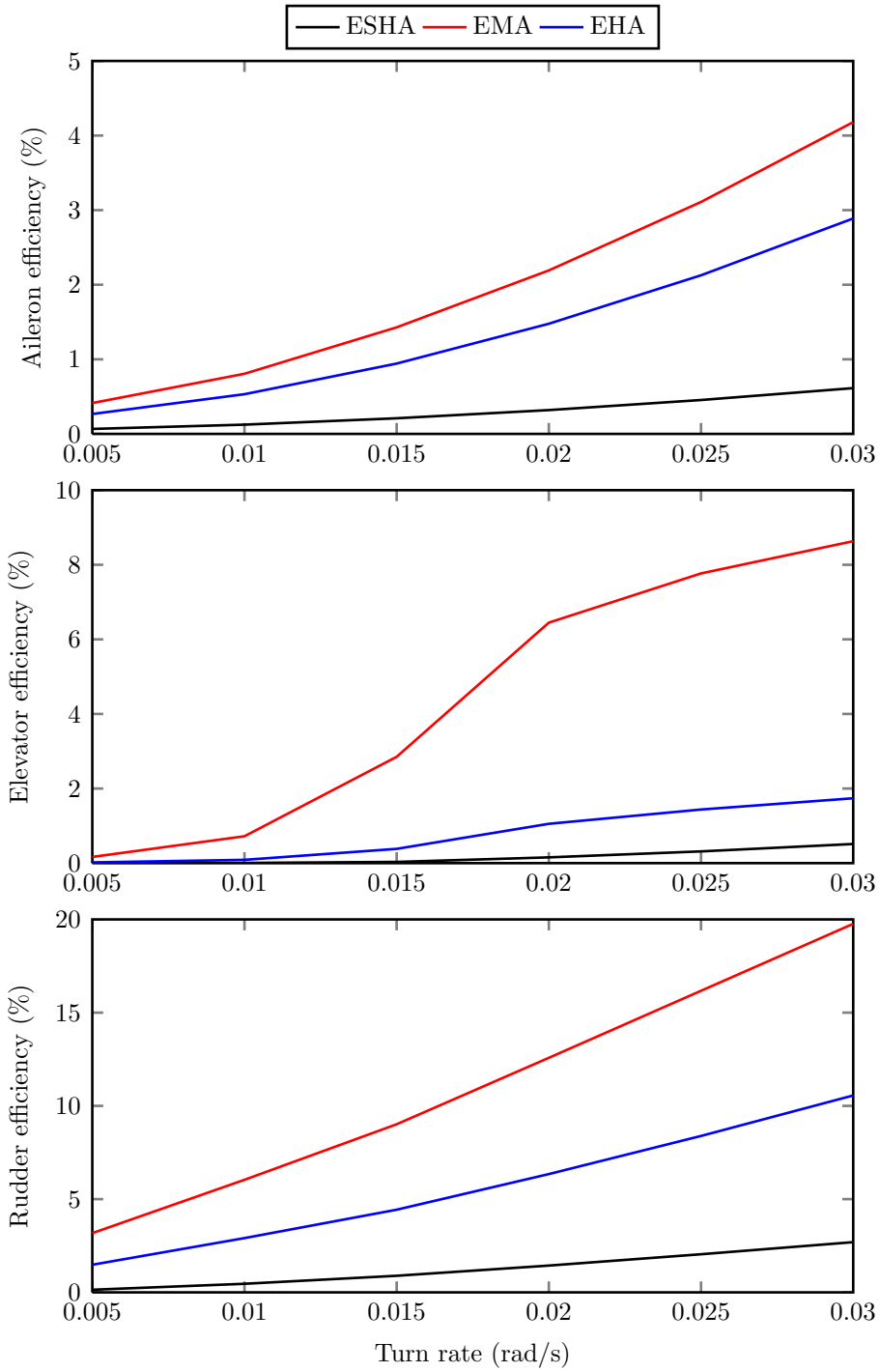

Figure 7.16: Efficiency of actuation technologies (average mechanical energy delivered to load / average energy from supply) during a 150° turn, at descent condition (129 m/s, 3333 m). Top figure: Aileron, Middle: Elevator, Bottom: Rudder

does not move to a lower aerodynamic force position, therefore the energy consumption does not go below the 0° line at any turn rate. This behaviour is decided almost entirely by the functions of downwash at the tail and angle of attack at the trimmed flight condition, thus it is dependent on the 6-DOF aircraft model used.

While every aileron actuation technology uses less power at the higher airspeed and altitude case, the same is not true for the elevator. The ESHA energy decreases as before but the electric actuators both use more energy in the higher dynamic pressure flight condition. This is because the efficiency of the ESHA increases from Figure 7.11 to Figure 7.16 while the electric actuators' efficiency decreases. As with the aileron case, the mechanical energy delivered increases with dynamic pressure, but the relative increase of efficiencies offset this. Overall, the energy demanded from the aircraft is reduced.

The rudder energy consumptions in Figure 7.19 do not vary much from the results in Figure 7.14. The mechanical energy delivered decreases with increasing dynamic pressure, but so to do the efficiencies of each actuator technology; affecting the EMA the most and the ESHA the least. Overall the ESHA energy demand stays the same but the electric actuators require marginally less power at the higher and faster flight condition.

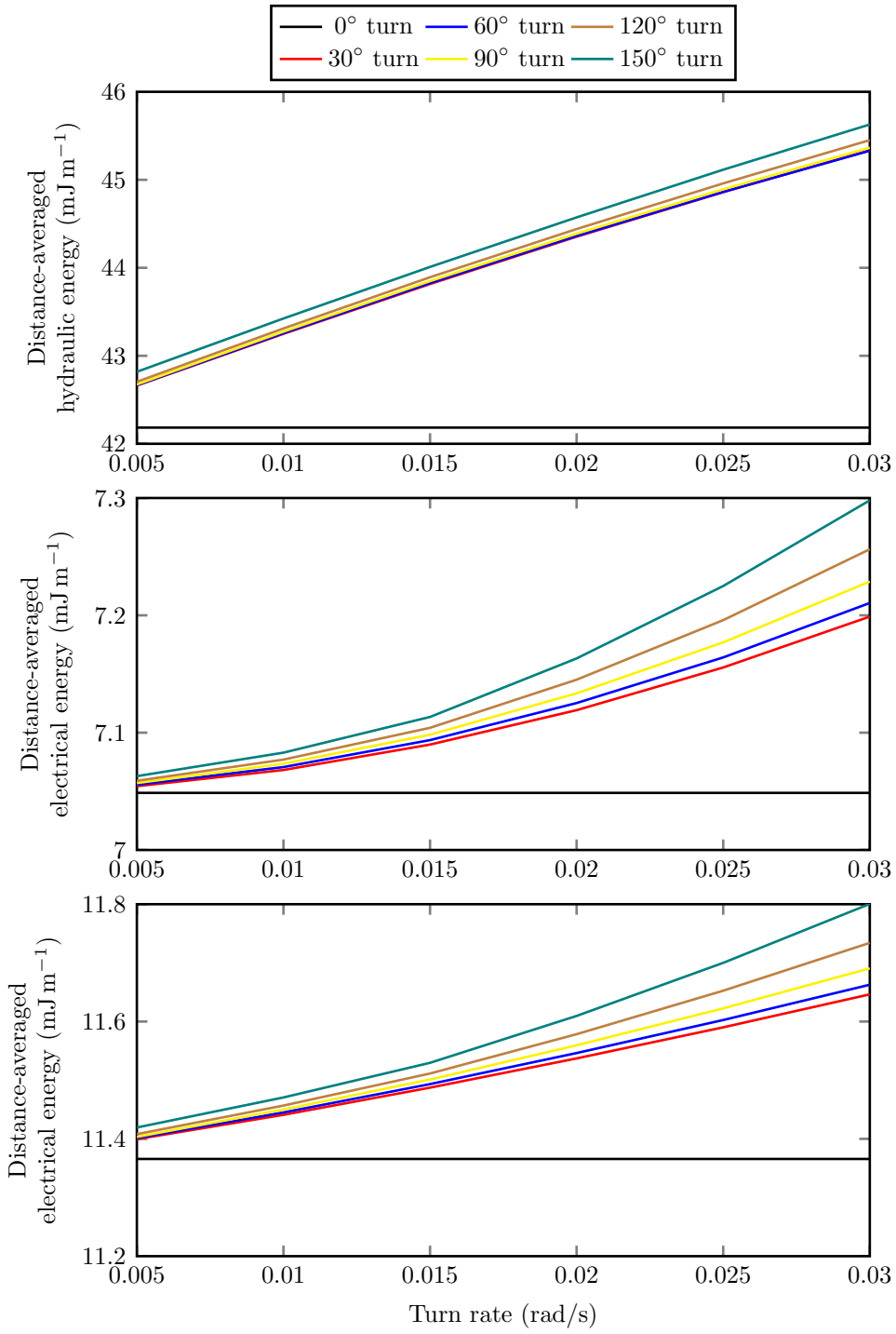

Figure 7.17: Distance-averaged energy demands from ailerons during turn rate sweep of all heading changes, using three actuation technologies at descent condition (129 m/s, 3333 m). Top figure: ESHA, Middle: EMA, Bottom: EHA

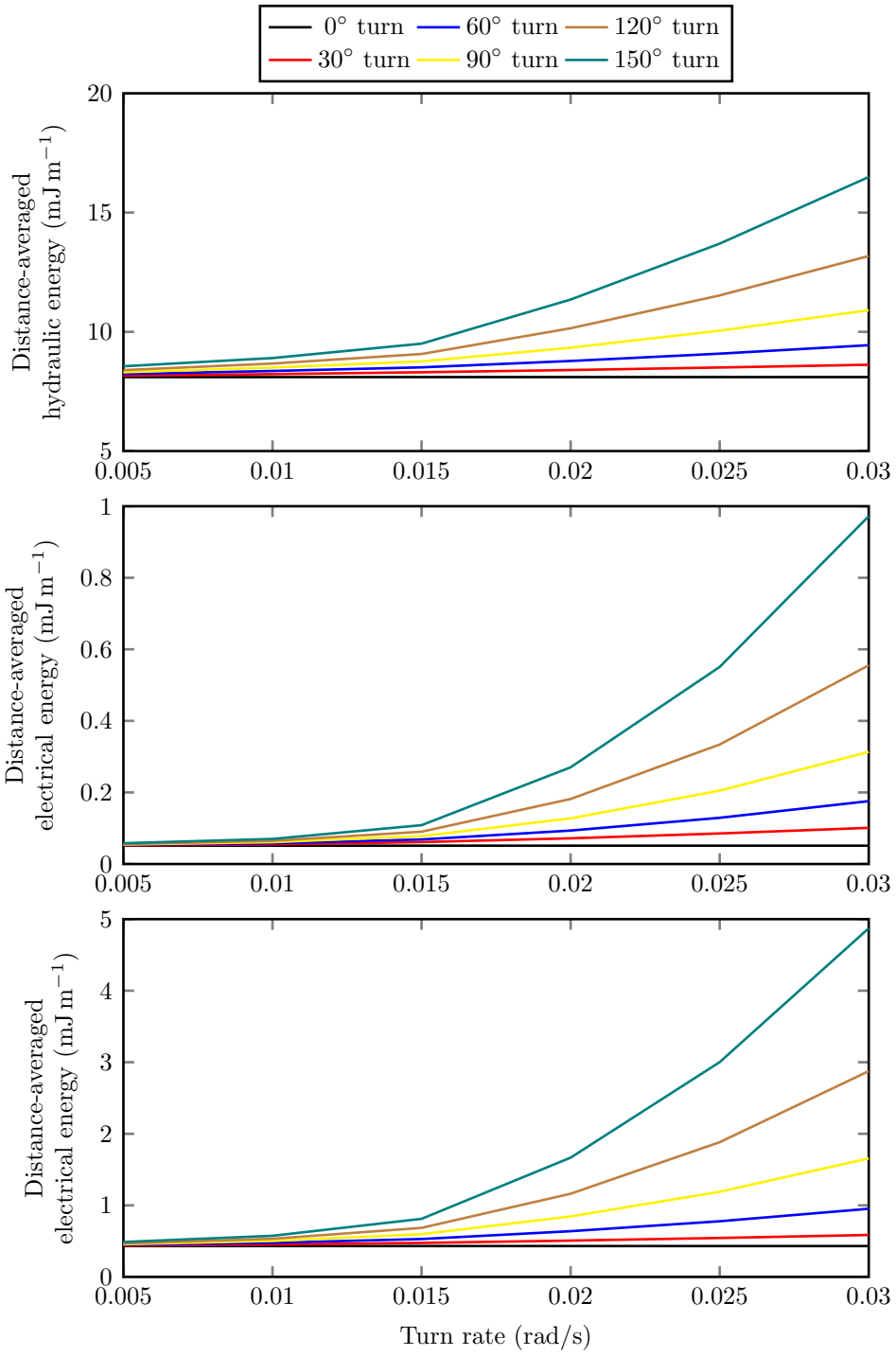

Figure 7.18: Distance-averaged energy demands from elevators during turn rate sweep of all heading changes, using three actuation technologies at descent condition (129 m/s, 3333 m). Top figure: ESHA, Middle: EMA, Bottom: EHA

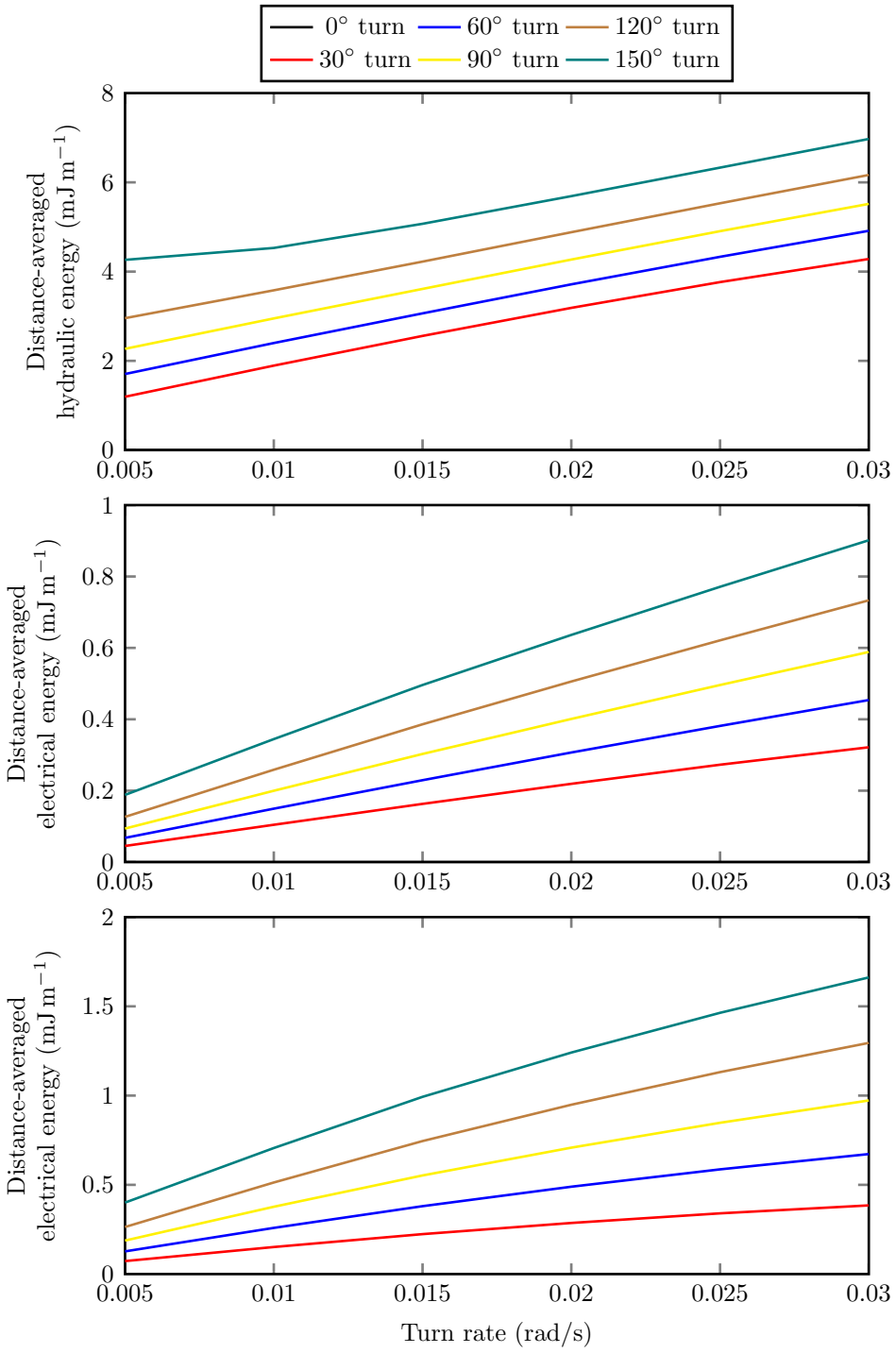

Figure 7.19: Distance-averaged energy demands from rudder during turn rate sweep of all heading changes, using three actuation technologies at descent condition (129 m/s, 3333 m). Top figure: ESHA, Middle: EMA, Bottom: EHA

Cruise - 233 m/s, 10000 m The cruise condition represents another step increase in dynamic pressure; but as before, the nonlinear efficiency characteristics of the actuators mean it is not necessarily true to expect proportional increases in actuator energy consumption. The mechanical energy output from the aileron and elevator actuators in Figure 7.20 increases as one would expect at a higher dynamic pressure, however the rudder decreases. The increased dynamic pressure again induces an increased efficiency for all aileron actuators, but decreased efficiency for the elevator and rudder.

Overall, because the efficiency of the aileron actuators more than doubles (in the EMA case) as the dynamic pressure increases to cruise condition, the energy consumed by all technologies in Figure 7.22 reduces from the descent condition in the previous section of results.

As noted previously, since the commanded turn rates are the same as in the approach and descent phases, the bank angle and turn radius increases with the increased aircraft velocity. Because the load force on an aileron during a steady state banked turn is only marginally higher than during steady level flight, the increased power requirement is offset by the significantly increased efficiency.

One issue that arises in the cruise condition is failure of the aircraft to achieve a stable turn above 0.01 rad/s. With the thinner air there is less excess thrust available to maintain the lift required to maintain altitude, which becomes particularly accentuated at high bank angles. The effect is the same as that seen in Figure 7.5 but amplified; the deviations from trimmed altitude and airspeed are greater, even at a lower turn rate.

The problem is most evident in the aileron energy consumption plots in Figure 7.22, where the data becomes distorted over 0.01 rad/s. Combined with the nonlinear efficiency data for the aileron shown in Figure 7.21, the

average energy required at the highest turn rate is lower than that at a low turn rate. This is not true in the real world; the turn rate on the x axis of the figures is a turn rate *command*, the aircraft does not necessarily achieve it when the bank angle required is too large to allow proper longitudinal control. If the x axis was plot using the achieved turn rate, which is lower for a given y axis datapoint, the high turn rate power consumption would increase.

The elevator and rudder data in Figures 7.23 and 7.24 show the same trends seen in the descent case described previously. The elevator experiences a significant increase in energy demand, due to the very high loads it experiences during the high bank angle turns executed in the cruise condition. The rudder on the other hand sources less power compared with the descent condition; because it exerts a lower force for a slightly shorter amount of time.

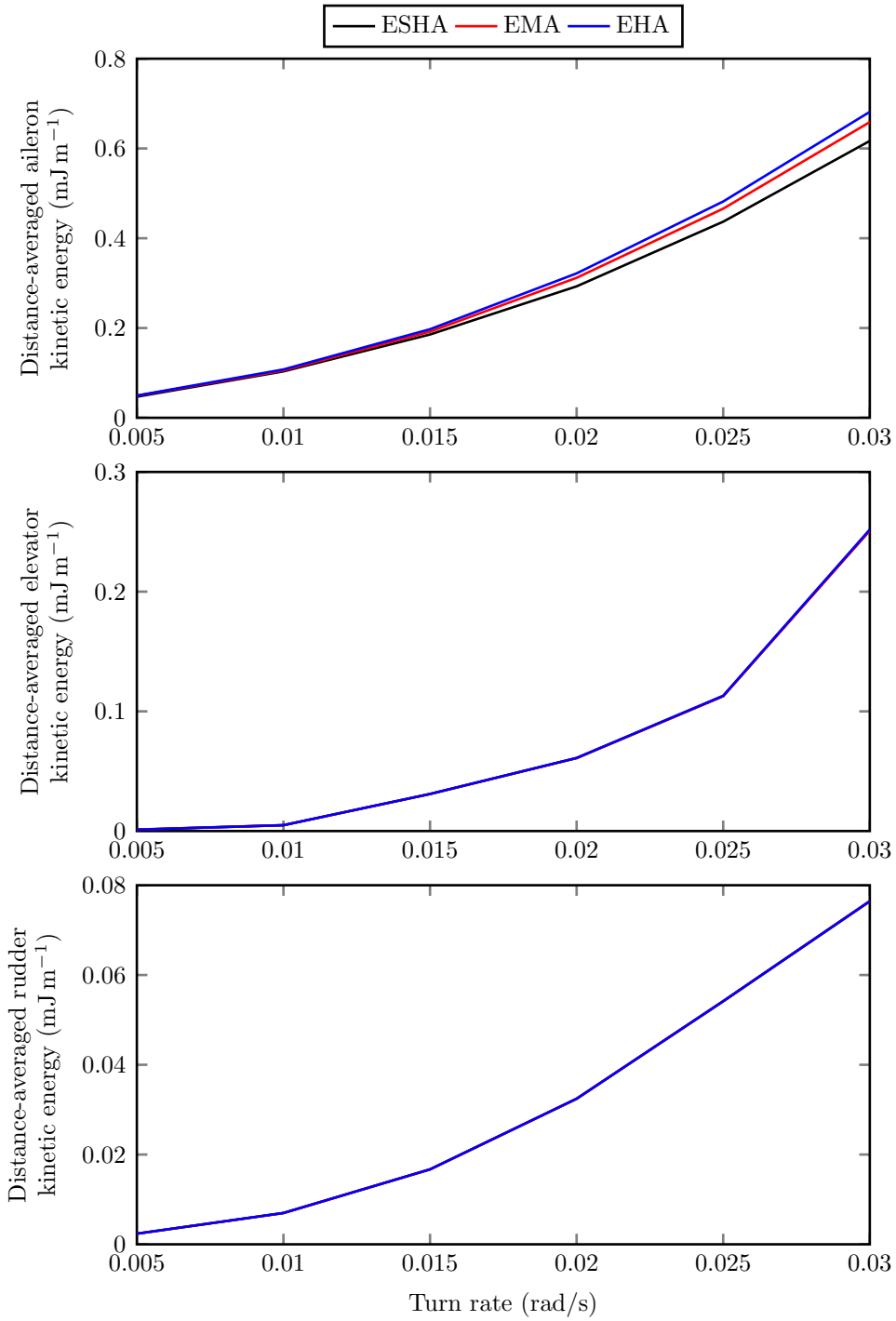

Figure 7.20: Distance-averaged mechanical energy of output piston for all technologies during a 150° turn, at cruise condition (233 m/s, 10000 m). Top figure: Aileron, Middle: Elevator, Bottom: Rudder

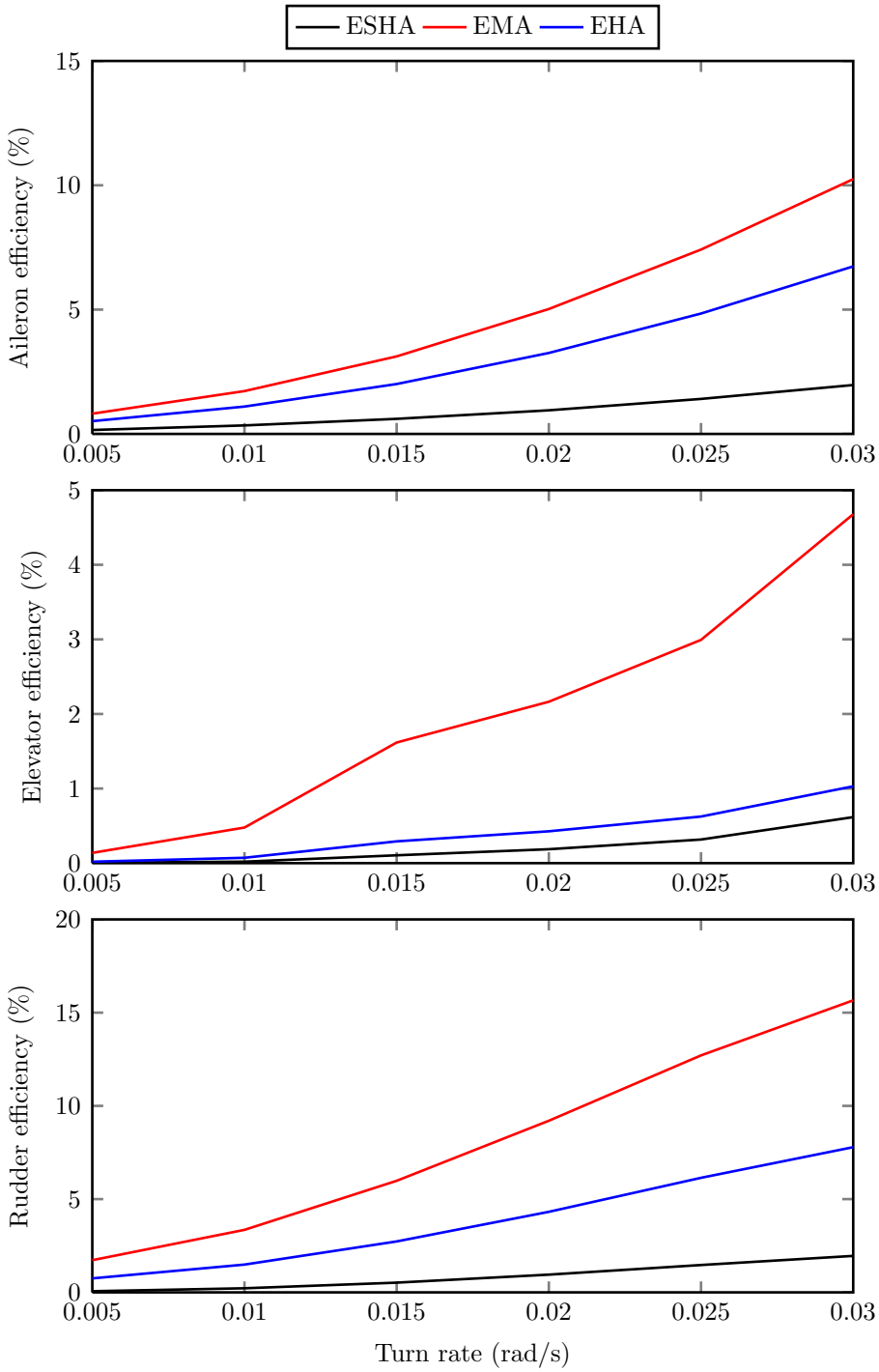

Figure 7.21: Efficiency of actuation technologies (average mechanical energy delivered to load / average energy from supply) during a 150° turn, at cruise condition (233 m/s, 10000 m). Top figure: Aileron, Middle: Elevator, Bottom: Rudder

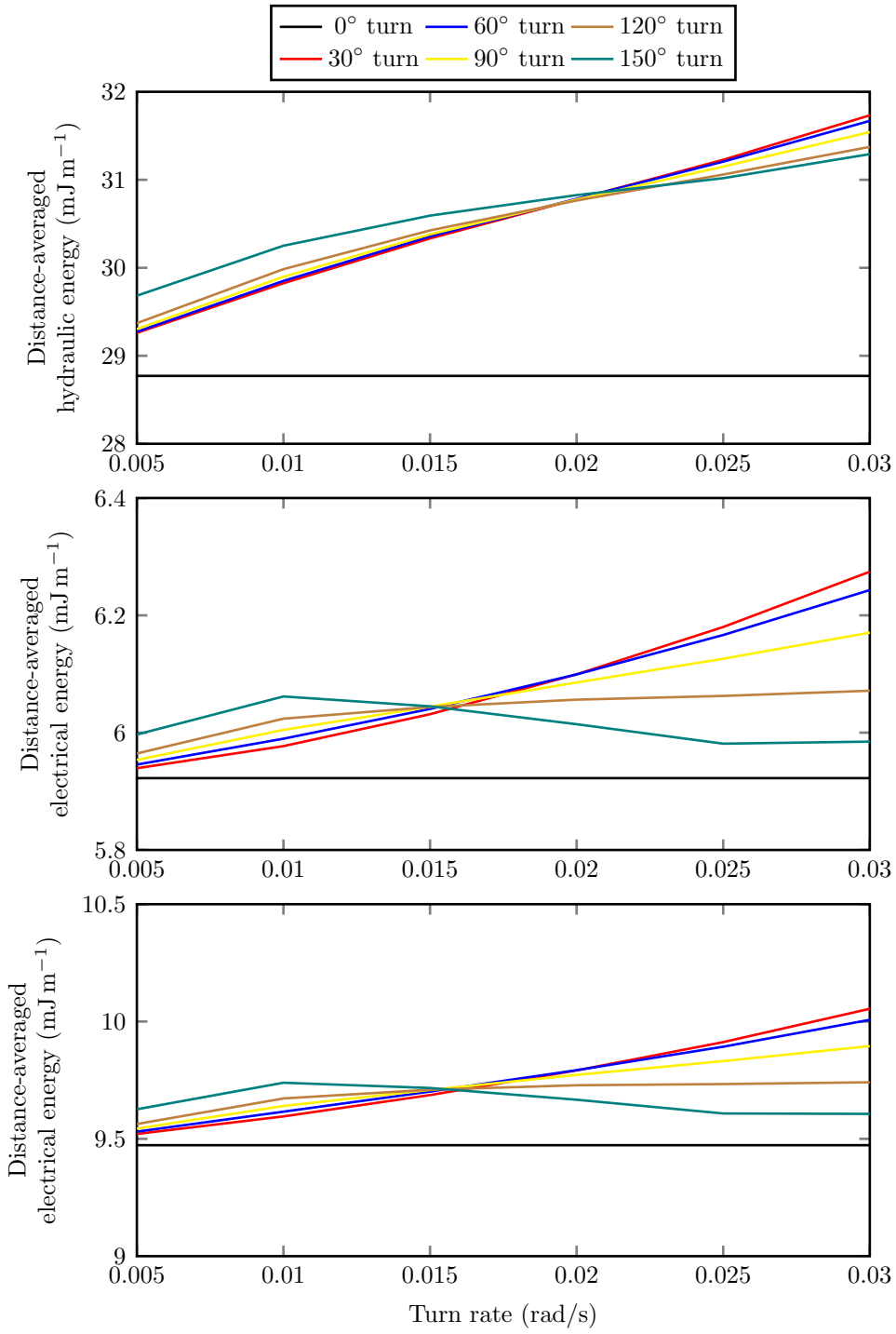

Figure 7.22: Distance-averaged energy demands from ailerons during turn rate sweep of all heading changes, using three actuation technologies at cruise condition (233 m/s, 10000 m). Top figure: ESHA, Middle: EMA, Bottom: EHA

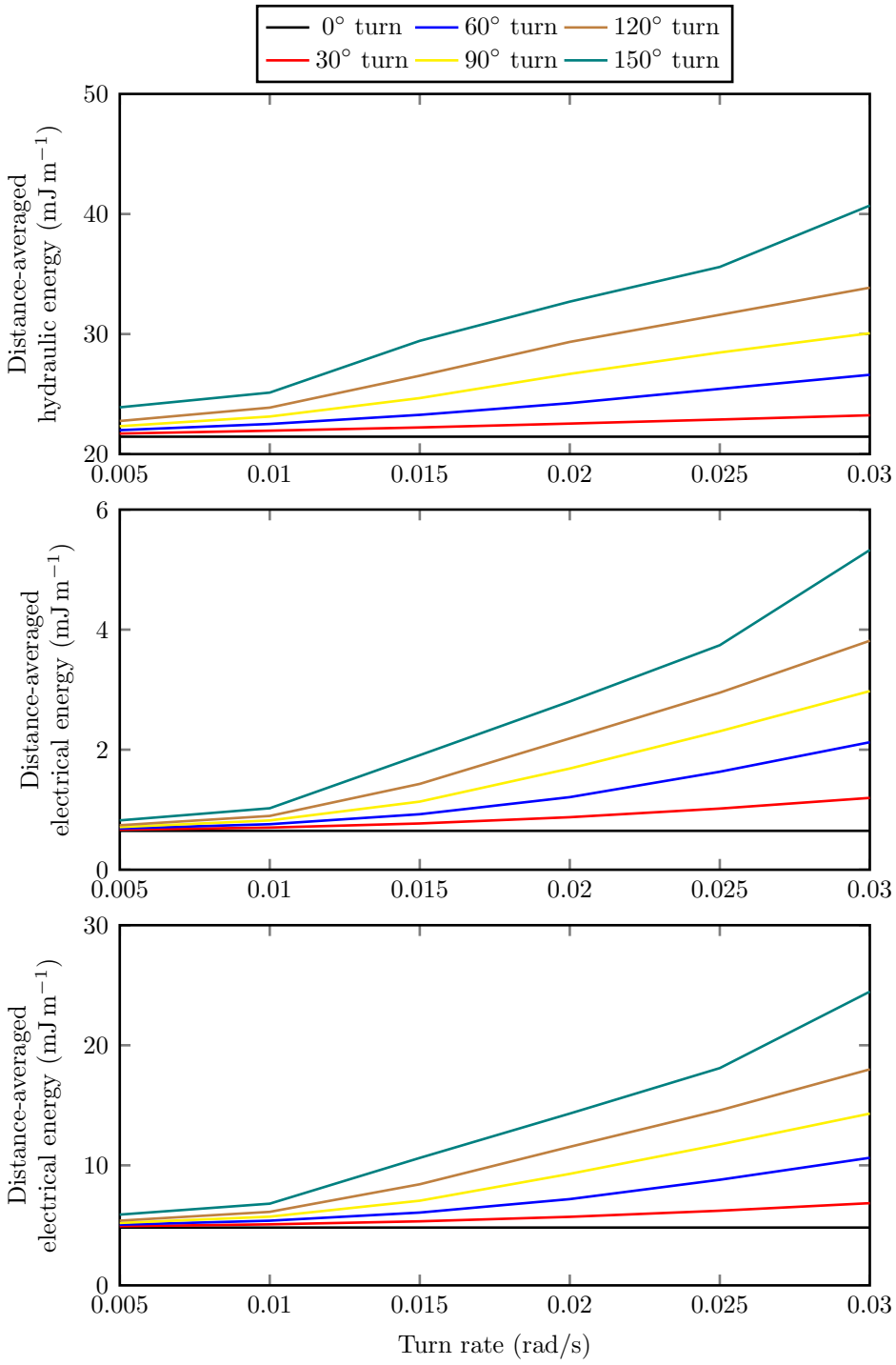

Figure 7.23: Distance-averaged energy demands from elevators during turn rate sweep of all heading changes, using three actuation technologies at cruise condition (233 m/s, 10000 m). Top figure: ESHA, Middle: EMA, Bottom: EHA

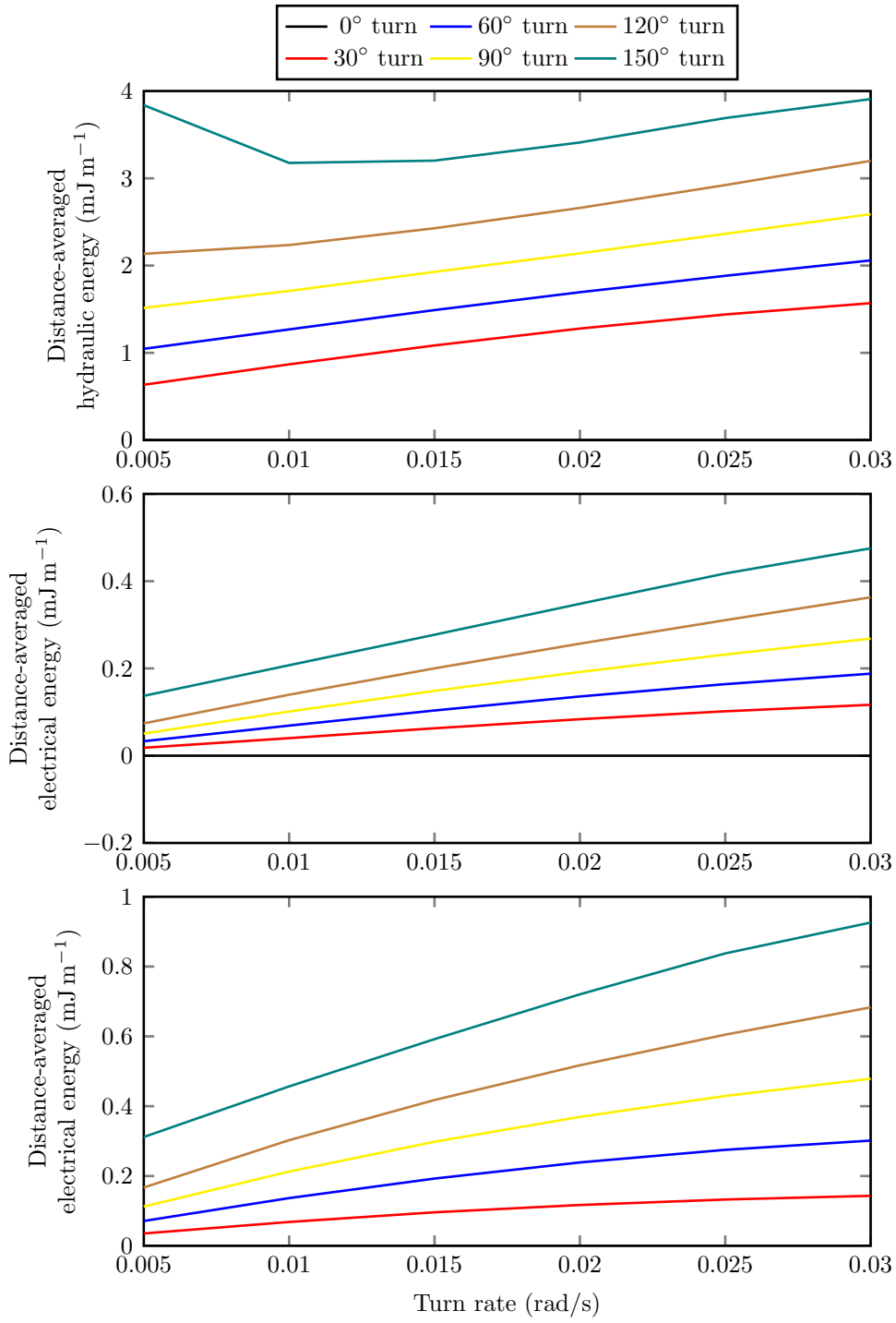

Figure 7.24: Distance-averaged energy demands from rudder during turn rate sweep of all heading changes, using three actuation technologies at cruise condition (233 m/s, 10000 m). Top figure: ESHA, Middle: EMA, Bottom: EHA

7.1.2.3 Force-speed statistical flights

The final presentation of data consists of the statistical representation of flights for actuator design, testing and simulation. This technique is presented by Maré [3] and is used to bench test actuators; the data is usually sourced from flight tests. This thesis demonstrates another method to generate statistical actuator operating point data for arbitrary trajectories.

The figures are not exhaustive; they are intended to show a cross section of results, consisting of:

- ESHA, EMA and EHA actuators at approach condition (102.9 m/s - 200 knots) 150° turn
- EHA at 3 flight conditions, 150° turn
- EHA doing 30° , 90° , 150° turns at approach speed

ESHA, EMA and EHA at approach It is when viewing these figures that the variation in energy consumption can really be appreciated. There is no better way of compiling the two components of mechanical power; force and velocity onto a single plot. Variations occur between Figures 7.25, 7.26 and 7.27 due to slight differences in the controllers and dynamics of each actuator and the different performances under load. Because the complete model includes feedback from aerodynamic loads to actuators to overall aircraft motion, any variation in dynamic performance at any layer of the combined model will affect every other layer.

The aileron data in the three figures all function at similar operating points, falling within the 48 kN stall force of the aileron specification in Table 3.1. Another point to be noticed is that the majority of the time is spent in positive power flow quadrants of the force-speed plots. This is where

the product of force and speed is positive and indicates a flow of energy from aircraft to external airflow. When the product is negative it implies the load force is aiding the motion of the actuator and can potentially be used for regeneration. The relative minority of data in this condition implies the limited benefit of regeneration in flight control actuators.

One point to notice is that the apparent trim location of the data plots (where the crossing of data occurs) is not located at 0 kN because of the constant load force on the ailerons. This means the actuator is delivering a constant power even in the 'neutral' position.

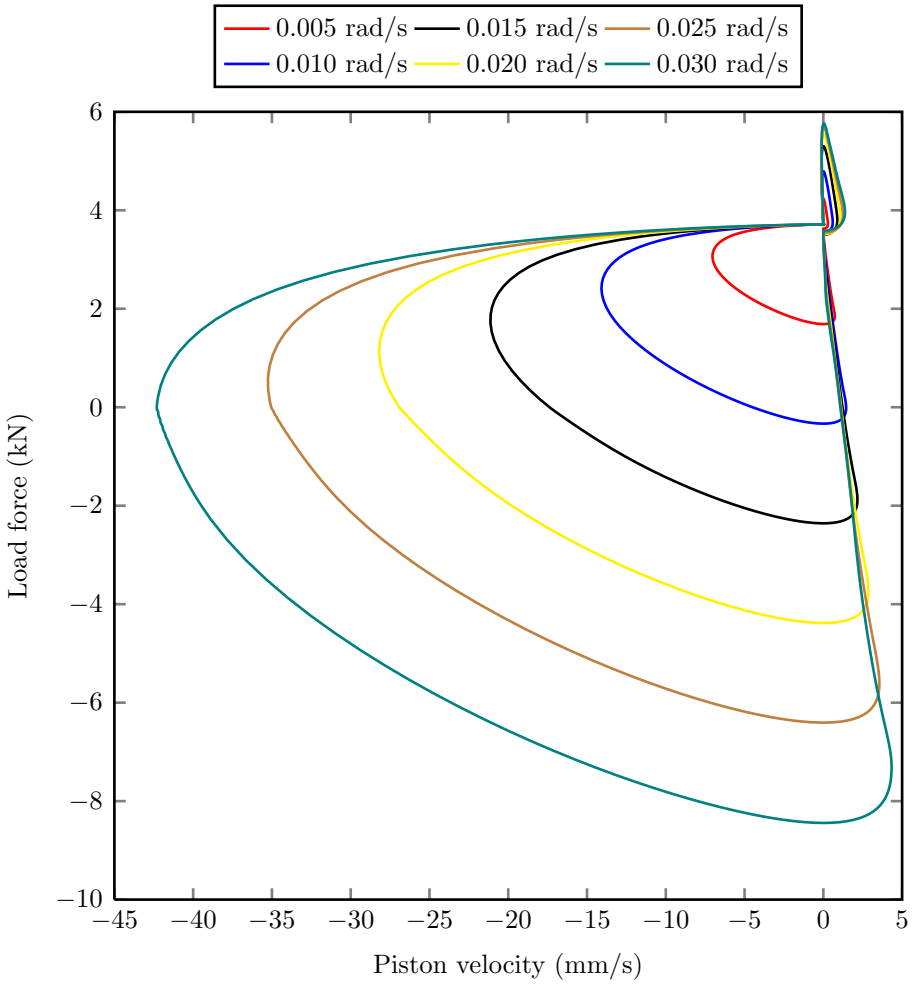

Figure 7.25: Load-velocity plot of ESHA aileron during a 150° turn at approach (102.9 m/s, 1000 m), at six different turn rates

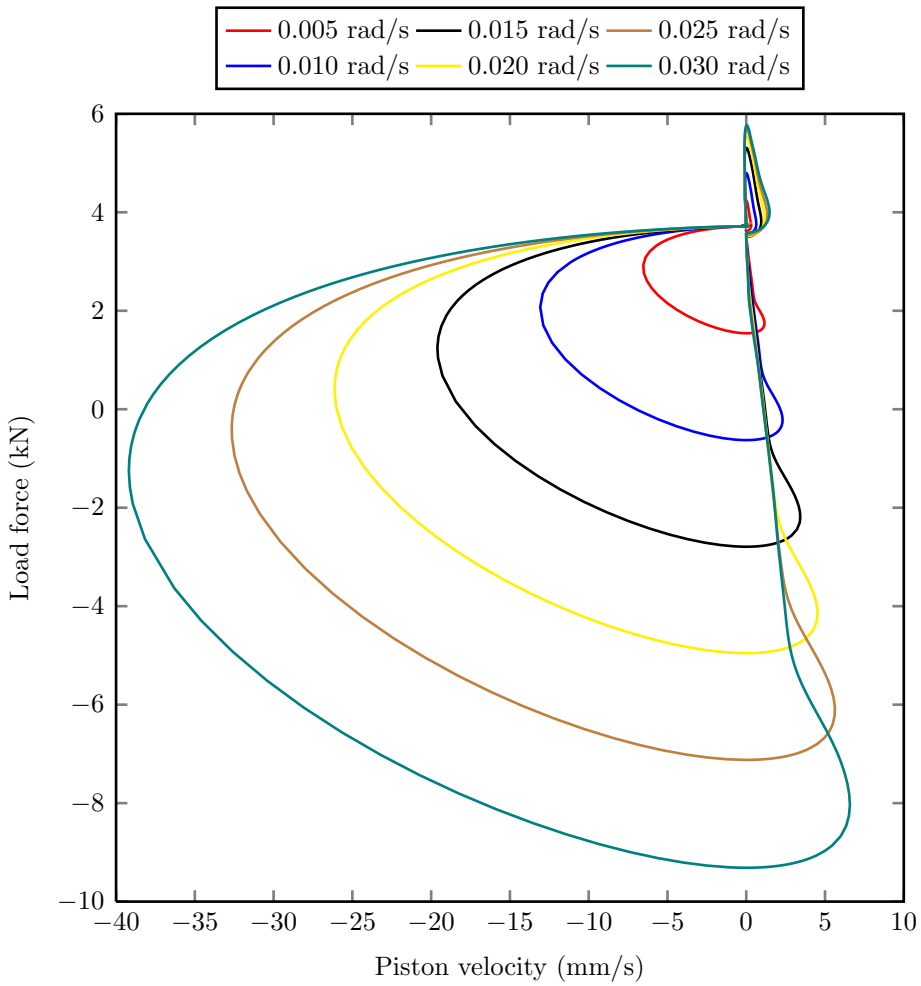

Figure 7.26: Load-velocity plot of EMA aileron during a 150° turn at approach (102.9 m/s, 1000 m), at six different turn rates

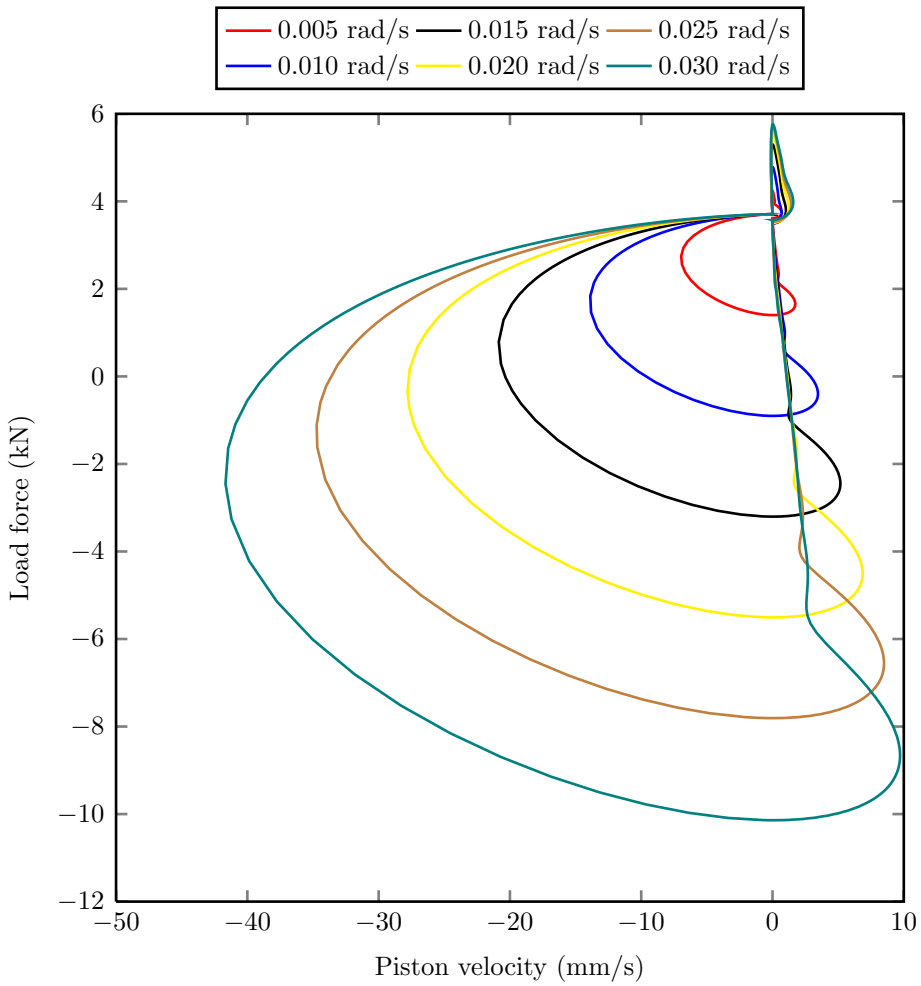

Figure 7.27: Load-velocity plot of EHA aileron during a 150° turn at approach (102.9 m/s, 1000 m), at six different turn rates

EHA at three flight conditions This section demonstrates the change in force-speed statistical flight data across different flight conditions, presenting data for the approach phase in Figure 7.27, Figure 7.28 and Figure 7.29. The trim point in each figure occurs at an increasing load force as the dynamic pressure increases with increasing velocity. The approach and descent phases appear well controlled whereas the cruise condition shows manifestations of the uncontrolled, high bank rate turns executed at the highest turn rates. (NB: The first result has already been shown in Figure 7.27).

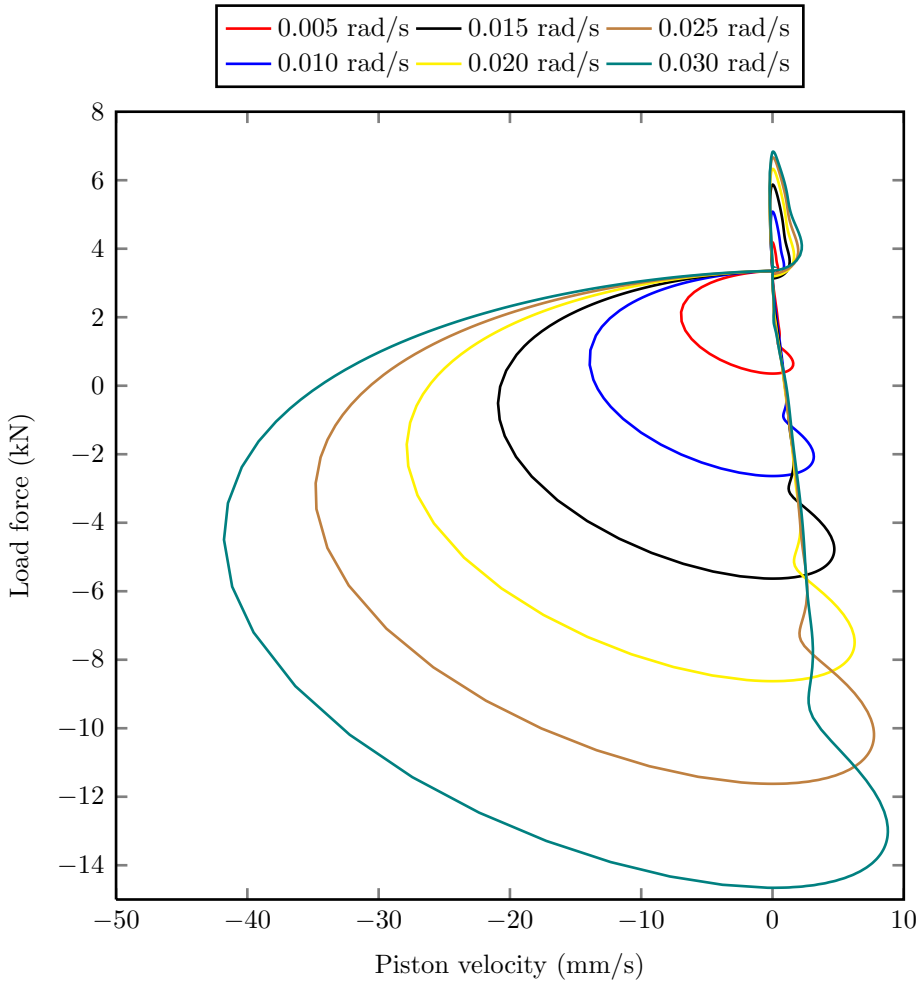

Figure 7.28: Load-velocity plot of EHA aileron during a 150° turn at descent (129 m/s, 3000 m), at six different turn rates

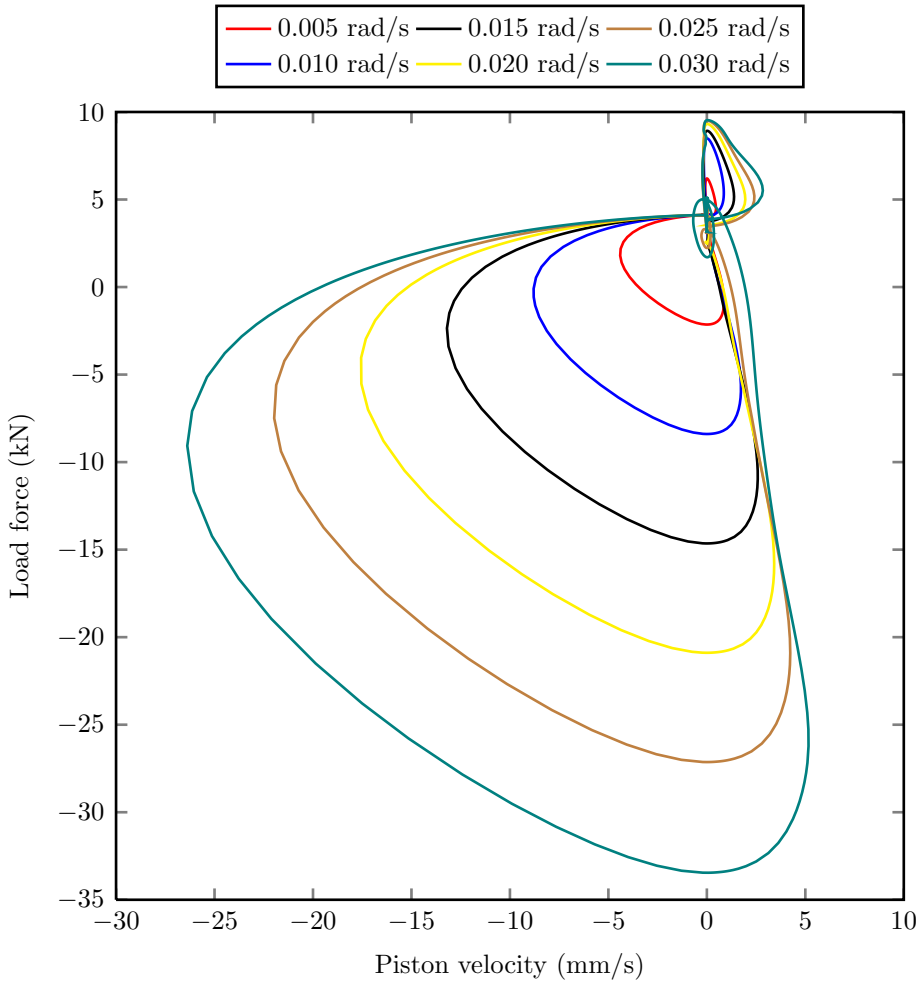

Figure 7.29: Load-velocity plot of EHA aileron during a 150° turn at cruise (233 m/s, 10000 m), at six different turn rates

EHA executing three different turns The force-speed data presented for the different turn angles shows minimal variation between the 150° , 90° and 30° turns in Figures 7.27, 7.30 and 7.31. As discussed previously in section 7.1.2.2 (page 283), the duration of the steady state segment of the manoeuvre does not have a significant affect on the actuator load envelope. In each case the maximum load force is around 41 kN and the maximum velocity equal to about 10 mm/s. (NB: The first result for the 150° turn has

already been shown in Figure 7.27).

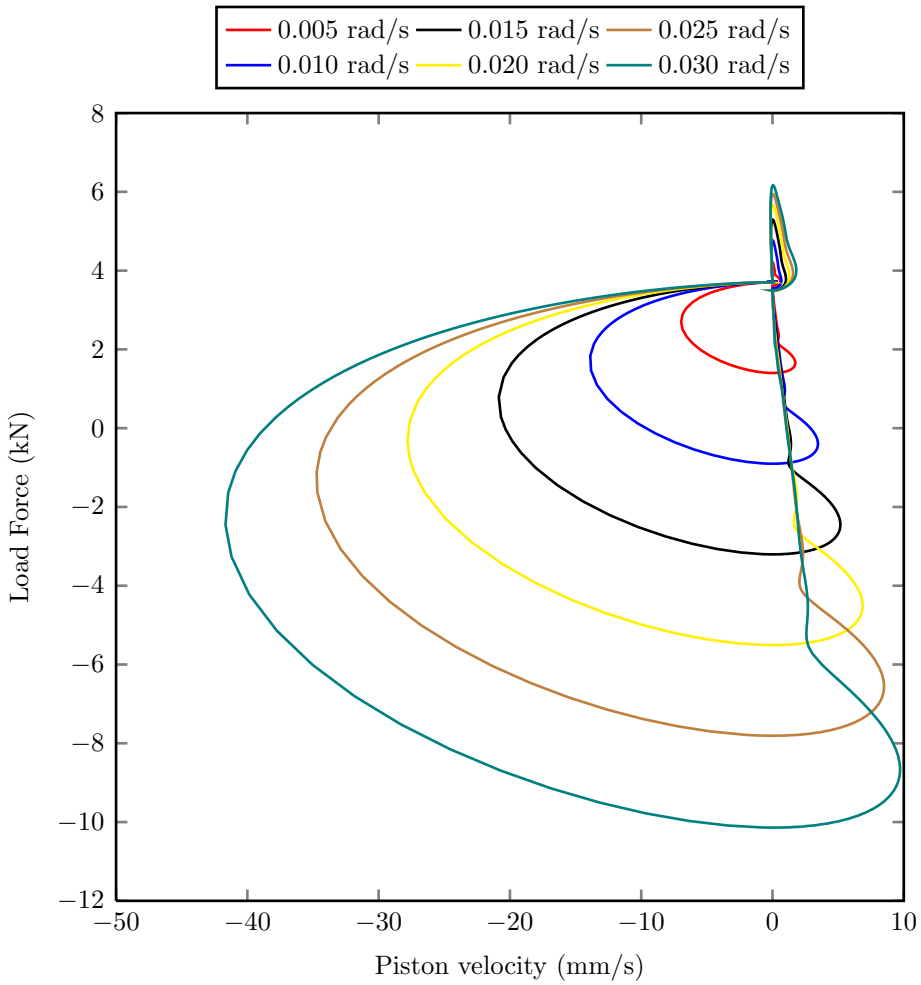

Figure 7.30: Load-velocity plot of EHA aileron during a 90° turn at approach (102.9 m/s, 1000 m), at six different turn rates

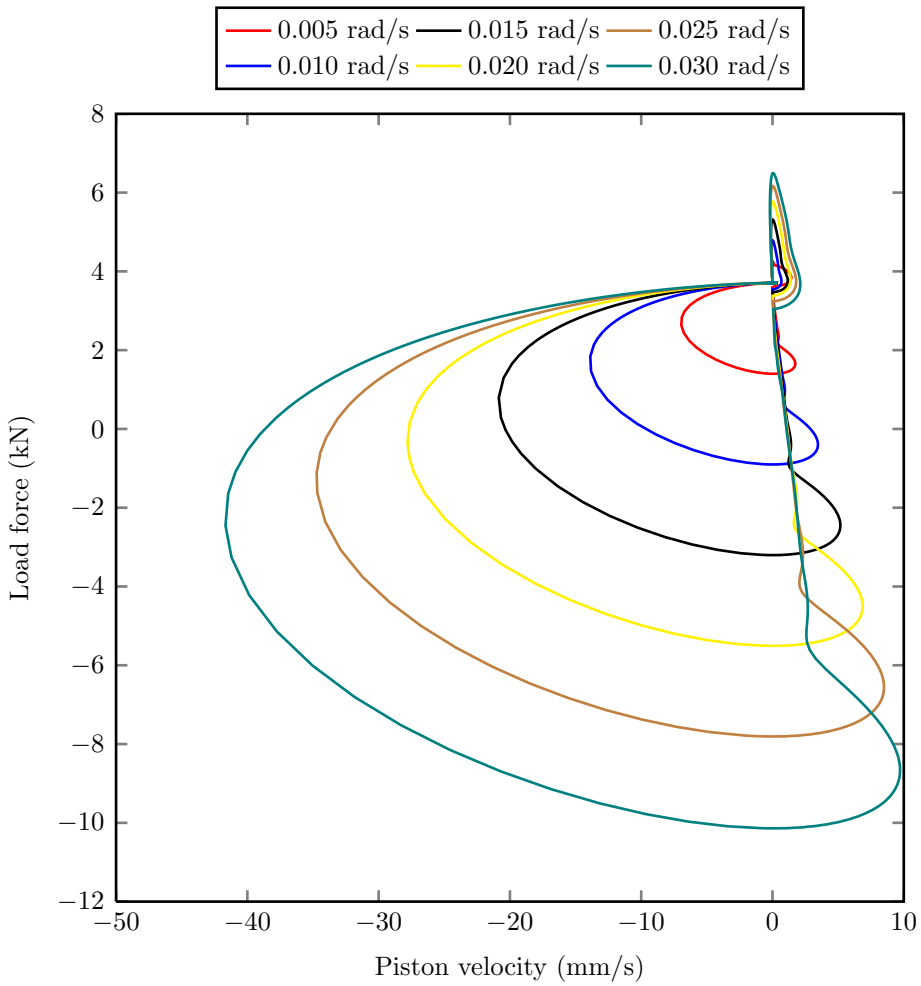

Figure 7.31: Load-velocity plot of EHA aileron during a 30° turn at approach (102.9 m/s, 1000 m), at six different turn rates

7.1.3 Comparing the Simulation to Real World Actuator Data

7.1.3.1 Discussion

With any simulation exercise there should be a period of reflection where the modeller looks at the results, relates them to the real system and questions: "Are these results reasonable?". When the sizing requirements of the A320 actuators are considered from Table 3.1 (page 127) the power estimates of this case study would appear to be very low.

Taking the aileron as an example, the product of maximum force (48 kN) and no load rate (90 mm/s) is 4.3 kW. Of course, the actuator cannot achieve both stall force and no load rate at the same time so using a rough approximation of 50% of this figure gives a peak mechanical power delivered of 2.2 kW. Why then, does the simulated aileron power peak at around 600 W in Figure 7.9?

It would be reasonable to estimate a safety factor of 2 would be applied, reducing the sizing case from 2.2 kW to 1.1 kW, but this still leaves 500 W unaccounted for between the real world actuator and the simulation peaks. This discrepancy could certainly be introduced by the steady air mass which had to be adopted in the simulation to achieve reasonable execution times; turbulent air introduces a significantly more dynamic operating condition to the flight control surfaces. This is investigated further by applying turbulence to the simulation in the following subsection (7.1.3.2).

Estimation can provide 'ball park' figures to help gain validity and confidence in the results, but hardware in the loop test data is always the preferred option. While this is often hard to come by without close ties to an industrial partner, 'pseudo-data' can occasionally be found in the public domain. Figure 7.32 shows the operating envelope of an A320 aileron actuator for a

complete two hour flight. The figure, although not providing absolute data shows how small an area of the requirements envelope the actuator operates in during a typical flight. The actuator can be seen to reach no more than about 15% of the maximum speed and around 80% of the maximum load force. Assuming '100%' on the speed and hinge moment (or force) axes equals the values documented in Table 3.1 (page 127), the product of these two values equates to a mechanical output power of about 518 W, but assuming again that the actual power is 50% of this the true peak output power is approximately 260 W.

Much attention is given to the component modelling and the losses within the actuators, but this thesis does not explicitly model significant losses such as magnetically induced eddy currents or hysteresis, but attempts to represent them in a functional manner through overall efficiency. They are numerically quantified through larger than realistic friction to give approximately valid total efficiency.

One factor that is not given much consideration in judging the validity of actuator power consumption is the control loop that provides the actuator with input commands. A higher deflection angle obviously causes a higher aerodynamic load force and a higher deflection rate can significantly increase the power demand. However, with the short stroke lengths of flight control actuators it can be rare that maximum velocities of the actuator pistons are seen (corroborated by the flight data in Figure 7.32).

7.1.3.2 Simulating Power Consumption in Realistic Conditions

Simulating the dynamic power consumption of the flight control actuators faster than real time required some assumptions to be made. Discontinuous friction models had to be avoided and wind was ignored to allow maximum

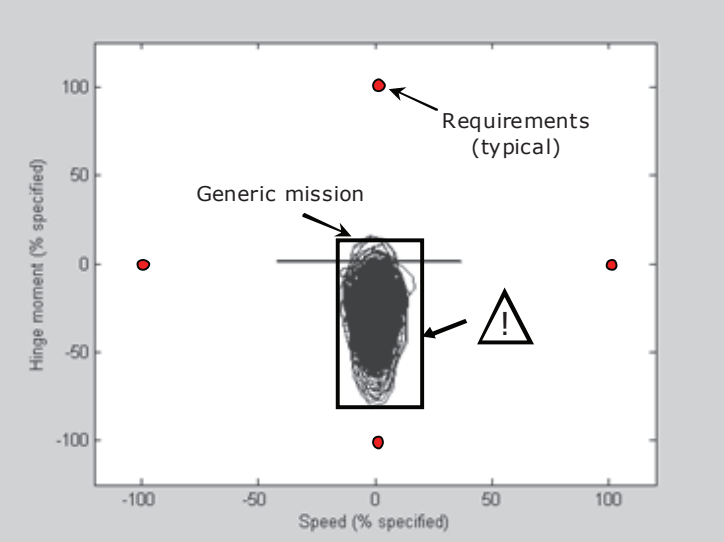

Figure 7.32: Aileron load profile for a typical two hour A320 flight [3]

simulation speed by applying variable step solvers. This section looks to run a shortened experiment to quantify the power consumptions with the additional realism (and simulation time) that can be gained by including these factors. A single manoeuvre will be performed with turbulent conditions while using a more realistic discontinuous Coulomb friction model.

It becomes unrealistic at this point to simulate the full system at the same time, because the time steps must be so small that simulation times can be impractically large. Instead the aircraft model and aero-load estimator will be run in isolation from the actuator models, by using them to generate transient position command and load force signals for the actuators. The actuator models are then run separately, which allows greater detail to be studied such as discontinuous friction models and highly transient input signals. Breaking the loop in this way means actuator behaviour cannot be reflected in the aircraft's motion, for example actuator stall will not limit the rate of manoeuvres that can be executed by the aircraft.

The experiment is conducted in cruise (Mach 0.78, 10000 m) with a 150°

turn to simulate a high aileron peak power scenario. The trajectory flown by the aircraft in moderately turbulent conditions is shown in blue in Figure 7.33, where the 2D projected ground track is shown in dashed grey. To generate the wind vectors a Dryden turbulence model is applied and configured to a probability of exceedance of high altitude intensity of 10^{-3} and a scale length at medium/high altitudes of 533.4 m.

The aircraft can be seen to experience significant turbulence compared to the steady-air simulations performed throughout this thesis. The flight controller has to perform a lot of corrective action to the flight controls to maintain the altitude and airspeed in Figure 7.34. During the turn from 0° to 150° shown in Figure 7.35 the roll angle is highly transient, while the banked period between around 100 second and 250 seconds is still clearly visible.

The actuator input data that is gathered by running the 6-DOF and aero-load estimator through turbulent conditions is shown in Figure 7.36. The aileron position is continuously changing as the flight controller keeps the aircraft on course, which combine with variations in the aircraft speed and angle of attack to compute a similarly dynamic load force. The piston velocity is of particular interest, because it is here where significant amounts of power are required to achieve the motion that results in the control surface positions in the top figure.

Indeed, it is apparent that the negative aileron deflection to roll the aircraft into the turn which occurs at about 112 seconds is difficult to discern amongst the noise. This implies that aileron sizing is focussed strongly on turbulent handling qualities and not so much on roll performance. Thus, peak power estimates of the model are more likely to line up with the real actuator specifications in the turbulent conditions shown here. This can be seen in Figure 7.37 where the mechanical power delivered by the cylinder

regularly approaches the 260 W that is estimated from J C Maré's data in the previous subsection (7.1.3.1). Additionally, the peak electrical power increases to around 900 W when a discontinuous Coulomb friction model is applied, although as discussed elsewhere in this thesis the electrical input powers are not easily validated without experimentation.

When failure cases are considered in addition to the turbulent flight requirements, such as maintaining control margins in asymmetrical flight (e.g. single engine failure) it can be appreciated why such high power actuators are specified even though they will very rarely be expected to deliver this power. This chapter has sought to quantify the low power estimates produced in the rest of this thesis, while showing the improvement in realism when slow, detailed simulations are conducted. The mechanical power delivered has been semi-quantitatively validated against statistical flight data for an A320 and the two show similar ranges of power output.

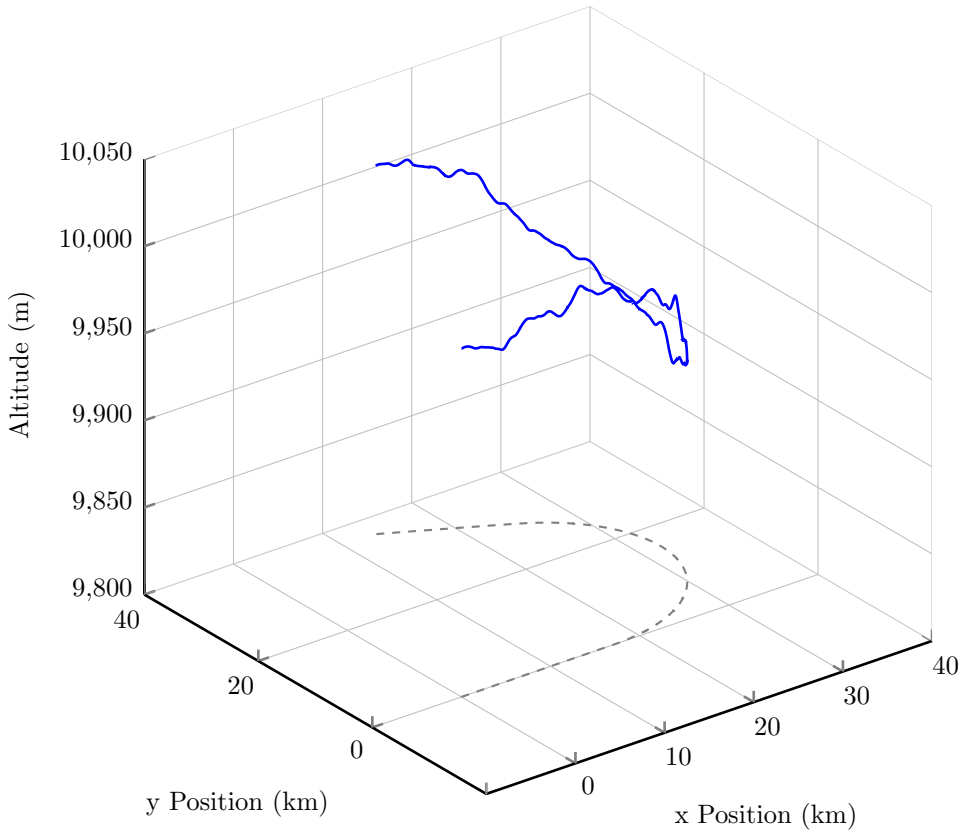

Figure 7.33: Trajectory flown during 150° turn in moderately turbulent conditions

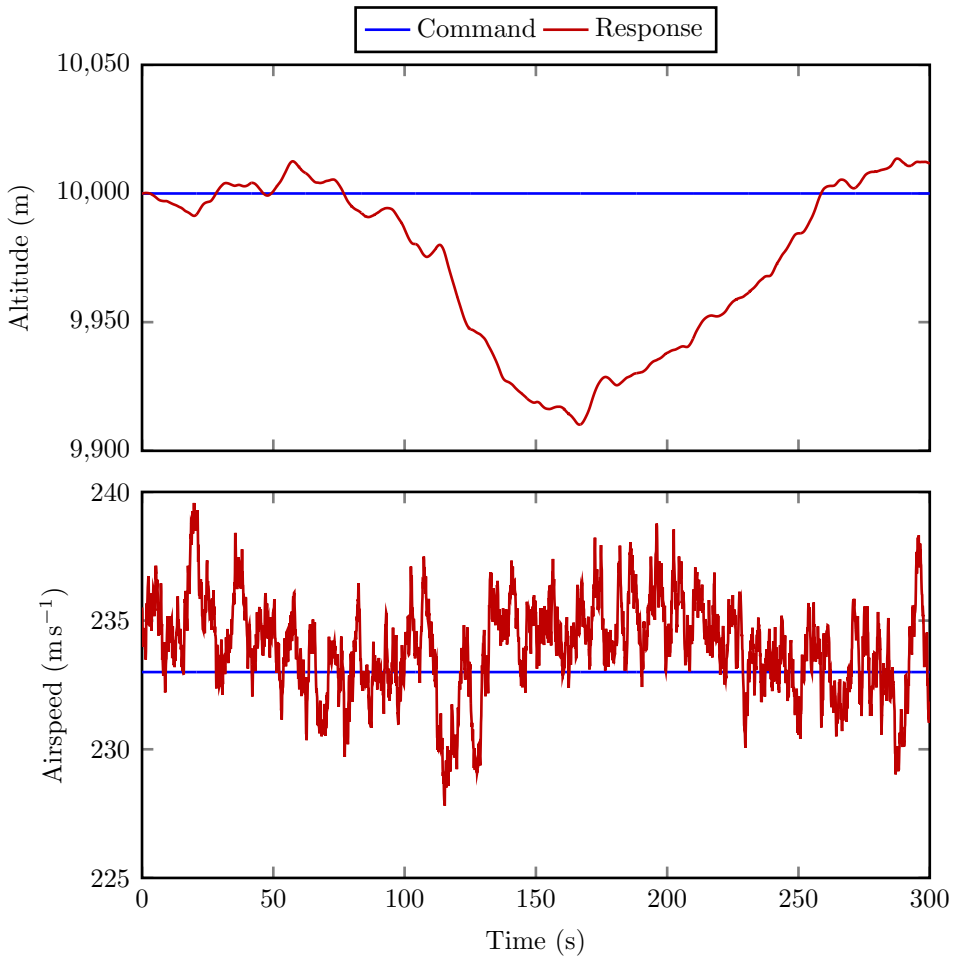

Figure 7.34: Altitude and airspeed during 150° turn in moderately turbulent conditions

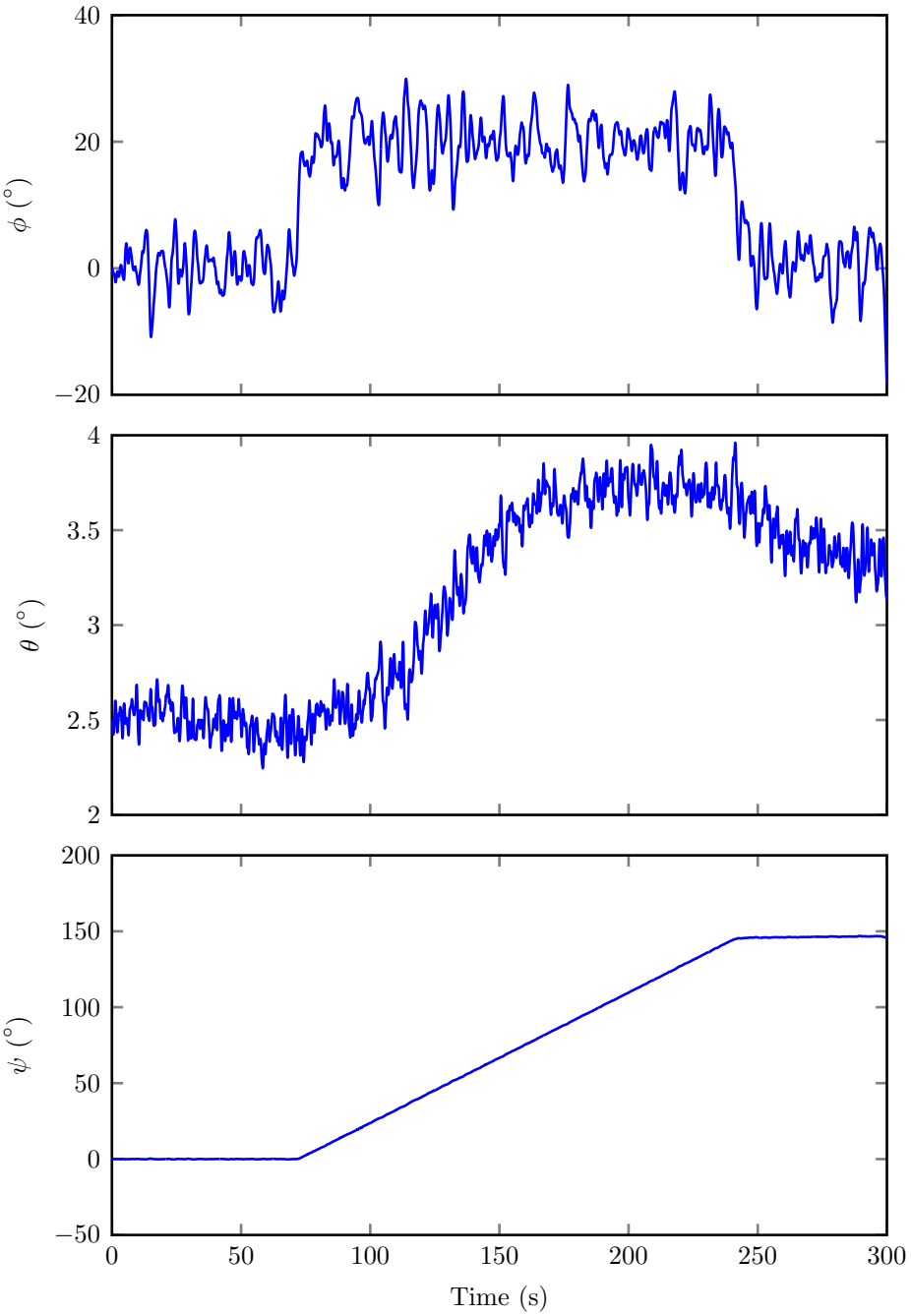

Figure 7.35: Euler angles during 150° turn in moderately turbulent conditions

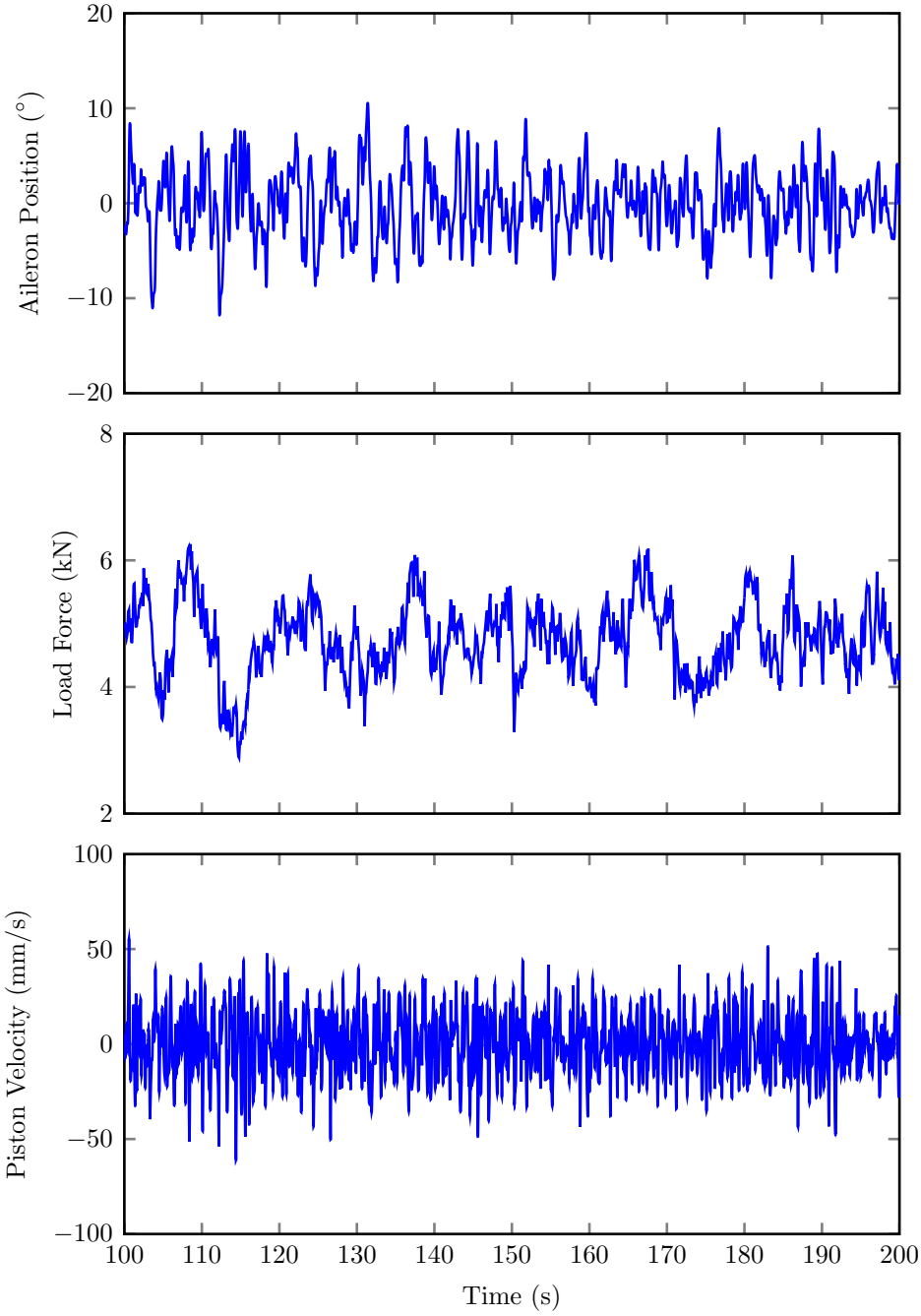

Figure 7.36: Actuator position and load data during 150° turn in moderately turbulent conditions

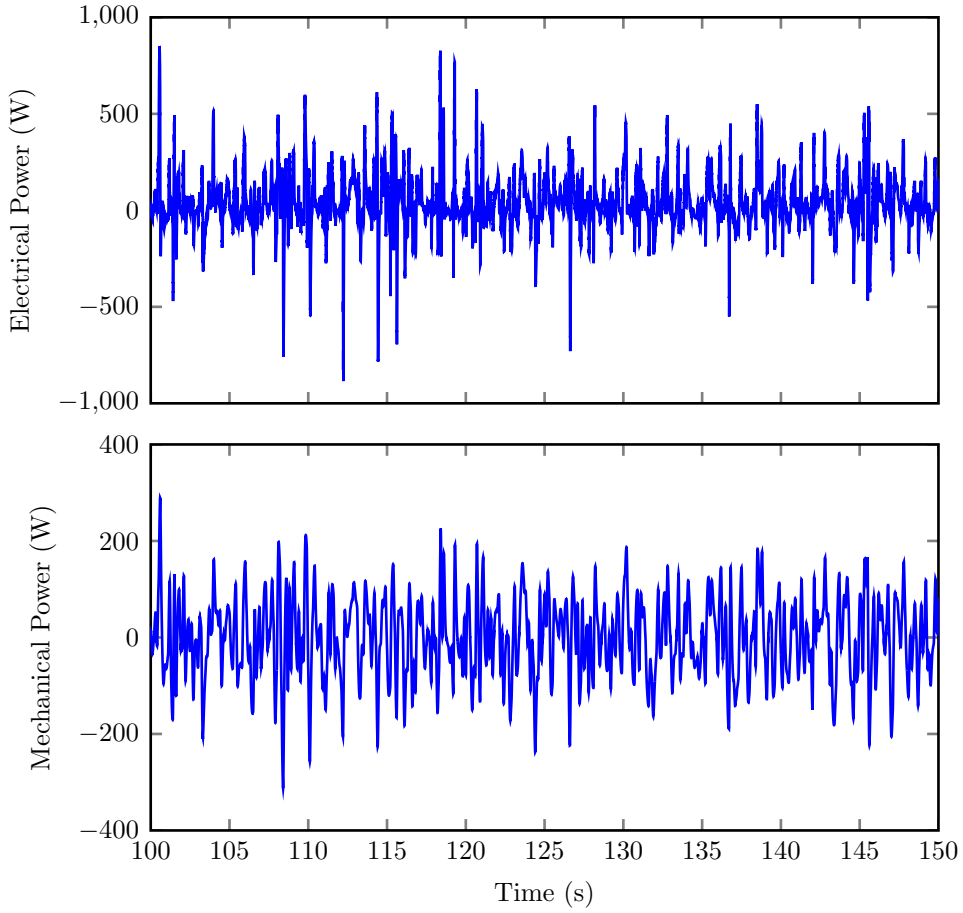

Figure 7.37: Power delivered and consumed by EHA during 150° turn in moderately turbulent conditions

7.2 Aerosonde - Weather Reconnaissance UAV

7.2.1 Aircraft Description

The Aerosonde is a small UAV with a wingspan of around 3 metres (Figure 7.38). It was developed originally to collect weather data such as temperature and pressure in remote areas. This includes flying into weather systems which would be considered unsafe for a manned aircraft (such as hurricane storm cells). It has a single engine which consumes liquid fuel and has been tuned to provide long endurance. In 1998 the aircraft achieved the first unmanned flight across the Atlantic ocean in just under 27 hours [188]. The long endurance capability makes efficient power management important; for this reason the Aerosonde is considered to be a worthwhile case study platform for this thesis.

It has small electrical actuators to provide flight control power [189], which are considered to be electromechanical technology with BLDC motors. Power consumption of these units is low, but the aircraft can only supply a maximum of 190 watts [190] which makes them significant at aircraft level. Because of the single propeller, the aircraft has an unstable spiral model which requires constant asymmetric control deflection to cruise straight and level.

On an aircraft the size of small a UAV, hydraulic actuation technologies are generally not suitable because of the low forces experienced by the control surfaces. There would be a significant mass penalty incurred just to contain the pressure of the fluid in the cylinder even without delivering a large output force. For this reason the only actuation technology considered in this experiment is the EMA; this technology is commonly applied in remote control aircraft, but they are described as ‘servos’.

Figure 7.38: Aerosonde UAV [191]

The actuators are implemented using scaled down versions of the same model used for the A320; except very small permanent magnet BLDC motors and ball screws are used to size the actuators for sub-Newton load forces.

7.2.2 Results and Discussion

7.2.2.1 Time series results

The time series data for the Aerosonde follows the same order used previously in the A320 results section. The first plot in Figure 7.39 shows all the trajectories flown across the whole experiment. The power consumption results for all trajectories would require an impractical amount of space to show as time series data. Instead, they are combined through averages and presented starting from the total energy data in section 7.2.2.2 on page 338.

Presenting time series data requires the selection of a single heading change manoeuvre, once again chosen as the 150° turn. The spatial position of the aircraft in flat Earth axes is shown in Figure 7.40 for the manoeuvres presented in the following figures.

The turns are found to be well controlled by the guidance system; a smooth, constant radius turn is executed and only a small overshoot is seen. This is not optimal since the actuators have to apply power to reverse the heading rate by rolling to bank in the opposite direction. However, it does emphasise the use of the model to analyse the efficiency of the complete control system; from actuator controllers to the guidance loop. For this reason it has been decided to not retune the guidance controller and present the results as seen.

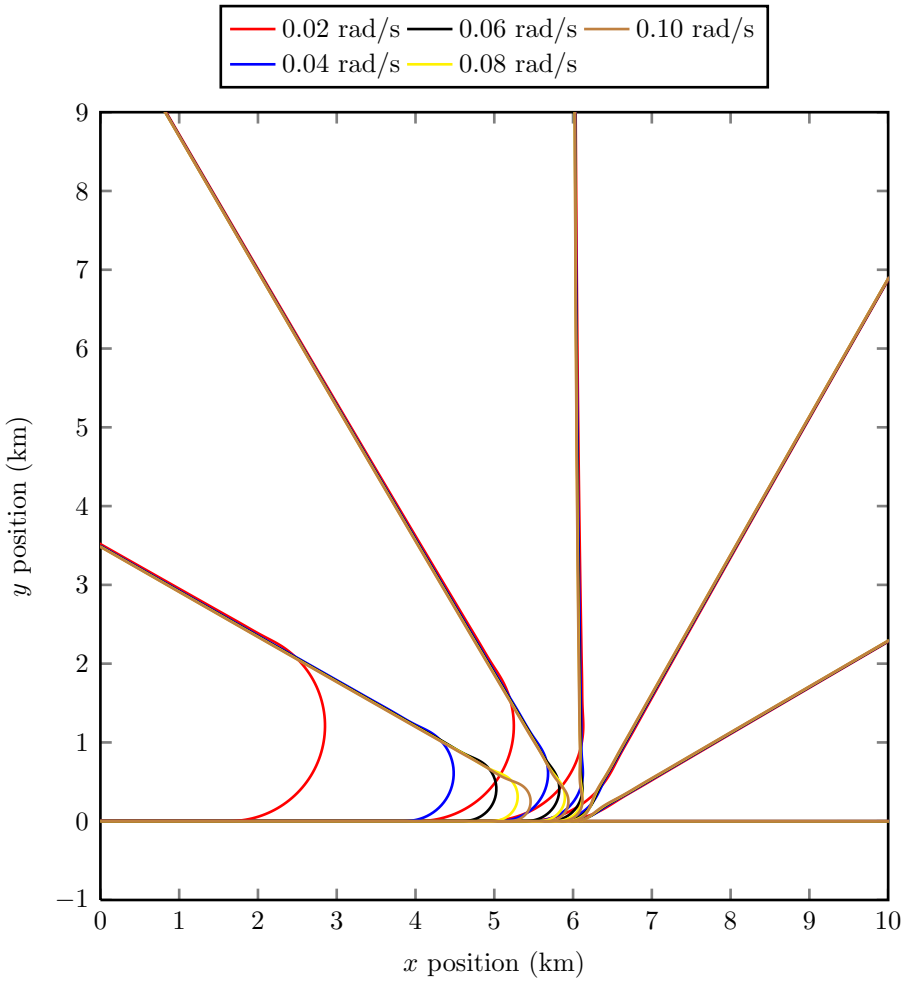

Figure 7.39: xy trajectories of Aerosonde heading and turn rate sweep at cruise condition (24 m/s, 1800 m)

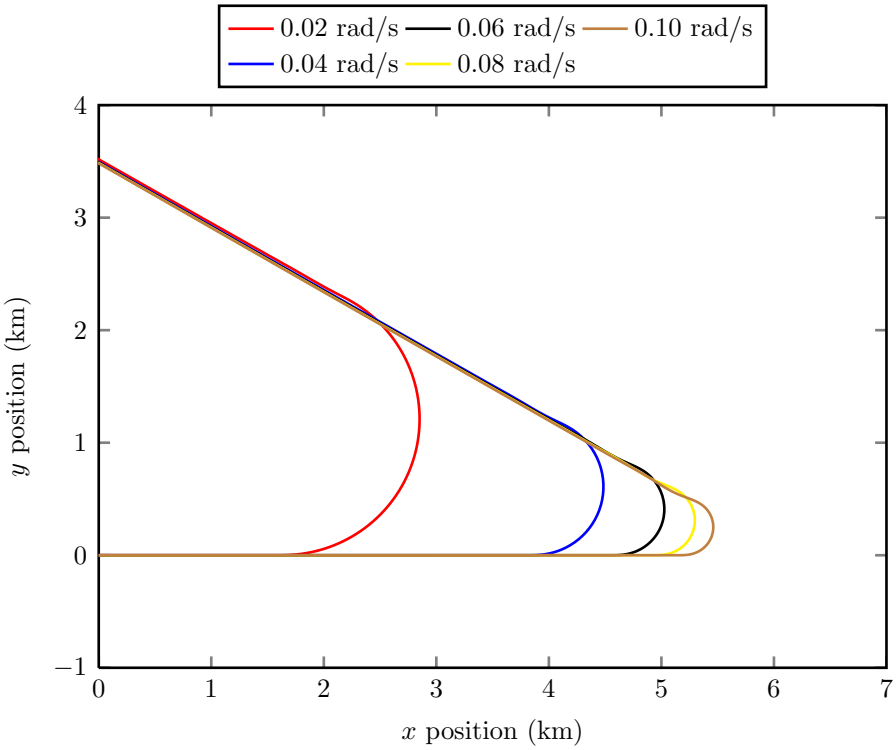

Figure 7.40: xy trajectories of Aerosonde turn rate sweep for a 150° turn, using EMAs at cruise condition (24 m/s, 1800 m)

The Euler angles of the aircraft while executing the five manoeuvres are shown in Figure 7.41. The roll and pitch angle amplitudes are seen to linearly increase with turn rate and the TECS FCS manages to retain full control over the longitudinal motion. This is further confirmed in Figure 7.42 where the airspeed is maintained within the range +0.075 m/s and -0.03 m/s and the altitude is kept within ±0.3 m of the setpoint.

As one would expect, the roll, pitch and yaw angles all increase with increasing turn rate. This has a more strenuous affect on the actuators which are required to both induce the higher angles and control the increased cross coupling between the axes of motion, which become prevalent at high bank angles.

One notable difference between the dynamics of the Aerosonde and A320 (other than the obvious - size) is the spiral instability due to roll moment induced by rotation of the propeller. In the Aerosonde there is only one engine, so the rotation cannot be balanced by a counter rotating second engine. This introduces a relationship between thrust and the aileron trim position to counteract the engine moment. Because of the yaw induced by the deflected ailerons, a rudder deflection is required to balance the yaw motion of the aircraft.

The net result is that during a steady level 'trimmed' flight condition, the ailerons and rudder will be at non-zero locations as a result of the engine torque, which can be seen in Figure 7.43. Also, while trim algorithms are applied to find all aircraft states and inputs to initialise it in a steady state condition; the aircraft remains spirally unstable. Because the numerical solvers used in Simulink always have some degree of error, a small numerical error soon amplifies until the spiral instability is exhibited. To achieve continuous stable flight a lateral autopilot is required to control the roll and

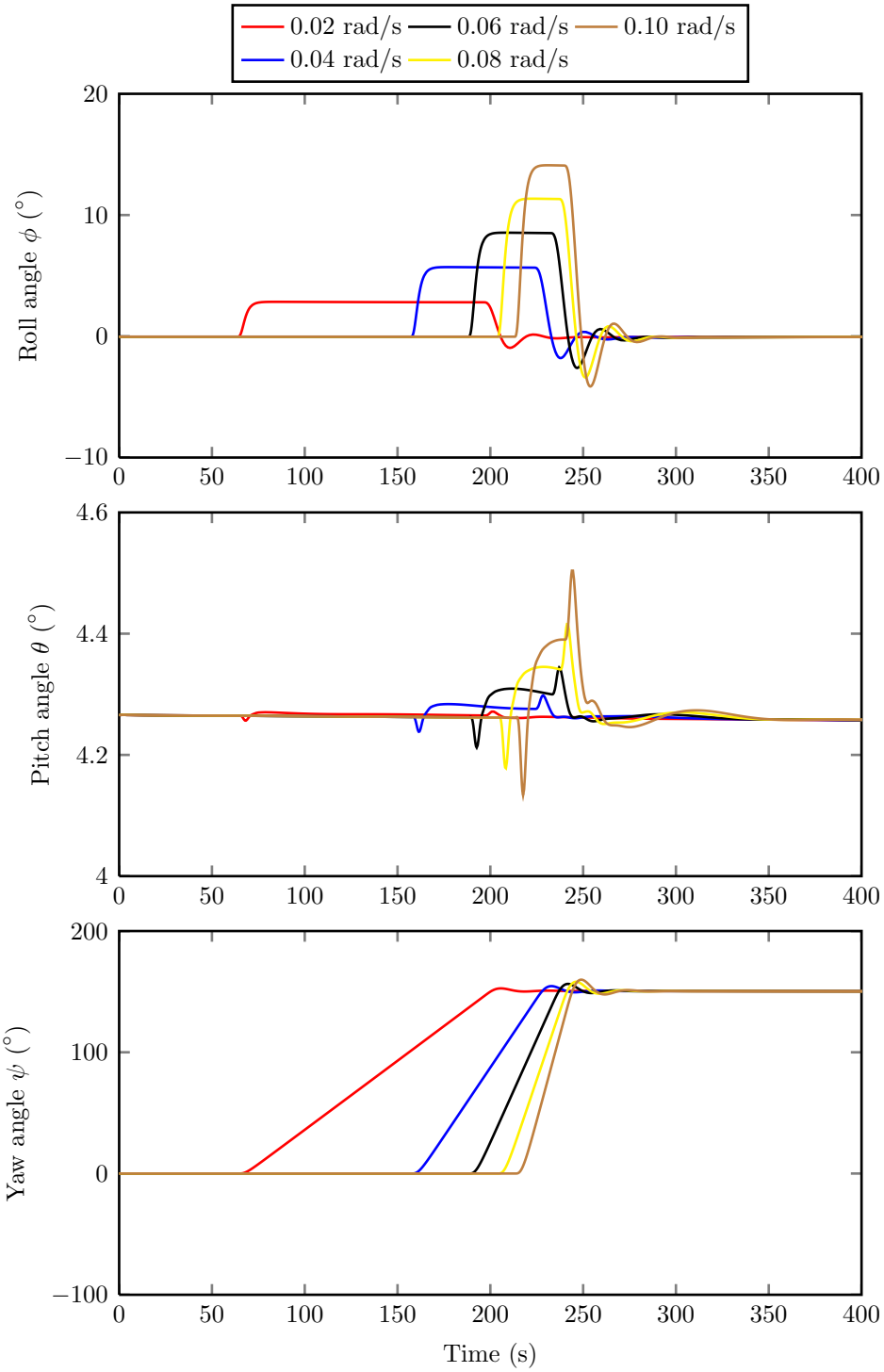

Figure 7.41: Aerosonde Euler angles during turn rate sweep, required to achieve a 150° turn using EMAs at cruise condition (24 m/s, 1800 m)

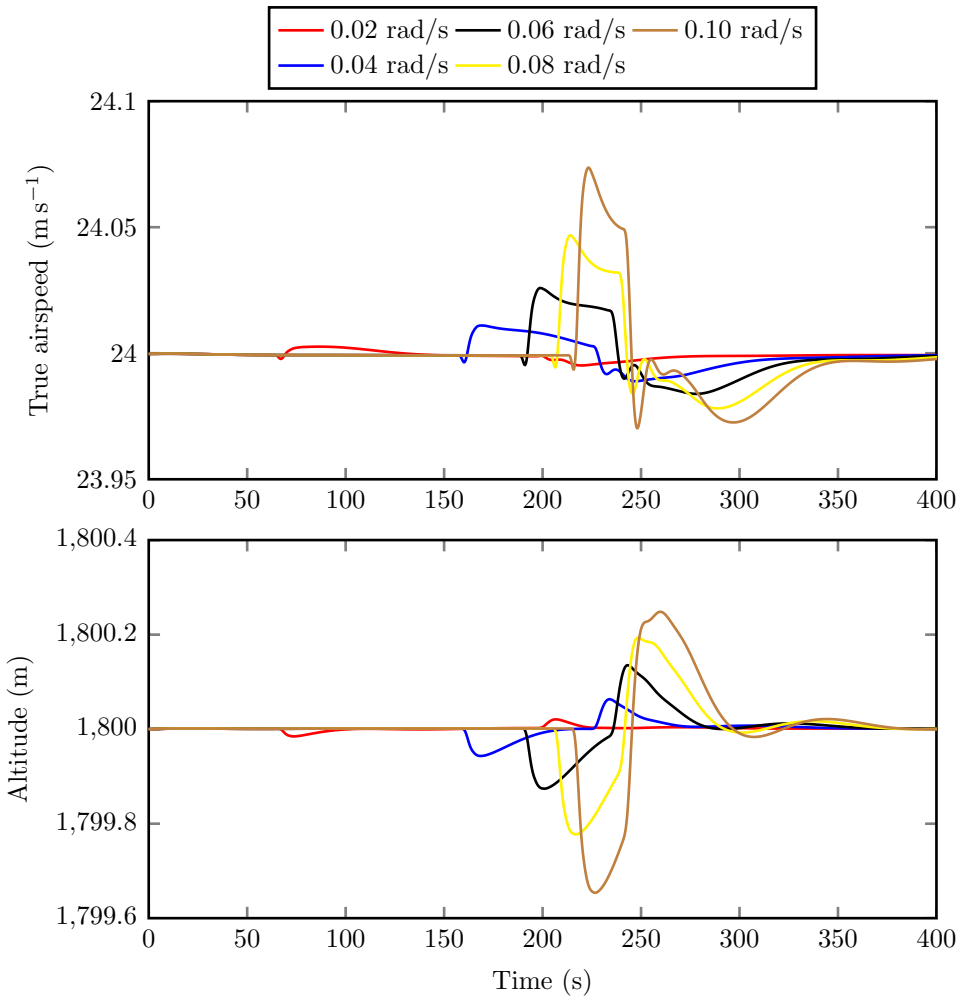

Figure 7.42: Altitude and airspeed of Aerosonde during turn rate sweep, achieving a 150° turn using EMAs at cruise condition (24 m/s, 1800 m)

yaw moments.

The same aerodynamic load estimation code is used from the A320 case, which models the aerodynamic hinge moment at any steady state flight condition as a linear function of control surface deflection. Thus, it is expected to see the load forces (Figure 7.44) showing the same trends as surface deflection (Figure 7.43), but with a different amplitude.

Given the small size of the aircraft the power consumption is expected to be low, which is confirmed by the mechanical power delivered to the control surfaces in Figure 7.45 and electrical power sourced from the supply in Figure 7.46. Of course, the power drawn from the supply must be greater than that delivered due to the inefficiencies in the power transfer which is the result observed in the data.

In the time series power consumption figures, all positive power flow signifies power taken from the aircraft and delivered to the airflow around the control surfaces. Negative power is seen when a control surface retracts from a deflected position; in this case the aerodynamic load is aiding the retraction. This means power can be regenerated from the airflow back into the aircraft systems, either to increase efficiency or to reduce the mass of the dissipative resistor used to convert regenerated energy to heat.

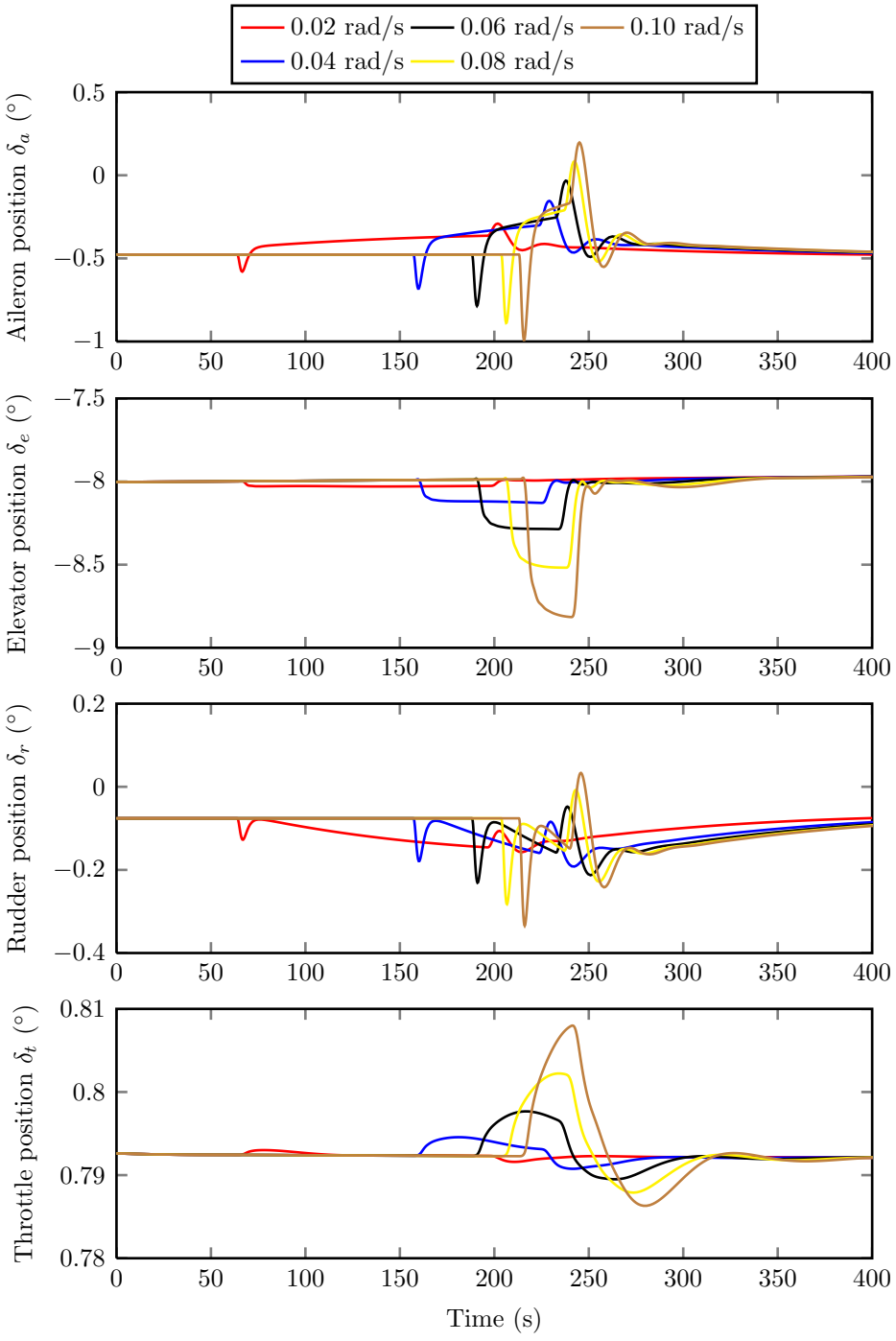

Figure 7.43: Aerosonde control inputs during turn rate sweep, required to achieve a 150° turn using EMAs at cruise condition (24 m/s, 1800 m)

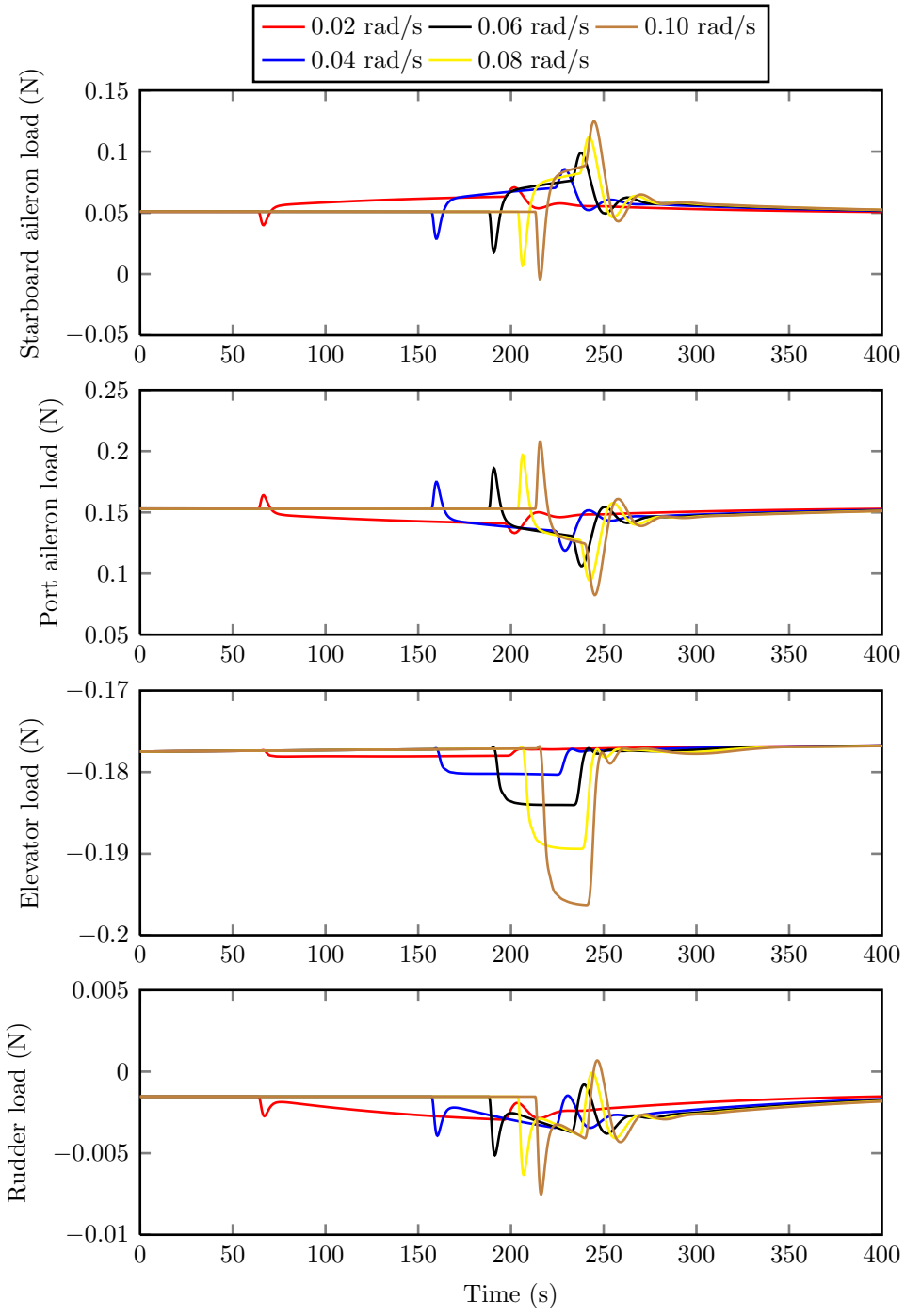

Figure 7.44: Aerosonde aerodynamic load forces during turn rate sweep, required to achieve a 150° turn using EMAs at cruise condition (24 m/s, 1800 m)

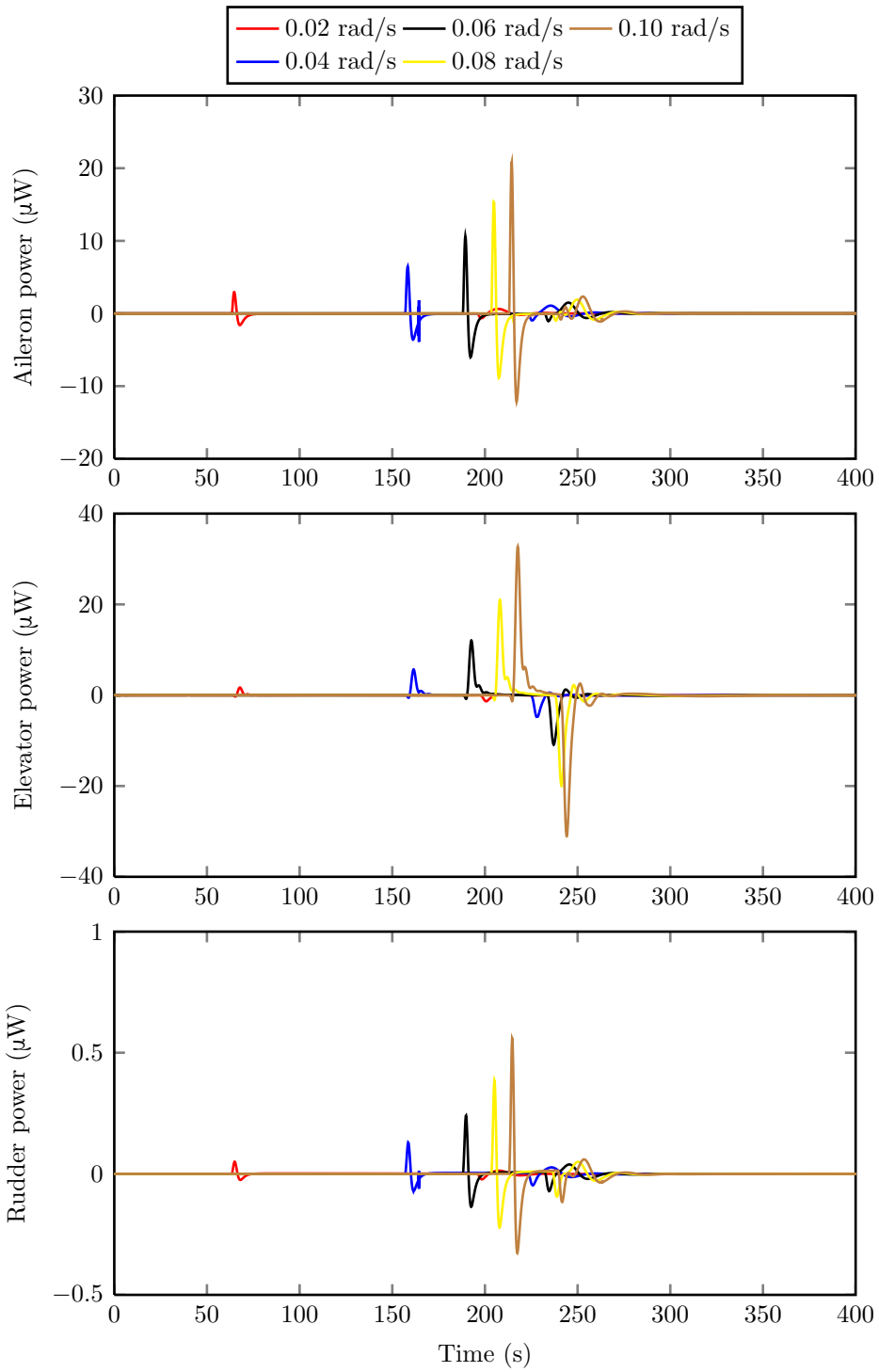

Figure 7.45: Aerosonde actuator mechanical power delivered during turn rate sweep, required to achieve a 150° turn using EMAs at cruise condition (24 m/s, 1800 m)

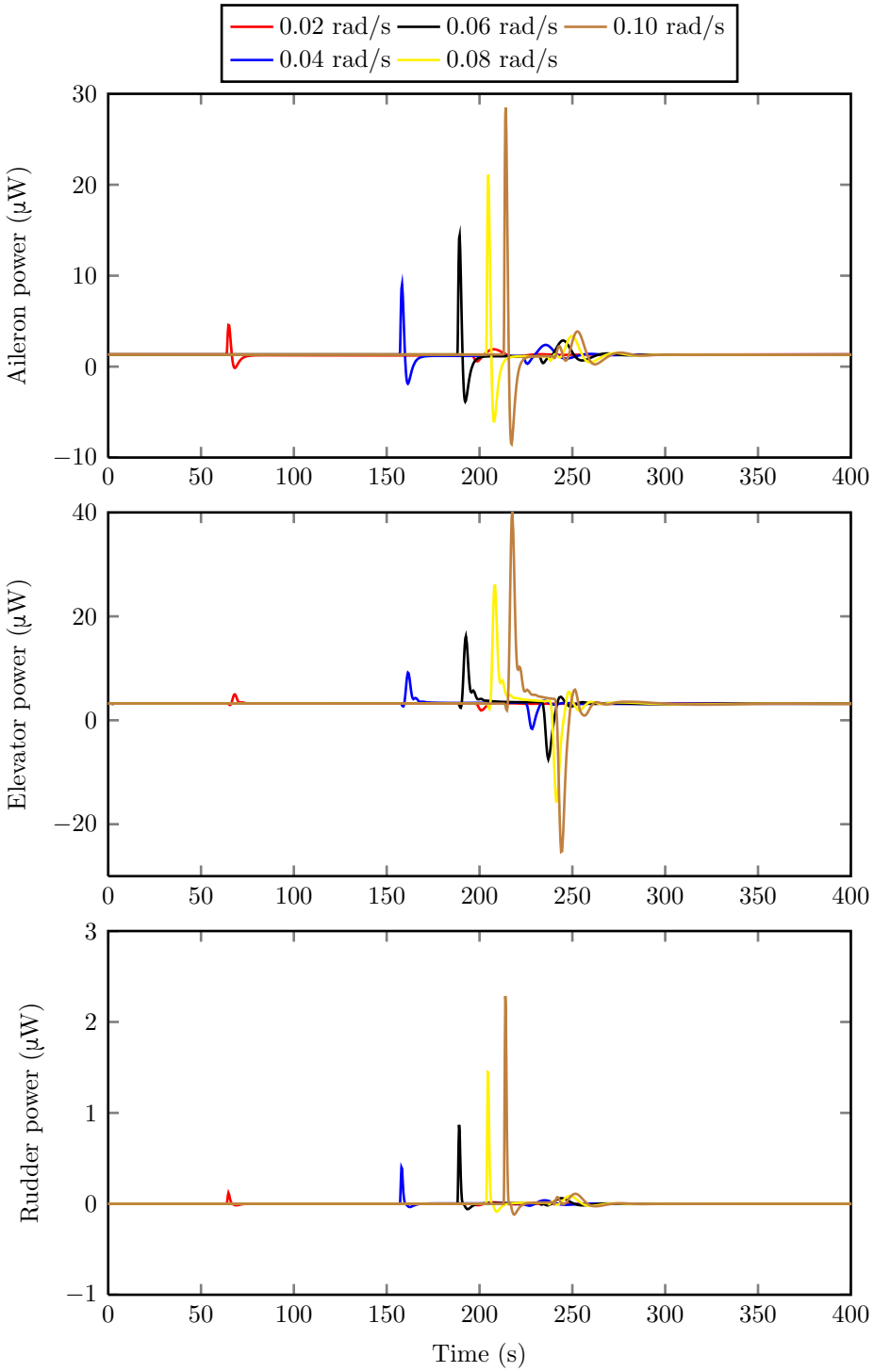

Figure 7.46: Aerosonde actuator electric power required during turn rate sweep, required to achieve a 150° turn using EMAs at cruise condition (24 m/s, 1800 m)

7.2.2.2 Total energy consumed

Presenting the results from multiple flight trajectories in a compact form requires the data to be reduced from a time series form to a function of turn rate. This section presents the full results of energy consumption as a function of turn rate, while seeking to also provide some explanation for the trends seen.

Cruise (24 m/s, 1800 m) It makes sense to first present the mechanical power delivered to the airflow through the control surfaces before analysing the efficiency of power conversion and total energy required from the source.

The mechanical energy output from the piston is shown in Figure 7.47 and follows the same trends discussed for the A320 in section 7.1.2.2. Every control surface requires more energy supplied to it to induce a higher rate of turn. This is expected; the interesting characteristics to investigate are how the efficiency of the actuators changes during different manoeuvres, since these depend strongly on the design and specification of the motor and ball screw.

The average efficiency of each actuator is shown in Figure 7.48 and follows the previously found trends for the aileron and elevator of the A320. For these two surfaces the increasing turn rates induce a higher load force on the actuator (shown in Figure 7.49) and makes them operate more efficiently.

An unusual reaction is seen from the rudder actuator, where the efficiency decreases with increasing turn rate. This can be explained using Figure 7.49; as the turn rate increases the aerodynamic load on the rudder reduces. This is because the position required to maintain steady level flight requires a larger deflection than that during a coordinated turn to the left. It can be assumed that this is unique to a left turn since a right turn will mean the

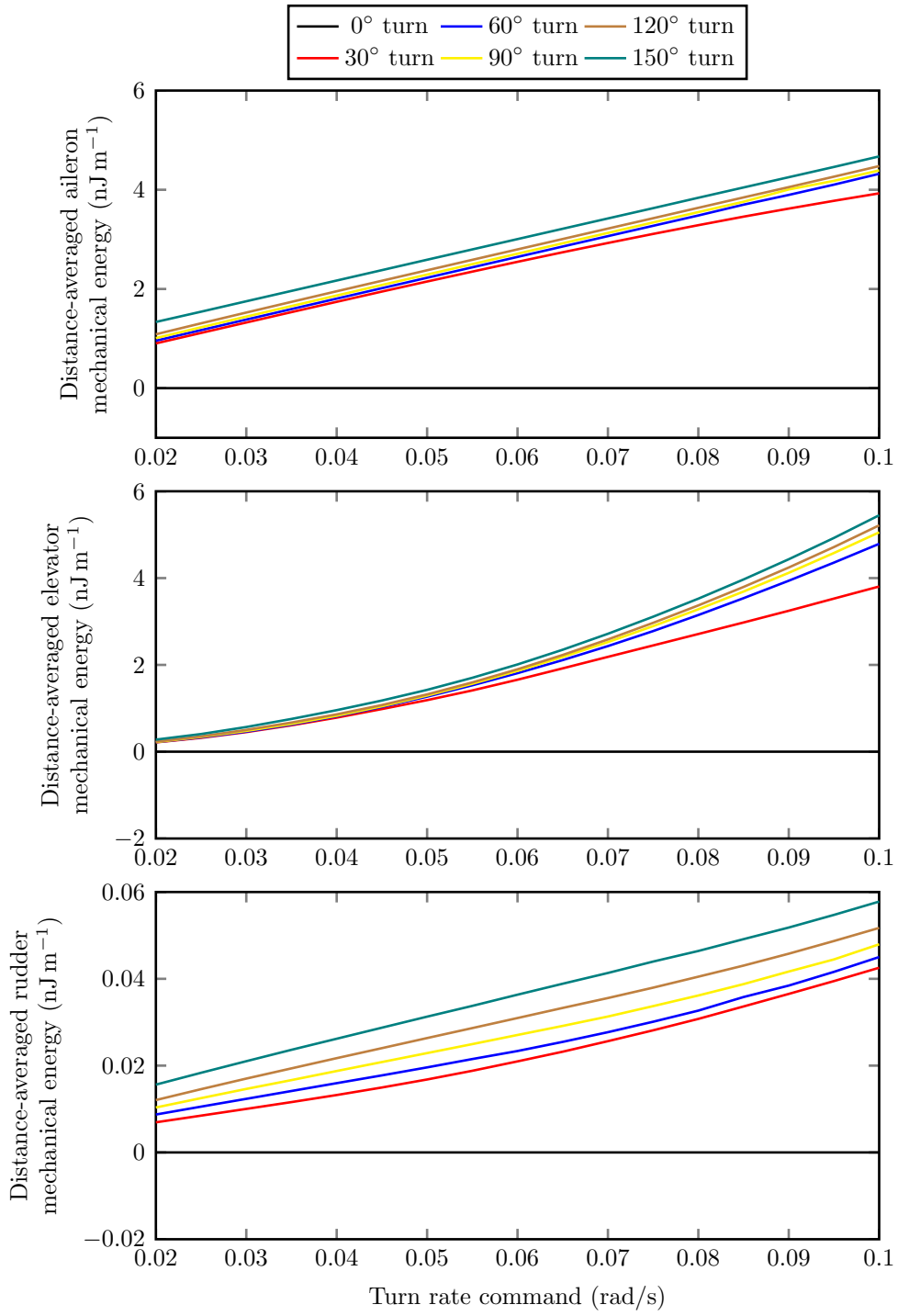

Figure 7.47: Distance-averaged mechanical energy delivered to the Aerosonde control surfaces during a turn rate sweep of all heading changes, at cruise condition (24 m/s, 1800 m). Top figure: ailerons (total), Middle: elevator, Bottom: rudder

rudder has to move in an opposite direction, to a position exposed to even higher aerodynamic forces.

The mechanical energy delivered combines with efficiency to form the energy required from the power supply, which is presented in Figure 7.50. This shows each actuator using less energy on average at lower turn rates, which is expected for the same reasons as the mechanical energy in Figure 7.47. For very low turn rates the ailerons even use less power than when travelling in a straight line since the motor torque aids the rolling of the aircraft. This is unique to the direction of turn and would be opposed by an increase in energy required when turning in the opposite direction.

Since the energy problem is aircraft centric; the energy consumption of each actuator is not of as much interest as the total consumption. Figure 7.51 shows the combined energy demand of the actuation system, as well as the fuel burnt during the manoeuvres. For very low turn rates there is a decrease in energy consumed; this is not exploitable to save power unless a flight plan consisting of only left turns is planned - something which is of quite limited use.

The fuel burn data is included since actuation power is only a small fraction of the power required to propel the aircraft. It does not make sense to optimise for minimum actuation energy if it comes at a more significant expense to fuel burn. It should be remembered that in this model, the fuel burn does not change based on secondary power consumption. It is mainly a function of drag and the increased thrust required to maintain altitude during a banked turn.

The final figure (Figure 7.51) provides the most important data for trajectory optimisation uses of the model. The average fuel burn plot shows an unexpected trend which is particularly noticeable for the 150° turn; at

the lowest manoeuvre rates the average fuel burnt begins to increase. This is deduced to be caused by a skewing of the average fuel burn data by the distance travelled, caused by using a guidance algorithm which does not take into account the TTB. As the manoeuvre rate increases (along with the bank angle required), the TTB increases. This causes skewing of the data across the plot, which becomes particularly pronounced at the low end of the manoeuvre rates. This is because low turn rates mean low TTB (and thus lower trajectory tracking error and relatively shorter distance travelled). The skewing occurs on all distance averaged figures but is particularly noticeable on the fuel burn plot because the range of data is particularly narrow to begin with.

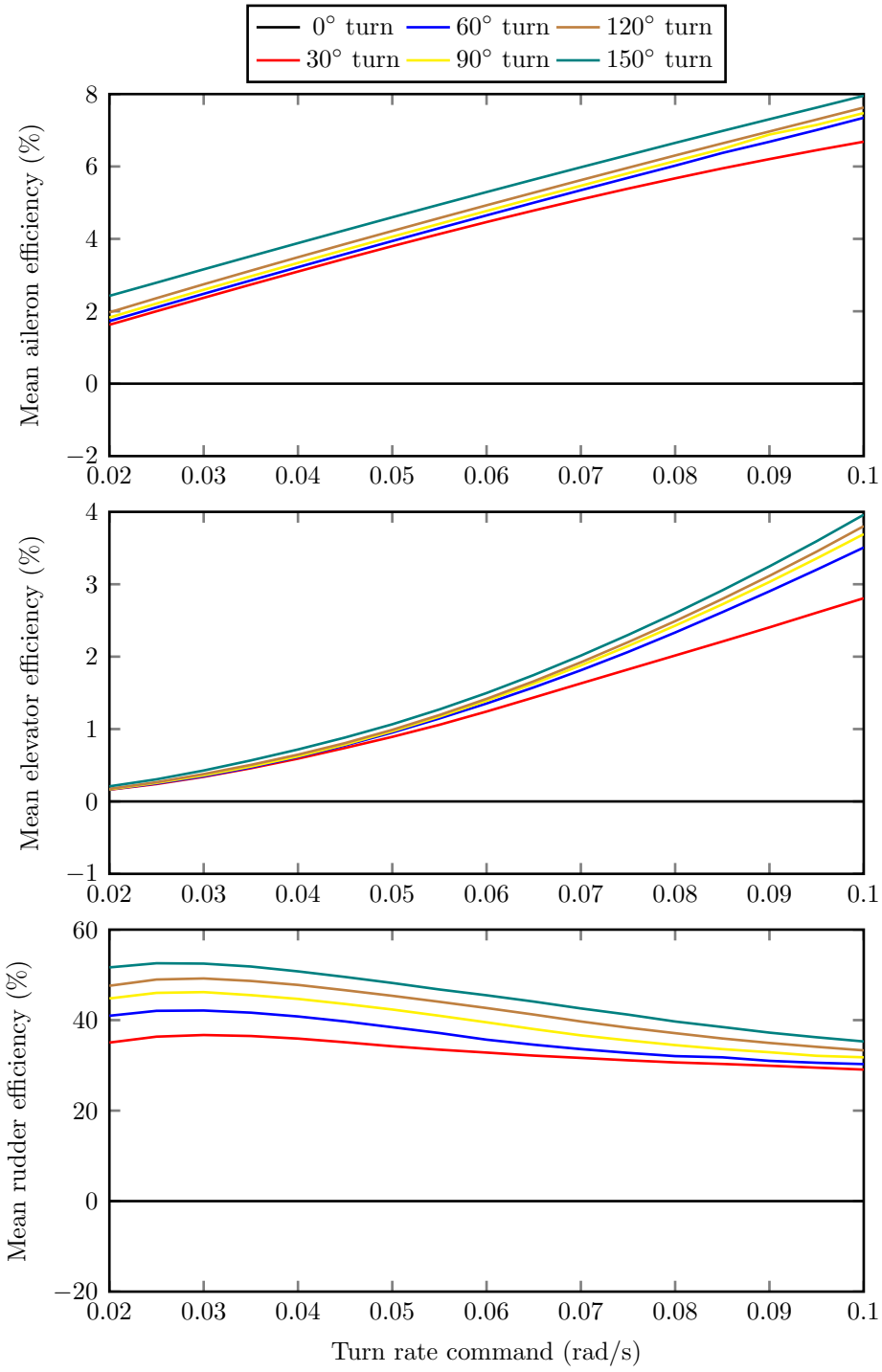

Figure 7.48: Efficiency of the energy conversion from the Aerosonde electrical supply to mechanical output at control surfaces during a turn rate sweep of all heading changes, at cruise condition (24 m/s, 1800 m). Top figure: ailerons (total), Middle: elevator, Bottom: rudder

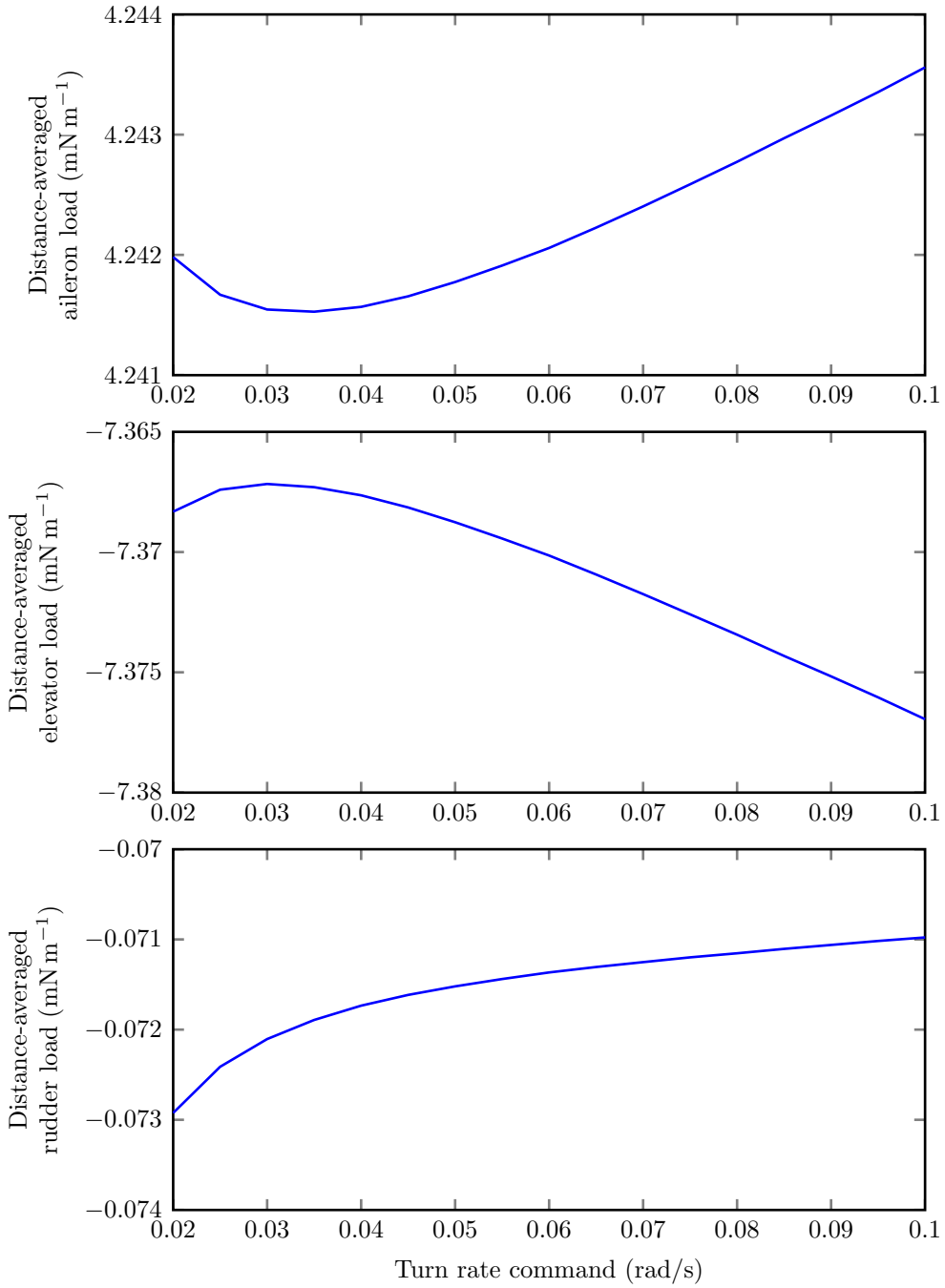

Figure 7.49: Distance-averaged aerodynamic load force on Aerosonde control surfaces during turn rate sweep of 150° turn, at cruise condition (24 m/s, 1800 m). Top figure: starboard aileron, Middle: elevator, Bottom: rudder

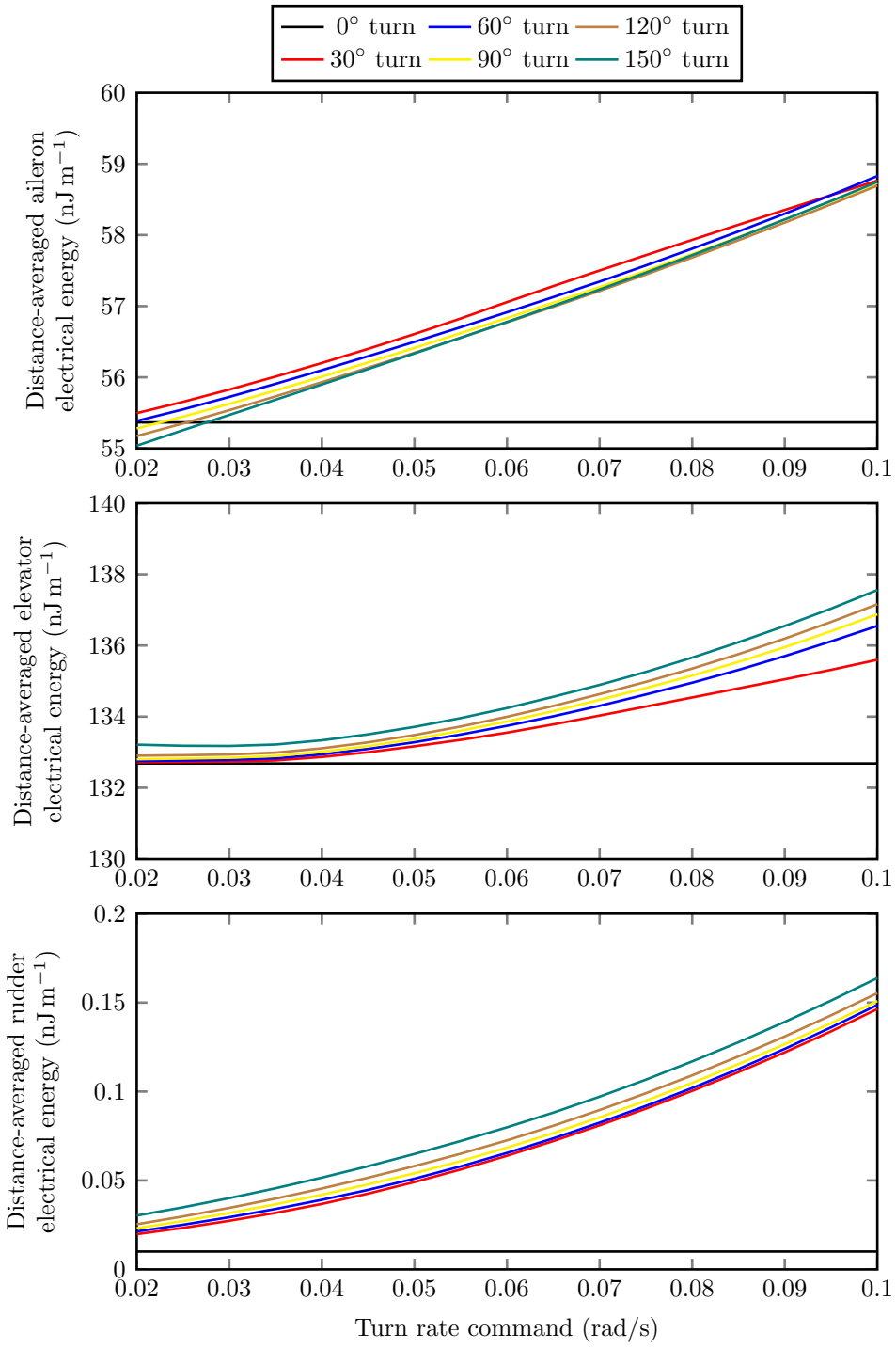

Figure 7.50: Distance-averaged energy demands of Aerosonde actuators during turn rate sweep of all heading changes, using three actuation technologies at cruise condition (24 m/s, 1800 m). Top figure: aileron total, Middle: elevator, Bottom: rudder

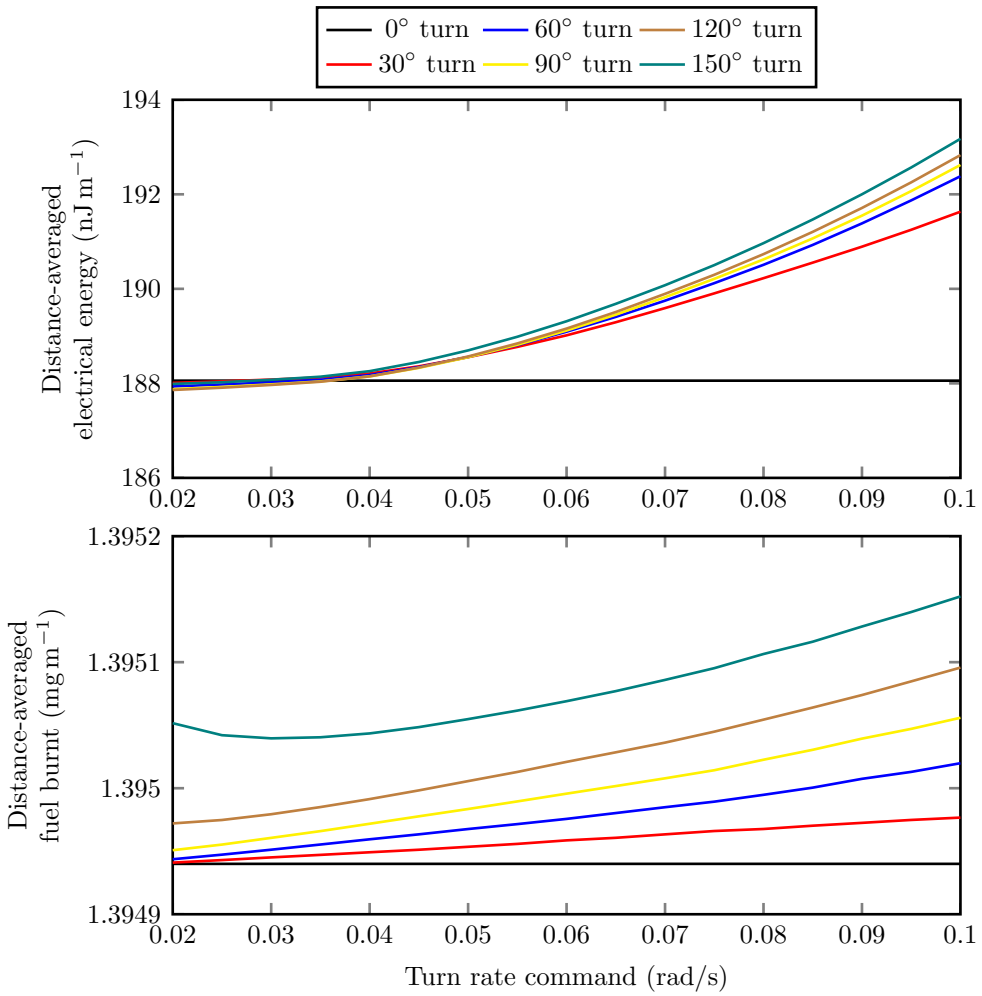

Figure 7.51: Total energy demand of Aerosonde actuation system during turn rate sweep of all heading changes, using EMA at cruise condition (24 m/s, 1800 m). Top figure: total actuator energy, Bottom: average fuel burnt

7.2.2.3 Force-speed statistical flights

Reducing the data further into statistical force-speed 'flights' allows the visualisation of operating quadrant. The data can also be useful for conducting experiments on laboratory test actuators, by supplying them with realistic load forces and velocity commands. This data is typically recorded during flight tests, but the technique presented in this thesis provides another method of generating actuator input data for arbitrary trajectories.

Data is shown for three heading changes: 150° (Figure 7.52), 90° (Figure 7.53) and 30° (Figure 7.54) turns at cruise (24 m/s, 1800 m). Since the flight condition and dynamic pressure remain unchanged, the range of force and velocity do not change much between the different manoeuvres. What does become evident is the effect on the actuators of the inability of the aircraft to achieve high turn rates (e.g. 0.1 rad/s) for short turns in Figure 7.54.

Although not presented for the 30° turn, the time series data for the 150° manoeuvre in Figure 7.41 shows the highest turn rate is only in a banked attitude for around 30 seconds. During this time, the airspeed and altitude does not stabilise (Figure 7.42). It is comprehensible therefore that when demanding a 0.1 rad/s turn rate for a 30° manoeuvre, the 6-DOF, FCS and guidance algorithm do not allow the fidelity of control required to achieve a high rate steady state banked turn in such a short period of time.

What these plots should convey is the detail in actuator data generated for dynamic aircraft manoeuvres. Where these had previously been generated by pilots following flight testing procedures in real aircraft with data logging, they could now be produced for a wide range of manoeuvres without the expense of flight tests. Although the actuators and aerodynamic load estimation models are not accurately validated for any of the aircraft in this

thesis, with suitable validation it would be possible to generate useful data with significantly reduced expense and increased repeatability.

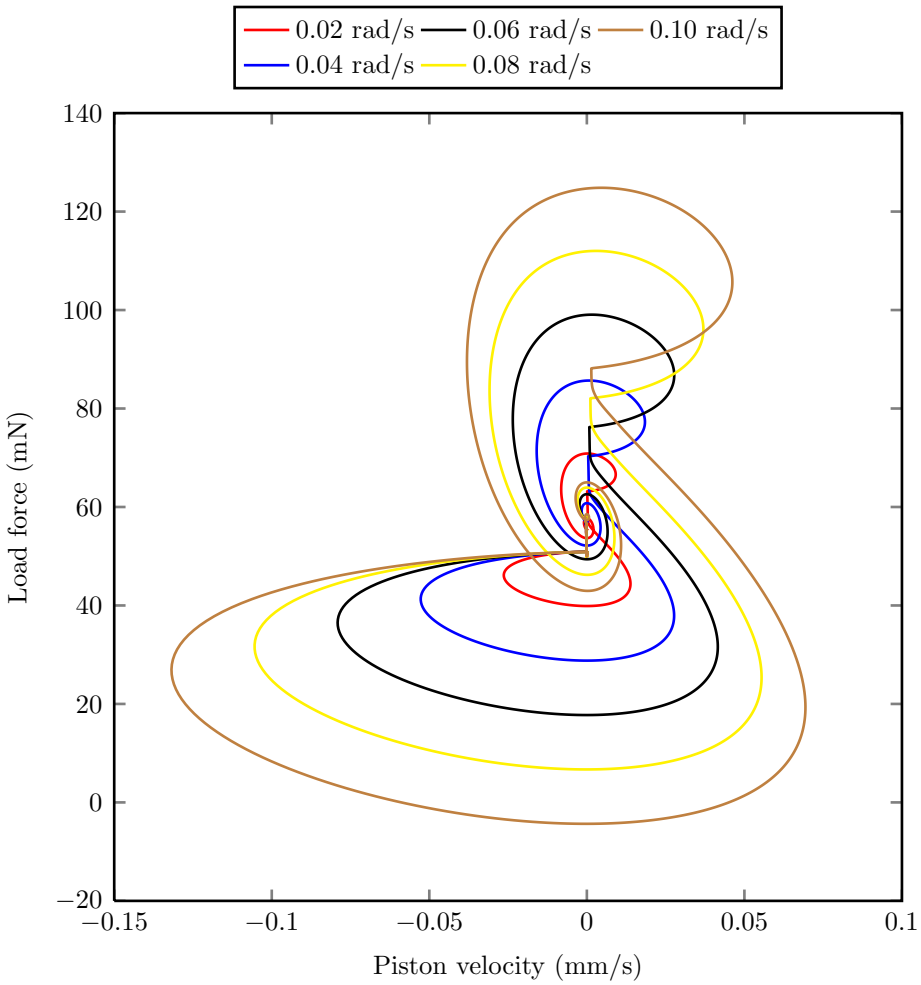

Figure 7.52: Load-velocity plot of Aerosonde aileron EMA during a 150° turn during cruise (24 m/s, 1800 m) at five different turn rates

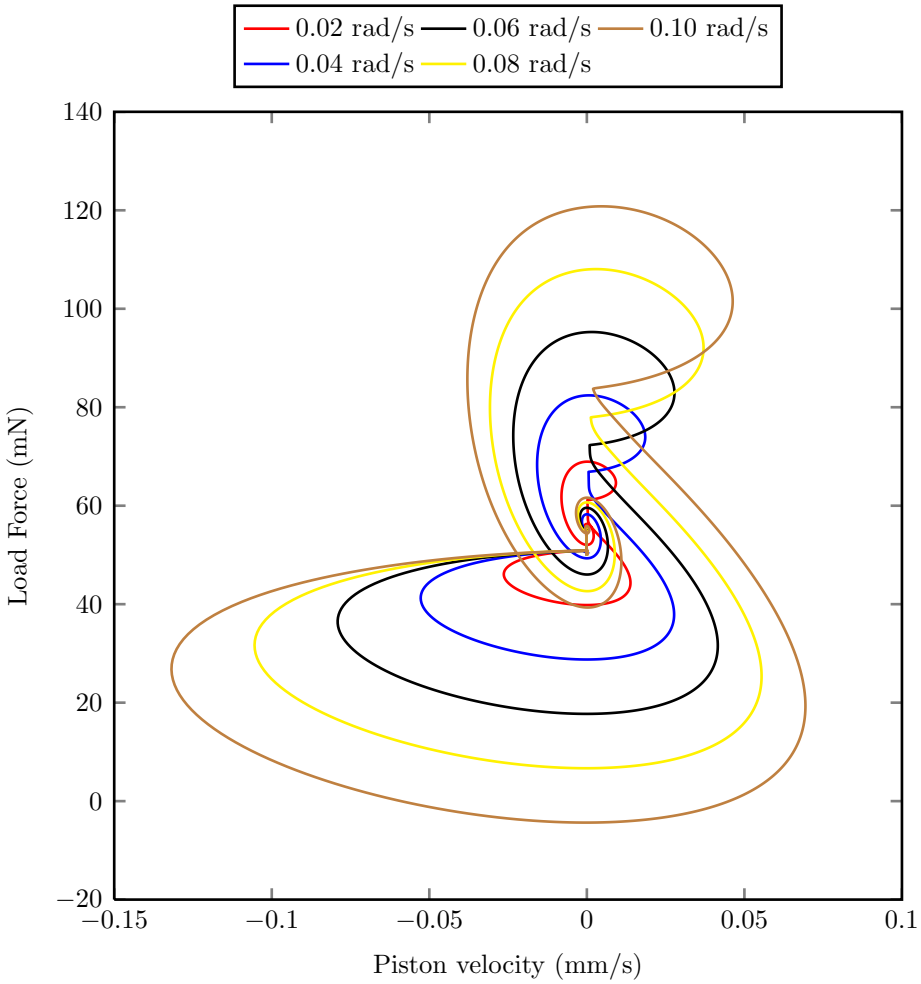

Figure 7.53: Load-velocity plot of Aerosonde aileron EMA during a 90° turn during cruise (24 m/s, 1800 m) at five different turn rates

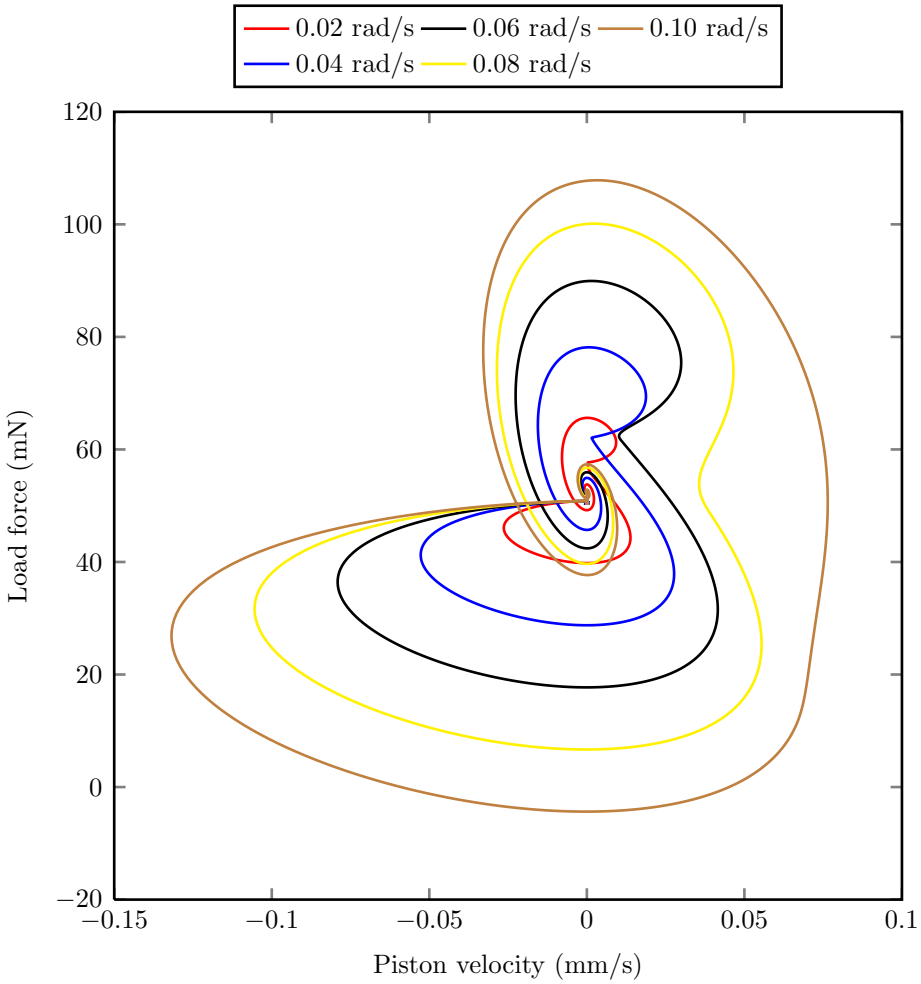

Figure 7.54: Load-velocity plot of Aerosonde aileron EMA during a 30° turn during cruise (24 m/s, 1800 m) at five different turn rates

7.2.2.4 Long flight with wind

One criticism of this work has been the exclusion of wind and turbulence; an effect which can considerably increase the power consumption of an actuator and cause problems with heat build up in the motor. Most motors are designed to use their rotational velocity to induce airflow which aids their cooling.

In the case of an aircraft which intends to continue flying straight and level through turbulence, the control surfaces experience time varying aerodynamic forces which their actuators have to oppose by applying time varying power. Achieving this at zero velocity has proven a challenge in the development of electric actuators, since maximising cooling and minimising mass often have to be traded off. Being able to generate repeatable and predictable test data to conduct laboratory experiments on prototypes is considered a very useful function.

For the last analysis in this thesis, the Aerosonde model is supplied with wind vectors generated by a Dryden turbulence model. The turbulence is set low enough that the aircraft can maintain control but with relative difficulty.

The aircraft is given a longer waypoint list than has previously been used, to represent a simulated flight path traversing a route defined by the eight waypoints shown in Figure 7.55. The aircraft follows the route without any noticeable deviation, but looking at the Euler angles in Figure 7.56 as it flies along the route shows the increased effort that must be applied by the actuators. For example, the ailerons provide a rolling moment to induce angular acceleration; when a roll moment is applied by the turbulence model, the actuators must apply power to counteract the unwanted rolling motion. This occurs repeatedly while the aircraft is trying to fly straight and level,

causing roll angle variations in the range of $\pm 1^\circ$.

As would be expected under turbulent conditions, the altitude and airspeed tracking loses accuracy, increasing to around ± 4 m and ± 0.8 m/s in Figure 7.57. As discussed in the previous paragraph, the control effort required to maintain stable flight is continually varying according to the filtered white noise of the Dryden turbulence model. This is reflected through the control surface position plot in Figure 7.58.

As a final conclusion to the potential use of the combined 6-DOF and actuator model, the force-speed plot of an aileron experiencing turbulent conditions is shown in Figure 7.59. The data is unrecognisable when compared to the force-speed plots shown previously, because the aircraft executes both left and right turns and experiences noisy aerodynamic loads. This could prove to be a cost effective method of generating dynamic data for assessing actuator performance, power consumption and efficiency in the laboratory with data representing a wide range of adverse conditions.

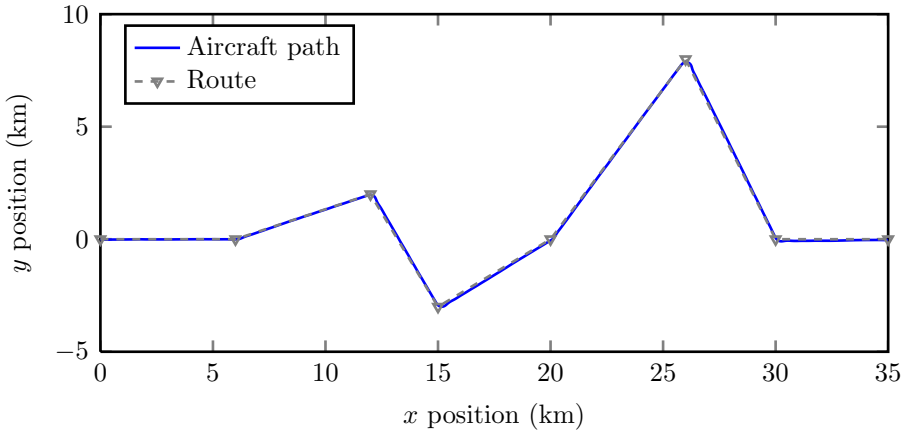

Figure 7.55: xy trajectory of Aerosonde at cruise (24 m/s, 1800 m), including Dryden turbulence model

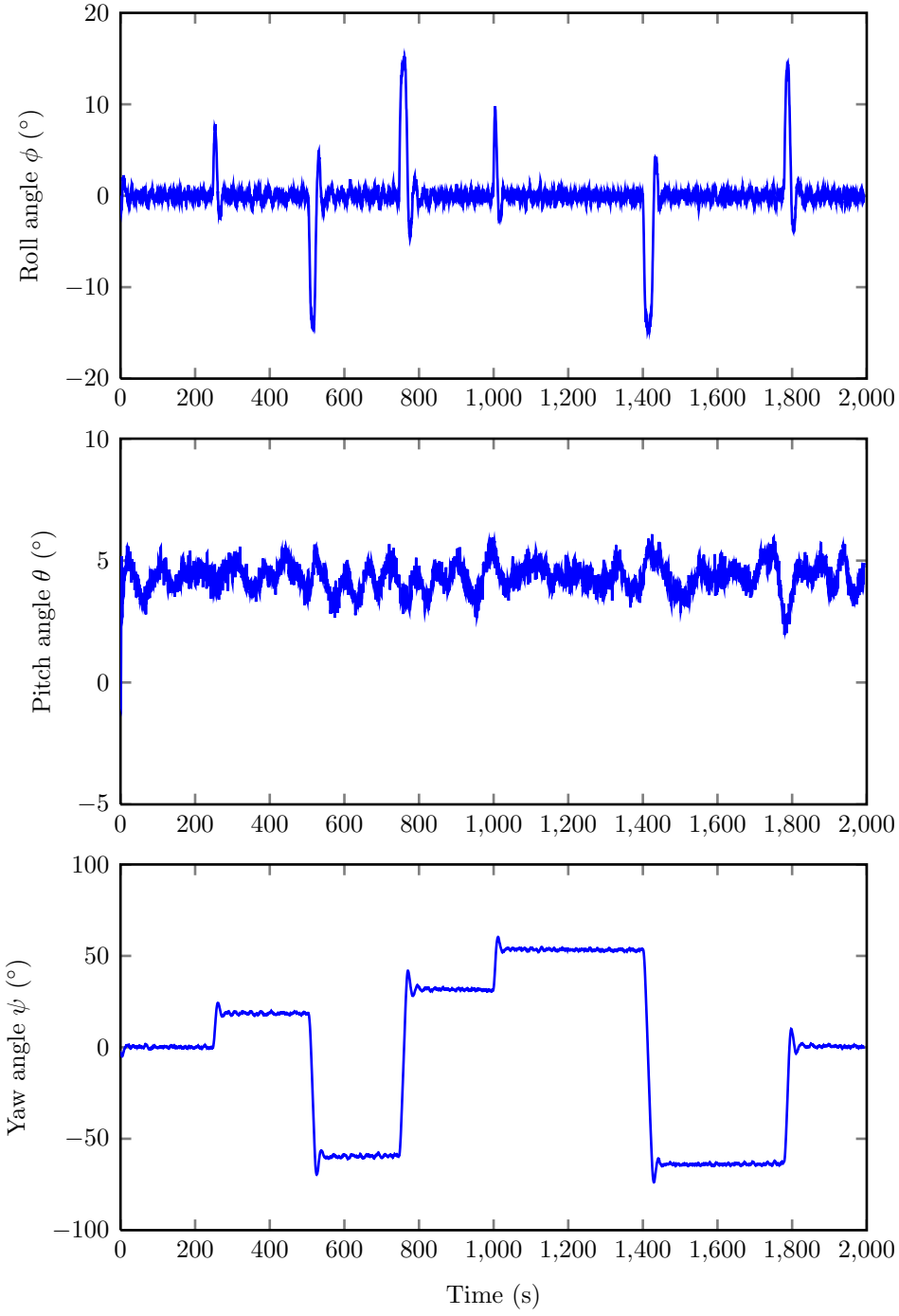

Figure 7.56: Euler angles of Aerosonde at cruise (24 m/s, 1800 m), including Dryden turbulence model

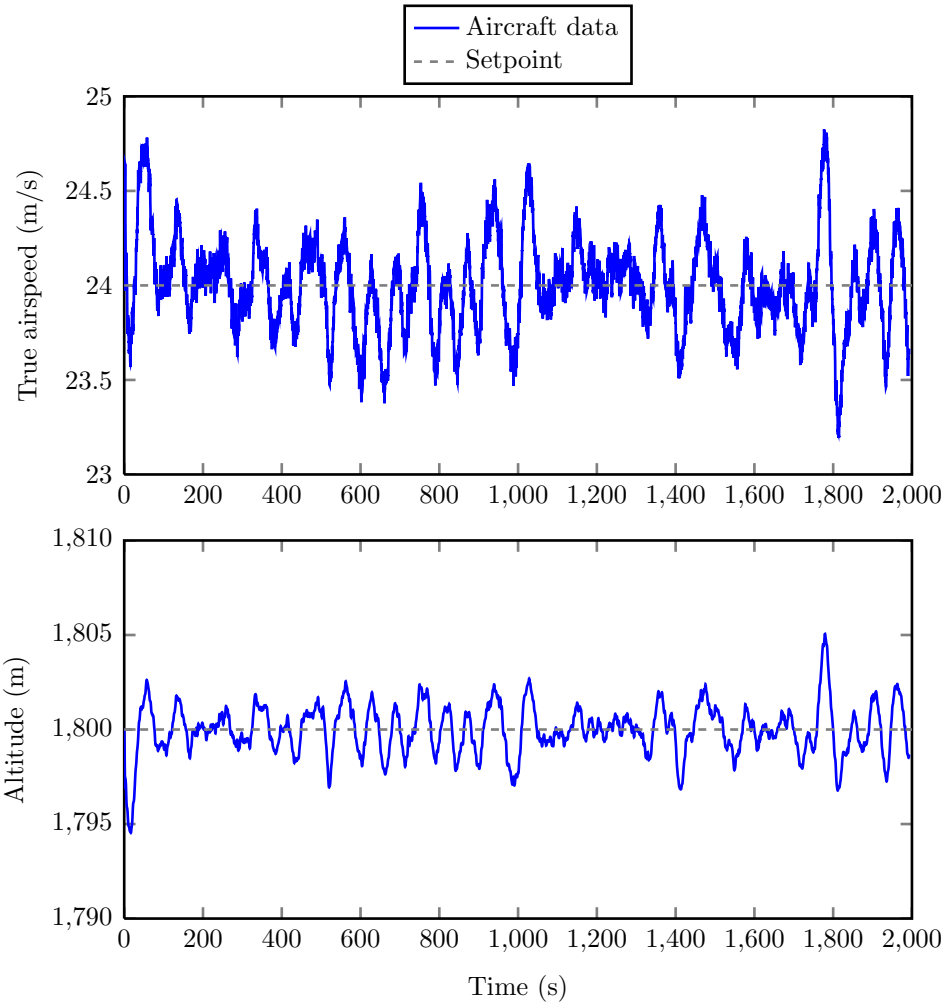

Figure 7.57: Altitude and airspeed of Aerosonde at cruise (24 m/s, 1800 m), including Dryden turbulence model

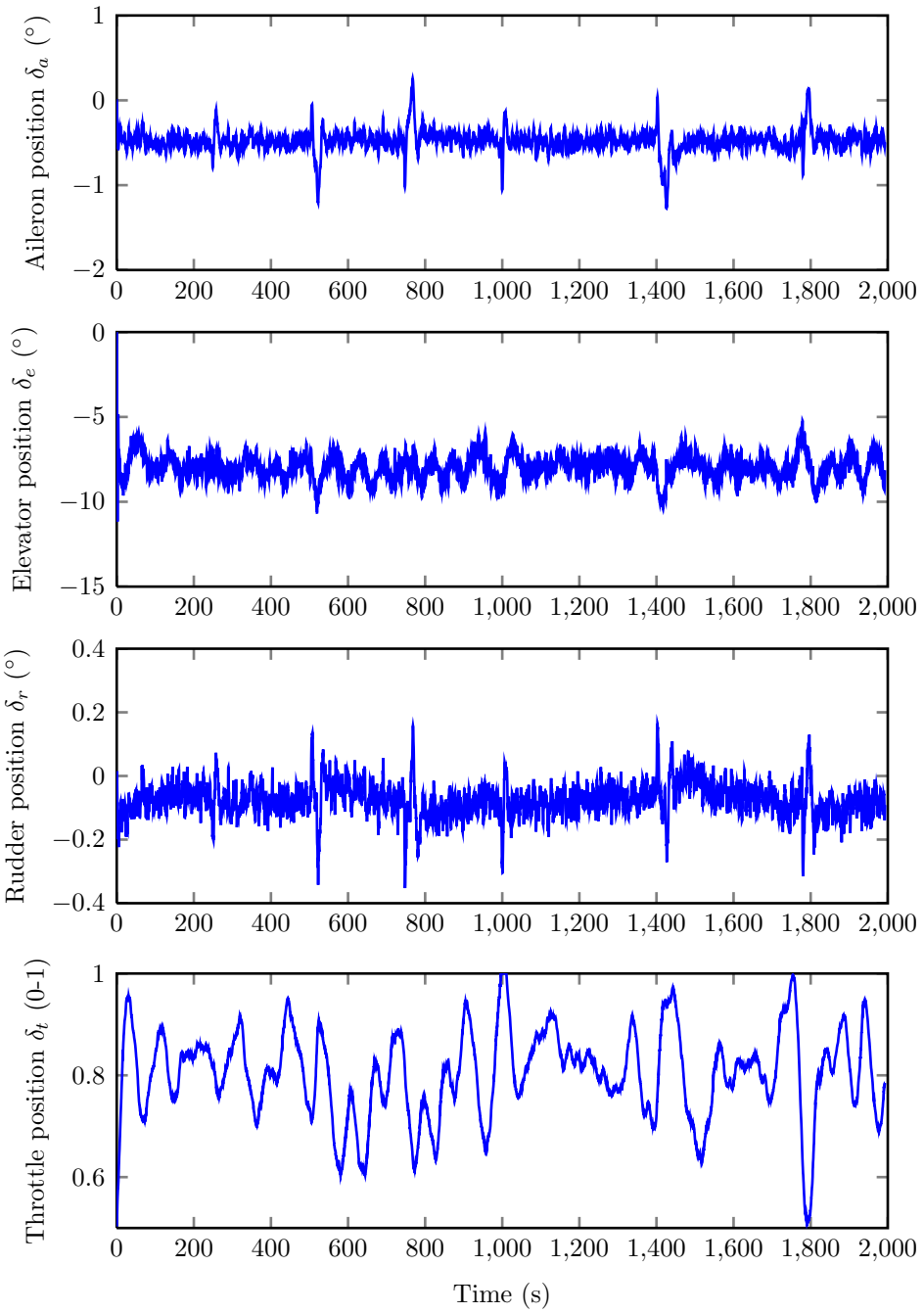

Figure 7.58: Control inputs of Aerosonde at cruise (24 m/s, 1800 m), including Dryden turbulence model

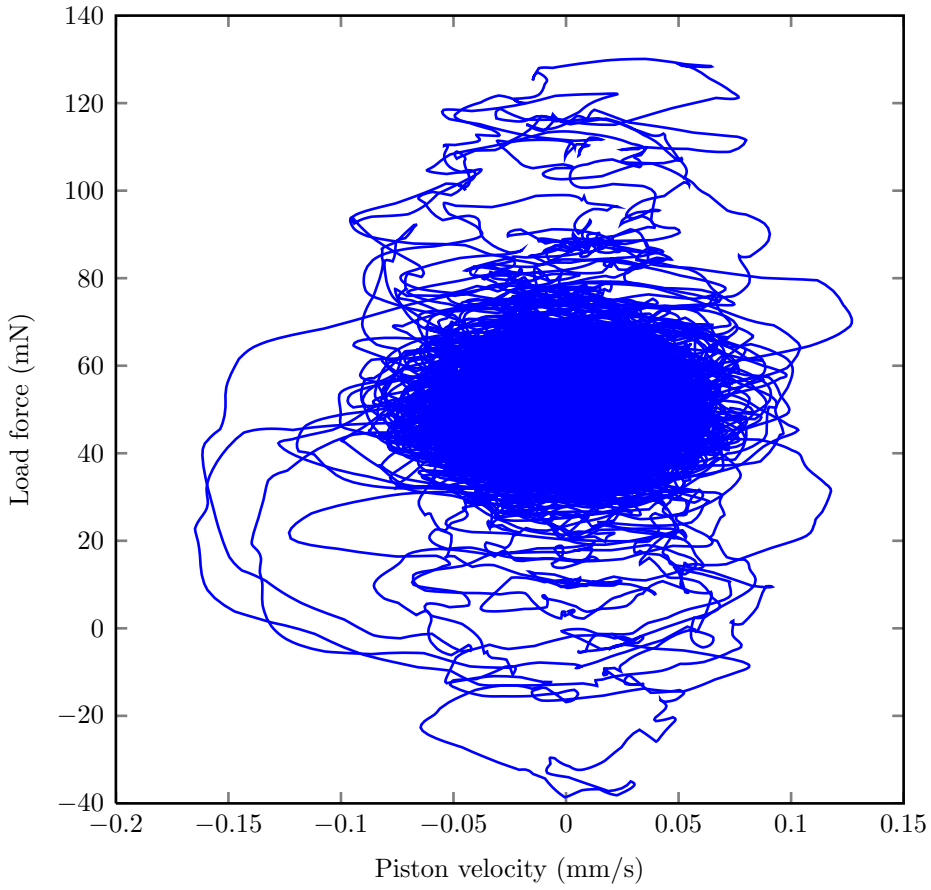

Figure 7.59: Force-speed plot of Aerosonde aileron at cruise (24 m/s, 1800 m), including Dryden turbulence model

Chapter 8

Conclusions and Future Work

8.1 Conclusions

A dynamic simulation of an aircraft and its primary flight control actuation system has been successfully created in this thesis. The actuators are implemented as low frequency functional level models, intended to capture the major dynamics which contribute to the primary power consumption. Three types of actuator are included: electro-servohydraulic actuators (ESHAs), electromechanical actuators (EMAs) and electrohydrostatic actuators (EHAs) which represent the current state of the art (hydraulic) and the two most prominent electrically powered alternatives. Aerodynamic loads on the control surfaces are estimated using lookup tables and first order approximations.

The complete aircraft model is equipped with a flight control and guidance system to allow it to follow trajectories automatically. The complete system is optimised for simulation speed and achieves faster than real time execution on a desktop computer. It is difficult to provide numerical results on the simulation speed because it is very strongly affected by the behaviour of the variable step numerical solver. With no turbulence and straight level flight, speeds of hundreds of times faster than real time are achievable. When noisy

signals are present due to poor control systems or turbulence models, the speed can reduce to less than real time.

A set of guidelines are collated from the experience gained in producing this work, which lay the groundwork for further development of computationally efficient combined aircraft and systems simulations. The models designed in this work are implemented in Simulink, which is inherently a single threaded application. Where appropriate, references have been made to alternative methods of achieving complete aircraft simulations using distributed solvers. These naturally lend themselves to multithreaded simulations and look to be capable of scaling to larger computing clusters more readily than the method presented in this thesis. Given that the recent trend in processor development has seen improved performance through application of multi core technology, rather than continual increase in clock speed; distributed solvers are thought to be of significant interest for the future.

Once the model had been created and tested, it was used to map the power consumptions of the actuation system during banked turn manoeuvres for two types of aircraft: an Airbus A320 and an Aerosonde UAV. The conclusion from both is that the aircraft actuation system uses less energy when executing low bank angle, large turn radius turns. However, the overall power consumption of the actuation system is extremely small. It is therefore unlikely to be recommended to change how aircraft manoeuvre just to save small amounts of fuel - the impact on ground track following is significant when bank angles become too low.

This conclusion does not make the modelling work futile; it would benefit strongly from the inclusion of other airframe systems models and a means of relating their energy demands back to the engines to assess fuel burn. Because of the dynamic interaction between the aircraft model and the ac-

tuators, the flight control actuation system is considered to be the most challenging system to model dynamically (compared to the environmental control system or wing ice protection system). This reasoning follows because there is a tightly closed loop between the aircraft and actuators; the aircraft gives position commands and load forces to the actuators and the actuators give their achieved surface positions in response. Importantly, the dynamics of the aircraft affects the operating condition of the actuators and the dynamics of the actuators affect the aircraft trajectory.

On the other hand, the environmental control and ice protection systems operation does not have a significant affect on aircraft trajectory. For the most part, reasonably accurate power consumption models for these systems only require air data such as altitude and airspeed from an aircraft model. As such they can be driven from a reduced order flight performance model; attaching them to a 6-DOF is merely a case of feeding the correct inputs into the models. The loop can only be closed with the engines if the engine models have the ability to compute the affect on thrust and fuel consumption from power off-takes.

When all three major secondary power consumers are included in a simulation, flight trajectories can be flown dynamically to generate test data for any of these systems - without real flight testing. This concept is explored in section 7.1.3 of this thesis for power analysis in turbulent flight; load - speed data of the actuators is recorded and applied to separate actuator models, but the signals can also be applied to hardware design and test rig analyses.

One point that should be made clear about the work conducted is that a fairly unique FCS is implemented in order to achieve robust simulations. The total energy control system is a novel design which manages the energy states of the aircraft's axes of motion. It is not commonly used in current

aircraft designs; it could be argued that this would have an effect on how the actuators are controlled and therefore, what load - speed profiles and power consumptions are obtained. This is a valid point, but the same would be true of any flight controller that is implemented. Indeed, this may not be a problem in some situations where the influence of the control systems on actuator performance is the target of the study. If a controller is tuned to push an actuator hard, by inducing high deflection angles and high linear rates then the peak power consumption will clearly be higher than a smoother controller that has a more relaxed attitude to manoeuvring the aircraft. The only real solution to remove the dependency on the control systems is to switch to inverse models which do not need controllers.

During the approach flight phase the relative efficiencies of the three aileron actuation technologies show the EMA has the highest efficiency at 2.2%, the EHA is 1.5% and the ESHA has the lowest efficiency at 0.4% when executing a turn. These efficiencies are computed using the ratio of energy input and output instead of power, because the output power is frequently zero. These figures are based on electric actuator models which exclude the servo drive power losses, if they were included as discussed in section 3.4 the results may change significantly.

When considering the relative merit of turning at different rates to reduce energy consumption by the actuators it is helpful to know how much each actuation technology is affected by the higher peak loads during higher rate turns. Considering the 150° turn during the approach condition, the ESHA uses 4.23% more energy to achieve a turn at a turn rate of 0.03 rad/s compared to a 0.005 rad/s manoeuvre. The EMA uses 1.67% more and the EHA uses 1.54% more to achieve the same turns. It can therefore be concluded that implementing some scheme of reduced turn rate turns in appropriate

situations would have the largest benefit for reducing energy consumption in current hydraulically powered actuation systems, compared to electrical actuators.

Also of interest is how much each actuation technology is affected by the increased steady state loads during the longer turns to greater heading changes. At approach conditions the ESHA exhibits a 0.15 mJ/m increase in average energy consumption (a 0.24% increase) as the turn rate increases from 30° to 150°. The EMA increases less at 0.06 mJ/m (0.55%) and the EHA is 0.1 mJ/m (0.56%). As evidenced by the results, different heading changes make a smaller percentage difference to the ESHA energy consumption than either of the electrical actuators, but this is due to the fact the overall energy consumption of the ESHA is between 3 and 6 times greater than the electric actuators.

From the preliminary results obtained in this work, it can generally be stated that hydraulic actuators have the lowest efficiency, electro-hydrostatic are the middle and electromechanical is the highest efficiency technology *in flight*. There are situations when the hydraulic actuator efficiency is the highest: i.e. at stall force, but this is a rare occurrence in flight. Conversely, it can also be deduced that at low loads (which dominate the load profiles in flight), electric actuators experience lower losses than the hydraulic system because power is not continuously dissipated by a leaking servovalve. This conclusion is however based on numerous assumptions; while the author has produced this work to the highest standard possible, it is simply unfair to make direct comparisons between the different technologies without performing experiments to validate the results.

Power conversion efficiency is only one aspect of the operational efficiency which is going to have an impact on airline operations. The different

technologies have varying components with unique life cycle requirements; hydraulic fluid needs replacing, but electric actuators have higher cooling demands in service and potentially an increase in aircraft specific fuel consumption due to increased mass. Every aspect of an actuator from its design and manufacture through to its installation, operation, maintenance and end of life disposal have an influence on whether a device can be called 'efficient'. Such is the depth and complexity of this topic that it is left in the domain of future work.

At the start of this work, it was supposed that modelling an aircraft, its actuators and its control systems would be the most useful way of quantifying the power consumption of the actuators. There were several reasons behind this; one was that by using direct models, it is possible to represent more realistically the physical effects inside the actuators and how they affect the closed loop controlled actuators.

Although not directly useful for power estimation, direct models allow the simulation of various failure modes and estimation of their affect on the dynamics of the controlled system as a whole. Thus, it is possible to assess the manoeuvrability of an aircraft (with suitable additions to the actuator models) with, for example, failed motor windings or worn ball screws.

Another reason was to include the affect on power consumption of the control systems themselves; allowing the quantification of power consumption due to poorly tuned controllers or control algorithms as a whole.

In retrospect, whilst these are worthwhile techniques to accomplish, the author feels a new direction would be beneficial for future dynamic power consumption estimation tools. By using inverse models for the actuators, aircraft or both; it is possible to avoid simulating the control systems entirely.

An inverse aircraft model is supplied with the desired trajectory as an

input and it provides the required control deflections to achieve that trajectory. An inverse actuator model is given the desired piston motion as an input and it computes the required input voltage and current to achieve the demand.

By default this technique has the weakness of not directly including physical limitations; if the actuator model is given a motion profile which is beyond the specification (e.g. linear velocity too high), the model will happily output a required voltage and current which is larger than the actuators' rated values. Presuming this is handled by preconditioning the input profiles or some other method, by removing the closed loops the simulation has the potential to increase in speed significantly.

This work cannot answer whether the ideal solution is a fully inverse simulation of both aircraft and actuator models, or a hybrid technique most likely using a direct aircraft and inverse actuator model. Depending on the goals of the engineer; it must be fully considered whether the realism added by simulating control systems adds value to their research.

A highly integrated simulation such as that achieved in this work takes a lot of labour, iteratively improving every layer until the package works smoothly as a whole. For tasks where the framework is required to be adjusted to represent different aircraft with ease; inverse simulation should definitely be under consideration.

8.2 Proposed Future Work

- Improve friction models. The results of this work cannot be used to draw validated conclusions of which actuators are the most efficient since friction plays a dominant role in assessing this. The friction models are not validated by experiment and can be highly variable based on

both micro and macroscopic properties. A suitable first step to improve the accuracy would be to include Maré's work from [133].

- Replace actuator models with experimentally validated models, preferably supplied by the manufacturer (if possible).
- Without experimentally validated models, friction models could be improved using using Maré's method of estimating friction curves from limited datasheet 'mechanical efficiency' and other such data [132].
- In this work the focus has been on mechanical losses in the actuators themselves; the obvious next step is to include losses in the additional components. For example, the electrical losses in the servo drives which supply power [84, 3], transmission losses in the hydraulic tubing and leakage in the engine driven pumps.
- The technique used in this thesis is not very scalable due to Simulink's single threaded nature. Future development should investigate methods such as that used by Krus [14] to apply distributed solvers for complex system modelling. Currently this is not possible using Simulink so it relies on cutting edge software such as Hopsan or Dymola.
- There is definitely a case for investigating the use of inverse models of either the aircraft, actuators, or both to improve the speed of execution. Inverse models require no controllers; since control systems have to be tuned specifically to the aircraft and actuators, inverse modelling may also lend itself to producing a tool which can be adapted to simulate many aircraft using database parameters.
- The direct modelling technique applied in this work could be used to investigate the effect of actuator failures on the whole aircraft; e.g. by

modifying friction to represent different types of jams, studying how motor phase failure affects flight dynamics or even predicting component lifetime using realistic flight trajectories instead of averaged data.

- The model could be used to investigate uncertainty in flight controls; how can minor variations in actuator behaviour affect the *actual* trajectory an aircraft takes?

Appendix A

Definition of Inputs, Outputs and Internal Constants

NB: All values listed in this section apply for the aileron, elevator and rudder actuators but are only mentioned once.

A.1 Electro-servohydraulic System

A.1.1 Inputs

Table A.1: Inputs

Parameter	Variable	Variable precision	Range
Control surface position command	δ_c	double	$[-\delta_{max}: \delta_{max}]$
Actuator load force	F_L	double	$[-F_{Stall}: F_{Stall}]$

A.1.2 Constants

Table A.2: Servo valve Constants

Parameter	Variable	Variable precision
Torque motor coil inductance	L_t	double
Torque motor coil resistance	R_t	double
Saturation current of torque motor	I_{vsat}	double
Natural frequency of servo valve	ω_n	double
Damping factor of second order servo valve	ζ	double
Rated flow of servo valve (at rated pressure)	Q_r	double

Table A.3: Hydraulic Cylinder Constants

Parameter	Variable	Variable precision
Piston surface area	A_c	double
Bulk modulus	β_e	double
Combined pump and piston leakage coefficient	C_{12}	double

Table A.4: Piston Constants

Parameter	Variable	Variable precision
Actuator stroke	L_c	double
Mass of piston & load	M	double
Viscous friction coefficient between piston and cylinder	B_{vcyl}	double

Table A.5: Hydraulic Power Supply Constants

Parameter	Variable	Variable precision
Maximum flow of hydraulic pump	Q_p	double
Volume of trapped oil between pump and servo valve	V_t	double
Maximum working pressure in system	$PressurePa$	double
Variable displacement pump efficiency	η_{vdp}	double

A.1.3 Outputs

Table A.6: Electro-servohydraulic system outputs

Parameter	Variable	Variable precision
Control surface angle	δ	double
Engine off-take shaft power	$P_{EngineShaft}$	double

A.2 Electromechanical System

A.2.1 Inputs

Table A.7: Inputs

Parameter	Variable	Variable precision	Range
Control surface position command	δ_c	double	$[-\delta_{max}: \delta_{max}]$
Actuator load force	F_l	double	$[-F_{Stall}: F_{Stall}]$

A.2.2 Constants

Table A.8: DC Motor Constants

Parameter	Variable	Variable precision
Armature resistance	R_a	double
Armature inductance	L_a	double
Torque constant	K_t	double
Back e.m.f. constant	K_v	double
Rotor inertia	J	double
Ball screw inertia	J_{bs}	double
Viscous damping coefficient for motor	B_v	double
Crossover sharpness of Coulomb friction curve for motor	K_{cm}	double

Table A.9: Ball Screw and Nut Constants

Parameter	Variable	Variable precision
Stroke	L_c	double
Screw pitch	p	double
Motor stiffness	K_m	double
Load mass	M_l	double
Viscous damping coefficient of screw	B_v	double

A.2.3 Outputs

Table A.10: Electromechanical system outputs

Parameter	Variable	Variable precision
Control surface angle	δ	double
Electrical system off-take power	$P_{Electrical}$	double

A.3 Electro-hydrostatic System

A.3.1 Inputs

Table A.11: Inputs

Parameter	Variable	Variable precision	Range
Control surface position command	δ_c	double	$[-\delta_{max}: \delta_{max}]$
Actuator load force	F_l	double	$[-F_{Stall}: F_{Stall}]$

A.3.2 Constants

Table A.12: DC Motor Constants

Parameter	Variable	Variable precision
Armature resistance	R	double
Armature inductance	L	double
Torque constant	K_t	double
Back e.m.f. constant	K_b	double
Rotor inertia	J_m	double
Viscous damping coefficient for motor	B_{vm}	double
Crossover sharpness of Coulomb friction curve for motor	K_{cm}	double

Table A.13: Hydraulic Cylinder Constants

Parameter	Variable	Variable precision
Piston surface area	A_c	double
Bulk modulus	β_e	double
Combined pump and piston leakage coefficient	C_{12}	double

Table A.14: Piston Constants

Parameter	Variable	Variable precision
Piston Stroke	L_c	double
Piston Mass	M	double
Piston Damping	B_{vcyl}	double

Table A.15: Fixed Displacement Pump Constants

Parameter	Variable	Variable precision
Pump displacement	D_p	double
Pump efficiency	η_p	double

A.3.3 Outputs

Table A.16: Electro-hydrostatic system outputs

Parameter	Variable	Variable precision
Control surface angle	δ	double
Electrical system off-take power	$P_{Electrical}$	double

A.4 Control Surface Geometric Model

A.4.1 Inputs

Table A.17: Inputs

Parameter	Variable	Variable precision	Range
Actuator Linear Displacement	x	double	$\left[-\frac{L_c}{2} : \frac{L_c}{2}\right]$

A.4.2 Constants

Table A.18: Control Surface Geometric Constants

Parameter	Variable	Variable precision
Distance between actuator pivot point and control surface pivot point	a	double
Distance between actuator attachment points	b	double
Distance between actuator attachment points at neutral position	b_0	double
Lever arm length (equal to *Lever* in the aeroload estimator)	c	double
Installation angle (Refer to Figure 3.42)	β	double
Installation angle at neutral position	β_0	double
Maximum control surface deflection	δ_{max}	double

A.4.3 Outputs

Table A.19: Control Surface Outputs

Parameter	Variable	Variable precision
Control surface deflection	δ	double

A.5 Aeroload Estimator

A.5.1 Inputs

Table A.20: Aeroload Estimator Inputs

Parameter	Variable	Variable precision	Range
Ratio of flap chord to wing chord	$cf/\bar{c}$	double	[0.1:0.4]
Wing thickness ratio	$t/\bar{c}$	double	[0.0:0.15]
Reynolds number	R_e	double	[10e6:10e8]
Trailing edge angle	Φ''	double	$\left[0: \frac{20\pi}{180}\right]$
Trailing edge shape factor	TEs	double	[0:0.2]
Lever arm length of installation	$Lever/c$	double	Any
Angle of attack	α	double	[-12:12]
Control surface deflection	δ	double	[-20:20]
Air density	ρ	double	Any
True air speed	v_{TAS}	double	Subsonic
Surface area of control surface	A_w	double	[>0]
Mean chord of control surface	$\bar{c}$	double	[>0]
Mach number	M	double	[0:0.8]

A.5.2 Constants

Table A.21: Aeroload Estimator Constants

Parameter	Variable	Variable precision
None		

A.5.3 Outputs

Table A.22: Aeroload Estimator Outputs

Parameter	Variable	Variable precision
Load force	F_l	double

Appendix B

Model Constants

NB: In Matlab the variables are organised into structures by control surface and type of actuator; ie: Aileron.ESHA.Ac or Elevator.EMA.R. This allows all models to be loaded without overwriting each others' data.

B.1 Electro-Servohydraulic System

Table B.1: Servo valve

Parameter	Units	Matlab Variable	Aileron	Elevator	Rudder
L_t	H	Lt	0.59	0.59	0.59
R_t	Ω	Rt	100	100	100
I_{vsat}	A	Iv	0.02	0.02	0.02
ω_n	rad s^{-1}	wn	534	534	534
ζ	-	Sv	0.48	0.48	0.48
Q_r	m^3s^{-1}	Qr	1.33E-04	5.10E-05	1.50E-04
P_r	Pa	Pr	0	0	0

Table B.2: Hydraulic Cylinder

Parameter	Units	Matlab Variable	Aileron	Elevator	Rudder
A_c	m^3	Ac	0.0026	0.0015	0.0024
β_e	Pa	Be	1.60E+09	1.60E+09	1.60E+09
C_{12}	$m^3s^{-1}Pa^{-1}$	C_12	1.00E-13	1.00E-13	1.00E-13

Table B.3: Piston

Parameter	Units	Matlab Variable	Aileron	Elevator	Rudder
L_c	m	Lc	0.044	0.06	0.11
M	kg	M	10	10	10
B_{vcyl}	Nsm^{-1}	Bv_cyl	150	150	150

Table B.4: Hydraulic Power Supply

Parameter	Units	Matlab Variable	Aileron	Elevator	Rudder
Q_p	$\mathrm{m}^3\mathrm{s}^{-1}$	Qp	0.0024	0.0024	0.0024
V_t	m^3	Vt	5.00E-04	5.00E-04	5.00E-04
$PressurePa$	Pa	PressurePa	20.684E6	20.684E6	20.684E6
η_{vdp}	-	eta_vdp	0.91	0.91	0.91

Table B.5: ESHA Position Control

Parameter	Units	Matlab Variable	Aileron	Elevator	Rudder
K_p	-	Kp	4.85	8.90	9.74
K_i	-	Ki	75.57	41.57	43.65
K_v	-	Kv	1.00E-4	1.00E-4	1.00E-4
K_f	-	Kf	*Lookup table*	*Lookup table*	*Lookup table*

B.2 Electromechanical System

Table B.6: DC Motors

Parameter	Units	Matlab Variable	Aileron	Elevator	Rudder
Motor			**M1054K**	**M1053K**	**M1453L**
R	Ω	R	0.36	0.48	0.22
L	H	L	0.0017	0.002	0.0019
K_t	$\mathrm{NmA^{-1}}$	Kt	0.4949	0.4699	0.7749
K_b	$\mathrm{V\ rad^{-1}s^{-1}}$	Kb	0.495	0.47	0.775
J_m	$\mathrm{kg\ m^2}$	Jm	6.20E-04	4.80E-04	0.0016
B_{vm}	$\mathrm{Nms\ rad^{-1}}$	Bv	3.03E-04	1.62E-04	2.02E-04
K_{cm}	-	Kcm	1.1	1.1	1.1
C_{oul}	Nm	Coul	0.2	0.2	0.7
I_{stall}	A	Istall	16.76	14.37	28.78

Table B.7: Ball Screw and Nut

Parameter	Units	Matlab Variable	Aileron	Elevator	Rudder
L_c	m	Lc	0.044	0.06	0.11
p	$\mathrm{mrad^{-1}}$	p	1.66E-04	1.05E-04	3.17E-04
K_m	$\mathrm{Nm^{-1}}$	Km	1.00E+07	1.00E+07	1.00E+07
K_s	$\mathrm{Nm^{-1}}$	Ks	1.80E+05	1.80E+05	1.80E+05
B_s	$\mathrm{Nsm^{-1}}$	Bs	1200	1200	1200
M_s	kg	M_S	2	2	2
M_L	kg	M_L	0.6	0.6	0.6
B_{vs}	$\mathrm{Nsm^{-1}}$	B_vs	50796	50796	50796
K_{cs}	-	Kcs	1.1	1.1	1.1
τ	-	tau	1	1	1
J_{BS}	$\mathrm{kgm^2}$	J_BS	0	0	0

Table B.8: EMA Position Control

Parameter	Units	Matlab Variable	Aileron	Elevator	Rudder
K_p	-	Kp	3.46	7.69	7.90
K_i	-	Ki	75.00	75.00	50.07
K_v	-	Kv	0.50	0.50	0.70
K_f	-	Kf	0.22E-5	0.19E-5	0.16E-5

B.3 Electro-hydrostatic System

Table B.9: DC Motors

Parameter	Units	Matlab Variable	Aileron	Elevator	Rudder
Motor			**M1054K**	**M1053K**	**M1453L**
R	Ω	R	0.36	0.48	0.22
L	H	L	0.0017	0.002	0.0019
K_t	$\mathrm{NmA^{-1}}$	Kt	0.4949	0.4699	0.7749
K_b	$\mathrm{V\ rad^{-1}s^{-1}}$	Kb	0.495	0.47	0.775
J_m	$\mathrm{kg\ m^2}$	Jm	6.20E-04	4.80E-04	0.0016
B_{vm}	$\mathrm{Nms\ rad^{-1}}$	Bv	3.03E-04	1.62E-04	2.02E-04
K_{cm}	-	Kcm	1.1	1.1	1.1
C_{oul}	Nm	Coul	0.2	0.2	0.7
I_{stall}	A	Istall	16.76	14.37	28.78

Table B.10: Hydraulic Cylinder

Parameter	Units	Matlab Variable	Aileron	Elevator	Rudder
A_c	m^3	Ac	0.0026	0.0015	0.0024
β_e	Pa	Be	1.60E+09	1.60E+09	1.60E+09
C_{12}	$m^3s^{-1}Pa^{-1}$	C_12	1.00E-13	1.00E-13	1.00E-13

Table B.11: Piston

Parameter	Units	Matlab Variable	Aileron	Elevator	Rudder
L_c	m	Lc	0.044	0.060	0.110
M	kg	M	10	10	10
B_{vcyl}	Nsm^{-1}	Bv_cyl	150	150	150

Table B.12: Fixed Displacement Pump

Parameter	Units	Matlab Variable	Aileron	Elevator	Rudder
D_p	m^3s^{-1}	Dp	6.5949E-7	1.5411E-7	7.4392E-7
η_p	-	eta_p	0.85	0.85	0.85
$PressurePa$	Pa	PressurePa	20.684E6	20.684E6	20.684E6

Table B.13: EHA Position Control

Parameter	Units	Matlab Variable	Aileron	Elevator	Rudder
K_p	-	Kp	3.20	6.47	6.96
K_i	-	Ki	80	40	70
K_v	-	Kv	2	0.5	1.5
K_f	-	Kf	0.25E-5	0.60E-5	0.28E-5

B.4 Control Surface Geometric Model

Table B.14: Control Surface Parameters

Parameter	Units	Matlab Variable	Aileron	Elevator	Rudder
a	m	a	0.2594	0.2638	0.3323
b	m	b	0.2775	0.2875	0.3625
b_0	m	b0	0.2555	0.2575	0.3075
c	m	c	0.045	0.0573	0.126
β	$^\circ$	Beta	1.9058	1.9003	1.6317
β_0	$^\circ$	Beta0	1.3965	1.3518	1.1819
δ_{max}	$^\circ$	delta_max	30	30	25

B.5 Aeroload Estimator

Table B.15: DC Motors

Parameter	Units	Matlab Variable	Aileron	Elevator	Rudder
$cf/\bar{c}$	-	cfc	0.25	0.25	0.25
$t/\bar{c}$	-	tc	0.12	0.12	0.12
Φ''	rad	phi_dash_dash	$\frac{15\pi}{180}$	$\frac{15\pi}{180}$	$\frac{15\pi}{180}$
TEs	-	TEs	0.12	0.12	0.12
$Lever$	m	c	0.0450	0.0573	0.1260
A_w	m^2	Aw	1.676	3.962	7.447
$\bar{c}$	m	cbar	0.6304	0.7604	1.3377

Bibliography

[1] J. M. Pointon, "Thermal management of electromechanical actuation on an all-electric aircraft," Ph.D. dissertation, Cranfield University, 2007.

[2] C. J. Simsic, "Electric actuation system duty cycles," in *IEEE Proceedings of the National Aerospace and Electronics Conference*, vol. 2, 1991, pp. 540–545.

[3] J. Maré and M. Budinger, "Comparative analysis of energy losses in servo-hydraulic, electro-hydrostatic and electro-mechanical actuators," in *11th Scandinavian International Conference on Fluid Power*, Linköping, Sweden, 2009.

[4] A. Trentin, P. Zanchetta, P. Wheeler, and J. Clare, "Power flow analysis in electro-mechanical actuators for civil aircraft," *IET Electric Power Applications*, vol. 5, no. 1, p. 48, 2011.

[5] D. H. Klyde, D. M. Smith, and C. Harris, "Describing functions for higher order actuator models with rate limiting," in *AIAA Atmospheric Flight Mechanics Conference*, Monterey, California, 2002.

[6] The World Bank. (2010) Air transport, registered carrier departures worldwide. [Accessed: 10/1/2013]. [Online]. Available: http://data.worldbank.org/indicator/IS.AIR.DPRT/countries?display=graph

[7] D. Nieuwenhuisen and R. D. Muynck, "Optimizing inbound aircraft streams using aircraft derived data and RTA functionality," in *28th International Congress of the Aeronautical Sciences*, Brisbane, Australia, 2012.

[8] T. Jomier, "MOET Technologies Technical Report D0.02.3," MOET Consortium, Tech. Rep., 2009.

[9] Linköping University. (2013) Hopsan Project. [Accessed: 9/3/2013]. [Online]. Available: http://www.iei.liu.se/flumes/system-simulation/hopsan?l=en

[10] P. Krus and J. Nyman, "COMPLETE AIRCRAFT SYSTEM SIMULATION FOR AIRCRAFT DESIGN - PARADIGMS FOR MODELLING OF COMPLEX SYSTEM," *ICAS Congress*, 2000.

[11] P. Krus, "Complete aircraft simulation for distributed system design," in *Recent Advances in Aerospace Actuation Systems and Components*, Toulouse, France, 2001.

[12] P. Krus, B. Johansson, and L. Austrin, "Concept Optimization of Aircraft Systems Using Scaling Models," in *Recent Advances in Aerospace Actuation Systems and Components*, Toulouse, France, 2004.

[13] P. Krus and C. Jouannet, "Whole Mission Simulation for Aircraft Preliminary Design," *48th AIAA Aerospace Sciences Meeting*, no. January, pp. 1–11, 2010.

[14] P. Krus, "Whole Aircraft Simulatition for System design and optimisation in preliminary design," Linköping University, Tech. Rep., 2012.

[15] R. W. Pratt, *Flight Control Systems - Practical Issues in Design and Implementation*. Institution of Engineering and Technology, 2000.

[16] G. Warwick, "A320: Fly-by-wire airliner," *Flight International*, Aug. 1986.

[17] A. Kulshreshtha, "Remote actuation control system: aircraft flight control for hydraulic-servo and electric actuation," in *Recent Advances in Aerospace Actuation Systems and Components*, Toulouse, France, 2007.

[18] J. Charrier and A. Kulshreshtha, "Electric actuation for flight & engine control system: Evolution, current trends & future challenges," in *45th AIAA Aerospace Sciences Meeting and Exhibit*, Reno, USA, 2007.

[19] W. P. Lear, "Remote and automatic electric controls for aircraft," *Journal of the Franklin Institute*, vol. 238, no. 1, pp. 9–35, 1944.

[20] D. P. Rubertus, L. D. Hunter, and G. J. Cecere, "Electromechanical Actuation Technology for the All-Electric Aircraft," *IEEE Transactions on Aerospace and Electronic Systems*, vol. 20, no. 3, pp. 243–249, 1984.

[21] D. van den Bossche, "EHA Application to commercial transports the Aérospatiale approach," in *Recent Advances in Aerospace Hydraulics*, Toulouse, France, 1998.

[22] S. Croke and J. Herrenschmidt, "More electric initiative - power-by-wire actuation alternatives," in *IEEE Proceedings of the National Aerospace and Electronics Conference*, vol. 2, 1994, pp. 1338–1346.

[23] J. B. Leonard, "All-Electric Fighter Airplane Flight Conrol Issues, Capabilities, and Projections," *IEEE Transactions on Aerospace and Electronic Systems*, vol. 20, no. 3, pp. 234–242, 1984.

[24] R. I. Jones, "The more electric aircraft - assessing the benefits," *Proceedings of the Institution of Mechanical Engineers, Part G: Journal of Aerospace Engineering*, vol. 216, pp. 259–269, 2002.

[25] P. Jänker, F. Claeyssen, B. Grohmann, M. Christmann, T. Lorkowski, R. LeLetty, O. Sosniki, and A. Pages, "New Actuators for Aircraft and Space Applications," in *11th International Conference on New Actuators*, Bremen, Germany, 2008.

[26] R. Doddannavar, A. Barnard, and S. Mackay, *Practical Hydraulic Systems*. Newnes, 2005.

[27] M. Rabie, *Fluid Power Engineering*. McGraw-Hill, 2009.

[28] Airbus S.A.S, *A320 Flight crew operating manual*, 2010.

[29] Airbus. (2009) All about the A320 series. [Accessed: 12/9/2010]. [Online]. Available: http://www.airbus.com/en/aircraftfamilies/a320/index.html

[30] R. J. McLaughlin and E. D. Shaw, "F/A-18 Aileron Smart Servoactuator," in *IEEE Proceedings of the National Aerospace and Electronics Conference*, vol. 1, 1989, pp. 338–345.

[31] B. Lantto, H. Ellstrom, H. Gavel, M. Jareland, S. Steinkellner, A. Jarlestal, and M. Landberg, "Modeling and Simulation of Gripen's Fluid Power Systems," in *Recent Advances in Aerospace Actuation Systems and Components*, Toulouse, France, 2004.

[32] J. Mautin, "Hydraulic system definition and simulation," in *Recent Advances in Aerospace Actuation Systems and Components*, Toulouse, France, 2001.

[33] L. D. Blackman, "Integrated hydraulic system simulation: a new modular approach with Simulink," in *Recent Advances in Aerospace Actuation Systems and Components*, Toulouse, France, 2001.

[34] Mathworks. (2012) Mathworks Simscape. [Accessed: 16/11/2012]. [Online]. Available: http://www.mathworks.co.uk/products/simscape/

[35] L. D. Blackman, "Detailed dynamic model for variable displacement pumps a new approach with Simulink," in *Recent Advances in Aerospace Actuation Systems and Components*, Toulouse, France, 2001.

[36] R. Galatolo and G. D. Rito, "Modelling the Dynamics of a Direct-Drive Servovalve for Fail-Operative Primary Flight Control Actuators," in *Recent Advances in Aerospace Actuation Systems and Components*, Toulouse, France, 2004.

[37] T. Nguyen, A. D. L. Chevasneri, and S. Sandler, "Direct drive servo valve," in *Recent Advances in Aerospace Actuation Systems and Components*, Toulouse, France, 2004.

[38] G. Scheffel, "Energy Efficiency in Hydraulics - Potential savings with valve-controlled linear actuators," Parker, Tech. Rep., 2009.

[39] G. D. Jenney, "Simple fly-by-wire actuator," in *IEEE Proceedings of the National Aerospace and Electronics Conference*, vol. 2, 1991, pp. 522–528.

[40] A. Escobosa, "Digitalhydrostatic servoactuation," in *IEEE Proceedings of the National Aerospace and Electronics Conference*, vol. 1, 1994, pp. 571–578.

[41] Eaton Aerospace, "Airbus A318, A319, A320 & A321 Overview - Eatons Aerospace Product Capabilities," Tech. Rep., 2003. [Online]. Available: http://www.eaton.com/Eaton/ProductsServices/Aerospace/LiteratureLibrary/index.htm

[42] Eaton Aerospace, "Vickers Engine-Driven Pump for Boeing's B737-600 / 700 / 800 / 900 (Model PV3-240-18)," Tech. Rep., 2012.

[43] Parker, "Piston Pumps Series P2 / P3 - Variable Displacement," Tech. Rep. Catalogue HY11-2600/UK, 2003.

[44] M. F. Valdo, "Servo hydraulic technology in flight control," in *Workshop on Innovative Engineering for Fluid Power and Vehicular Systems*, São Paulo, Brazil, May 2012.

[45] MOOG, "Electrohydraulic Valves... A Technical Look," Tech. Rep. [Online]. Available: http://www.moog.com/literature/ICD/Valves-Introduction.pdf

[46] N. Hanson, "Hydraulic Proportional and Closed Loop System Design," Bosch Rexroth, Tech. Rep., 2011. [Online]. Available: http://www.cmafh.com/enewsletter/PDFs/Hydraulic_Proportional_Closed_Loop_System_Design.pdf

[47] T. M. Menshawy, M. A. Moghazy, and A. H. Lotfy, "Investigation of Dynamic Performance of an Electro-Hydraulic Proportional System," in *Aerospace Sciences & Aviation Technology*, vol. 13, 2009.

[48] Bosch Rexroth, "Hydraulic cylinder , mill type - Series CDH2 / CGH2 / CSH2," Tech. Rep., 2011.

[49] O. Cochoy, S. Hanke, and U. B. Carl, "Concepts for position and load control for hybrid actuation in primary flight controls," *Aerospace Science and Technology*, vol. 11, pp. 194–201, 2007.

[50] M. A. Davis, "High Performance Electromechanical Servoactuation using Brushless DC Motors," Moog Technical Bulletin, Tech. Rep., 1984.

[51] J. J. Gribble, P. C. Kjaer, C. Cossar, L. Kelly, J. J. Bremner, T. J. E. Miller, C. J. Maxwell, R. Capewell, and D. G. Moorhouse, "Feasibility study of a large switched reluctance spoiler actuator system," *IEE Colloquium (Digest)*, no. 260, 1998.

[52] S. C. Jensen, G. D. Jenney, and D. Dawson, "Flight test experience with an electromechanical actuator on the F-18 Systems Research Aircraft," in *19th Digital Avionics Systems Conference*, 2000.

[53] W. Norton, "Advanced Electromechanical Actuation System (EMAS), Flight Test," USAF, Tech. Rep., 1986.

[54] K. Thompson, "Notes on "The electric control of large aeroplanes"," *IEEE Aerospace and Electronic Systems Magazine*, pp. 19–24, 1988.

[55] R. Alden, "C-141 and C-130 power-by-wire flight control systems," in *IEEE Proceedings of the National Aerospace and Electronics Conference*, vol. 2, 1991, pp. 535–539.

[56] M. E. Roth, "Electromechanical actuation for thrust vector control applications," in *IEEE Proceedings of the National Aerospace and Electronics Conference*, vol. 3, 1990, pp. 1351–1353.

[57] G. R. Sundberg, "Advanced launch system (ALS): Electrical actuation and power systems improve operability and cost picture," in *IEEE Proceedings of the National Aerospace and Electronics Conference*, vol. 3, 1990, pp. 1346–1350.

[58] C. Fulmer, "40 HP Electro-Mechanical Actuator," NASA, Tech. Rep. NASA-CR-198509, October 1996.

[59] D. J. Kopala and C. Doell, "High performance electromechanical actuation for primary flight surfaces," in *Recent Advances in Aerospace Actuation Systems and Components*, Toulouse, France, 2001.

[60] Y. Lin, E. Baumann, D. M. Bose, R. Beck, and G. D. Jenney, "Tests and Techniques for Characterizing and Modeling X-43A Electromechanical Actuators," NASA, Tech. Rep. NASA/TM-2008-214637, December 2008.

[61] C. Whitley and J. Roper, "Development, manufacture & flight test of spoiler EMA system," in *Recent Advances in Aerospace Actuation Systems and Components*, Toulouse, France, 2007.

[62] A. Garcia, J. Cusido, J. A. Rosero, J. A. Ortega, and L. Romeral, "Reliable electro-mechanical actuators in aircraft," *IEEE Aerospace and Electronic Systems Magazine*, vol. 23, no. 8, pp. 19–25, 2008.

[63] F. Perni, L. Pizzoni, and N. Borgarelli, "Ballscrews for the More Electric Aircraft," in *Recent Advances in Aerospace Actuation Systems and Components*, Toulouse, France, 2004.

[64] F. Y. Annaz, "Worthy test programmes and developments of smart electromechanical actuators," *Smart Materials and Structures*, vol. 16, no. 1, pp. 140–148, 2007.

[65] F. Y. Annaz, "Architecture philosophy in high integrity electromechanical actuators," in *5th International Symposium on Mechatronics and Its Applications*, 2008, pp. 1–6.

[66] G. M. Raimondi, R. D. McFarlane, C. M. Bingham, K. Atallah, D. Howe, P. H. Mellor, R. Capewell, and C. Whitley, "Large electromechanical actuation systems for flight control surfaces," in *IEE Colloquium (Digest)*, no. 260, 1998.

[67] C. Gerada, K. J. Bradley, C. Whitley, and G. Towers, "Integrated machine design for electro mechanical actuation," in *IEEE International Symposium on Industrial Electronics*, 2007, pp. 1305–1310.

[68] C. Gerada and K. J. Bradley, "Integrated PM machine design for an aircraft EMA," *IEEE Transactions on Industrial Electronics*, vol. 55, no. 9, pp. 3300–3306, 2008.

[69] D. van den Bossche, "The A380 Flight Control Electrohydrostatic Actuators: Achievements and Lessons Learnt," in *25th International Congress of the Aeronautical Sciences*, Hamburg, Germany, 2006, pp. 1–8.

[70] J. W. Bennett, "Fault tolerant electromechanical actuators for aircraft," Ph.D. dissertation, Newcastle University, 2010. [Online]. Available: https://theses.ncl.ac.uk/dspace/handle/10443/990

[71] J. Babinski, "Condition monitoring for flight control actuation systems," in *Recent Advances in Aerospace Actuation Systems and Components*, Toulouse, France, 2007.

[72] A. Isturiz, J. Vinals, and S. Fernandez, "Development of an aeronautical electromechanical actuator with real time health monitoring capability," in *Recent Advances in Aerospace Actuation Systems and Components*, Toulouse, France, 2010.

[73] J. Maré and M. Budinger, "Comparative analysis of energy losses in servo-hydraulic, electro-hydrostatic and electro-mechanical actuators - Presentation," in *11th Scandinavian International Conference on Fluid Power*, Linköping, Sweden, 2009.

[74] A. M. Lowe, H. Fu, J. Lewe, D. N. Mavris, and S. Lee, "Architecture Analysis for Regenerative Energy Management in an Electromechanical Actuation System Design," in *AIAA Aviation Technology, Integration, and Operations (ATIO)*, Virginia Beach, USA, September 2011, pp. 1–9.

[75] S. Kim, "Modeling and fault analysis of BLDC motor based servo actuators for manipulators," in *Proceedings - IEEE International Conference on Robotics and Automation*, Pasadena, CA, 2008, pp. 767–772.

[76] S. L. Botten, C. R. Whitley, and A. D. King, "Flight Control Actuation Technology for Next-Generation All-Electric Aircraft," *Technology Review Journal*, vol. Fall/Winter, pp. 55–68, 2000.

[77] T. M. Jahns and R. C. van Nocker, "Electric controls for a high-performance EHA using an interior permanent magnet motor drive,"

in *IEEE Proceedings of the National Aerospace and Electronics Conference*, vol. 1, 1989, pp. 346–354.

[78] J. Wang, Z. Zhao, and X. Sun, "Comparisons of electric machines used for the electro-mechanical actuation systems in all-electric airplane," in *Sixth International Conference on Electrical Machines and Systems*, vol. 2, 2003, pp. 665–668.

[79] R. M. Crowder, *Electric Drives and Electromechanical Systems*. Butterworth-Heinemann, 2006, vol. 1st.

[80] P. Wheeler, W. C, and G. Towers, "Design and reliability of a rudder EMA with an integrated permanent magnet machine and matrix converter drive," in *Recent Advances in Aerospace Actuation Systems and Components*, Toulouse, France, 2007.

[81] M. E. Elbuluk and M. D. Kankam, "Motor drive technologies for the power-by-wire (PBW) program: options, trends and tradeoffs," *IEEE Aerospace and Electronic Systems Magazine*, 1995.

[82] M. E. Elbuluk and M. D. Kankam, "Speed sensorless induction motor drives for electrical actuators: schemes, trends and tradeoffs," in *IEEE Proceedings of the National Aerospace and Electronics Conference*, vol. 1, 1997, pp. 137–144.

[83] J. Conard, E. Gilson, and F. Labrique, "Sensorless Speed Control of an Asynchronous Motor - a Military Aircraft Application," in *Recent Advances in Aerospace Actuation Systems and Components*, Toulouse, France, 2004.

[84] M. Torabzadeh-Tari, "Analysis of Electro-Meachanical Actuator Systems in More Electric Aircraft Applications," Ph.D. dissertation, Royal Institute Of Technology, Stockholm, 2005. [Online]. Available: http://urn.kb.se/resolve?urn=urn:nbn:se:kth:diva-255

[85] T. A. Haskew and D. E. Schinstock, "Optimal design of electromechanical actuators for active loads," *IEEE/ASME Transactions on Mechatronics*, vol. 3, no. 2, pp. 129–137, 1998.

[86] Exlar. (2012) Roller Screw Basics. [Accessed: 11/11/2012]. [Online]. Available: http://www.exlar.com/pages/3-Roller-Screw-Basics

[87] S. Grand and J. Valembois, "Electromechanical Actuators Design for Thrust Vector Control," in *Recent Advances in Aerospace Actuation Systems and Components*, Toulouse, France, 2004.

[88] M. Budinger, J. Liscouet, F. Hospital, and J. Maré, "Estimation models for the preliminary design of electromechanical actuators," *Proceedings of the Institution of Mechanical Engineers, Part G: Journal of Aerospace Engineering*, vol. 226, no. 3, pp. 243–259, Oct. 2012.

[89] S. Frischemeier, "Electrohydrostatic actuators for aircraft primary flight controls - types, modelling and evaluation," in *5th Scandinavian International Conference on Fluid Power*, Linköping, Sweden, 1997.

[90] M. Bildstein, "EHA for Flight Testing on Airbus A321 – Power losses of fix pump EHA versus variable pump EHA," in *Recent Advances in Aerospace Hydraulics*, Toulouse, France, 1998.

[91] Y. Ji, L. Qiu, Z. Wang, and X. Qi, "Research on pump and valve combined scheme of EHA," in *Recent Advances in Aerospace Actuation Systems and Components*, Toulouse, France, 2007.

[92] R. Rammer, P. Konstanzer, T. C. Lüth, and P. Jänker, "Potential of piezo hydraulic actuators for aerospace," in *Recent Advances in Aerospace Actuation Systems and Components*, Toulouse, France, 2007.

[93] A. Arnaud, "An approach to EHA standardisation," in *Recent Advances in Aerospace Hydraulics*, Toulouse, France, 1998.

[94] British Standards Institution, *Aerospace - Electrohydrostatic actuator (EHA) - Characteristics to be defined in procurement specifications*, British Standards Institution Std., 2011.

[95] B. Thoraval, "Flight Control EHAs: Towards high powers," in *Recent Advances in Aerospace Hydraulics*, Toulouse, France, 1998.

[96] D. G. Moorhouse, M. Carl, and M. Bildstein, "Electro hydrostatic actuator for primary flight controls of very large aircraft," in *Recent Advances in Aerospace Actuation Systems and Components*, Toulouse, France, 2001.

[97] A. Nintzel, "Design study for an electrohydrostatic actuator for an A330/A340 inboard aileron," in *Recent Advances in Aerospace Actuation Systems and Components*, Toulouse, France, 2001.

[98] D. van den Bossche, "'More electric' control surface actuation, a standard for the next generation of transport aircraft," *Control*, September 2004.

[99] X. Le Tron. (2007) A380 Flight Controls Overview. DGLR. [Accessed: 19/10/2012]. [Online]. Available: http://www.fzt.haw-hamburg.de/pers/Scholz/dglr/hh/text_2007_09_27_A380_Flight_Controls.pdf

[100] M. Todeschi, "A380 flight control actuation - Lessons learned on EHAs design," in *Recent Advances in Aerospace Actuation Systems and Components*, Toulouse, France, 2007.

[101] T. Ford, "Actuation systems development," *Aircraft Engineering and Aerospace Technology*, vol. 70, no. 4, pp. 265–270, 1998.

[102] R. M. Crowder and C. J. Maxwell, "Simulation of a prototype electrically powered integrated actuator for civil aircraft," *Proceedings of the Institution of Mechanical Engineers, Part G: Journal of Aerospace Engineering*, vol. 211, no. 6, pp. 381–394, 1997.

[103] K. Kang, M. Pachter, C. H. Houpis, and S. Rasmussen, "Modeling and control of an electro-hydrostatic actuator," in *IEEE Proceedings of the National Aerospace and Electronics Conference*, vol. 1, 1995, pp. 545–556.

[104] V. Pastrakuljic, "Design and modeling of a new electro hydraulic actuator," Ph.D. dissertation, University of Toronto, 1995. [Online]. Available: http://www.nlc-bnc.ca/obj/s4/f2/dsk3/ftp04/MQ45467.pdf

[105] R. Kang, Z. Jiao, and S. Wu, "The nonlinear accuracy model of electro-hydrostatic actuator," in *2008 IEEE Conference on Robotics, Automation and Mechatronics*, 2008, pp. 107–111.

[106] R. Kang, J. Maré, and Z. Jiao, "Nonlinear Modeling and Control Design of Electro-Hydrostatic Actuator," *Proceedings of the JFPS International Symposium on Fluid Power*, pp. 665–670, 2008. [Online]. Available: http://www.jfps.jp/proceedings/toyama2008/pdf/p2-15.pdf

[107] L. Dinca, J. Corcau, M. Lungu, and A. Tudosie, "Mathematical Models and numerical simulations for electro-hydrostatic servo-actuators," *International Journal of Circuits, Systems and Signal Processing*, vol. 2, no. 4, pp. 229–238, 2008.

[108] B. Johansson and P. Krus, "Object-oriented and distributed modelling of a multi-domain aircraft actuation system," in *Proceedings of The*

Fifth International Conference on Fluid Power Transmission and Control, Hangzhou, China, 2001, pp. 344–349.

[109] S. Miller. (2008) Electrical and Hydraulic actuation of an aileron. [Accessed: 15/7/2009]. [Online]. Available: http://www.mathworks.com/matlabcentral/fileexchange/19621

[110] K. Li and S. Wang, "Multidisciplinary modeling method and simulation for Electro-Hydrostatic Actuator," *2010 IEEE Conference on Industrial Electronics and Applications*, pp. 544–548, Jun. 2010.

[111] M. Garrison and S. Steffan, "Two-fault tolerant electric actuation systems for space applications," in *Collection of Technical Papers - AIAA/ASME/SAE/ASEE 42nd Joint Propulsion Conference*, vol. 8, 2006, pp. 5949–5964.

[112] B. Waffner, "Modular Triple-Simplex redundant EHA developed for MOOG R&D," in *Recent Advances in Aerospace Hydraulics*, Toulouse, France, 1998.

[113] L. Siivonen, J. Aaltonen, M. Linjama, and M. Vilenius, "Fault-tolerant control of EHA with digital hydraulic valve system," in *Recent Advances in Aerospace Actuation Systems and Components*, Toulouse, France, 2007.

[114] V. A. Skormin and J. Apone, "On-line diagnostics of a variable displacement pump of a flight actuation system," in *IEEE Proceedings of the National Aerospace and Electronics Conference*, vol. 1, 1995, pp. 503–510.

[115] B. Johansson, J. A. Anderson, and P. Krus, "Thermal modelling of an electro-hydrostatic actuation system," in *Recent Advances in Aerospace Actuation Systems and Components*, Toulouse, France, 2001.

[116] W. Takebayashi and Y. Hara, "Thermal Design Tool for EHA," in *Recent Advances in Aerospace Actuation Systems and Components*, Toulouse, France, 2004.

[117] J. A. Anderson, "Variable displacement electro-hydrostatic actuator," in *IEEE Proceedings of the National Aerospace and Electronics Conference*, vol. 2, 1991, pp. 529–534.

[118] F. De Bona and G. Jacazio, "Simulation of mechanical drives with generalized power losses," *Mathematical and Computer Modelling*, vol. 11, pp. 1178–1182, 1988.

[119] D. Olaru, G. C. Puiu, L. C. Balan, and V. Puiu, "A new model to estimate friction torque in a ball screw system," *Product Engineering*, pp. 333–346, 2005.

[120] G. C. Puiu, D. Olaru, and V. Puiu, "Friction torque and efficiency in ball-screw systems," *Acta Tribologica*, vol. 17, pp. 25–29, 2009.

[121] J. Suše, "A Study on the Ball Screw Friction Torque," in *Students Conference STC2011*. Prague: Czech Technical University, 2011.

[122] P. Kumar and M. Khonsari, "On the role of lubricant rheology and piezo-viscous properties in line and point contact EHL," *Tribology International*, vol. 42, no. 11-12, pp. 1522–1530, Dec. 2009.

[123] T. A. Harris and M. N. Kotzalas, *Essential concepts of bearing technology*, 5th ed. CRC Press, 2006.

[124] J. Wensing, "On the dynamics of ball bearings," Ph.D. dissertation, University of Twente, 1998. [Online]. Available: http://doc.utwente.nl/32063

[125] C. Hős, "Dynamic Behaviour of Hydraulic Drives," Ph.D. dissertation, Budapest University of Technology and Economics, 2005.

[126] M. Kim and S. Chung, "Friction identification of ball-screw driven servomechanisms through the limit cycle analysis," *Mechatronics*, vol. 16, no. 2, pp. 131–140, Mar. 2006.

[127] A. Kamalzadeh, "Precision control of high speed ball screw drives," Ph.D. dissertation, University of Waterloo, 2008. [Online]. Available: http://www.uwspace.uwaterloo.ca/handle/10012/4189

[128] V. Lampaert, J. Swevers, and F. Al-Bender, "Experimental comparison of different friction models for accurate low-velocity tracking," in *Proceedings of the 10th Mediterranean Conference on Control and Automation*, Lisbon, Portugal, 2002.

[129] W. Karam, "Générateurs de forces statiques et dynamiques à haute puissance en technologie électromagnétique," Ph.D. dissertation, University of Toulouse, 2007, [French]. [Online]. Available: http://eprint.insa-toulouse.fr/archive/00000182/

[130] W. Karam and J. Maré, "Modelling and simulation of mechanical transmission in roller-screw electromechanical actuators," *Aircraft Engineering and Aerospace Technology*, vol. 81, no. 4, pp. 288–298, 2009.

[131] V. J. Majd and M. A. Simaan, "A continuous friction model for servo systems with stiction," in *IEEE Conference on Control Applications*, 1995, pp. 296–301.

[132] J. Maré, "System level modelling of mechanical losses in actuators," in *Proceedings of the 20th International Conference on Hydraulics and Pneumatics*, Prague, Czech Republic, 2008.

[133] J. Maré, "Friction modelling and simulation at system level: a practical view for the designer," *Proceedings of the Institution of Mechanical Engineers, Part I: Journal of Systems and Control Engineering*, vol. 226, no. 6, pp. 728–741, Apr. 2012.

[134] S. Lauckner, "Thermal Analysis and Simulation of the A380 Hydraulic System," in *Recent Advances in Aerospace Actuation Systems and Components*, Toulouse, France, 2004.

[135] B. Etkin and T. Teichmann, *Dynamics of Flight: Stability and Control*, 3rd ed. Wiley, 1996.

[136] M. V. Cook, *Flight dynamics principles*. Butterworth-Heinemann, 2007.

[137] D. Hull, *Fundamentals of airplane flight mechanics*. Springer, 2007.

[138] A. Tewari, *Atmospheric and Space Flight Dynamics: Modeling and Simulation with MATLAB and Simulink*. Birkhäuser, 2007.

[139] R. W. Beard and T. W. McLain, *Small unmanned aircraft: Theory and practice*. Princeton University Press, 2012.

[140] Mathworks. (2012) 6DoF (Euler Angles). [Accessed: 27/11/2012]. [Online]. Available: http://www.mathworks.co.uk/help/aeroblks/6dofeulerangles.html

[141] G. Fillola, M. Le Pape, and M. Montagnac, "Numerical simulations around wing control surfaces," in *24th International Congress of the Aeronautical Sciences*, 2004. [Online]. Available: http://www.icas.org/ICAS_ARCHIVE_CD1998-2010/ICAS2004/PAPERS/028.PDF

[142] B. Galbraith. (2004) DATCOM Predicted Aerodynamic Model. [Accessed: 15/10/12]. [Online]. Available: www.holycows.net

[143] T. Melin. (2010) Tornado Vortice Lattice Method. [Accessed: 21/2/2011]. [Online]. Available: http://www.redhammer.se/tornado/

[144] D. Scholz, "Equations for a preliminary actuator design," Deutsche Airbus, Tech. Rep. TN-EV52-360/91, 1991. [Online]. Available: Equationsforapreliminaryactuatordesign

[145] D. van den Bossche, "A380 primary flight control actuation system," in *Recent Advances in Aerospace Actuation Systems and Components*, Toulouse, France, 2001.

[146] A. A. Lambregts, "Automatic Flight Controls," Federal Aviation Administration, Tech. Rep. KNVLPAP6, 1998. [Online]. Available: https://faaco.faa.gov/attachments/KNVLPAP6.pdf

[147] A. A. Lambregts, "Automatic Flight Control Systems - An interactive Video Teletraining and Self-Study Course," Federal Aviation Administration, Tech. Rep., 1999.

[148] A. A. Lambregts, "Generalized Automatic and Augmented Manual Flight Control," Berlin Technical University, Tech. Rep., May 2006.

[149] A. A. Lambregts, "Functional integration of vertical flight path and speed control using energy principles," *Proceedings of the 1st Annual NASA Aircraft Controls Workshop*, pp. 389–409, 1983.

[150] K. R. Bruce, "Design and Verification by Nonlinear Simulation of a Mach/CAS Control Law for the NASA TSRV," Boeing Commercial Airplane Company, Tech. Rep. NASA CR-178029, 1986.

[151] K. R. Bruce, "Integrated autopilot/autothrottle for the NASA TSRV B-737 aircraft: design and verification by nonlinear simulation," Tech. Rep. NASA CR-4217, 1989.

[152] K. R. Bruce, J. R. Kelly, and L. H. Person, "NASA B737 flight test results of the total energy control system," Seattle, Washington, Tech. Rep. NASA-CR-178285, 1987.

[153] P. Chudy and P. Rzucidlo, "TECS/THCS based flight control system for general aviation," in *AIAA Modeling and Simulation Technologies Conference*, 2009.

[154] M. H. J. Amelink, "Ecological Automation Design, Extending Work Domain Analysis," Ph.D. dissertation, TU Delft, 2010.

[155] M. Eladl, K. Eltohamy, B. Hill, T. Horne, B. Krasnovskiy, K. Leiphon, and S. Taylor, "Advanced Guidance and Control - Operational and

Safety Benefits," Federal Aviation Administration, Tech. Rep., June 2008.

[156] I. Kaminer and P. R. O'Shaughnessy, "4D-TECS Integration for NASA TSRV Airplane," Boeing Commercial Airplane Company, Seattle, Washington, Tech. Rep. June, 1989.

[157] R. Srivatsan, "Development and Simulation of an Advanced Total Energy Control System (Adv-TECS)," NASA, Tech. Rep. NASA-CR-198296, March 1996.

[158] R. Rysdyk and R. K. Agarwal, "Nonlinear Adaptive Flight Path and Speed Control Using Energy Principles," in *AIAA Guidance, Navigation, and Control Conference and Exhibit*, Monterey, California, 2002, pp. 1–11.

[159] D. C. Sederstrom, N. R. Zagalsky, and R. C. McLane, "Energy/Energy Rate Meter for Energy Management in Flight," Honeywell, Tech. Rep., 1973.

[160] A. A. Lambregts, R. Rademaker, and E. Theunissen, "A new ecological primary flight display concept," in *2008 IEEE/AIAA 27th Digital Avionics Systems Conference*, October 2008, pp. 1–20.

[161] L. F. Faleiro and A. A. Lambregts, "Analysis and tuning of a Total Energy Control System control law using eigenstructure assignment," *Aerospace Science and Technology*, vol. 3, no. 3, pp. 127–140, Apr. 1999.

[162] L. F. Faleiro and R. W. Pratt, "Eigenstrueture assignment applied to the design of an autopilot function for a civil aircraft," in *Flight control systems: practical issues in design and implementation*. Institution of Engineering and Technology, 2000.

[163] G. Looye, H. Joos, and D. Willemsen, "Application of an Optimization-based Design Process for Robust Autoland Control Laws," in *AIAA Guidance, Navigation, and Control Conference and Exhibit*, Montreal, Canada, 2001, pp. 1–11.

[164] G. Looye and H. Joos, "Design of autoland controller functions with multiobjective optimization," in *AIAA Guidance, Navigation, and Control Conference and Exhibit*, Monterey, California, 2002, pp. 1–11.

[165] M. A. Bruzzini, "Development of a TECS Control Law for the Lateral Directional Axis of the McDonnell Douglas F-15 Eagle," Ph.D. dissertation, University of Washington, 1994.

[166] P. Chudy and P. Rzucidlo, "Simulators for Pilot Assisting Module of Advanced Light Aircraft Concept," *Archive of Mechanical Engineering*, vol. LVIII, no. 3, pp. 275–289, 2011.

[167] P. Chudy and P. Rzucidlo, "Real-time simulations of environmentally friendly flight control system," in *9th IEEE International Symposium on Applied Machine Intelligence and Informatics*, Smolenice, Slovakia, 2011, pp. 161–164.

[168] B. Durham, "Equations of Motion," in *AOE 5214: Aircraft Dynamics and Control (Lecture Notes)*. Virginia Technical University, 2004, ch. 7.

[169] D. Allerton, *Principles of Flight Simulation*. Wiley, 2009.

[170] M. Casillas. (2010) Half-Space Test. [Accessed: 18/6/2012]. [Online]. Available: http://www.miguelcasillas.com/?p=4318/06/2012

[171] D. Scholz, "Development of a CAE-tool for the design of flight control and hydraulic systems," in *SAE AeroTech Congress*, Birmingham, UK, 1995.

[172] SAE International, "Description of Actuation Systems for Aircraft with Fly-By-Wire Flight Control Systems," *Society of Automotive Engineers*, no. AIR4253A, 2001.

[173] R. Poley, "DSP control of electro-hydraulic servo actuators," *Texas Instruments Application Report*, pp. 1–26, January 2005.

[174] Eaton Aerospace, "Vickers Inline Pump (Model PV3-240-2F / PV3-240-2G)," Tech. Rep., 2012.

[175] W. J. Thayer, "Transfer functions for Moog servovalves," MOOG, Tech. Rep., 1965.

[176] MOOG, "G77X Series Servovalves," Tech. Rep. [Online]. Available: http://www.moog.com/literature/ICD/g77xseriesvalves.pdf

[177] D. Kaiser, "Fundamentals of servo motion control," Parker Compumotor, Tech. Rep., 2002. [Online]. Available: http://www.compumotor.com/whitepages/ServoFundamentals.pdf

[178] X. Du, R. Dixon, R. M. Goodall, and A. C. Zolotas, "Modelling and control of a high redundancy actuator," *Mechatronics*, vol. 20, no. 1, pp. 102–112, 2010.

[179] Parker, "M Series Servo Motors Catalogue," Tech. Rep. [Online]. Available: http://divapps.parker.com/divapps/emn/prior_version_compumotor/cat/english/M_Series.pdf

[180] J. Roskam, *Airplane Design Vol. VI*. Roskam Aviation & Engineering Corporation, 1987.

[181] ElectroCraft. SCA-SS-70: ElectroCraft CompletePower Drives. [Accessed: 25/9/2011]. [Online]. Available: http://www.electrocraft.com/products/drives/SCA-SS-70/

[182] Parker. (2010) Compact EHA. [Accessed: 20/8/2010]. [Online]. Available: http://www.compact-eha.com

[183] MecVel. MecVel ALI2. [Accessed: 11/3/2013]. [Online]. Available: http://www.mecvel.com/public/ADC-ALI2.html

[184] RoboteQ. RoboteQ AX1500. [Accessed: 11/3/2013]. [Online]. Available: http://roboteq.com/brushed-dc-motor-controllers/ax1500-cost-optimized-2-x-30a-brushed-dc-motor-controller

[185] D. Lauria, "Damage estimation by simulated annealing for model-based PHM of aeronautical electro-mechanical actuators," Ph.D. dissertation, Politecnico di Torino, 2010.

[186] J. Herzog. (2012) A320 Enhanced (A320E) prototype (F-WWIQ) with sharklets at ILA Berlin Air Show 2012. [Accessed: 4/3/2013]. [Online]. Available: http://commons.wikimedia.org/wiki/File:F-WWIQ_Airbus_A320_sharklet_ILA_2012_07.jpg

[187] E. Obert, R. Slingerland, D. Leusink, T. van den Berg, J. Koning, J. van Tooren, and T. H. D. A. der Luchtvaart-en Ruimtevaarttechniek, *Aerodynamic Design of Transport Aircraft*. IOS Press, 2009.

[188] T. McGeer and J. Vagners, "Flying the Atlanticwithout a pilot," *GPS World*, no. February, 1999.

[189] Volz Servos. DA 15-BLDC Data Sheet. [Accessed: 3/8/2012]. [Online]. Available: http://www.volz-servos.com/en/download/files/data-sheets/DA_15-BLDC_en-uni.pdf

[190] AAI Corporation. (2010) Aerosonde Mark 4.7: Redefining Expeditionary. [Accessed: 20/2/2013]. [Online]. Available: http://www.aerosonde.com/pdfs/aerosonde-mark-47.pdf

[191] G. Goebel. (2009) Insitu Aerosonde "Laima" on display at the Seattle Museum of Flight. [Accessed: 4/3/2013]. [Online]. Available: http://en.wikipedia.org/wiki/File:Aerosonde_Laima_bottom_view.jpg